SEARCHES FOR NEUTRINOS FROM GAMMA RAY BURSTS WITH THE AMANDA-II AND ICECUBE DETECTORS

by

ERIK ALBERT STRAHLER

A dissertation submitted in partial fulfillment of the
requirements for the degree of

DOCTOR OF PHILOSOPHY
(PHYSICS)

at the

UNIVERSITY OF WISCONSIN – MADISON

2009

SEARCHES FOR NEUTRINOS FROM GAMMA RAY BURSTS WITH THE AMANDA-II AND ICECUBE DETECTORS

Erik Albert Strahler

Under the supervision of Professor Albrecht Karle
At the University of Wisconsin — Madison

Gamma-ray bursts (GRBs) are the most energetic phenomenon in the universe, releasing isotropic equivalent energies of $\mathcal{O}(10^{52})$ ergs over short time scales. While it is possible to wholly explain the keV-GeV observed photons by purely electromagnetic processes, it is natural to consider the implications of concurrent hadronic (proton) acceleration in these sources. Such processes make GRBs one of the leading candidates for the sources of the ultra high-energy cosmic rays as well as sources of associated high energy (TeV-PeV) neutrinos. We have performed searches for such neutrinos from 85 northern sky GRBs with the AMANDA-II neutrino detector. No signal is observed and upper limits are set on the emission from these sources. Additionally, we have performed a search for 41 northern sky GRBs using the 22-string configuration of the IceCube neutrino telescope, employing an unbinned maximum-likelihood method and individual modeling of the predicted emission from each burst. This search is consistent with the background-only hypothesis and we set upper limits on the emission.

Albrecht Karle (Adviser)

High energy experimental physics has largely become a field of collaborations, and neutrino astronomy in particular involves the combined efforts of many scientists from diverse institutions. I would like to acknowledge the hard work of the many physicists in the IceCube collaboration, without whom these analyses would have been impossible.

I owe thanks to Albrecht Karle, for first interesting me in gamma-ray bursts and for advice over the years. I am grateful for the opportunity he gave me to join IceCube and contribute.

Francis Halzen provided much useful insight on matters theoretical, and Gary Hill was of great help with many questions regarding statistics and event selection methods. Chad Finley helped me to (finally) figure out the log-likelihood analysis, and was a great sounding board for working out problems with signal weighting. Jon Dumm contributed invaluable advice on scripts and IceCube software.

The members of the GRB working group deserve special thanks, especially Ignacio Taboada. He was ever ready with suggestions, feedback, and advice. In analyzing IceCube data, I have been very fortunate to collaborate with Alexander Kappes and Phil Roth. Working with them has been more productive (and much more enjoyable) than it would have been alone.

Thanks of a different sort goes to Kael Hanson and Hagar Landsman. Kael involved me with DOM testing when I first joined the collaboration and Hagar helped me learn the intricacies of the testing framework. Without them I never would have had the opportunity to visit the south pole, one of the most unique experiences of my life.

Finally, I would like to thank my family and friends, both for encouraging me in my pursuit of physics, and probably more importantly, for providing me with so many great experiences through my years in Madison.

Contents

List of Tables

List of Figures

Chapter 1

Introduction

High energy neutrinos provide a unique perspective on the cosmos. As neutral and weakly interacting particles they point back to their sources over all energy ranges and distance scales. This can be contrasted to cosmic rays which are bent in galactic and intergalactic magnetic fields, or photons, which can be blocked by intervening matter or attenuated at high energies via pair production with background light. Thus neutrinos allow us to view the deep universe with a clarity unparalleled in other channels. In addition, the detection of astrophysical high energy neutrinos would be a clear signature of sources of hadronic acceleration. Such a detection would have extremely important consequences in the astrophysics community, as it could explain the origins of the mysterious ultra-high energy cosmic rays (UHECR). One of the most likely candidates for the production of cosmic neutrinos are the enigmatic Gamma-Ray Bursts. Extremely brilliant emitters of high energy photons over time scales ranging from tenths to thousands of seconds, GRBs have a rich observational history and well developed theories with predictions for neutrino fluxes of energy MeV-EeV.

1.1 The Cosmic Ray Connection

The cosmic rays are composed mostly of protons, with a small fraction of heavier elements that varies with energy. They are distributed nearly isotropically over the sky and universally follow a power law spectrum over many decades in energy (see Fig. 1.1). This spectrum falls as $E^{-2.7}$ up to $\sim 4\,\mathrm{PeV}$, where is steepens to $E^{-3.7}$. This change is spectral slope is known as the *knee*. Through the knee, the cosmic rays are thought to be galactic in origin, likely accelerated in supernova remnants (see section 1.1.1). A good phenomenological description of the steepening is a many-knee model (*poly gonato* from Greek) [1, 2]. Each element exhibits a cutoff in its spectrum due to the maximum acceleration possible in SNR, but heavier elements extend to higher energy. When added together, the spectrum is well modeled up to $\sim 10^{18.5}$ eV. At this point it hardens to $E^{-2.7}$ again, a feature known as the *ankle*. The ultra-high energy cosmic rays above the ankle are thought to be due to extragalactic sources. At the highest energies they will be suppressed by interactions with the cosmic microwave background (GZK effect).

Protons accelerated to ultra-high energy will produce neutrinos through interactions with surrounding matter. While the protons will be isotropized by intervening magnetic fields (except at the very highest energies), the neutrinos will stream straight to the Earth. If we can detect these high energy neutrinos we will unveil the sources of the UHECR.

1.1.1 Fermi Acceleration of Particles

First proposed in 1949, Fermi suggested that charged particles would elastically scatter off turbulent variations in magnetic fields, stochastically gaining energy. Let us follow his work and determine the energy change in each interaction. A further description may be found in [4].

Let us assume that the "magnetic mirrors" move randomly and have a characteristic velocity V while the particle moves with velocity v. We further assume that the clouds of gas containing these mirrors are massive and thus are essentially unaffected by collisions with particles. We thus choose the center of momentum frame of the cloud for our discussion. The particle energy incident at angle θ with the magnetic mirror is then given by

$$E' = \gamma(E + Vp\cos\theta) \tag{1.1}$$

and the momentum normal to the mirror surface is

$$p'_x = p'\cos\theta' = \gamma\left(p\cos\theta + \frac{VE}{c^2}\right) \tag{1.2}$$

In the elastic collision, energy is conserved in the center of momentum frame, and momentum is inverted. In the observer's frame this yields a final energy

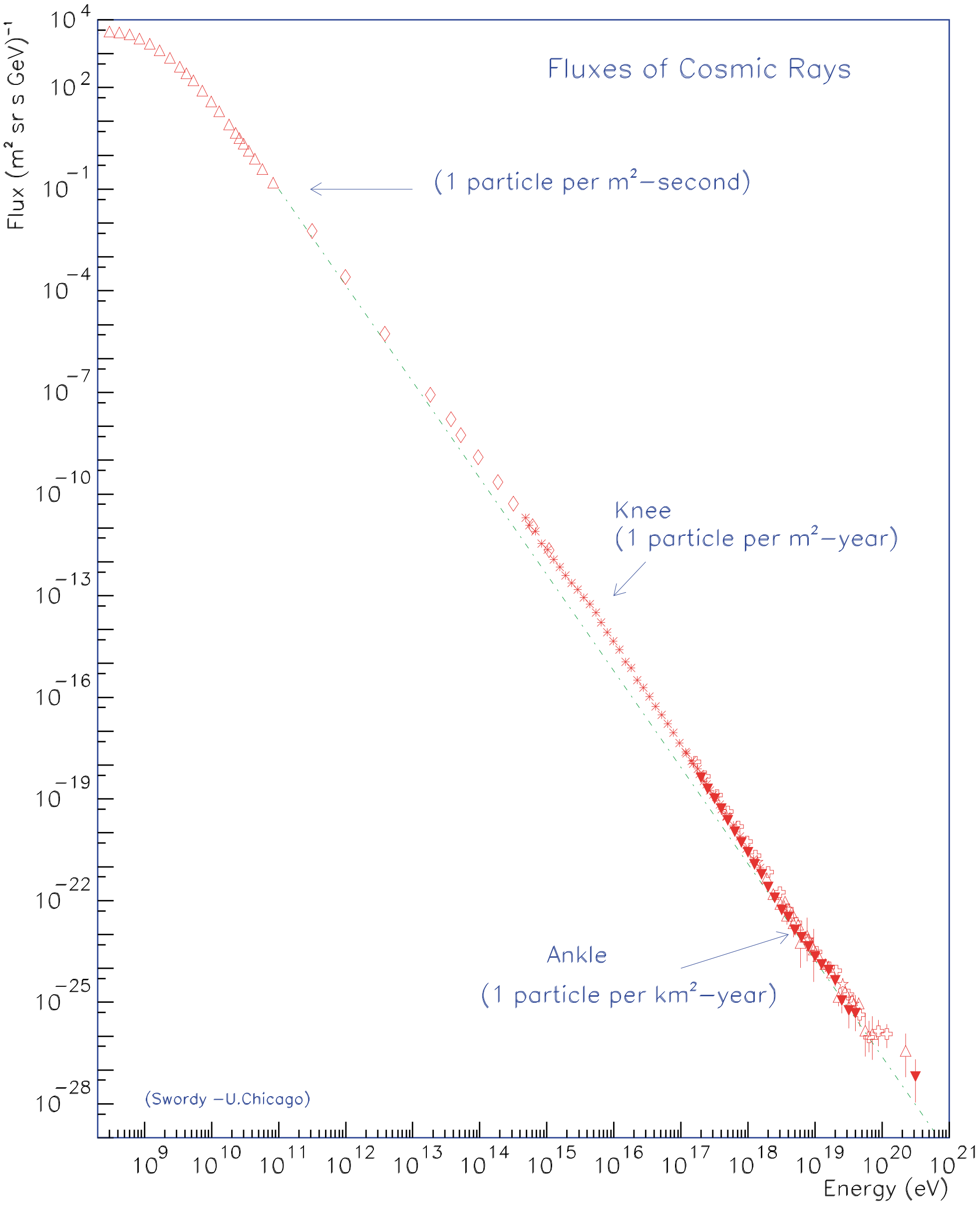

Figure 1.1: The cosmic ray energy spectrum at earth. Below the knee, the cosmic rays are thought to be galactic in origin. In the high energy tail, sources are unknown. (from [3])

$$E'' = \gamma(E' + V p'_x) \tag{1.3}$$

$$= \gamma^2 E \left[1 + \frac{2Vv\cos\theta}{c^2} + \left(\frac{V}{c}\right)^2 \right] \tag{1.4}$$

The change in energy is thus

$$E'' - E = \Delta E = \frac{2Vv\cos\theta}{c^2} + 2\left(\frac{V}{c}\right)^2 \tag{1.5}$$

where we have expanded to second order in V/c. Note that to first order the total energy change tends to zero, as the gain of head-on collisions is canceled by the loss in following collisions. This is not quite true, as the rates are proportional to the relative velocities of approach, $v + V\cos\theta$ and $v - V\cos\theta$. Thus, slightly more head-on collisions occur, yielding a net increase in energy. Averaging over all angles of incidence yields a total fractional energy change

$$\frac{\Delta E}{E} = \frac{8}{3}\left(\frac{V}{c}\right)^2 \tag{1.6}$$

This is Fermi's famous result, that the energy increases only with the 2nd order of V/c. While this mechanism indeed produces a power law, it is deficient for explaining the highest energy cosmic rays. The velocities of the clouds containing the mirrors are typically small relative to light, and the mean free path of cosmic rays is large, hence it would take an extremely long time to accelerate particles to the appropriate energies. Given turbulence on a sufficiently small scale such as in supernova remnants this can be overcome. However, we must also account for ionization losses which scale with energy. When combined, 2nd order Fermi acceleration cannot account for the cosmic ray spectrum.

If we could somehow find a situation in which every collision was head-on, Eq. 1.5 tells us that the energy would increase in every case and be proportional to V/c. This is the so-called 1st order Fermi acceleration. This can be achieved if strong shocks exist in the accelerator. There are two approaches to the problem; considering the diffusion equation that governs the evolution of the momentum distribution around the shocks [5], and following the behavior of individual particles [6].

We adopt the latter approach in the following.

Shocks occur when exploding gas (from e.g. a supernova) travels faster than the sound speed of the medium. These shocks travel through regions containing high energy particles moving in magnetic fields. The particles barely notice the presence of the shocks since they have much higher velocities and the shocks are thin compared to their gyroradii. Elastic scattering of the particles in turbulent magnetic fields both in front of and in the wake of the shock isotropizes their velocities. Thus, for a shock traveling at speed U, in the shock rest frame the upstream particles will appear to be approaching with that same speed. Energy, mass, and momentum must be conserved across the shock front, and this allows us to determine the resulting compression. For strong shocks the relation between the gas densities in the downstream and upstream regions is given by

$$\frac{\rho_2}{\rho_1} = \frac{\gamma_H + 1}{\gamma_H - 1} \tag{1.7}$$

Here γ_H is the ratio of specific heats and is 5/3 for a fully ionized plasma. Thus the compression ratio is a factor of 4. Conservation of mass implies

$$\begin{aligned} \rho_1 v_1 &= \rho_2 v_2 \\ v_2 &= \frac{1}{4} v_1 \end{aligned} \tag{1.8}$$

In the shock rest frame, the upstream gas has velocity $-U$ while the downstream gas has velocity $-1/4U$. We now consider both upstream and downstream regions individually. In the rest frame of the upstream gas (adding U to each side), the downstream particles approach the shock front with velocity $3/4U$. Similarly, in the rest frame of the downstream particles (adding $1/4U$ to each side), the upstream particles approach the shock front with speed $3/4U$. Due to the compressive properties of the shock, particles have head-on collisions no matter whether they are in the upstream or downstream regions, and those collisions occur with the exact same velocity relative to the shock. This is shown schematically in Fig. 1.2.

We can determine the fractional energy increase in each shock crossing in much the same way

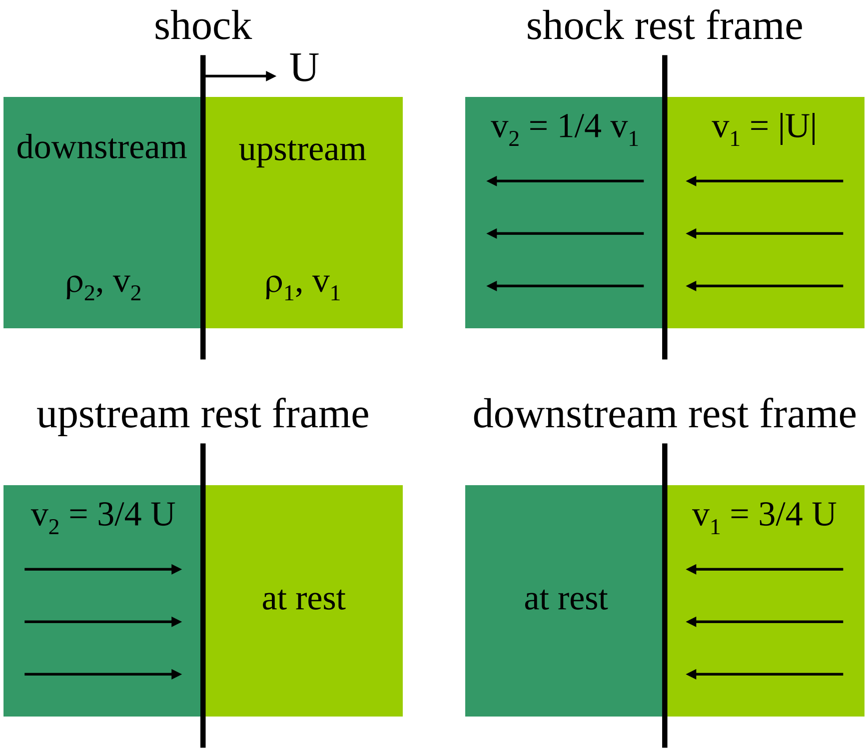

Figure 1.2: Schematic showing the process for 1st order Fermi acceleration across shock fronts. Top left panel depicts the shock propagating with velocity U through a high energy plasma. Top right panel shows the rest frame of the shock and the compression between the upstream and downstream regions. Because the velocities are isotropized by magnetic fluctuations, the relative velocity of the upstream region is given by U. Bottom left and right panels show the rest frame of the upstream and downstream regions, respectively. In each case, particles crossing the shock front undergo head-on collisions with gas at relative velocity $3/4U$.

as for the 2nd order mechanism. Encountering gas of velocity $V = 3/4U$, the energy increases by

$$E' = \gamma(E + p_x V) \tag{1.9}$$

In all the above we have taken the shocks to be non-relativistic while the particles are. Taking this into account, we arrive at

$$\frac{\Delta E}{E} = \frac{V}{c}\cos\theta \tag{1.10}$$

We average over incidence angles and probabilities to find

$$\langle\frac{\Delta E}{E}\rangle = \frac{4}{3}\frac{V}{c} \tag{1.11}$$

for each full crossing from the upstream to the downstream region and back. If we denote the energy increase in each interaction by $E = \beta E_0$ then

$$\beta = 1 + \frac{4}{3}\frac{V}{c} \tag{1.12}$$

Let us now assume that after each collision the particle has a probability P to pass through the shock front again. After k collisions we will then have a number of particles $N = P^k N_0$ with characteristic energy $E = \beta^k E_0$. These can be related through

$$\frac{N}{N_0} = \left(\frac{E}{E_0}\right)^{\frac{\ln P}{\ln \beta}} \tag{1.13}$$

Since N actually represents the number of particles with *at least* energy E, we then write the differential energy spectrum as

$$N(E)dE \propto \left(\frac{E}{E_0}\right)^{\frac{\ln P}{\ln \beta}-1} dE \tag{1.14}$$

We now determine the re-crossing probability P. The number of particles crossing the shocks is given by $1/4nc$ [4], where n is the number density. Conversely, in the downstream region, particles are carried away from the shock front (top right panel of Fig. 1.2). This occurs at a rate $1/4nU$. So the loss per unit time is given by U/c. We then have

$$P = 1 - \frac{U}{c} \tag{1.15}$$

We combine Eqs. 1.12 and 1.15 and plug into Eq. 1.14 to find

$$N(E)dE \propto E^{-2}dE \tag{1.16}$$

Thus we naturally arrive at a power law spectrum consistent with the observed and pervasive cosmic rays [1]. We must note, however, that there is a limit to how much acceleration is possible with this mechanism. Although much more efficient than 2nd order Fermi acceleration, the process is still slow and must combat energy loss processes. Taking this into account, we find that this process can account for cosmic ray acceleration in supernovae up to the knee. However, it is not possible to produce the highest energy cosmic rays with this method. To do so, we must employ much higher magnetic fields or larger acceleration regions [2]. We depict this in Fig. 1.3 and note that gamma-ray bursts are one of the few source classes in which the conditions for UHECR acceleration are indeed met.

---

[1] Steepening to an $E^{-2.7}$ spectrum is thought to be due to losses in the intervening space.

[2] We should also note that this discussion has been limited to non-relativistic shock acceleration. The relativistic case is much more complicated and we do not discuss it in detail here. It has the property however, of rapidly increasing the energy of particles with each crossing of the shock front and is thus appropriate for UHECR acceleration.

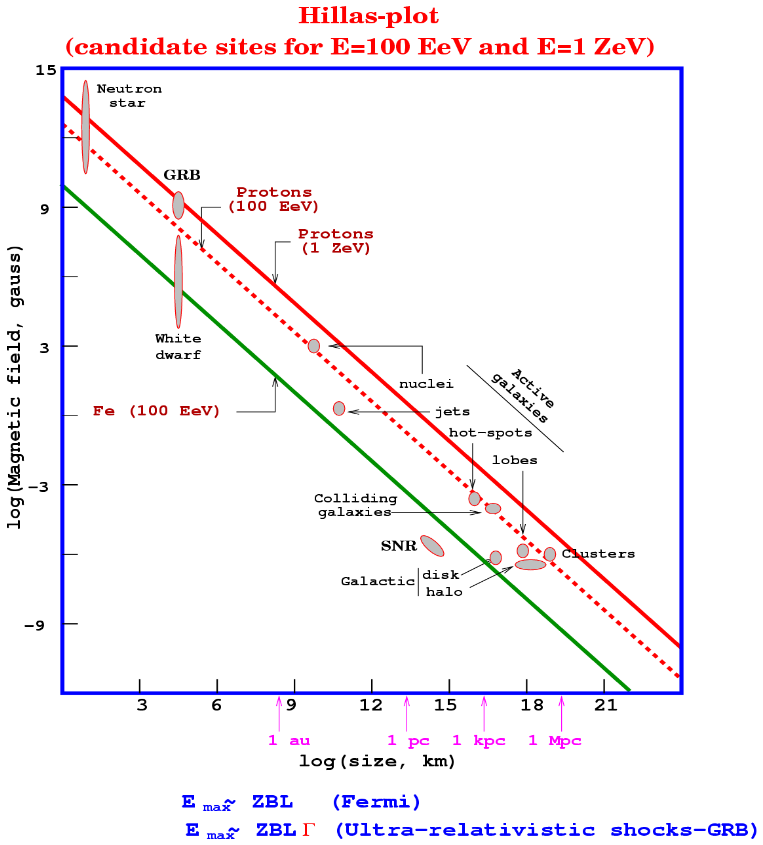

Figure 1.3: The famous Hillas diagram illustrating the relationship between magnetic fields and source size necessary to accelerate nuclei to ultra-high energies via the Fermi mechanism. (adapted from [7])

1.2 Previous Work

Previous searches for high energy neutrino emission from gamma-ray bursts have been conducted using data collected with the AMANDA and IceCube detectors. A variety of search strategies have been employed covering a range of emission models and detection channels. Triggered searches in the muon channel [8, 9, 10], triggered and rolling searches in the cascade channel [11], and analyses dedicated to single, spectacular bursts [12, 13] have all failed to detect neutrinos from GRBs. Upper limits have been set, but to date none exclude the most popular scenarios. We build on this previous body of work in the analyses presented in this thesis and place all results in context in our conclusions.

1.3 Organization of the Thesis

- Chapter 2 reviews the history of gamma-ray burst observations and presents the phenomenological framework that has been developed to explain them. We then describe the production of neutrinos in GRB explosions through photomeson interactions and detail resulting spectra occurring from the various phases of the emission.

- Chapter 3 describes the ways in which high energy astrophysical neutrinos may be detected at the earth. The process is followed through interaction, lepton production, and subsequent emission of Čerenkov radiation. Optical properties of the detection medium are considered. We discuss how the arrival times and amplitudes of the emitted light may be used to reconstruct events, and present the algorithms used in these reconstructions.

- Chapter 4 describes the satellites that observe the photon flux from GRBs and localize their positions. The AMANDA and IceCube neutrino detectors are then presented, including layout, hardware, and data acquisition systems.

- Chapter 5 explains the selection criteria for the inclusion of observed GRBs in our search. We describe the blinding procedure and the determination of emission windows. The spatial and temporal information for all bursts in our analyses are listed.

- Chapter 6 explains the process of creating simulated signals and backgrounds. The generation of primaries is described, as well as the modeling of propagation through the atmosphere and earth, energy losses, interaction, and the detector response to the emitted light.

- Chapter 7 presents a stacked search for muon neutrinos from GRBS using the AMANDA-II detector. 85 GRBs observed in the northern hemisphere in 2005-2006 are considered. Event selection and optimization of background rejection are presented in detail.

- Chapter 8 describes a search for muon neutrino emission from 41 GRBs using the 22-string configuration of the IceCube detector. An unbinned likelihood method is utilized for the first time in stacked searches for GRBs, maximizing the sensitivity of the analysis.

- Chapter 9 reviews the sources of systematic error in the analyses presented. Contributions from theory, ice properties, and hardware are considered, as well as the effect of seasonal variation in the atmospheric muon rate.

- Chapter 10 presents a summary of the work conducted in this thesis and places it in the context of previous results. Prospects for the future are discussed.

Chapter 2

Gamma-ray Bursts

Gamma-ray Bursts (GRBs) are the most energetic events in the universe, outshining all other sources over their short emission windows. Initially thought to be galactic in origin due to the fluxes observed, they are now known to occur at cosmological distances. They are one of the prime candidates for the acceleration of the highest energy cosmic rays and concurrent astrophysical neutrinos.

2.1 History

Gamma-ray bursts were discovered as a byproduct of efforts to enforce the partial test ban treaty of 1963. This treaty prohibited the testing of nuclear weapons underwater, in the atmosphere, and in space. The Vela satellites [14] were designed to detect the gamma radiation from such a nuclear detonation. The satellites were operated in pairs on opposite sides of a high circular orbit and timing information was used to determine the direction of sources. During data taking by Vela 5a and 5b in 1969, a strange phenomenon was discovered [1]; short, intense bursts of γ-rays from outside their orbits rather than within. This topology meant that the sources were astrophysical rather than terrestrial. When the data was declassified in 1973, the observations of 16 such bursts were published [15]. Shortly thereafter, a collimated gamma-ray telescope aboard the OSO-7 satellite was able to confirm the direction of one of the events [16]. The IMP-6 was able to measure spectral characteristics of the bursts [2] and determined that the emission peaked in γ-rays and was thus not just the high energy tail of some x-ray phenomenon [17]. These observations, all in rapid succession, spurred a wealth of theoretical papers about the sources of these bursts. Unfortunately this was the

---

[1] though it was not noticed in 1972 when the backlog of non-nuclear detonation γ-ray events began to be analyzed

[2] using a hard x-ray detector intended to study solar flares

beginning of an experimental dark age that would not see an end for nearly 20 years.

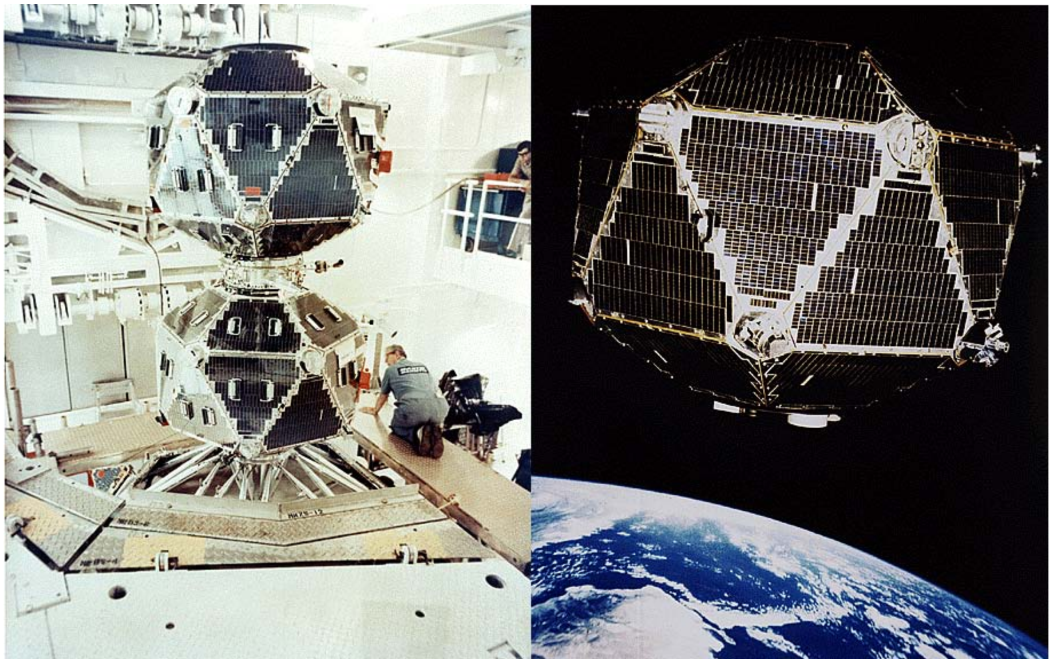

Figure 2.1: The Vela 5 satellite system. On the left is the Vela 5a and 5b pair joined before launch. On the right is the Vela 5b satellite in low Earth orbit

The Burst and Transient Source Experiment (BATSE) [18] was launched aboard the Compton Gamma Ray Observatory (CGRO) satellite on April 5, 1991. This was the first experiment dedicated to the observation of gamma ray photons associated with transients. Its energy range (20 keV - 1 MeV) and all-sky field-of-view allowed it to detect GRBs at an average rate of 1/day throughout its 9 year mission, observing 2704 GRBs in total. This high rate of detection quickly increased statistics, and studies were able to be conducted on the distributions of the GRB population. It was found that the durations of GRBs follow a bimodal distribution [19]; so-called “short” bursts with a duration $\lesssim 2\,\mathrm{s}$ and “long” bursts with a duration $\gtrsim 2\,\mathrm{s}$. This distribution can be seen in Fig. 2.2. The short bursts were found to display harder energy spectra than the long, leading to the supposition that different underlying processes were at work in the 2 classes. The second major finding was in the spatial distribution of the GRB population. Until this point, most people had thought that the bursts must be galactic in origin, due to the fluxes observed (some theories even place the source of the GRBs in the Oort Cloud). It was therefore a great surprise when BATSE observed that GRBs are distributed isotropically both in number and in fluence [20] (see Fig. 2.3. In a galactic source model, the brightest bursts would be distributed along the galactic plane. This lack of clustering gave evidence that GRBs are cosmological phenomena, which implied huge energies of $10^{50} - 10^{54}$ ergs in the case of isotropic emission from the sources.

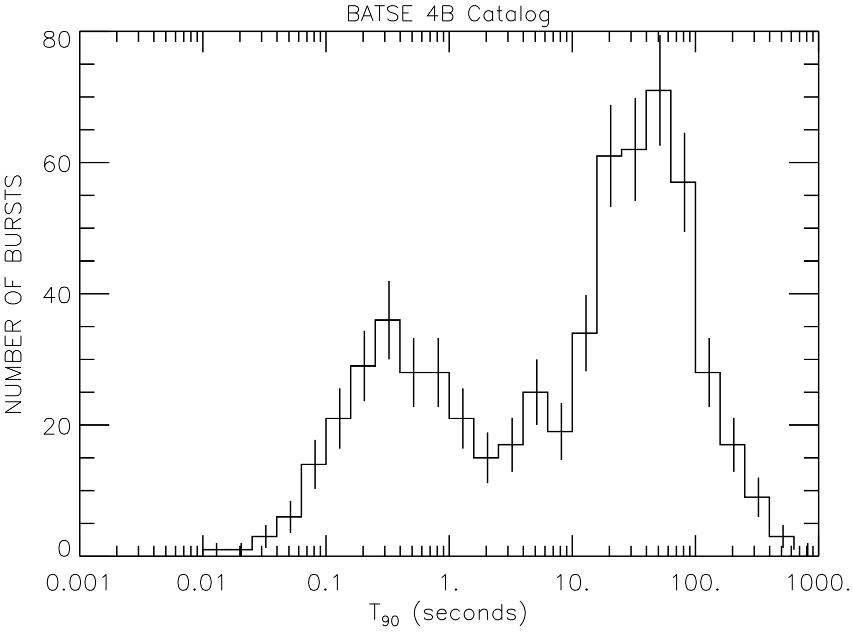

Figure 2.2: Distribution of GRB Durations for the BATSE 4B Catalog (through August 1996). Durations are given as T_{90}, the time in which 5% to 95% of the γ-ray emission occurs. The bimodal distribution separates GRBs into 2 classes; long and short (based on data from [21])

The hypothesis of cosmological origin was confirmed by the BeppoSAX satellite [22] in 1997. BeppoSAX was able to localize GRBs with arcminute precision, and more importantly, was able to distribute that information to ground-based observatories much more rapidly than had previously been achieved. In addition, they were able to make x-ray observations of GRB afterglow. These multi-wavelength afterglow observations led to the first observation of an optical counterpart to a GRB at cosmological distance [23].

The Swift satellite [24, 25] (see section 4.1.1), launched in 2004 opened a new window on understanding GRBs. It was designed to have rapid slewing capability and incorporates γ-ray, x-ray,

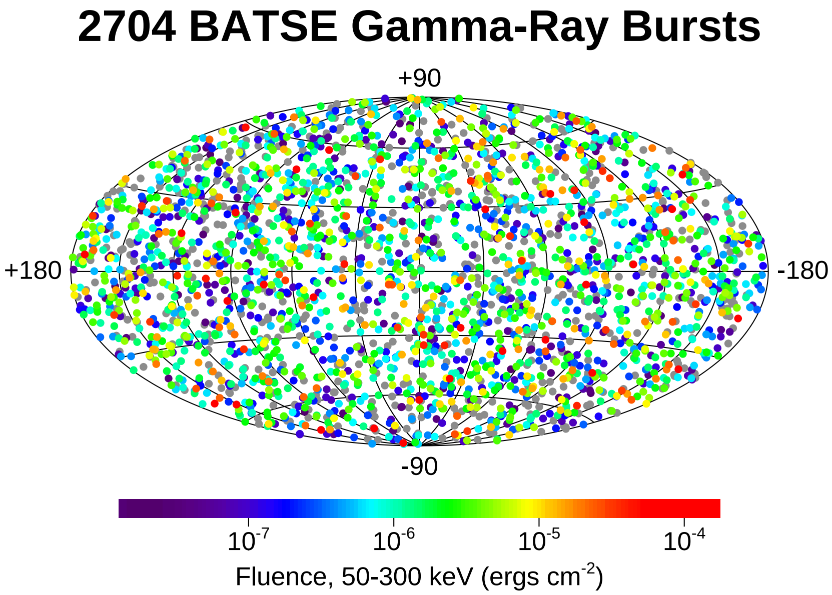

Figure 2.3: Spatial Distribution of the full BATSE GRB sample. The isotropic spatial distribution in both number and fluence implies cosmological origins. (from [18])

and ultraviolet detectors onboard. This has allowed detailed studies of the transition between the prompt and afterglow emission phases and the first measurements of afterglow emission from short GRBs [26]. Rapid dissemination of (usually) arcsecond localizations to ground-based telescopes results in redshift measurements for ∼25% of all bursts. It has been found that the GRB population extends to higher redshifts than imagined, with observed distances up to z=6.7 [27].

After nearly a decade without a full-sky GRB detector, the Fermi Gamma Space Telescope [28] (formerly GLAST) was launched in July of 2008. A true successor to CGRO, Fermi possesses both a wide field Gamma-ray Burst Monitor (GBM) and a more focused, higher precision detector (the Large Area Telescope, or LAT). The LAT is analogous to the EGRET experiment aboard CRGO, extending the energy range to 300 GeV. Fermi is able to slew to point the LAT at some GRBs detected by the GBM, thus yielding a huge potential range of energies for GRB observations. This has led to the detection of >10 GeV photons from bursts [29], raising new questions as to the source physics. With a detection rate of ∼200/yr Fermi will continue to provide valuable new data in the quest to understand the mysteries of GRBs.

2.2 Fireball Model

Long GRBs are thought to be caused by the core collapse of massive stars into black holes [30, 31]. This hypothesis is strengthened by the association of some long GRBs with abnormal type Ic Supernovae (SNe) [3]. The first such correlation was between GRB980425 and SN1998bw [32] with several other observations strengthening the connection to date. Long GRBs are always observed to occur in star-forming regions. Short GRBs, on the other hand, are thought to be associated with the merger of two compact objects (e.g. neutron stars) [33]. In either case, the accreting matter is thought to spin rapidly, creating a disk [34]. At some point, the radiation pressure exceeds the gravitational infall, and an explosion occurs, ejecting an $e^{\pm}$, γ, and baryon plasma along the rotation axis, with this fireball being fed by rapid accretion of matter from the disk. This wind accelerates to relativistic velocities and randomizes and dissipates energy via internal shocks. It is thought that the observed γ-rays are the result of synchrotron radiation from the accelerated electrons in the very high magnetic fields of the burst environment [35, 36]. Let us consider the observations that lead to this fireball phenomenology in order to better understand the physics of GRBs and why it is reasonable to expect high energy neutrino emission.

2.2.1 Energy Spectra

The energy spectra of most GRBs are well described by the *Band function* [37], which models the low energy component as a power law with exponential cutoff, smoothly transitioning to a steeper power law at higher energies. While the fit is purely empirical and makes no claims with regards to the burst physics, it is in agreement with a model of synchrotron emission from accelerated electrons which then undergo cooling above some break energy. We simplify the picture slightly by taking the photon spectra to be a broken power law, with the normalization chosen such that the fluence integral matches that fit by the Band function.

---

[3] This class of supernovae are known as hypernovae and are characterized by smooth spectra, higher than usual energy, and strong radio emission.

$$\frac{dN(E_\gamma)}{dE_\gamma} = f_\gamma \times \begin{cases} \epsilon_\gamma^{(\alpha_\gamma-\beta_\gamma)}\ E_\gamma^{-\alpha_\gamma} & \text{for } E_\gamma < \epsilon_\gamma \\ E_\gamma^{-\beta_\gamma} & \text{for } E_\gamma \geq \epsilon_\gamma \end{cases} \tag{2.1}$$

$$\mathcal{F}_\gamma = \int dE_\gamma E_\gamma \frac{dN(E_\gamma)}{dE_\gamma} \tag{2.2}$$

where $\mathcal{F}_\gamma$ is the measured photon fluence. The break energy varies for each burst, but has a typical value of $\epsilon_\gamma \sim 250\,\text{keV}$ [4]. Long bursts tend to have spectral indices scattered around $\alpha_\gamma \sim 1$ and $\beta_\gamma \sim 2$ while short GRBs are harder by one power in energy on average.

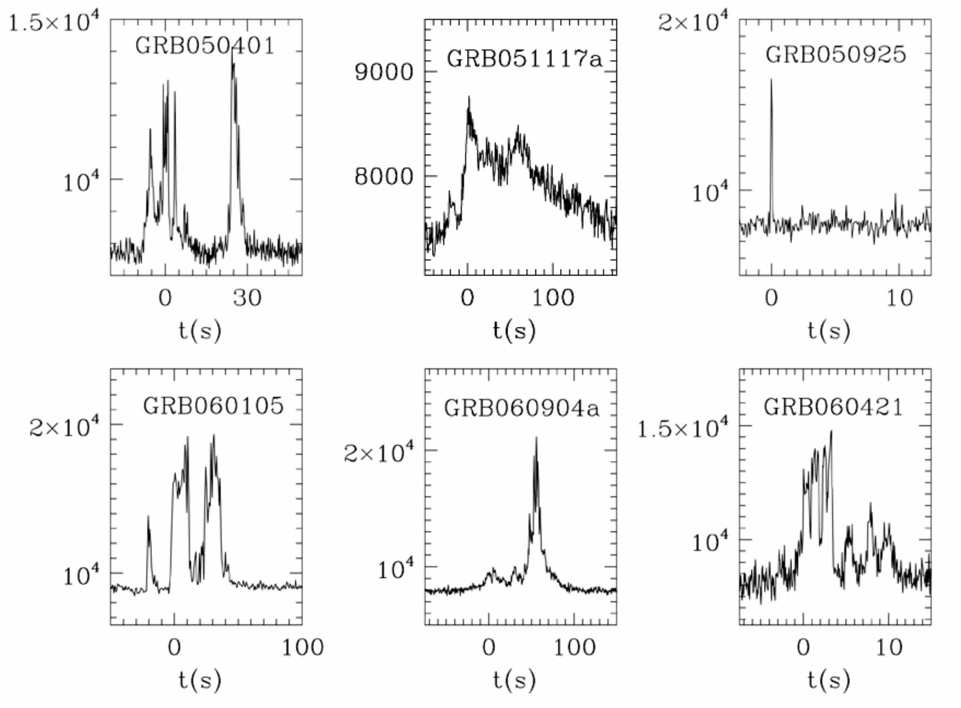

Figure 2.4: Lightcurves for several gamma-ray bursts. Note that all bursts exhibit unique temporal characteristics and some have short timescale variability. (from [25])

---

[4] We note that the Swift detector (see section 4.1.1) is transparent to γ-rays above 150 keV and thus does not detect the spectral break for the majority of GRBs it observes.

2.2.2 Compactness

GRBs experience variability on millisecond timescales (see Fig.2.4). The finite speed of light places constraints on the source size. For a source of diameter d, any temporal variability of scale smaller than $\Delta t \sim \frac{d}{c}$ will be smeared out by delays in travel time. This means that the compact progenitor must satisfy:

$$R_{GRB} \lesssim \frac{c\Delta t}{2} \tag{2.3}$$

For observed timescales of $\Delta t \sim 0.01\,\mathrm{s}$, this gives a characteristic radius of $R_{GRB} \lesssim 1500\,\mathrm{km}$. For comparison, the radius of a neutron star is typically $\sim 12\,\mathrm{km}$. In the case that the compact object is a black hole, the source size can be defined by the Swartschild radius:

$$R_{Swartschild} = \frac{2GM}{c^2} \tag{2.4}$$

This relation yields an upper limit to the possible source mass of a GRB progenitor, supposing that it is a black hole.

$$M < \frac{c^2 R_{GRB}}{G} \sim 2 \times 10^{33} kg \sim 1000 M_{\odot} \tag{2.5}$$

The isotropic distribution observed by BATSE (see Fig. 2.3) implies that GRBs are cosmological in nature. Coupled with the measured fluences $\mathcal{F}_\gamma$ and the standard Λ_{CDM} cosmology, this leads to high corresponding energies at the source, E_γ^{iso}, of $\sim 10^{51} - 10^{54}$ ergs. Given that GRBs have durations spanning from 0.1 s to >100 s, this results in luminosities, L_γ^{iso} of $\sim 10^{49} - 10^{52}$ erg/s. Here we assume isotropic emission of the energy. If we take the typical photon energy in a GRB to be ϵ_γ [5] then we can determine the number density of photons in the source:

$$n_\gamma = \frac{L_\gamma^{iso}}{4\pi R^2 c\,\epsilon_\gamma\,(1+z)} \approx 1.5 \times 10^{30}\mathrm{cm}^{-3} \tag{2.6}$$

The above implies that the photons should be thermalized due to the high optical depth of the

---

[5] This is reasonable given that emission tends to peak at the break energy, and that most of the photons will be emitted at the peak.

plasma, which is at odds with the observed high energy emission well above the pair production threshold. This is known as the *compactness problem*.

In order to resolve this apparent crisis, we note that given the mass limit imposed by Eq. 2.5 and the observed luminosities of $\mathcal{O}(10^{52})$ erg/s, the progenitor far exceeds the Eddington limit and thus must drive a wind from the surface. We consider the case that the expansion is highly relativistic and thus the photons will appear to be emitted in a cone of opening angle θ due to aberration. The geometry is illustrated in Fig. 2.5. The observed time delay between spectral features is now given by

$$\Delta t_{obs} = \frac{\Delta t(c - v\cos\theta)}{c} \tag{2.7}$$

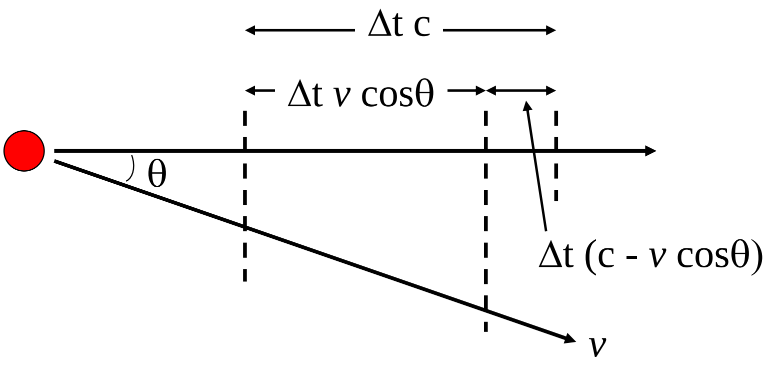

Figure 2.5: Effect of relativistic aberration on time variability. The relativistically expanding plasma is beamed into an opening angle θ. An observer situated along the line of sight will observe a different time between spectral features than is intrinsic to the source.

We write the expansion velocity v in terms of the Lorentz factor Γ and Taylor expand (assuming large Γ) to get

$$v \approx (1 - \frac{1}{2\Gamma^2})c \tag{2.8}$$

Similarly, the opening angle will be small so the same technique may be applied. Combining terms yields

$$\Delta t_{obs} \approx \Delta t \left(\frac{1}{2\Gamma^2} + \frac{\theta^2}{2} \right) \tag{2.9}$$

Since the beaming angle θ is inversely related to the Lorentz factor, we arrive at

$$\Delta t_{obs} \lesssim \frac{\Delta t}{\Gamma^2} \tag{2.10}$$

$$R_{GRB} \approx c \Delta t_{obs} \Gamma^2 \tag{2.11}$$

Similarly, the intrinsic luminosity of the GRB is reduced by a factor Γ^3 and the individual photon energies by a factor Γ. We determine that the plasma becomes optically thin for $\Gamma > 100$. Such a Lorentz factor also places the bulk of photons below the pair production threshold. Direct measurements by Molinari et al. [38] give $\Gamma \sim 400$.

2.2.3 Emission Mechanism

Assuming now an outflow with $\Gamma \geq 100$, the jet must collide with the ISM and slow down. While this external shock may account for observed afterglow emission, the time and distance scales on which it occurs preclude it from being the cause of the prompt emission as it cannot produce the observed temporal variability. We turn instead to internal shocks within the jet. While the jet moves with a bulk Lorentz factor Γ, individual ejections from the progenitor will have varying speeds. When faster shells overtake slower shells, shocks will occur. At these shock fronts, electrons may be accelerated via the Fermi mechanism (outlined in section 1.1.1). Due to the shock compression of the fluid and the high velocity of expansion, the acceleration is both very efficient and fast. These electrons then emit photons via synchrotron (and perhaps inverse Compton) radiation, resulting in the observed keV-GeV emission. Such an internal shock acceleration scenario both accounts for rapid temporal variability as well as a power law energy spectrum. It is natural that protons would also be accelerated in these shocks, potentially leading to neutrino production.

2.2.4 Collimated Emission - Reducing the Energy Budget

While the energy budget for GRBs is extreme, it may be reduced if the emission is collimated. In this case, the required energy is reduced by a factor $\Omega/4\pi$ where Ω is the opening angle of the collimated jet. This would be experimentally observable by a temporal break in the afterglow emission. The reason for this break comes from the interaction between the relativistic beaming effect and the intrinsic beaming of the jet. The highly relativistic outflow from the GRB is Lorentz-beamed into an angle of $1/\Gamma$. As the fireball propagates through the interstellar medium (ISM) it is slowed and the bulk Lorentz factor decreases, thus increasing the beaming angle. At some point, the outflow will have slowed enough such that $1/\Gamma > \Omega$ and a flux deficit will be observed as a steepening of the spectra. This jet break has a unique signature in several ways. First, it is *achromatic* - that is, since it is a purely hydrodynamic effect, it affects all wavelengths equally. Second, it does not impact the physics of the burst itself, so no effect on the electron or photon spectral index is expected. Further details may be found in [39, 40].

Clear evidence of multi-color optical breaks with consistent radio data was observed in the case of GRB990510 [41], among others (see Fig. 2.6). Based on the observed temporal jet breaks for a sample of several tens of bursts, Frail et al. [42] and Bloom et al. [43] calculated the corresponding jet collimation angles and GRB energies. They found that all GRBs in the sample were narrowly clustered around emission energies of $E_\gamma \sim (5\times10^{50} - 1.3\times10^{51}$ ergs, as seen in Fig. 2.7. Thus, GRBs have an energy budget on par with bright Supernovae, suggesting a correlation, and the observed variances in luminosity and fluence can be attributed to differences in the jet opening angle rather than intrinsic properties. Furthermore, this suggests that the true rate of GRBs is much higher, as we only observe bursts with collimated emission along line of sight.

While the idea of beamed emission is attractive in that it reduces the energy budget of GRBs to levels more in line with other astrophysical phenomena (e.g. supernovae), recent data calls these conclusions into question. It was expected that Swift, with its multi-wavelength observational capabilities, would measure jet breaks for many GRBs. This has not turned out to be the case however, with very few bursts displaying temporal breaks that are consistent with the jet break model. The current experimental and theoretical status of jet breaks is more fully covered in [44].

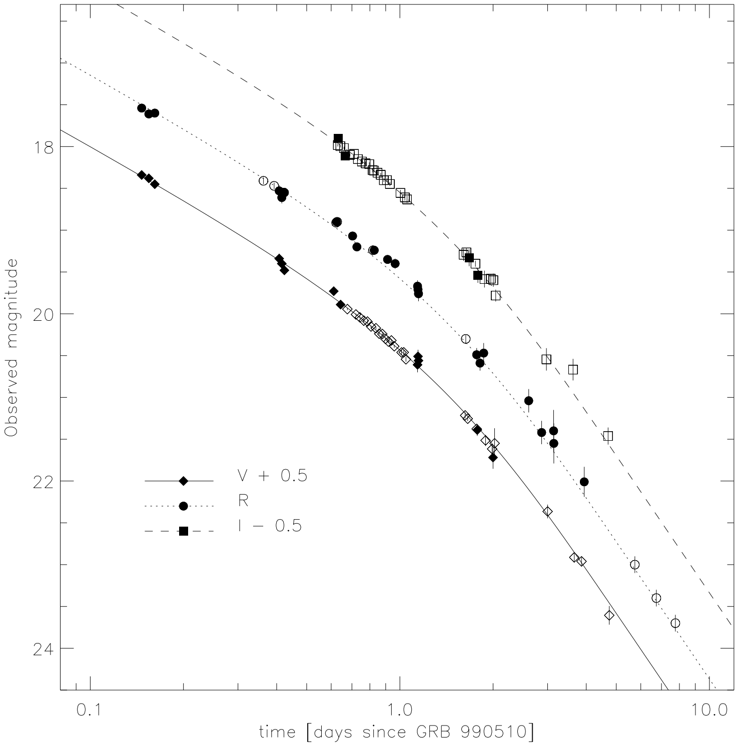

Figure 2.6: Observation of achromatic jet breaks in GRB990510. The wavelength independence of the break times agrees with the jet break model. (from [41])

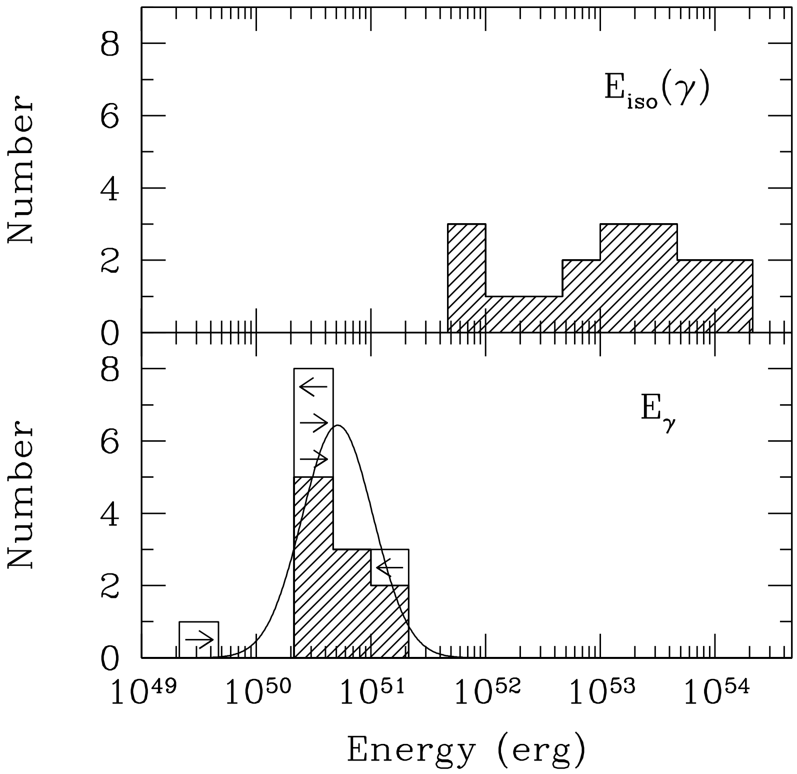

Figure 2.7: Calibrated GRB energy in the case of beamed emission. Upper panel shows calculated isotropic equivalent energy for GRBs with measured redshift. Lower panel shows energy after taking into account jet collimation angle Ω calculated from jet break times. (from [42])

2.3 Neutrino Production

If hadrons (typically protons) are accelerated along with electrons in the fireball phenomenology described above, neutrinos will be produced due to subsequent interactions. The energy spectra of these neutrinos will depend on the environment and type of these interactions.

2.3.1 Prompt Neutrinos

Waxman and Bahcall showed that protons may interact with the internal shock prompt emission gamma-rays to produce pions via the delta resonance [45].

$$p + \gamma \rightarrow \Delta \rightarrow n + \pi^{+} \tag{2.12}$$

$$\rightarrow p + \pi^{0} \tag{2.13}$$

Charged pions decay to neutrinos and associated leptons, while neutral pions produce high energy photons [6].

$$\pi^{+} \rightarrow \mu^{+} + \nu_{\mu} \tag{2.14}$$

$$\mu^{+} \rightarrow \bar{\nu}_{\mu} + e^{+} + \nu_{e} \tag{2.15}$$

$$\pi^{0} \rightarrow \gamma + \gamma \tag{2.16}$$

These processes result in a neutrino flavor ratio at the source of $(\nu_e, \nu_\mu, \nu_\tau)$ =(1:2:0) [7].

Eq. 2.12 indicates that the produced neutrino spectra should track the γ-ray spectra of Eq. 2.1, as the combined center of mass energy of the interacting proton and photon must exceed the threshold for production of the Δ-resonance:

---

[6] This TeV-scale gamma emission is the target of GRB searches by Imaging Air Čerenkov Telescopes such as MAGIC as well as surface arrays such as MILAGRO.

[7] Here, and in the rest of this thesis, we treat neutrinos and antineutrinos equally. The minor differences in cross-section are taken into account in signal weighting but we shall not explicitly differentiate.

$$E'_p \geq \frac{m_\Delta^2 - m_p^2}{4E'_\gamma} \tag{2.17}$$

where primes indicate the co-moving frame of the fireball. We estimate that each of the four final state particles in the π^+ decay chain given by Eqs. 2.12 and 2.14 contains equal energy, and that on average, a fraction $\langle x_{p\to\pi}\rangle \simeq 0.2$ of the proton energy is transferred to pions in each interaction. Thus each neutrino is expected to possess ∼5% of the proton energy.

The condition of Eq. 2.17 indicates that interactions of protons with high energy photons will produce lower energy neutrinos, and vice versa. For each proton energy, then, the neutrino spectrum traces the broken power law of Eq. 2.1. Assuming protons are accelerated with the same spectrum as electrons, we then sum over proton energies to find the resultant neutrino spectra.

$$\frac{dN(E_\nu)}{dE_\nu} \propto \begin{cases} E_\nu^{-\alpha_\nu} & \text{for } E_\nu < \epsilon_\nu^b \ ; \ \alpha_\nu = 3 - \beta_\gamma \\ E_\nu^{-\beta_\nu} & \text{for } \epsilon_\nu^b \leq E_\nu < \epsilon_\nu^s \ ; \ \beta_\nu = 3 - \alpha_\gamma \end{cases} \tag{2.18}$$

We relate the break in the neutrino spectrum to that of the observed photons by converting Eq. 2.17 to the observer's frame.

$$\begin{aligned} \epsilon_\nu^b &= \frac{1}{4}\langle x_{p\to\pi}\rangle \ \frac{m_\Delta^2 - m_p^2}{4\epsilon_\gamma} \ \frac{\Gamma^2}{(1+z)^2} \\ &= 7.5 \times 10^5 \,\text{GeV} \ \frac{1}{(1+z)^2} \left(\frac{\Gamma}{10^{2.5}}\right)^2 \left(\frac{\text{MeV}}{\epsilon_\gamma}\right) \end{aligned} \tag{2.19}$$

At high energy, the lifetime of the produced pions and muons $\tau'_{\pi,\mu}$ exceeds the synchrotron loss time t'_s. This introduces a further cooling break into the neutrino spectrum. t'_s is dependent on the energy density of the magnetic field in the jet, $U'_B = B'^2/8\pi$, and for pions is given by:

$$t'_s = \frac{3m_\pi^4 c^3}{4\sigma_T m_e^2 E'_\pi U'_B} \tag{2.20}$$

where $\sigma_T = 0.665 \times 10^{-24}\,\text{cm}^2$ is the Thompson cross-section. The magnetic energy density can be related to the fraction of the internal energy of the plasma that is carried by the magnetic field. We denote this fraction by ξ_B and write

$$4\pi R^2 c\Gamma^2 U'_B = \xi_B L_{int} \tag{2.21}$$

We determine the collision radius R by noting that the colliding shells of the jet have velocities that vary by $\Delta v \sim c/2\Gamma^2$, where, as previously, Γ represents the average Lorentz factor of the fireball. Given the observed time variability t_{var}, these shells then collide at a time $t_c \sim ct_{var}/\Delta v$, which corresponds to a radius $R \simeq 2\Gamma^2 ct_{var}$. The total luminosity is related to the observed photon luminosity through the electron energy fraction of the jet, $L_{int} = L_\gamma^{iso}/\xi_e$. [46, 47]

The pion lifetime is given by

$$\begin{aligned}\tau'_\pi &= \tau_\pi^0 \frac{E'_\pi}{m_\pi c^2} \\ &= 2.6 \times 10^{-8} \frac{E'_\pi}{m_\pi c^2}\end{aligned} \tag{2.22}$$

Equating Eq. 2.20 with Eq. 2.22 yields the pion energy where synchrotron losses begin to suppress the neutrino emission. Recalling the each ν_μ carries 1/4 of the pion energy, and converting to the observer's frame, we find

$$\epsilon_\nu^s = 10^7\,\mathrm{GeV}\,\frac{1}{1+z}\sqrt{\frac{\xi_e}{\xi_B}}\left(\frac{\Gamma}{10^{2.5}}\right)^4\left(\frac{t_{var}}{0.01\,\mathrm{s}}\right)\sqrt{\frac{10^{52}\,\mathrm{erg/s}}{L_\gamma^{iso}}} \tag{2.23}$$

We note that in the above the equipartition fractions ξ_e and ξ_B are not measured and no good theoretical method exists for estimating them. We set them each to be 0.1 in all future calculations. This estimate is supported by afterglow observations [48]. Muons live about 100 times longer and thus the energy scale at which their decay products ($\bar{\nu}_\mu$ and ν_e) begin to be suppressed is a factor of 10 lower. The decay probability is approximately given by the ratio of the cooling time to the decay time $t'_s/\tau' \propto E_\nu^{-2}$ and thus we expect the neutrino spectrum to steepen by 2 powers in energy above ϵ_ν^s ($\gamma_\nu = \beta_\nu + 2$). Combining with Eq. 2.18 we arrive at

$$\frac{dN(E_\nu)}{dE_\nu} = f_\nu \times \begin{cases} \epsilon_\nu^{b\,(\alpha_\nu - \beta_\nu)}\ E_\nu^{-\alpha_\nu} & \text{for } E_\nu < \epsilon_\nu^b \\ E_\nu^{-\beta_\nu} & \text{for } \epsilon_\nu^b \le E_\nu < \epsilon_\nu^s \\ \epsilon_\nu^{s\,(\gamma_\nu - \beta_\nu)}\ E_\nu^{-\gamma_\nu} & \text{for } E_\nu \ge \epsilon_\nu^s \end{cases} \tag{2.24}$$

It now remains to determine the normalization f_ν. The neutrino fluence is proportional to the measured gamma-ray fluence $\mathcal{F}_\gamma$

$$\int dE_\nu E_\nu \frac{dN(E_\nu)}{dE_\nu} = x \cdot \int dE_\gamma E_\gamma \frac{dN(E_\gamma)}{dE_\gamma} = x \cdot \mathcal{F}_\gamma \tag{2.25}$$

The constant of proportionality x contains several terms. It includes the fraction of jet proton energy lost to pion production f_π, a factor $1/f_e$ that accounts for the fraction of total energy expected in protons respective to electrons, and a factor 1/8. This final term is due to the fact that only half of the photomeson interactions produce neutrinos (the others produce π^0) and each of those reactions creates four final state leptons. f_π can be estimated from the size of the shocks and the mean free path for photomeson interactions.

$$f_\pi \propto \frac{\Delta R'}{\lambda_{p\gamma}} = N_{int} \tag{2.26}$$

The number of interactions is related to the photon energy density which is in turn a function of the GRB luminosity in the comoving frame [8]. We follow the derivation of [46] and reformulate to ensure an energy transfer ≤ 1:

$$f_\pi = 1 - (1 - \langle x_{p\to\pi} \rangle)^{N_{int}} \tag{2.27}$$

$$N_{int} = \left(\frac{L_\gamma^{iso}}{10^{52}\,\mathrm{erg/s}}\right) \left(\frac{0.01\,\mathrm{s}}{t_{var}}\right) \left(\frac{10^{2.5}}{\Gamma}\right)^4 \left(\frac{\mathrm{MeV}}{\epsilon_\gamma}\right) \tag{2.28}$$

---

[8] Here we note that we assume isotropic emission, but also divide by a spherical shell. In the case of beamed emission, the luminosity decreases, but cancels with the decreased solid angle.

An analytical approximation of the integration over neutrino energies yields a simple relationship between the neutrino flux normalization and the gamma-ray fluence.

$$f_\nu \approx \frac{1}{8}\frac{1}{f_e}\frac{f_\pi}{\ln(10)}\mathcal{F}_\gamma \tag{2.29}$$

A quasi-diffuse flux may be determined by summing over all bursts in a year and dividing by the full sky solid angle. This was done by Waxman and Bahcall, assuming each GRB followed a spectrum calculated from averages of the BATSE population [49]. Assuming 1000 GRBs per year based on the BATSE rates, they calculated the diffuse flux shown in Fig. 2.8. This will hereafter be referred to as the Waxman-Bahcall prompt GRB flux. The normalization is comparable to what one would get assuming that all the ultra-high energy cosmic rays originate from GRBs. The average parameters used in this calculation are shown in Table 2.1.

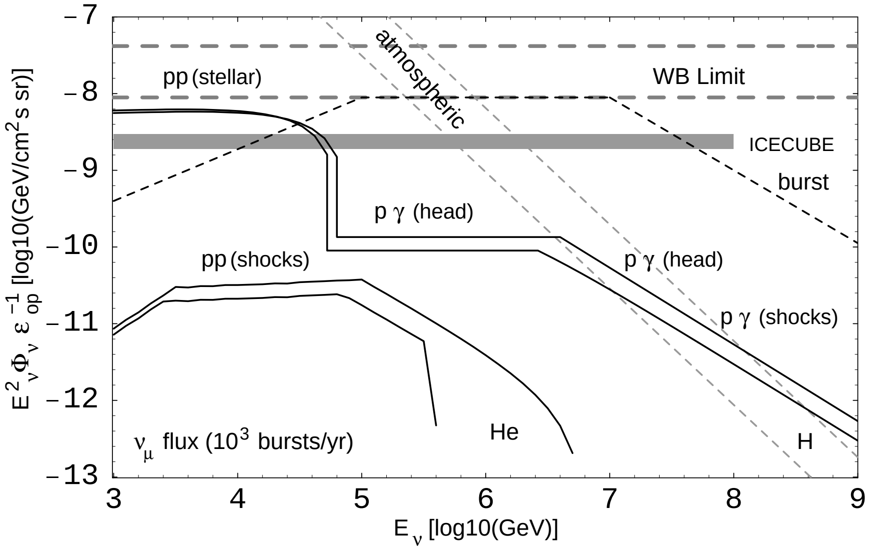

Figure 2.8: Diffuse muon neutrino flux predictions for the prompt and precursor emission phases. 1000 GRBs/yr. are assumed. Black dashed-line indicates the prompt flux calculated with average parameters measured by BATSE. Solid black lines correspond to precursor neutrino predictions for progenitors with a hydrogen envelope (H) and no envelope (He) for varying shock and jet radii. Fluxes are shown at the source and will be reduced by a factor of 2 at Earth due to oscillations. (from [50])

Photon Parameter	Average Value
z	1
ϵ_γ	$1\,\mathrm{MeV}$
α_γ	1
β_γ	2
ϵ_ν^b	$10^5\,\mathrm{GeV}$
ϵ_ν^s	$10^7\,\mathrm{GeV}$
L_γ^{iso}	10^{52} erg/s
Γ	315
t_{var}	$0.01\,\mathrm{s}$
ξ_e	0.1
ξ_B	0.1
f_e	0.1

Table 2.1: Average parameters used to calculate the Waxman-Bahcall diffuse GRB neutrino flux for the prompt emission phase.

2.3.2 Precursor Neutrinos

The relativistic jets that are thought to be responsible for the prompt photon emission of GRBs must first penetrate the sub-stellar environment of the progenitor. In this region, no photon emission is expected as the star is highly optically thick. However, shock-accelerated protons may interact with thermalized photons and nucleons of the jet as well as with cold nucleons in the stellar plasma to produce neutrinos [50]. This so-called *precursor* emission occurs at smaller radii and lower Lorentz factors than the observed prompt photons.

Neutrinos from $p\gamma$ interactions both in the jet and in the surrounding plasma will be highly suppressed due to the extreme magnetic fields of the progenitor and the subsequent synchrotron losses of pions and muons. On the other hand, pp interactions in the unshocked plasma will not be affected in this way. Assuming a proton injection spectrum with an E^{-2} power law, Razzaque et al. performed detailed simulations of the pp interactions both at the jet head and in the shocks, taking into account synchrotron as well as inverse Compton losses in order to determine the resulting neutrino flux. This spectrum cuts off at the energy threshold for pion/kaon production above which no neutrinos from pp interactions are expected. However, above the Δ resonance threshold, the suppressed $p\gamma$ interactions begin to play a small role. The resulting diffuse flux can be seen in Fig. 2.8 for several progenitor types and sizes. Further details of the calculations can be found in [50, 51].

2.3.3 Afterglow Neutrinos

X-ray, optical, and radio afterglows have been observed in association with many GRBs. In the standard picture, these are the result of collisions of the expanding fireball with the circumburst matter. It has been proposed that the low energy photons are then created via synchrotron radiation of electrons accelerated in shocks moving inwards. These photons are observed to follow a power law spectrum which steepens on average by a power of 1/2 above a break energy determined by the relation between the synchrotron cooling time and the expansion time of the ejecta [51]. These spectral indices vary between bursts, but are scattered around average values of $\alpha_x \sim 3/2$ and $\beta_x \sim 2$.

In the hadronic picture, these mildly-relativistic reverse shocks will also accelerate protons to ultra-high energies [52]. Following the same processes as in the prompt emission scenario, these protons will interact with the afterglow photons to produce neutrinos. However, since the reverse shocks happens at large radii of $\sim 10^{17}$ cm, we do not expect significant synchrotron losses of pions and muons. In this case, assuming the average photon spectra above, the neutrinos can be described as

$$\frac{dN^a(E_\nu)}{dE_\nu} = A_\nu^a \times \begin{cases} E_\nu^{-1} & \text{for } E_\nu < \epsilon_\nu^b \\ E_\nu^{-3/2} & \text{for } E_\nu \geq \epsilon_\nu^b \end{cases} \tag{2.30}$$

The break energy ϵ_ν^b is related to the photon break energy via Eq. 2.19 and for the observed afterglow cooling breaks of $0.1 - 1\,\text{keV}$, we have

$$\epsilon_\nu^b = (0.7 - 7) \cdot 10^9 (1+z)^{-2}\,\text{GeV} \tag{2.31}$$

In [52], ϵ_ν^b is fixed at 10^8 GeV and A_ν^a is determined to be $10^{-10}\,\text{GeV}\,\text{cm}^{-2}\,\text{s}^{-1}\,\text{sr}^{-1}$ by assuming that the observed flux of ultra high energy cosmic rays is due entirely to GRBs. Neutrinos of energy up to $\sim 10^{19}$ eV could be produced, although strong suppression is expected above this energy as protons are not observed above $\sim 10^{20}$ eV.

2.4 Neutrino Oscillation

Solar Neutrinos were first detected by the Homestake experiment in the late 1960s, using a large tank of chlorine to capture solar ν_μ [53, 54]. However, only 1/3 of the neutrinos predicted by the solar model were detected, leading to the well known "solar neutrino problem". This was solved by the Sudbury Neutrino Observatory in 2001 with an experiment that measured the total solar neutrino flux over all flavors. [55] This was direct evidence of the oscillation between neutrino flavors that would occur if the neutrinos were massive.

The mass eigenstates are mixed via the Maki-Nakagawa-Sakata (MNS) matrix to produce the flavor eigenstates:

$$\begin{bmatrix} \nu_e \\ \nu_\mu \\ \nu_\tau \end{bmatrix} \begin{bmatrix} c_{12}c_{13} & s_{12}c_{13} & s_{13}e^{-i\delta} \\ -s_{12}c_{23} - c_{12}s_{23}s_{13}e^{i\delta} & c_{12}c_{23} - s_{12}s_{23}s_{13}e^{i\delta} & s_{23}c_{13} \\ s_{12}s_{23} - c_{12}c_{23}s_{13}e^{i\delta} & -c_{12}s_{23} - s_{12}c_{23}s_{13}e^{i\delta} & c_{23}c_{13} \end{bmatrix} \begin{bmatrix} \nu_1 \\ \nu_2 \\ \nu_3 \end{bmatrix} \tag{2.32}$$

where $c_{ij} = \cos\theta_{ij}$ and $s_{ij} = \sin\theta_{ij}$. The phase δ is non-zero in the case that the oscillation is CP violating. The mass eigenstates propagate in time as plane waves. Since time and length are equivalent, we may write

$$|\nu_i(L)\rangle = e^{-im_i^2 L/2E}|\nu_i(0)\rangle \tag{2.33}$$

and since these eigenstates have different masses, they will propagate at different speeds. Because they are superpositions of the flavor eigenstates, this will cause interference between those flavor states, leading to oscillation over the propagation length. The probability that a neutrino of flavor α will oscillate to a neutrino of flavor β is then given by

$$P_{\alpha\to\beta} = |\langle\nu_\beta|\nu_\alpha(t)\rangle|^2 = \left|\sum_i U_{\alpha i}^* U_{\beta i} e^{-im_i^2 L/2E}\right|^2 \tag{2.34}$$

where $U_{\alpha i}$ indicates the MNS mixing matrix between those states. The solution in the full 3 flavor/mass theory is complicated, but includes a term

$$\sin^2(\frac{\Delta m_{ij}^2 L}{4E}). \tag{2.35}$$

In the simpler case of a 2 neutrino theory (such as $\nu_\mu \rightarrow \nu_\tau$ oscillation of atmospheric neutrinos, where the involvement of ν_e is very small), the mixing between flavors is given by

$$P_{\alpha\rightarrow\beta} = \sin^2 2\theta \sin^2\left(\frac{\Delta m^2 L}{4E}\right) \tag{2.36}$$

where θ and Δm^2 are the respective quantities in the 2 neutrino theory.

Cosmological baselines ensure that oscillation occurs and it can be shown that this typically leads to a conversion of the (1:2:0) source flavor ratio to a flavor ratio at earth of $\sim$ (1:1:1) [56]. However, Kashti and Waxman showed that π and μ energy losses modify this flavor ratio to (1:1.8:1.8) at high energies [57]. This conversion takes place over several decades in energy and for GRBs typically occurs between 100 TeV and 1 PeV.

Chapter 3

Neutrino Detection and Reconstruction

3.1 Interaction

Neutrinos have extremely low cross-sections and interact only rarely via the weak force, even at high energies [58]. Sometimes, however, a high energy neutrino will interact with an ice or rock nucleus in or near the detector volume through the charged current interaction

$$\nu_l + N \to l + X \tag{3.1}$$

where X is the nuclear remnant.[1] The rate of these interactions depends on energy and angle of incidence, as shown in Fig. 3.1.

For the analyses presented in this thesis, we consider the case where the daughter lepton of Eq. 3.1 is a high energy muon. Such daughter muons are highly relativistic and will deviate only slightly in direction from the primary, with an angular offset given by $\psi = 0.7^\circ \times (E_\nu/\mathrm{TeV})^{-0.7}$ [59]. At the energies of primary interest ($\sim 100\,\mathrm{TeV}$), muons have a range of about 10 km [60]. This has the fortuitous effect of vastly increasing the effective area of any detector built to view these muons, as they need not originate in the instrumented volume, merely pass through it.

---

[1] Neutral current interactions also take place, but these create very different signatures (cascades) in the detector and are outside the scope of this thesis.

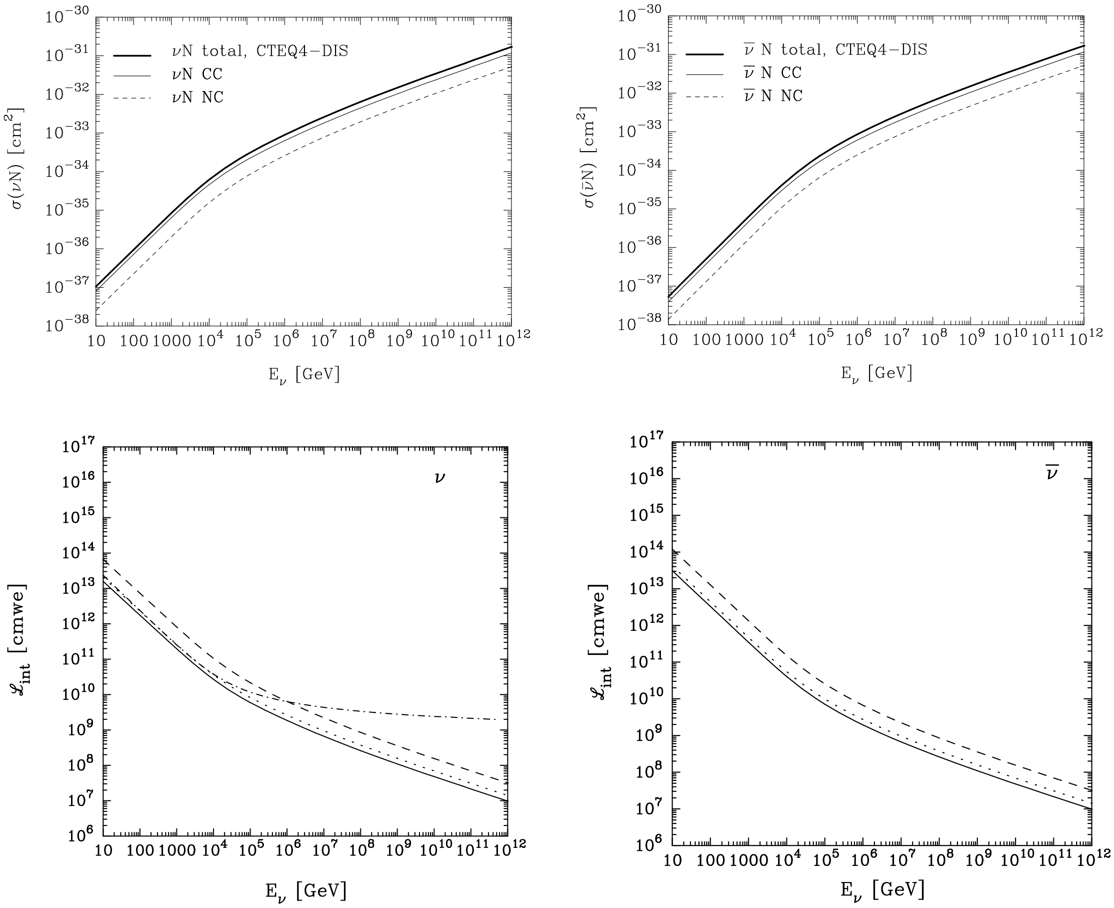

Figure 3.1: Upper panels show the νN and $\bar{\nu}N$ cross-sections for all flavors as a function of energy. Dashed line, neutral current interactions; thin solid lines, charged current interactions; thick solid line, total. The curves in these figures are calculated from the CTEQ4 parton distribution functions, however we use updated cross-sections using CTEQ6 in our analyses. The lower panels show the energy dependent decrease in the interaction length (in units of cm water equivalent). Dotted line, charge current; dashed line, neutral current; solid line, total interaction length. Ignore the dot-dashed line in the lower left panel. The diameter of the Earth is 1.1×10^{10} cmwe, so above 40 TeV, vertical events begin to be attenuated. As energy increases, one must shift angle towards the horizon to compensate for this earth absorption effect. (from [58])

3.2 Čerenkov Radiation

When a charged particle travels through some transparent medium (e.g. water or ice) at a velocity exceeding the speed of light in that medium [2], a characteristic radiation is emitted [62, 63]. This radiation is the result of transitions to ground state of atoms excited by the electromagnetic field of the passing particle. Due to constructive interference, it is emitted in a cone of opening angle

$$\cos\theta_c = \frac{1}{\beta n(\lambda)} \tag{3.2}$$

where β is the ratio of the particle velocity to that of light in vacuum and n is the wavelength dependent refractive index of that medium [64] (see Fig. 3.2). For ice, we have $n = 1.31$, and β is taken to be 1 for very high energy particles, thus the opening angle of the emitted Čerenkov cone is $\theta \sim 41^\circ$. The arrival time of light in the detector may be used to reconstruct this cone and thus determine the direction of the incoming particle.

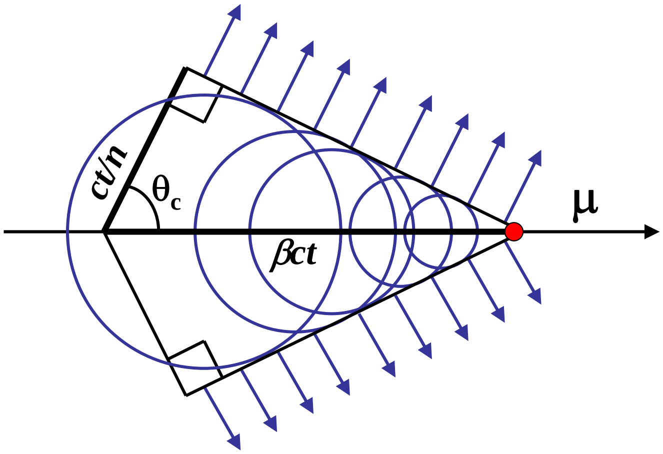

Figure 3.2: Schematic illustrating the characteristic conical opening angle of Čerenkov radiation.

The number of emitted photons per unit length is dependent on the wavelength and is give by the Frank-Tamm formula [64]:

---

[2] The full treatment considers the difference between the phase and group velocities in the medium and introduces a small angular difference, which we neglect. This approximation was shown to be valid for AMANDA and IceCube in [61].

$$\frac{d^2N}{dxd\lambda} = \frac{2\pi\alpha z^2}{\lambda^2}\sin^2(\theta_c(\lambda)) \tag{3.3}$$

Here we denote the fine structure constant as α, and explicitly note the wavelength dependence of the Čerenkov angle. As the number of emitted Čerenkov photons is strongly wavelength dependent, we expect the emission to peak in the blue, around 400 nm. The glass typically used in detectors has a UV cutoff near 300 nm (see Chapter 4 and Fig. 4.5(b)) and ice begins to lose transparency above about 500 nm (see Section 3.5. We integrate Eq. 3.3 over this wavelength range and find that we expect about 200 photons per cm to be emitted along the track.

3.3 Muon Energy Losses

Particles traveling through a medium generally experience energy losses of the form

$$-\frac{dE}{dx} = A(E) + B(E)E. \tag{3.4}$$

The first term dominates at low energies where losses are due to ionization and excitation. The ionization losses are in most cases given by the Bethe-Bloch formula [65]:

$$-\frac{dE}{dx} = \frac{z^2e^4N_e}{4\pi\epsilon_0^2m_ec^2\beta^2}\left[ln\left(\frac{2m_ec^2\beta^2}{\bar{I}(1-\beta^2)}\right) - \beta^2\right] \tag{3.5}$$

where z is the charge, N_e is the electron number density of the target, and $\bar{I}$ is the mean ionization potential of the target. However, in the case of highly relativistic particles, such as the muons created by astrophysical neutrinos, we cannot ignore the back-reaction of the target electrons on the field of the moving particle. Jackson [66] gives a good treatment of this effect, with the net result being that energy losses due to ionization are somewhat smaller at high energies than Eq. 3.5 would indicate.

The second term in Eq. 3.4 dominates as energy increases. The radiative processes making up this term are stochastic in nature and include Bremsstrahlung, photonuclear interactions, and e^+e^- pair production. In all cases, secondary particles are created which are still highly relativistic and emit Čerenkov radiation in their own right. This enhances the radiation of the bare muon and allows for the possibility of energy reconstruction in a neutrino detector. Fig. 3.3 shows the relative contributions to the energy loss as the muon energy increases. Stochastic losses begin to dominate around 1-10 TeV.

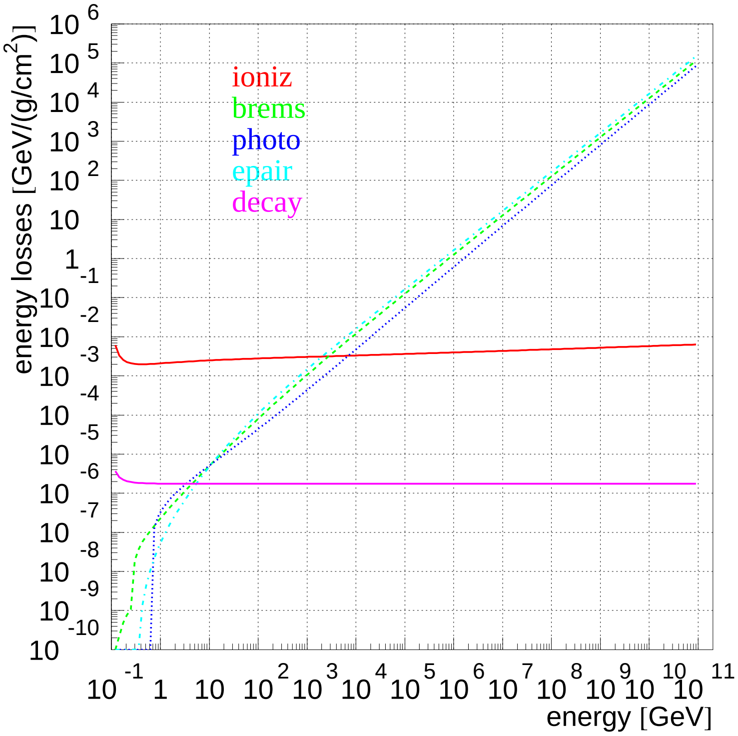

Figure 3.3: Muon energy loss in ice as a function of energy. Stochastic processes dominates above ∼1 TeV. In this regime, the detectable Čerenkov photons increase proportional to the energy of the muon, and energy reconstruction becomes possible. (from [67])

3.4 Backgrounds

The principles of detecting the muons induced by astrophysical neutrinos are straightforward, and given a large enough detector, one should be able to see a signal. However, the backgrounds are daunting. High energy cosmic rays bombarding the atmosphere interact with nucleons to produce extensive air showers. These large cascades contain both hadronic and leptonic components. The decay lengths of these particles depend both on type and on energy. Charm mesons have exceptionally short decay lengths, and they quickly convert into *prompt atmospheric neutrinos*. This flux is expected to closely follow the $E^{-2.7}$ power law of the incident cosmic rays, though the normalization is highly uncertain due to lack on knowledge of the relevant cross-sections. We typically use the Naumov RQPM model [68] as it gives the most conservative estimates.

Kaons and pions have longer decay lengths and often interact in the atmosphere before decaying. In the case that they do decay, however, they produce the *conventional atmospheric neutrinos*:

$$\pi^+(K^+) \rightarrow \mu^+ + \nu_\mu \tag{3.6}$$

$$\pi^-(K^-) \rightarrow \mu - + + \bar{\nu}_\mu \tag{3.7}$$

Due to partial disappearance in the atmosphere, conventional neutrinos follow a steepened $E^{-3.7}$ power law. Some of the muons of Eq. 3.7 also decay to neutrinos, but many more penetrate the earth. At high energies these *atmospheric muons* can travel for many kilometers before ranging out, and many reach the detector.

Both atmospheric muons and neutrinos are produced isotropically over the whole sky. However, only the neutrinos reach the detector from all angles. Muons are absorbed as the Earth travel distance increases, dropping to zero at the horizon (see Fig. 3.4). It is instructive here to take a moment to define our detector coordinate system. The horizon is taken to be the boundary between muon contaminated and muon free regions of the sky and is assigned a zenith angle of 90°. For a detector located at the south pole, particles from the southern sky are said to be downgoing (below the horizon, zenith $0 - 90°$), while those from the northern sky are said to be upgoing (above the horizon, zenith $90 - 180°$). In the downgoing region, muons dominate neutrinos by a factor 10^6. We therefore typically use the Earth as a filter and concentrate on searches in the northern sky, where the sole remaining background is atmospheric neutrinos. Fig 3.5 demonstrates the principle.

If we had perfect knowledge of each particle, we would then only have to deal with separating the softer spectrum isotropic atmospheric neutrinos from the the higher energy GRB neutrinos that come from known directions at specific times. However, our reconstructions are not perfect, and about 0.1% of atmospheric muons are misreconstructed as upgoing tracks. This means that the muon background still dominates neutrinos by a factor 10^3. Furthermore, there exists a particular class of event where a pair of downgoing muons arrive in space and time such that they produce

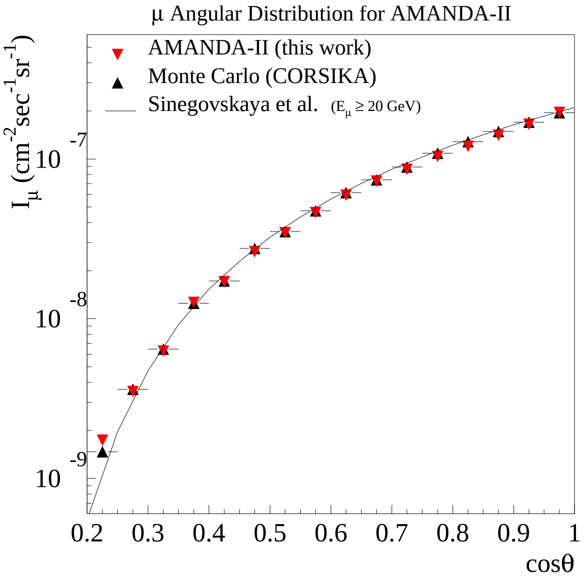

Figure 3.4: The angular distribution of atmospheric muons. $\cos\theta = 0$ is the horizon, while $\cos\theta = 1$ is vertically downgoing. (from [69])

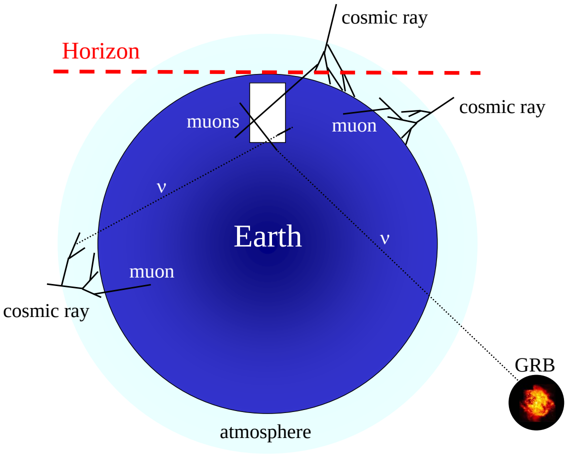

Figure 3.5: Use of the Earth as a filter for atmospheric muons. Above the horizon, only neutrinos reach the detector.

a combined light pattern that mimics an upgoing track. This can occur when one muon skims the bottom of the detector and shortly thereafter another passes through the top. We discuss the rejection of these single and coincident muon backgrounds and the differentiation between atmospheric and signal neutrinos in detail in Chapters 7 and 8.

3.5 Ice Properties

The glacial ice of the South Pole has a unique depth structure. Precipitation containing varying amounts of particulate matter was deposited over geological time scales, creating horizontal layers in the deep ice. These dust layers vary the absorption and scattering lengths of photons in the ice and thus must be well understood to ensure accurate reconstruction. A detailed study was conducted to map the structure of these layers [70] and a model of the ice called Millennium was constructed. It was noticed, however, that the reconstruction techniques used in AMANDA, upon which this ice model were fitted, introduced a systematic smearing in the dust layers. A deconvolution of this smearing effect to produce a more realistic depth profile of the ice resulted in the AHA ice model. This model also introduced clearer ice below the largest dust peak at 2050 meters in depth.

At the Čerenkov emission peak of 400 nm, optical absorption is typically 110 m, and effective scattering length is about 20 m. This is defined as

$$\lambda_s^{eff} = \frac{\lambda_s}{(1 - \langle \cos\theta_s \rangle)} \tag{3.8}$$

where λ_s is the scattering length and θ_s is the scattering angle [71]. For comparison, water in the Mediterranean has an absorption length of ∼40 m and a scattering length of ∼130 m at similar wavelengths [72]. Fig. 3.6 illustrates the optical properties of the ice enclosing both the AMANDA and IceCube detectors.

3.6 Reconstruction

Given the detection principles outlined above, an ideal detector will consist of an array of photomultiplier tubes (PMTs) to capture the Čerenkov emission of daughter muons, instrumenting a large volume in an optically clear medium. We present details of two such detectors, AMANDA and IceCube, in Chapter 4. Assuming such an array, we now consider the question of how to reconstruct the direction and energy of a neutrino-induced muon given the timing and amplitude information collected by the full set of PMTs. A full treatment may be found in [71].

We let the parameters of the track be denoted by the set of values $\mathbf{a}$ and the measured quantities by $\mathbf{x}$. We then seek to maximize the likelihood that the set of x_i can be explained by a given track $\mathbf{a}$

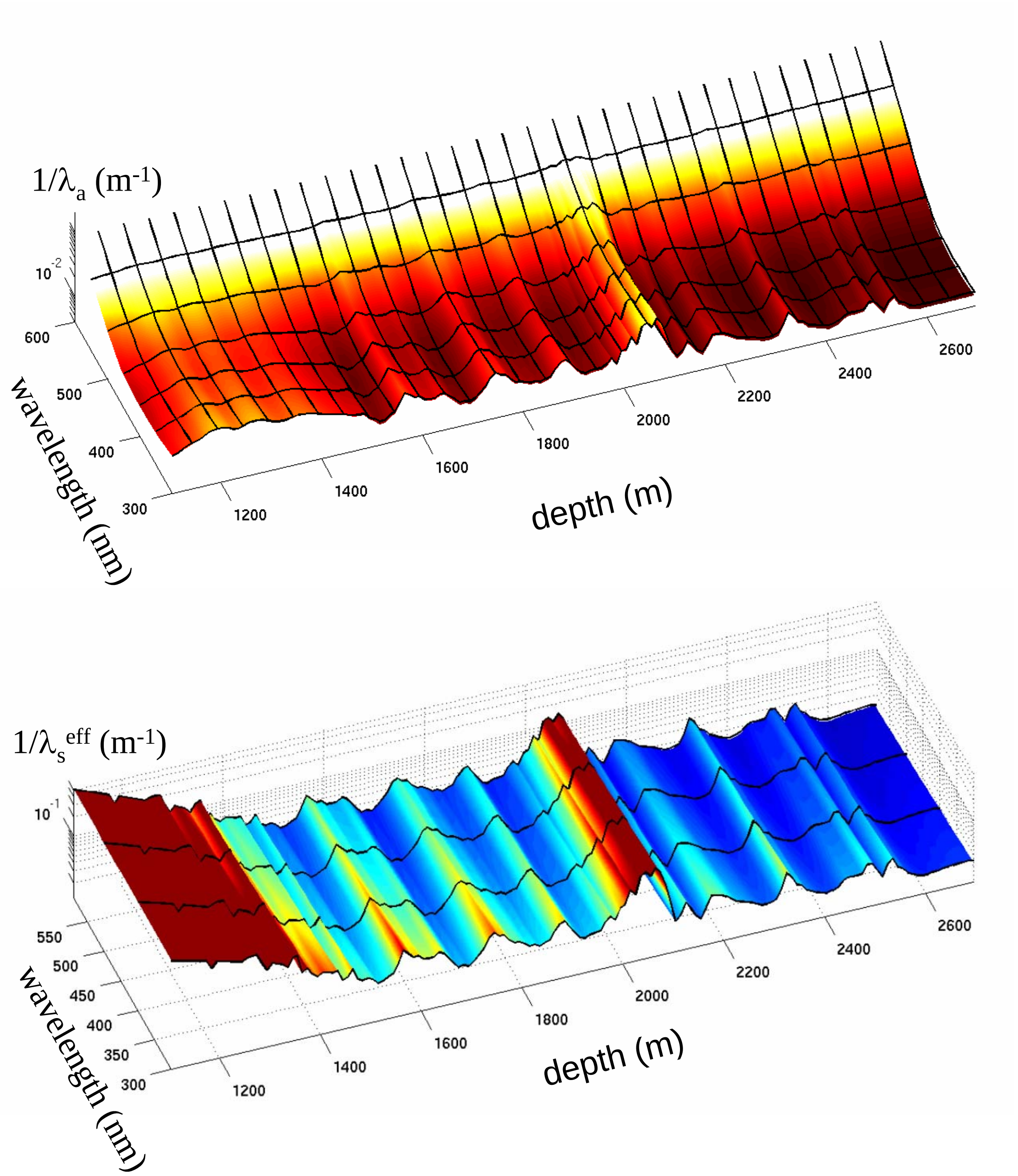

Figure 3.6: Optical properties of south pole ice as a function of wavelength and depth for the AHA ice model. Upper panel depicts inverse absorption length. Lower panel depicts inverse effective scattering length. The rapid increase in scattering above 1400 m indicates the presence of air bubbles in the ice.

$$\mathcal{L}(\mathbf{x}|\mathbf{a}) = \prod_i p(x_i|\mathbf{a}). \tag{3.9}$$

In the above $p(x_i|\mathbf{a})$ is the *probability density function* (PDF) for observing the value x_i given a hypothetical track described by $\mathbf{a}$. Fig. 3.7 depicts a coordinate system where the track is described by a vertex time, position and energy $(t_0, \mathbf{r}_0, E_0)$ and a momentum $\hat{\mathbf{p}}_0$. The vertex is an arbitrary point along the track. We assume a single, non-stopping muon creates the light pattern in the detector.

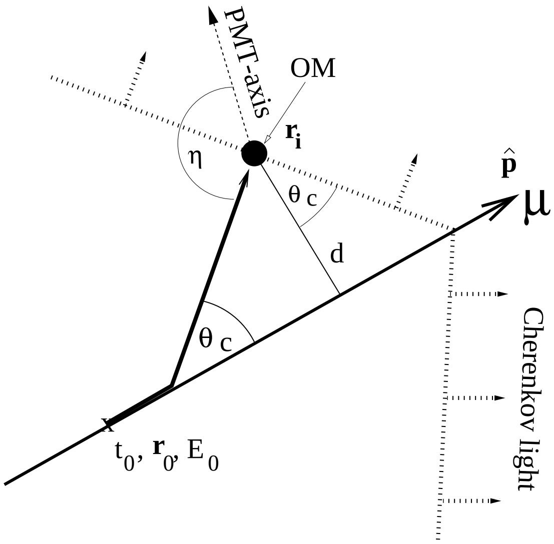

Figure 3.7: Schematic illustrating the parameters used in the reconstruction of muon tracks. The orientation and position of each PMT with respect to the hypothetical muon track is fully specified. (from [71])

The measured values $\mathbf{x}$ are detector dependent. For AMANDA, they include the time and duration (time over threshold) of each pulse as well as the amplitude of the largest pulse in the PMT (t_i, TOT_i, A_i). In IceCube, the amplitude of each individual pulse in the hit series is recorded, giving full waveform information. While the full amplitude information has been shown to improve track reconstruction [73], the hit times provide the most powerful tool. We therefore consider the simplified case of determining $p(t|\mathbf{a})$.

The likelihood PDF can be written in terms of time residuals; that is, the difference in time between when a hit is recorded and when it is expected given a Čerenkov cone and the geometry shown in Fig. 3.7.

$$t_{res} \equiv t_{hit} - t_{geo} \tag{3.10}$$

$$t_{geo} = t_0 + \frac{\hat{\mathbf{p}} \cdot (\mathbf{r}_i - \mathbf{r}_0) + d \tan\theta_c}{c} \tag{3.11}$$

t_{geo} thus represents the time of a so-called *direct hit*, for light that travels exactly along the Čerenkov cone without scattering. The shape of the time residual distribution is in general distorted by several effects (PMT jitter, dark noise, stochastic energy losses along the energy track) and furthermore, the broadness of the distribution is dependent on the distance of a given PMT from the track, due to scattering of light in the ice. For the same reason, the orientation η of the PMT with respect to the track can increase t_{res}, as light may have to back scatter to reach the collection face. We can thus write a likelihood based on the arrival times of single photons[3] at each hit module

$$\mathcal{L}_{SPE} = \prod_{i=1}^{N_{hits}} p_1(t_{res,i}|\mathbf{a}) \tag{3.12}$$

where p_1 is the corresponding probability density function. We describe the specific form of the PDF in section 3.6.4.

In addition to advanced (and time-consuming) likelihood reconstructions, it is also possible to make quick first-guess reconstructions to get an initial idea of the track direction. This information can then be used as a seed in the likelihood searches to reduce the maximization requirements. We now present an overview of the first-guess and advanced directional and energy reconstructions that are used in the analyses presented in this thesis.

3.6.1 Line-Fit

LINE-FIT is a fast first-guess reconstruction algorithm that neglects the complicated emission pattern of Čerenkov light in a realistic medium and instead assumes that all light travels along a

---

[3] SPE denotes Single Photo-Electron.

single path with velocity $\mathbf{v}$, with a vertex point $\mathbf{r}$. The locations of hit PMTs, $\mathbf{r}_i$, are then given by

$$\mathbf{r}_i \approx \mathbf{r} + \mathbf{v} \cdot t_i. \tag{3.13}$$

χ^2 for this distribution is given by

$$\chi^2 \equiv \sum_{i=1}^{N_{hit}} (\mathbf{r}_i - \mathbf{r} - \mathbf{v} \cdot t_i)^2 \tag{3.14}$$

and may be analytically minimized to give

$$\mathbf{r} = \langle \mathbf{r}_i \rangle - \mathbf{v} \cdot \langle t_i \rangle \tag{3.15}$$

$$\mathbf{v} = \frac{\langle \mathbf{r}_i \cdot t_i \rangle - \langle \mathbf{r}_i \rangle \cdot \langle t_i \rangle}{\langle t_i^2 \rangle - \langle t_i \rangle^2} \tag{3.16}$$

where $\langle x_i \rangle$ denotes the mean of x with respect to all hits in the event. LINE-FIT thus gives a rapid and analytical determination of both the vertex $\mathbf{r}$ and the direction $\mathbf{v}/|\mathbf{v}|$ of an event which may then be fed to more sophisticated algorithms as a seed.

3.6.2 Direct Walk

The DIRECT WALK algorithm is another very efficient first guess reconstruction that utilizes only a subset of hits in an event that are most likely to be caused by direct (unscattered) photons. The algorithm proceeds in several steps. First a straight line is created between each pair of hit PMTs in an event that have more than 50 m separation. The geometry of the array gives the direction (θ, ϕ) of these *track elements*, with vertex $\mathbf{r}_0$ given as the midpoint between the PMTs and vertex time t_0 as the average of the hit times.

Each of these pair-wise track elements then has a number of *associated hits* defined by their times residuals with respect to t_0 and distances from the track element. Those track elements with too few associated hits or with too little variance in lever arms [4] are then rejected. Those track

---

[4] The lever arm L_i of a hit PMT i with respect to a track element is the distance between the vertex $\mathbf{r}_0$ and the point on the track element closest to the PMT i. A large variance in lever arms for a given track element indicates hit PMTs are well-spaced along the length of the track.

elements that remain become *track candidates*.

In the case that multiple candidates are found (often), a cluster search is performed. For each track candidate, the number of other candidates within 15° is counted and the cluster with the largest number of track candidates is selected. The direction of the Direct Walk track $(\theta_{\mathrm{DW}}, \phi_{\mathrm{DW}})$ is then the average of the direction of the track candidates in this best cluster.

3.6.3 JAMS

JAMS [74] (Just Another Muon Search) is a first guess algorithm specifically designed to address the problem of coincident muons. In order to reconstruct an event a set of N directions is chosen from a pre-determined grid. For each direction, the hit set is projected onto a plane perpendicular to that direction. If the initial direction were an actual muon track, then one would find several hits at similar distances from the track (we have projected out the separation in time). Thus clustering of hits is expected for "good" directions. In the case of an event composed of multiple tracks from different directions (coincident downgoing muons), one would see either multiple clusters or no structure. A set of criteria is applied to the hit separations to determine the degree and size of the clustering. For each valid cluster (direction) a simplified likelihood function consisting of a pair of Gaussians is maximized. The set of derived tracks is then ranked via topological quality parameters. While up to the three highest quality tracks are saved, we typically use the best as a seed to the full likelihood reconstructions.

3.6.4 Pandel Likelihood

The photon hit probabilities and arrival times can be determined via light propagation simulation and this information can be stored in look-up tables [75, 76]. However, use of these tables can be technically difficult from the computing standpoint, and thus it is beneficial to consider whether simpler options exist. One such solution is the parameterization of the distributions in the look-up tables with analytical functions using only a subset of parameters. Work done by the BAIKAL experiment based on data taken with laser light showed that p_1 of Eq. 3.12 can be written as the so-called *Pandel function*:

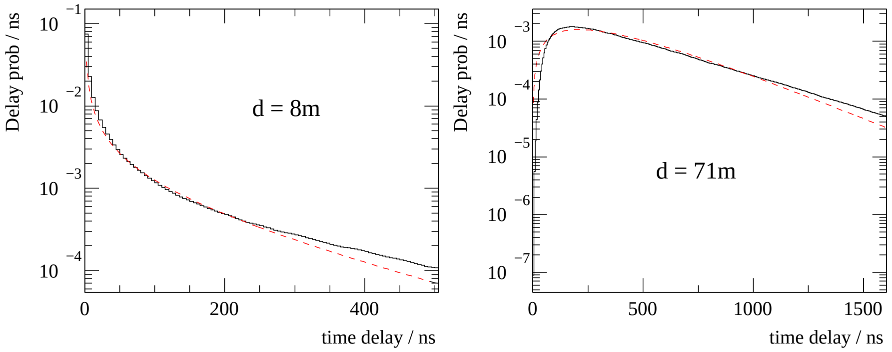

Figure 3.8: The Pandel function (dashed) is compared to a detailed light propagation simulation (solid) at two distances from the muon track. Close to the track (left) light is not scattered very much before reaching the PMT face and thus time residuals are small. Farther away (right), all light is scattering to some degree before hitting the PMT. (from [71])

$$p_P(t_{res}) \equiv \frac{1}{N(d)} \frac{\tau^{-d/\lambda} \cdot t_{res}^{d/\lambda-1}}{\Gamma(d/\lambda)} \cdot e^{-\left(t_{res}\left(\frac{1}{\tau}+\frac{c}{n\lambda_a}\right)+\frac{d}{\lambda_a}\right)} \tag{3.17}$$

where λ_a is the absorption length, n is the refractive index, d is the perpendicular distance from the muon track to the PMT as shown in Fig. 3.7, and $\Gamma(d/\lambda)$ is the Gamma function. $N(d)$ is a normalization factor given by

$$N(d) = e^{-d/\lambda_a} \cdot \left(1 + \frac{\tau c}{n\lambda_a}\right)^{-d/\lambda} \tag{3.18}$$

λ and τ are free parameters that are fit from the photon propagation simulation. Although the Pandel function was derived for isotropic, monochromatic, point-like sources of light, the freedom of choice in λ and τ makes it well suited for fitting the light pattern of a muon track as well. We fit the time residual distributions for a wide range of d and η and find that the signal for back-scattered light is well-modeled by frontal illumination of a PMT at a greater distance d_{eff}. Sample comparisons between the Pandel function and a detailed simulation of the photon propagation are shown in Fig. 3.8.

In practice, we also want to take into account PMT jitter, and the potential for negative time residuals from random noise in the detector. We therefore convolute the Pandel function with a

Gaussian. The function then describes the probability of observing the measured hits at each PMT. The total likelihood is given by summing the likelihoods for each PMT. This total is then globally maximized, allowing the hypothetical track parameters to vary freely.

$$\mathcal{L}_P \equiv \prod_{i=1}^{N_{hits}} p_P(t_{res,i}|\mathbf{a}) \tag{3.19}$$

The track described by $(\theta_\mathrm{P}, \phi_\mathrm{P})$ that maximizes Eq. 3.19 is then our best guess hypothesis for the muon direction.

3.6.5 Bayesian Likelihood

Bayes' Theorem states that the probability of a true set of track parameters **a** given a set of observed hits **x** is given by

$$P(\mathbf{a}|\mathbf{x}) = \frac{P(\mathbf{x}|\mathbf{a})P(\mathbf{a})}{P(\mathbf{x})} \tag{3.20}$$

$P(\mathbf{x}|\mathbf{a})$ is just the probability that an assumed track would generate the observed hit pattern, namely the Pandel likelihood function $\mathcal{L}_P$ described in Sec. 3.6.4. $P(\mathbf{x})$ is independent of the track **a** and is thus merely a normalization factor that may be ignored. $P(\mathbf{a})$, on the other hand, represents the probability of observing a track **a**, which depends on the characteristics of the track. We can leverage any number of event characteristics, but the dominant feature is the very strong zenith dependence of the atmospheric muon background, as seen in Fig. 3.4. Atmospheric muons are extremely abundant in the vertically downgoing region, but they become negligible near the horizon due to earth absorption. By weighting the likelihood with this angular dependence, some tracks which are reconstructed as up-going with the Pandel likelihood will instead become down-going, greatly reducing the mis-reconstructed muon contamination. We thus write the *Bayesian Likelihood* as:

$$\mathcal{L}_B \equiv \mathcal{L}_P \cdot P(\theta) \tag{3.21}$$

3.6.6 Iterative Reconstruction

The likelihood based event reconstructions described above require a track vertex and direction as a seed. We typically use the result of first-guess algorithms as this seed. However, it is possible that the reconstruction encounters a local minimum in the likelihood space. In order to mitigate this effect, we typically perform multiple iterations for the advanced reconstructions, with a variety of seed directions. This helps to ensure that the global minimum is found and that the best possible track is returned. The number of iterations to be performed is a trade-off between resolution and computing time and has diminishing returns. 16 to 64 iterations are typically performed, depending on the accuracy requirements of the specific reconstruction.

3.6.7 Energy Reconstruction

The all-sky neutrino flux induced by cosmic ray interaction in the atmosphere constitutes an irreducible background for astrophysical neutrino searches. In order to discriminate these atmospheric neutrinos from GRB neutrinos we can leverage several quantities. First and foremost is a statistical reduction when we consider only the temporal and spatial coordinates associated with the bursts. However, we can gain additional sensitivity by considering the differences in energy spectra. In general, atmospheric neutrinos follow a much steeper power law than that of the signal. Therefore, if we can reconstruct the energy of the daughter muon, we can get a good idea of the primary neutrino energy and thus assign it a probability of belonging to the signal or background population. We consider two useful methods for estimating the event energy, one simple and one complex.

3.6.7.1 N_{ch}

The number of hit PMTs (channels) in an event is known as N_{ch}. High energy muons tend to emit more light in the detector volume and thus create events with high values of N_{ch}, while the opposite is true for lower energy muons. However, this relation begins to break down when one considers high energy muons. The neutrino interaction vertex for such events may lie well outside the detector, and the muons would then travel several kilometers before traversing the instrumented volume. In this case, only a small fraction of the total energy of the track will be deposited. In addition, some tracks will skim the edges of the detector, hitting only a few PMTs. This effect can be seen in Fig. 3.9. In addition, the clarity of the ice affects the absorption of light, and thus the number of hit channels as well. This introduces a systematic depth dependence which must be taken into account. Nevertheless, N_{ch} represents a good, simple way to discriminate between varying spectra, as seen in Fig. 3.10.

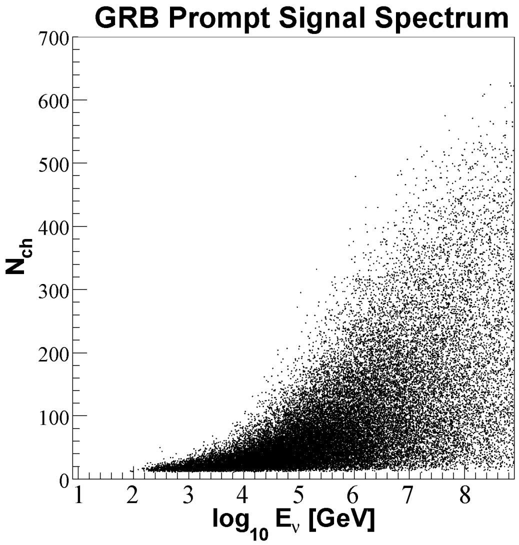

Figure 3.9: The energy estimator N_{ch} as a function of the primary neutrino energy. Even high energy neutrinos often deposit only small amounts of light within the detector and thus the distribution is strongly peaked at small N_{ch}.

3.6.7.2 Mue

The likelihood algorithm MUE [77] implements a much more sophisticated energy reconstruction method. Recall from section 3.3 that above about 1 TeV muon energy losses begin to be dominated by stochastic processes and that the energy loss per unit length becomes proportional to the energy. The likelihood based track reconstruction may then be extended to consider how well the photon density observed around a hypothetical track is described by an appropriate distribution function. This extended likelihood formulation is then maximized with an extra free parameter, yielding both a muon track and an energy estimator ϵ_{mue} at the distance of closest approach to the center of gravity of the hits in the event. In Fig. 3.11 we show the relative improvement in correlation between true energy and ϵ_{mue} as compared to the case of N_{ch} in Fig. 3.9. The excellent separation power between energy spectra is seen in Fig. 3.12. Fig. 3.13 quantifies the energy resolution achievable with

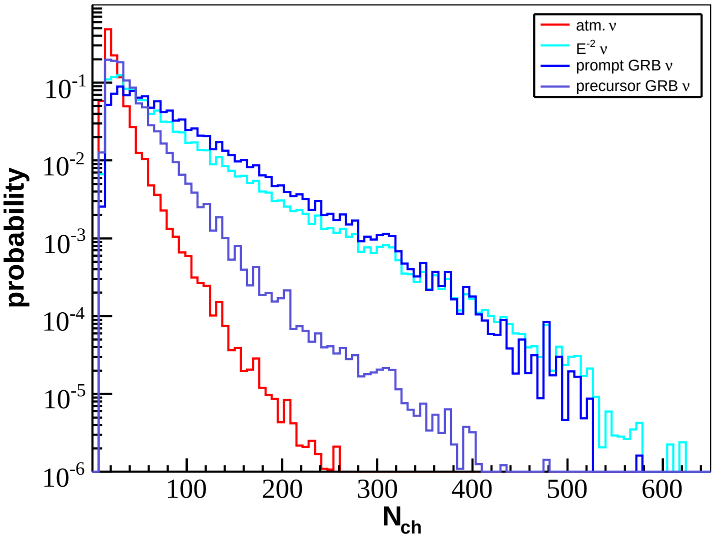

Figure 3.10: The N_{ch} distribution for various neutrino energy spectra. Even with its inherent limitations N_{ch} is a powerful discriminator between the soft atmospheric neutrino spectrum and the harder spectra of signal neutrinos. The high N_{ch} tail of the distribution gives strong background rejection potential.

ϵ_{mue} compared to other estimators. Resolution suffers at low energy where muon energy losses are only very weakly dependent on the energy of the muon. At the very highest energies PMTs closest to the track saturate with light and full information on the photon density is lost.

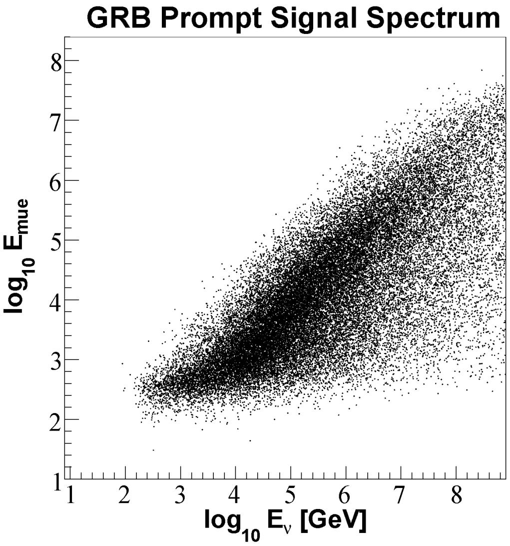

Figure 3.11: ϵ_{mue} as a function of neutrino energy. The agreement is much more linear than that shown for N_{ch} in Fig. 3.9.

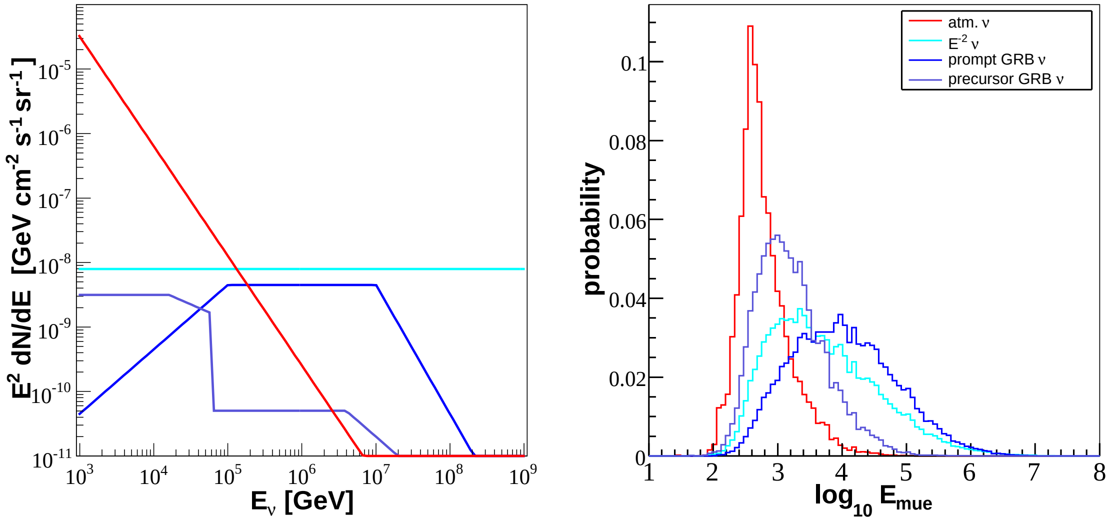

Figure 3.12: Distribution of the energy estimator ϵ_{mue} for various neutrino energy spectra (shown on left for reference). While it is possible to calibrate ϵ_{mue} to represent an energy in GeV, what is truly important is the shapes of the distributions. We therefore leave the parameter in its natural units of photon density per unit length (multiplied by PMT effective area). Notice the excellent separation between soft and hard energy spectra.

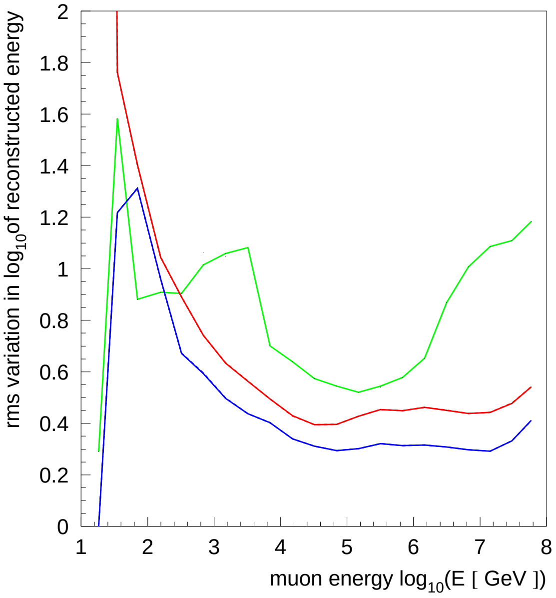

Figure 3.13: Comparison of the energy resolution for three estimators after calibration: blue for ϵ_{mue}, red for total charge per event, and green for N_{ch}. Resolution is defined as $\log_{10}(E_{reco}/E_{true})$. (from [77])

Chapter 4

Detectors

4.1 Satellites

While it is possible to search for neutrinos from untriggered GRBs [11] we typically use the temporal and spatial information collected by satellites to restrict our background. The main parameters of those satellites which observed GRBs included in our analyses are summarized in Table 4.1. We describe them in further detail below.

Satellite	Instrument	Energy Range	FOV	Resolution
Swift	BAT	15–150 keV	1.4 sr	4 arcmin
	XRT	0.2–10 keV	23.6’	5 arcsec
	UVOT	170–650 nm	17’	0.3 arcmin
HETE-II	FREGATE	6–400 keV	3 sr	–
	WXM	2–25 keV	1.6 sr	11 arcmin
	SXC	0.5-15 keV	0.9 sr	10 arcsec
INTEGRAL	SPI	20 keV–8 MeV	16°	2°
	IBIS	15 keV–10 MeV	9°	12 arcmin
	JEM-X	3–35 keV	4.8°	3 arcmin
Suzaku	HXD	10–600 keV	34°/4.5°	–
AGILE	GRID	30 MeV–50 GeV	3 sr	0.2°–5°
	Super-AGILE	10–40 keV	0.8 sr	3 arcmin

Table 4.1: Main Parameters of GRB-detecting Satellites. Note that only Swift may slew to align its high resolution x-ray and UV detectors with the direction of a burst detection. Other satellites rely on overlapping fields of view between instruments, greatly reducing detection rates.

4.1.1 Swift

The majority of the GRBs searched for in this thesis were first observed by the Swift satellite [25, 24], launched in November of 2004. Swift is specifically designed to serve as an optimal platform for the observation of transient sources over many wavelengths, with a detection rate of ~ 100 GRBs/yr. This capability is provided for by three onboard detectors. The Burst Alert Telescope (BAT) has a wide, 1.4 sr, field of view and is sensitive to the 15-150 keV energy range. It uses a coded mask to determine photon arrival direction with 1-4 arcmin precision. The X-ray Telescope (XRT) and UV and Optical Telescope (UVOT) are sensitive to lower energy ranges and are used to pinpoint the GRB location (0.3-5 arcsec resolution) and to study the characteristics of the afterglow. Fig. 4.1 depicts the satellite and detectors.

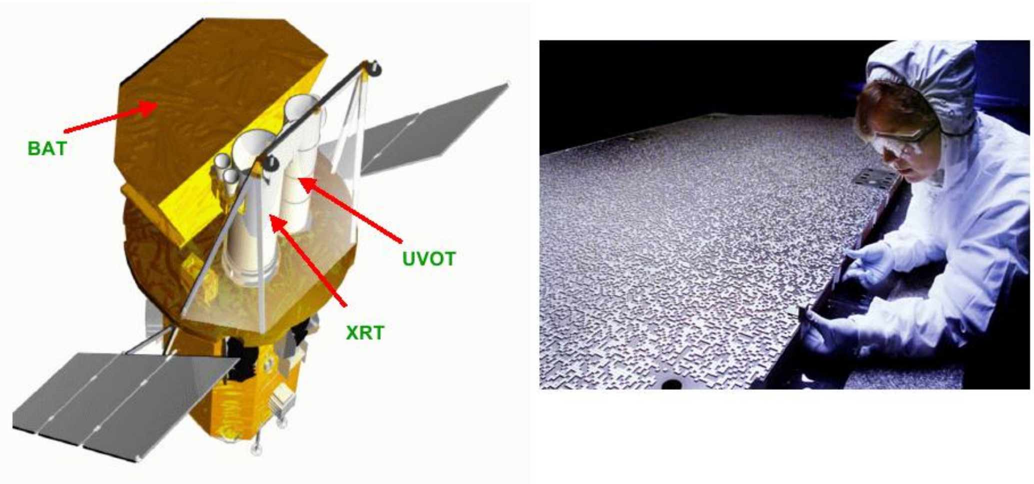

Figure 4.1: The Swift satellite. Left panel shows the satellite with BAT, XRT, and UVOT. Right panel shows the coded mask used for localization by the BAT. Swift was intended to be sensitive to the 15-350 keV energy range, but it was discovered that the mask was transparent to photons above 150 keV. This has the unfortunate effect of drastically reducing the number of photon spectral break energies observed.

When the BAT detects a burst, it rapidly transmits the location to other space and ground based observatories via the Gamma-ray Coordinates Network (GCN) [78]. Swift then autonomously slews to aim the XRT and UVOT at the source location within 20-75 s. Observations of the afterglow spectral lines lead to redshift determinations in about 25% of detected bursts. Swift may also be slewed manually to perform follow-up observations of GRBs initially detected by other satellites.

4.1.2 HETE-II

HETE-II, the High Energy Transient Explorer [79], was launched in 2000. It carries wide field x-ray (WXM) and γ-ray (FREGATE) instruments and is sensitive to the 0.5-400 keV energy band. The overlapping field of view of the detectors is about 2 sr. The satellite is capable of performing localizations with ~ 10 arcsec precision onboard within seconds of detecting a burst and transmitting these positions to ground-based observatories. Since HETE-II is always pointed anti-solar, it is guaranteed that optical telescopes will be able to make early afterglow measurements of detected bursts. HETE-II was the first satellite to detect the weaker subclass of bursts known as X-Ray Flashers (XRFs). Having long outlived its nominal mission of 2 years, the NiCD batteries on board are wearing down, and operation is sporadic.

4.1.3 INTEGRAL

The International Gamma-Ray Astrophysics Laboratory (INTEGRAL) [80] was launched in October 2002. It was designed to have high spectral and spatial resolution and to make simultaneous observations in the optical, x-ray, and γ-ray bands. The high energy payload consists of two instruments. The first is a spectrometer (SPI), able to detect the 20 keV - 8 MeV range, with an energy resolution of 2.2 keV at 1.33 MeV, and a spatial resolution of 2.5°. SPI has a field of view of 16°. The second instrument is an imager (IBIS), with a smaller field of view of 9°, but increased spatial resolution of 12 arcminutes. Like Swift, INTEGRAL utilizes a coded mask algorithm to perform localization.

4.1.4 IPN3

The 3rd Interplanetary Network (IPN3) [81] is a group of satellites that operate in concert to localize GRBs through triangulation of burst detection times. Normally, the highly precise instruments aboard satellites like Swift give much better positioning than IPN3, but in the case that a GRB occurs outside the field of view of the precision satellites, one can still extract useful localizations for afterglow followup or neutrino searches. Fig. 4.2 shows the method used to triangulate burst positions. The main satellites currently contributing to IPN3 include Swift, Konus-Wind, Ulysses, INTEGRAL, Suzaku, 2001 Mars Odyssey, RHESSI, MESSENGER, and AGILE. Taking effective fields of view and duty cycles of all satellites into account, IPN3 is a full-time, all sky GRB monitor.

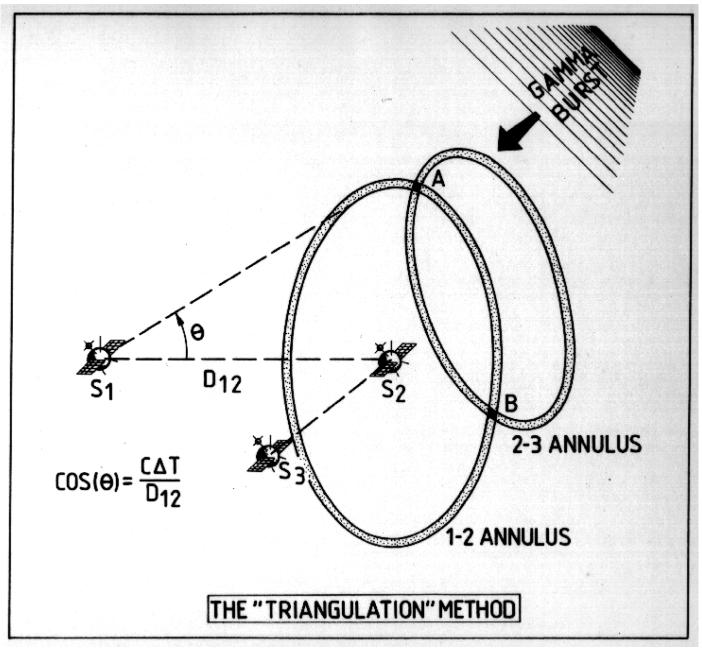

Figure 4.2: IPN3 uses a triangulation method to localize GRBs. An annulus of possible locations can be determined by detection of burst times by 2 satellites. The center is defined by the vector joining the two spacecraft, and the radius depends on the arrival times detected by each instrument. Satellites that are further apart provide more precise localizations. With more than two satellites, positions may be refined by finding the intersection of the pair-wise annuli. (from [81])

4.1.5 Suzaku

The Suzaku satellite [82] was developed by the Japanese Institute of Space and Astronautical Science (ISAS) and launched in July of 2005. It is the first satellite to carry an x-ray microcalorimeter, capable of very precise energy measurements. These x-ray spectrometers are sensitive to soft x-rays only, however. For detection of GRBs, Suzaku relies on its Hard X-Ray Detector (HXD), sensitive to the 10-600 keV energy band. The HXD has a field of view of 34° below 100 keV and 4.5° above 100 keV. Its primary mission is not as a GRB monitor, but it does detect some by coincidence.

4.1.6 AGILE

AGILE [83, 84] is a mission of the Italian Space Agency (ASI), and was launched in April of 2007. It carries a unique configuration of both a γ-ray (GRID, 30 MeV - 50 GeV) and hard x-ray (Super-AGILE, 18-60 keV) instrument. It has a 2.5 sr field of view above 30 MeV (0.8 sr in the keV band) and is able to localize bursts to within 1-3 arcminutes. AGILE is a multipurpose instrument, designed to study AGNs, GRBs, galactic sources, and unidentified γ-ray emitters. Until the Fermi Gamma Space Telescope was launched in 2008, it was the only satellite dedicated to gamma-ray astrophysics above 30 MeV. With GRID, AGILE is ideally suited to studying the high energy component of GRBs, before observed only rarely [1].

4.2 AMANDA-II

The Antarctic Muon and Neutrino Detector Array (AMANDA) [85] was deployed between 1995 and 2000 in the deep glacial ice of the south pole. It consists of an array of vertical strings of optical modules (OMs) deployed in the Antarctic Ice. The OMs are located at 10-20 m intervals along the length of the strings, at a depth of 1550 - 2050 m. The initial 10 strings (302 OMs) were deployed in a circular configuration of diameter $\sim$100 m between 1995 and 1997. This was called AMANDA-B10 [2]. 9 additional strings were deployed by 2000, creating an array of 677 OMs [3] and 200 m in diameter. Analog PMT signals are transmitted to the surface via cables [4].

4.2.1 The Optical Module and μDAQ

Each Optical Module (OM) is built around an 8 in. Hammamatsu R-5912-2 Photomultiplier tube. The PMT is enclosed in a glass sphere to withstand the pressure of the surrounding ice. After traveling $\sim$2 km to the surface, the analog signal has weakened from $\sim$1 V to $\sim$10 mV. It also undergoes broadening. These signals are then amplified with SWAMPs (SWedish AMPlifiers) and fed to two outputs, one prompt and one delayed. The prompt output is routed through a discriminator and then to the trigger and a TDC (Time to Digital Converter). The TDC records the times when a pulse rises above (leading edge) or falls below (trailing edge) the discriminator threshold and may record 16 such edges. The other output of the SWAMPs is delayed by 2 μs and fed to a peak-analog to digital converter (ADC). The ADC determines the maximum amplitude over all pulses in the

---

[1] EGRET observed about 10 GRBs during its 7 year lifetime. AGILE detection of GRBs by GRID is 5-10 per year.

[2] AMANDA-A was a 4 string array deployed at a depth of 800-1000 m. It was discovered that the ice at this depth contains many residual air bubbles which increase scattering of photons and make muon reconstruction impossible [86].

[3] Only about 540 OMs are used in the analysis presented in this thesis, due to problems with individual modules or entire strings.

[4] String 18 contains prototype DOMs (see Sec. 4.3.1) which digitize the signal onboard.

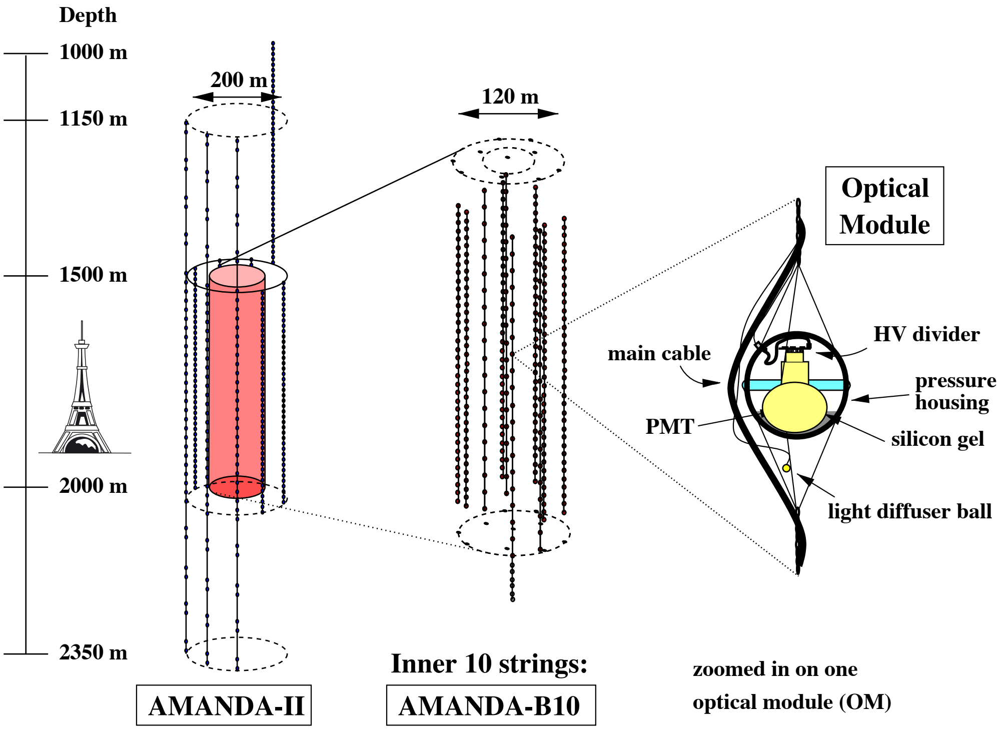

Figure 4.3: The AMANDA-II detector in the Antarctic ice with Eiffel tower graphic showing scale. Included is a schematic showing details of the Optical Module. (from [71])

OM and assigns this value to all hits in the channel. The trigger condition for events requires 24 hit channels within a time window of 2.5 μs. If this condition is met, the LE, TE and ADC values for each hit are transmitted to the surface, and a trigger is sent to a GPS clock to timestamp the event. This configuration of the data taking system is known as the μDAQ. A Transient Waveform Recording (TWR) system was installed later and operated exclusively after 2006 when μDAQ was shut off. As this thesis deals with the earlier dataset, we do not describe TWR in any more detail here.

4.2.2 Calibration

Because the signal is transmitted to the surface before digitization and time recording a calibration must be applied to relate the leading edge (LE) times with the PMT hit times. This calibration is performed by recording time-of-flight for YAG laser pulses sent from the surface down optical cables and reflected. These cables emit the laser pulse into the ice where it is recorded by PMTs and transmitted back to the surface. The time of this sequence then defines the offsets. The same principle is used to determine the relative geometry of the OMs in the array. After calibration, the B10 OMs (with coaxial or twisted-wire cables) have a timing resolution of 5 ns, while the optically cabled OMs have a resolution of 3.5 ns [71]. Amplitude calibration is performed by dividing the measure peak-ADC values by the most likely values that would be generated by single photoelectrons incident on the PMT.

4.3 IceCube

IceCube, when complete, will consist of 80 vertical strings of 60 Digital Optical Modules (DOMs) each, buried in the deep Antarctic ice between a depth of 1450 and 2450 meters. Each DOM consists of a 25 cm PMT enclosed in a glass pressure sphere, and associated electronics. The DOMs are spaced at 17 m vertical intervals on the strings, with inter-string spacing of $\sim$125 m, with the full detector instrumenting a physical volume of $\sim$1 km^3. The spacing is chosen to optimize the event reconstruction (see Chapter 3) for the energy range of primary interest (10 TeV to 10 PeV). At the surface location of each string are additional DOMs frozen in water tanks, implementing an extensive air shower array known as IceTop. In addition to cosmic ray physics, IceTop may be used as a veto for neutrino detection with IceCube. The analysis presented in this thesis makes use of the 22-string configuration of the detector, operational from April 2007 to April 2008.

4.3.1 The Digital Optical Module

The Digital Optical Module (DOM) [87] is the fundamental unit of the IceCube detector array. Each DOM is designed to collect light, capture and convert waveform data to digital signals, perform accurate timestamping, and transmit those signals to the surface. It consists of a 25 cm PMT (Hammamatsu R7081-02) with an average quantum efficiency of 20%, a 2 kV high voltage power supply, the DOM main board, a signal delay board, and an LED flasher board. These components are enclosed in a 13 mm thick glass pressure sphere. The glass and PMT are optically coupled via a gel chosen for its transmission qualities. The DOM is pressurized to 1/2 atmosphere with dry nitrogen to ensure the structural integrity of the enclosing sphere. Communications and power are supplied via a single twisted wire pair to the surface. Fig. 4.5 shows the wavelength dependence of the quantum efficiency and transmittance of the glass/gel.

The PMT converts detected light to electronic pulses with a gain determined by the applied high voltage. During the 22-string running period, the DOMs were operated at a nominal gain of $1{\times}10^7$. The raw analog signal is sent to the DOM main board and split between a trigger discriminator and the 75 ns signal delay board. If the discriminator threshold is surpassed (set to 0.25 SPE [5] for this dataset), the delayed signal is sent to an Analog Transient Waveform Digitizer (ATWD) [6] and to a PMT ADC. The ATWD contains 4 channels. The first 3 capture the PMT waveform with varying gain (x16, x2, x0.25) while the 4th channel is responsible for high-speed monitoring of various DOM functions (LC, clock, flashers, comms). The captured information is only digitized and buffered if triggered by additional logical conditions (see Sec. 4.3.2.1). In this case, usually only the highest gain channel is digitized. If this channel saturates (∼1% of the time), the lower gain channels are also digitized. The PMT ADC captures waveforms over a longer time scale of $6.4\,\mu$s.

Timestamping at the DOM level is accomplished via a 40 MHz free-running high stability crystal oscillator. Synchronization over the array is coordinated via a Reciprocal Active Pulsing (RAPCAL) [88] algorithm. With these processes, we are able to achieve a timing resolution of ∼2 ns.

Each DOM also contains an ultraviolet LED resident on the Mainboard and a dedicated flasher board containing 12 LEDs. The onboard LED can stimulate the local PMT with zero to 10s of photoelectrons which are used to measure transit times. The LEDs on the flasher board are used to stimulate remote DOMs for calibration purposes or to mimic cascade-like events.

4.3.2 IceCube DAQ

The 60 DOMs on each string are connected to the surface via a single cable where it terminates in a Surface Junction Box (SJB). The SJB also gathers the input from the 2 IceTop stations (each containing 2 DOMs) at the top of each string. These signals are then sent to the IceCube Laboratory (ICL) via a surface cable. Each string is controlled by a computer called a DOMHub, containing 8 DOM Readout (DOR) cards. The DOR card controls power, establishes boot-up, selects or loads

---

[5] 1 SPE is peak of the voltage output distribution measured for a large set of single photo electrons created in a PMT by incident photons. The SPE distribution and peak are measured for each DOM.

[6] There are actually 2 ATWDs resident on the DOM mainboard to reduce deadtime. The signal is sent to whichever is free.

code, initiates calibration, requests data transfer, and manages time calibration.

Absolute timestamping is achieved by a Master Clock using the GPS satellite radio-navigation system. Times are recorded in UTC and a static offset due to cable delays and GPS-UTC difference is applied.

4.3.2.1 Local Coincidence

DOMs are connected to their vertical neighbors via local coincidence (LC) links. This allows a DOM to transmit and receive LC tags from the DOMs above and below it. These LC tags may be propagated further up or down the string, creating local coincidence chains of length l (nearest neighbor=1, next-to-nearest neighbor=2, etc.). When a DOM is hit, it transmits an LC signal to its neighbors and opens a receptive time window of $\sim 1\mu$s. If it receives an LC tag from a neighboring DOM during this time window the hit satisfies the local coincidence condition. For the 22-string IceCube data taking run, a Hard Local Coincidence scheme was employed. In this mode, only hits with LC tags are digitized and sent to the surface. In this way, isolated hits which are likely to be noise do not use up valuable ATWD digitization time. Soft Local Coincidence is also possible, where all hits are transmitted, with only timing information being sent for those hits that do not satisfy LC conditions. This mode will first be used with the 59-string configuration of IceCube.

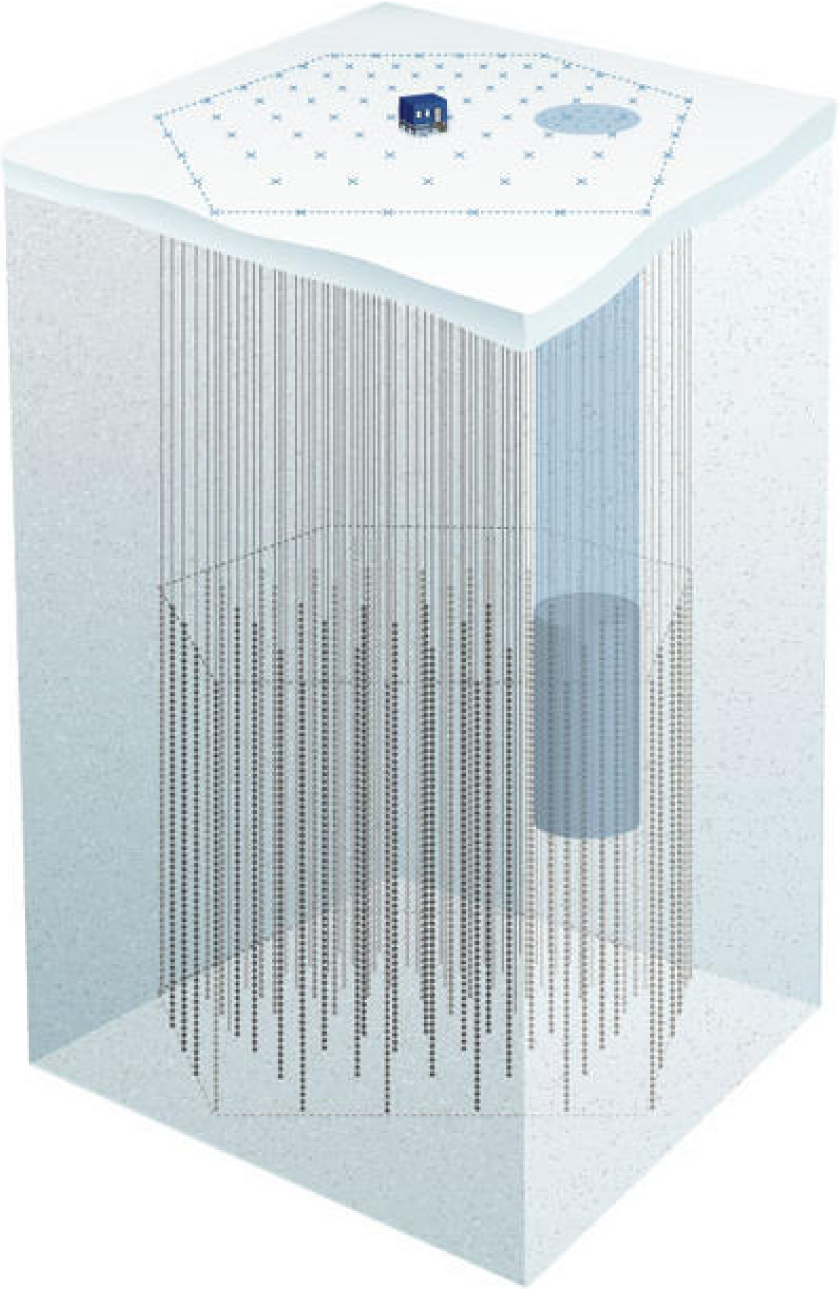

Figure 4.4: Schematic of the full IceCube detector. The shaded region indicates the location of AMANDA-II.

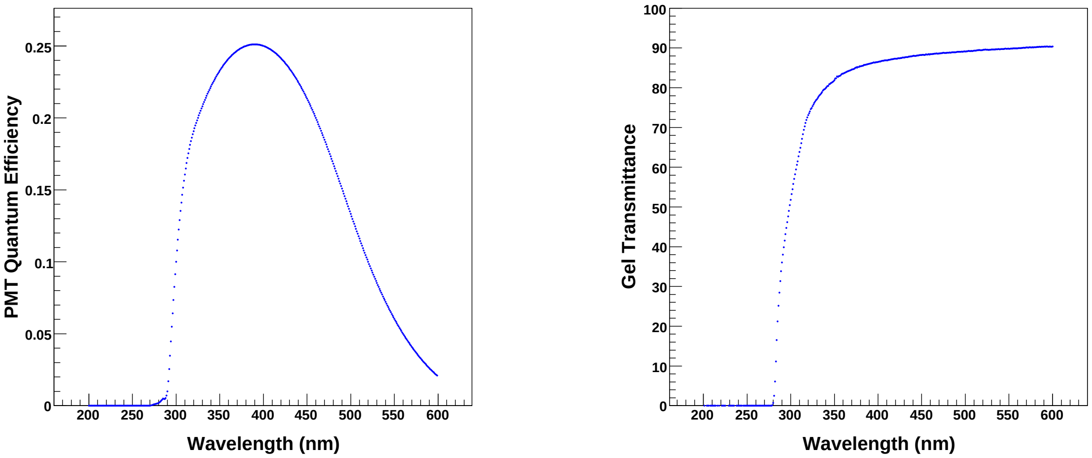

Figure 4.5: Wavelength dependence of DOM properties. Left panel shows the quantum efficiency of the PMT. It peaks at 400 nm, where the majority of Čerenkov photons are emitted. Right panel shows the transmittance of the gel. Note the sharp UV cutoff at ∼300 nm. The glass cuts off at higher wavelength. Above about 600 nm, the ice loses transparency. (see Fig. 3.6)

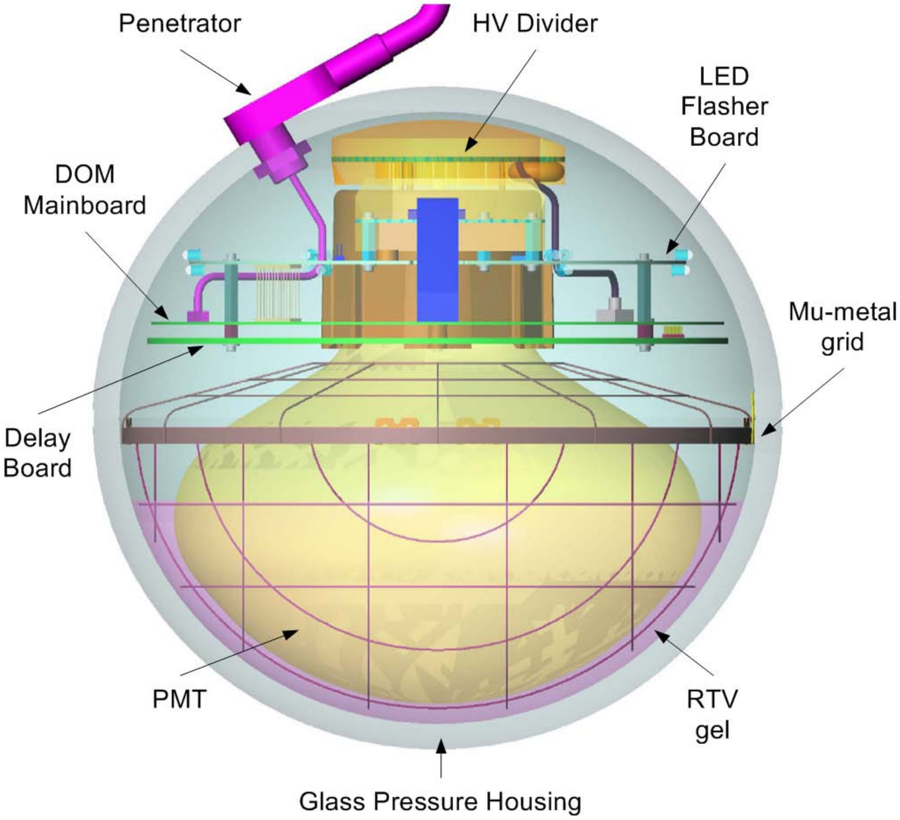

Figure 4.6: Schematic of an IceCube Digital Optical Module (from [87])

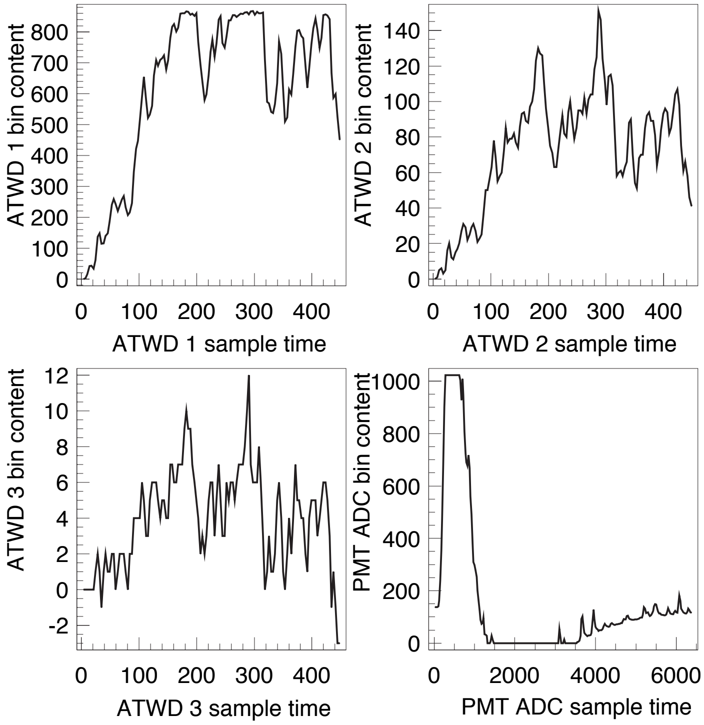

Figure 4.7: Sample waveforms from the 3 channels of the ATWD and the PMT ADC. Horizontal scale is in ns. Note that information lost from saturation of the high gain (upper left) channel is recovered by other channels. Distortion at long time in the PMT ADC signal is due to transformer droop and may be software corrected. (from [87])

Chapter 5

Gamma-Ray Burst Selection

5.1 Satellites

The goal of the analyses is to identify neutrinos that originate from gamma-ray bursts. Since the flux from any individual burst is expected to be low, we seek to maximize the number of potential sources and perform a stacked search. Therefore, we take as our initial sample all GRBs that triggered satellites during the periods of interest. We obtain information about each GRB from the *notices*, *circulars*, and *reports* distributed by the Gamma-Ray Burst Coordinate Network (GCN) [78]. These GCN communications can be easily referenced via the GRBLOG database [89].

Much of the background rejection power of the analysis comes from the good directional reconstruction of muons [1]. We thus in principle eliminate any bursts with a poor localization. However, as most bursts trigger the Swift satellite, with its very precise angular resolution (see Chapter 4), this does not turn out to be a concern. We further restrict ourselves to GRBs that occur in the northern hemisphere or just below the horizon. This allows us to take advantage of the shielding properties of the Earth with respect to atmospheric muons (see Chapter 3).

For the 2005-2006 AMANDA dataset, this results in a set of 119 well-localized, northern sky bursts. For the 2007-2008 22-string IceCube dataset, the number is 48. These numbers may be further reduced when checked against the status of the detectors.

---

[1] We also leverage knowledge of the emission window and differences in energy spectra between signal and background.

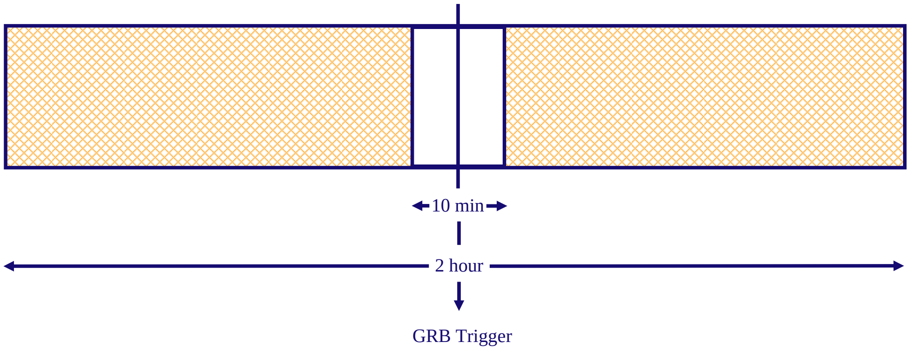

Figure 5.1: Definition of the blind time window surrounding a gamma-ray burst in the 2005-2006 AMANDA analysis. The principle for IceCube bursts is identical, though the window is extended.

5.2 Blindness

We do not want to bias our searches by looking at possible signal events when optimizing event selection. Rather, we seek to use a sample known to consist of only background events. This is known as blinding the analysis. In the case of GRBs, the procedure is straightforward. We choose a representative time window around each GRB trigger and set aside that data, to be looked at only in the final analysis. The remaining off-time data may then be used as a known signal-free sample with which to tune the analysis. This principle is illustrated in Figure 5.1. The size of the blinded time window depends on the specific analysis. For AMANDA, we chose to blind a 10 minute window centered on each GRB, extended for those bursts with extremely long prompt emission. This was sufficient to blind the prompt signal, as well as leaving the precursor window available for future work. In the case of IceCube, we wanted to perform a generic search with an extended time window, encompassing emission both before and after the observed photons, and thus we blinded a window of {-1,+3} hours around each GRB trigger.

5.3 AMANDA-II

Given the set of 119 northern hemisphere bursts observed by satellites during the 2005-2006 calendar years, we must determine for which bursts the AMANDA detector was taking data and operating stably. We must also determine a suitable duration for each GRB in order to accurately predict the associated on-time background.

5.3.1 Detector Stability Criteria

In order to determine the usability of each GRB in our sample, we first must associate bursts with runs in the detector. We reference the AMANDA monitoring pages [90] and determine by eye the runs corresponding to a two hour window surrounding each GRB, centered on the burst trigger time. Such a window will yield not only the on-time data (which we blind), but also enough off-time background to conduct detector stability studies for each burst in our sample. We note that we do not automatically remove bursts from consideration which occur during the typically noisy or "unstable" austral summer as is typically done. Nevertheless, several bursts are eliminated from the search, as shown in Table 5.1.

Burst	Problem	Burst	Problem
GRB050117	Not Filtered	GRB060111B	No Data
GRB050124	No Data	GRB060115	Not Filtered
GRB050126	No Data	GRB060121	Not Filtered
GRB050215A	Not Filtered	GRB060123	Not Filtered
GRB050215B	Not Filtered	GRB060124	Not Filtered
GRB050713A	No Data	GRB060203	No Data
GRB050716	No Data	GRB060206	No Data
GRB051211B	Not Filtered	GRB060210	No Data
GRB051221A	Not Filtered	GRB060908	No Data
GRB051211B	Not Filtered	GRB060927	No Data
GRB051227	Not Filtered	GRB061122	No Data
		GRB061126	No Data
		GRB061210	No Data
		GRB061222A	No Data

Table 5.1: GRBs lacking detector data in 2005-2006. Mass filtering was not conducted on data from parts of the austral summer construction season and the decision was made not to perform a specialized filter on those bursts that fell in this time period.

Table 5.2 shows several remaining bursts for which the two hour window of off-time data to be used for stability tests is incomplete. None of this missing data affects the blind windows and stability limited stability tests may be performed.

We perform three tests to the data surrounding each GRB to determine stability. All are performed on data that has undergone the first level of filtering to select upgoing events. While the

Burst	Problem
GRB051109A	Incomplete 2 hour window
GRB060501	Slightly incomplete 2 hour window
GRB060522	Slightly incomplete 2 hour window
GRB060906	Incomplete 2 hour window

Table 5.2: GRBs lacking full data in the off-time stability window in the 2005-2006 analysis.

data is highly background dominated at this filter level and thus little danger exists of observing potential signal in the on-time windows, we nevertheless choose to blind these windows to be conservative. First, we plot the rates in the extracted window as a function of time. Visual inspection will immediately reveal GRBs with extremely unstable data. We discovered several bursts that lack data during the blinded emission window and several in 2006 that exhibit very high detector rates. The runs corresponding to these windows were found to coincide with calibration runs of the IceCube detector, where LED flashers were being pulsed. For a few of these bursts, the flasher runs were not near the emission window and the average rates during the emission were found to be stable. These bursts were thus included in the analysis. To find more subtle stability issues we plot the distribution of detector event rate per 10 s interval and fit it with a Gaussian. Events in the tails reveal anomalously low or high rates. At low level, the times between events are expected to be Poisson distributed and thus can be fit with an exponential whose time constant matches the detector rate. These additional tests reveal no additional unstable bursts in the sample that were not first detected by the first test described above. However, they confirm the abnormal behavior of the detector in each case of problematic data. A sample set of stability plots can be seen in Fig. 5.2. Stability plots for all bursts in the 2005-2006 analysis can be found in Appendix E. Table 5.3 shows all bursts in the AMANDA analysis that exhibited unstable data in 2 hour window and the final disposition of those bursts. After all data is checked for stability, 86 northern hemisphere GRBs are found to have data suitable for analysis. We remove the exceptionally long burst GRB060218 [2], leaving a final sample of **85** gamma-ray bursts for the 2005-2006 AMANDA search.

---

[2] This burst had an emission spanning several thousand seconds and exhibited weak photon emission despite being relatively nearby. While GRB060218 is important to the gamma-ray burst community for its strong association with SN2006aj, it is not a suitable candidate for inclusion in this analysis.

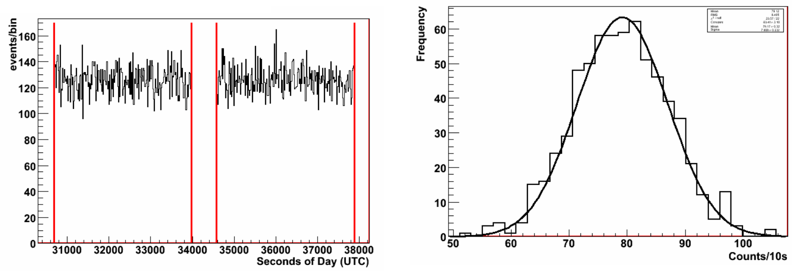

(a) event times

(b) rate distribution

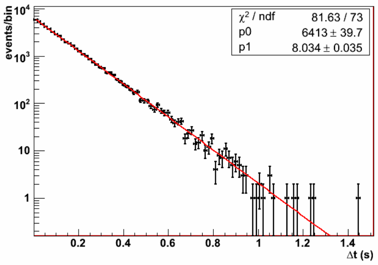

(c) time between events

Figure 5.2: Sample detector stability plots at filter Level 1 for GRB050319. Panel (a) shows the event times in a 2 hour window surrounding the trigger time. Panel (b) shows the distribution in the event rate per 10 s, fitted with a Gaussian. Panel (c) shows time difference between subsequent events in the detector, fitted with an exponential. Stability plots for all bursts in the 2005-2006 analysis can be found in Appendix E.

5.3.2 Burst Duration Determination

The duration of a GRB has typically been quantified by T_{90}, the time between which 5% and 95% of the observed photon emission occurs. Reliable T_{90} durations and start times relative to the satellite trigger are not readily available. The figures listed publicly on the Swift collaboration website [25] are first guesses, and not to be trusted. We investigated several methods for determination of burst duration.

After consultation with Craig Markwardt, a member of the Swift collaboration, we extracted duration information directly from the Swift data archives available online using the HEASARC software package FTOOLS [91], and verified against the published lightcurves. For HETE and Integral, only approximate T_{90} information is available, and start times must be extrapolated from the lightcurves (see Appendix D). For such bursts, we make conservative estimates of the burst duration in order to include the maximum possible emission.

Burst	Problem
GRB050408	Only have data for first 14.5 s of 34 s emission. Analyze shortened window
GRB050824	No data during GRB emission
GRB060105	Average rate during emission OK
GRB060110	Average rate during emission OK
GRB060111A	Extremely high rate during emission. Remove from analysis
GRB060202	Very high rate during emission. Remove from analysis
GRB060403	No data during GRB emission
GRB060413	No data during GRB emission
GRB060712	No data during GRB emission
GRB060825	Average rate during emission OK
GRB060929	Extremely high rate during emission. Remove from analysis

Table 5.3: GRBs with problems in the data in 2005-2006. Some GRBs with periods of anomalously high rates were shown to have average rates during the blinded time window and are accepted into the analysis.

Butler et al. [92] present an independent calculation of Swift burst durations through August 2007. They similarly extract the Swift data from the archives online. They use an automated algorithm to integrate the lightcurves and determine burst regions. These regions are extended backwards and forwards in time to include exponential tails in their fitted, de-noised lightcurves. They then calculate T_{90} information based on these burst regions, as well as supplying T_{90} error information. However, they do not supply T_{90} start times relative to trigger.

In private communications with Mike Stamatikos of the Swift collaboration, he agreed to perform more detailed determinations of burst duration as a comparison with the Butler et al. result. This work resulted in detailed T_{90} information for all Swift bursts in the sample, including error and start time relative to trigger. Interestingly, it was found that there existed large discrepancies between some of these values and those calculated by Butler et al. It was surmised this was in part the result of different noise reduction and baseline subtraction algorithms. As the numbers given by Stamatikos were calculated within the Swift data group, using the latest techniques, it was decided in the end to use these for our burst duration information. For those bursts not observed by the Swift satellite, we supplement this information with the durations extracted from the lightcurves as described above.

We further pad these durations by one second before and after to be somewhat more conservative. In unblinding, we start at the earlier of the trigger time or the T_{90} start time to ensure that no prompt emission is lost. These principles are illustrated in Fig. 5.3. Table 5.4 lists the full set of 85 GRBs used in the 2005-2006 AMANDA analysis, including all spatial and temporal information relevant to the search. The total prompt emission ontime for this analysis is 5343.8 s.

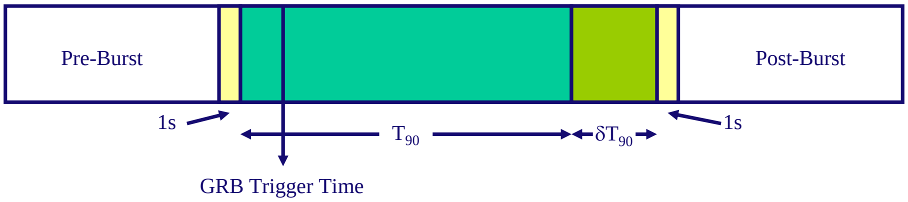

Figure 5.3: Burst duration definition for GRBs in the 2005-2006 dataset. Note that the pre-burst and post-burst regions remain blind for potential future precursor or afterglow emission searches.

Table 5.4: Spatial and Temporal Information for 85 GRBs Observed in 2005-2006

GRB	T_0	RA	Dec	T_1	T_2	Notes
GRB050319	09:31:18	154.2	43.5	-133.1	19.4	
GRB050401	14:20:15	247.9	2.2	-5.6	27.0	
GRB050408	16:22:51	180.6	10.9	0.0	14.5	T_{90} from lightcurve
GRB050410	12:14:25	89.7	79.6	-27.0	37.0	
GRB050416A	11:04:45	188.5	21.1	0.1	2.5	
GRB050416B	22:35:54	133.9	11.2	0.2	3.6	
GRB050421	04:11:52	307.3	73.7	0.2	8.6	
GRB050422	07:52:40	324.5	55.8	-11.3	68.7	
GRB050502A	02:13:57	202.4	42.7	0.0	20.0	T_{90} from lightcurve
GRB050502B	09:25:40	142.5	17.0	-15.9	1.3	
GRB050504	08:00:52	201.0	40.7	0.0	80.0	T_{90} from lightcurve
GRB050505	23:22:21	141.8	30.2	-8.6	50.2	
GRB050509A	01:46:28	310.6	54.1	-5.6	5.8	
GRB050509B	04:00:19	189.1	29.0	-0.01	0.04	
GRB050520	00:05:53	192.5	30.5	0.0	80.0	T_{90} from lightcurve
GRB050522	06:00:21	200.1	24.8	0.0	20.0	T_{90} from lightcurve
GRB050525A	00:02:53	278.1	26.3	0.3	9.2	
GRB050528	04:06:45	353.5	45.9	-5.5	4.0	
GRB050607	09:11:23	300.2	9.1	-11.4	36.6	

Continued on next page...

Table 5.4: (continued)

GRB	T_0	RA	Dec	T_1	T_2	Notes
GRB050712	14:00:27	77.7	64.9	-13.3	38.4	
GRB050713B	12:07:17	307.8	60.9	-0.0	56.9	
GRB050714A	00:05:56	43.6	69.1	0.0	40.0	T_{90} from lightcurve
GRB050802	10:08:02	219.3	27.8	-1.9	28.1	
GRB050803	19:14:00	350.7	5.8	63.7	150.1	
GRB050813	06:45:09	242.0	11.2	0.02	0.46	
GRB050814	11:38:57	264.2	46.4	-10.1	143.9	
GRB050815	17:25:19	293.6	9.1	-0.4	7.6	
GRB050819	16:23:55	358.8	24.9	-11.8	36.2	
GRB050820A	06:34:53	337.4	19.6	0.0	750.0	
GRB050827	18:57:15	64.3	18.2	-22.8	25.3	
GRB050904	01:51:44	13.7	14.1	24.4	198.6	
GRB050925	09:04:33	303.5	34.3	0.1	0.2	
GRB051006	20:30:33	110.8	9.5	-116.0	24.0	
GRB051008	16:33:21	202.9	42.1	-1.6	10.8	
GRB051016B	18:28:09	132.1	13.6	0.2	4.2	
GRB051021A	13:21:57	29.1	9.1	-10.0	28.0	T_{90} from lightcurve
GRB051022	13:07:58	359.0	19.6	50.0	250.0	T_{90} from lightcurve
GRB051105A	06:26:41	265.3	34.9	0.0	0.06	
GRB051109A	01:12:20	330.3	40.8	-2.5	34.7	
GRB051109B	08:39:39	345.5	38.7	-6.8	7.4	
GRB051111	05:59:41	348.1	18.4	-3.8	56.0	
GRB051114	04:11:30	226.3	60.2	0.0	2.2	
GRB051117A	10:51:20	228.4	30.9	-10.6	125.8	
GRB060105	06:49:28	297.5	46.4	-17.8	36.6	
GRB060108	14:39:11	147.0	31.9	-2.6	11.7	
GRB060109	16:54:41	282.7	32.0	1.4	116.9	
GRB060110	08:01:17	72.7	28.4	0.3	25.3	
GRB060204B	14:34:24	211.8	27.7	-19.5	119.9	
GRB060211A	09:39:11	58.4	21.5	54.0	180.4	
GRB060211B	15:55:15	75.1	15.0	-9.9	18.9	
GRB060219	22:48:05	241.8	32.3	-55.1	7.0	
GRB060312	01:36:12	45.8	12.8	-25.7	19.6	
GRB060319	00:55:42	176.4	60.0	2.5	13.1	
GRB060323	14:32:36	174.4	50.0	-3.7	21.7	
GRB060421	00:39:23	343.6	62.7	-1.0	11.2	
GRB060424	04:16:19	7.4	36.8	-17.6	19.9	
GRB060427	11:43:10	124.2	62.7	-8.0	54.0	
GRB060428B	08:54:38	235.4	62.0	-15.0	81.0	
GRB060501	08:14:58	328.4	44.0	-0.7	21.2	
GRB060502A	03:03:32	240.9	66.6	-3.7	24.7	
GRB060502B	17:24:41	278.9	52.6	0.0	0.2	

Continued on next page...

Table 5.4: (continued)

GRB	T_0	RA	Dec	T_1	T_2	Notes
GRB060507	01:53:12	89.9	75.2	-3.5	179.7	
GRB060510B	08:22:14	239.2	78.6	31.0	301.7	
GRB060512	23:13:20	195.7	41.2	-3.6	4.8	
GRB060515	02:27:52	127.3	73.6	2.1	54.4	
GRB060522	02:11:18	323.0	2.9	5.3	69.3	
GRB060526	16:28:30	232.8	0.3	0.3	298.5	
GRB060602A	21:32:12	149.6	0.3	4.5	66.6	
GRB060607B	23:32:44	42.0	14.7	0.6	28.2	
GRB060717	09:07:38	170.9	29.0	-0.2	2.8	
GRB060801	12:16:15	213.0	17.0	0.1	0.6	
GRB060805	04:47:49	220.9	12.6	-1.2	4.3	
GRB060807	14:41:35	252.5	31.6	-22.3	21.0	
GRB060814	23:02:19	221.3	20.6	1.0	146.3	
GRB060825	02:59:57	18.1	55.8	-2.0	6.0	
GRB060904A	01:03:21	237.7	45.0	-1.0	79.1	
GRB060906	08:32:46	40.7	30.4	-39.9	3.6	
GRB060912A	13:55:54	5.3	21.0	-0.1	4.9	
GRB060923A	05:12:15	254.6	12.3	-40.8	10.8	
GRB060923C	13:33:02	346.1	3.9	8.9	77.3	
GRB060926	16:48:41	263.9	13.0	0.2	8.2	
GRB061002	01:03:29	220.4	48.7	-1.6	16.0	
GRB061019	04:19:06	91.6	29.5	-167.8	12.5	
GRB061028	01:26:22	97.2	46.3	56.4	162.6	
GRB061110B	21:58:45	323.9	6.9	-13.7	120.3	

Columns: T_0 – time of satellite trigger (UTC), RA – right ascension of GRB [°], Dec – declination of GRB [°], T_1 – window start relative to trigger [s], T_2 – window end relative to trigger [s]

5.4 IceCube

During the IceCube 22-string running period, 48 GRBs were observed by satellites in the northern hemisphere. We perform stability studies similar to those used in the AMANDA analysis to determine the suitability of individual bursts for analysis. A somewhat more conservative and robust method is chosen to determine burst durations. In addition, in order to model the neutrino flux from each burst, we must record the parameters of the photon emission. We extract these data from *GCN circulars*, *GCN reports*, and the online databases for the satellites [78, 25, 84, 79, 80].

5.4.1 Detector Stability Criteria

During the 22-string IceCube data taking period, a special GRB filter ran online at the pole. GCN notices were sent via satellite, triggering data extraction when bursts occurred. The filter extracted raw data in a two hour window surrounding the trigger time of each burst for which an alert was issued. The original purpose of this filter was to allow for the selection of specialized event selection for GRB analyses starting at a very low level as well as providing an estimate of the off-time background rate. However, studies showed that the standard upgoing muon filtering provided an excellent starting point for northern hemisphere GRB searches, and experience with the 2005-2006 AMANDA analysis proved that in order to have sufficient statistics for accurate background rejection, the entire year's off-time data was needed [3]. The data from the GRB filter is thus used to measure the stability of the detector in the time surrounding each burst.

We perform the same stability checks as in the AMANDA analysis, looking at the event times, rate distribution, and times between events in the two hour stability region. A sample of these tests is shown in Fig. 5.4. Of the 48 bursts originally in the northern sky sample, 7 are removed due to various problems with the detector (see Table 5.5). One of these bursts, GRB080319B, was the subject of a dedicated analysis [13] which served as a proof of concept for the application of an unbinned likelihood method to GRB searches. This leaves a final sample of **41** gamma-ray bursts for the 2007-2008 IceCube analysis.

5.4.2 Burst Duration Determination

A major goal in the IceCube analysis was to avoid the uncertainty and decision making that was inherent in the determination of burst durations in the 2005-2006 analysis. In light of this, an approach was adopted that gave consistent and conservative values for the duration of each burst. In the *GCN Report* issued for each GRB, a quantity known as the T_{100} of the burst is given. This

---

[3] The filtered data is still very valuable for GRB searches focusing on the southern hemisphere [93] or searches for GRB neutrino-induced cascades which are sensitive over the full sky [94].

[4] This exceptionally bright burst occurred during a detector maintenance period, when only 9 strings were operating. Due to its high interest to the astrophysical community, an individual analysis of this burst was conducted. For details, see [13].

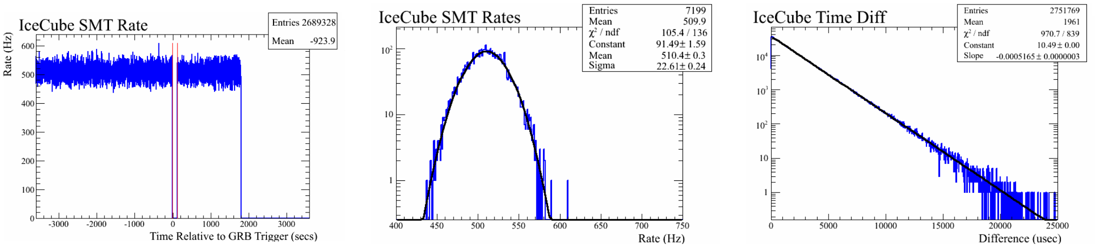

(a) event times (b) rate distribution (c) time between events

Figure 5.4: Sample detector stability plots for GRB070724. Panel (a) shows the event times in a 2 hour window surrounding the trigger time. Note the loss of data at the end of the window. Panel (b) shows the distribution in the event rate per 10 s, fitted with a Gaussian. Panel (c) shows time difference between subsequent events in the detector, fitted with an exponential.

Burst	Problem
GRB070610	missing strings 29,38
GRB070714A	no data
GRB070810A	no data
GRB080122A	no data
GRB080207A	occurred during flasher run
GRB080210	high rates, probable flasher run
GRB080319A	no data
GRB080319B	no IC22 data [4]

Table 5.5: GRBs with problems in the data in 2007-2008. It was decided to include GRB070610 in the analysis and produce a special simulation for this burst that took into account the reduced number of strings.

is defined as the full time window used to integrate the burst fluence. Inspection of the associated light curves reveals that T_{100} is a conservative determination of the burst duration that includes all relevant prompt emission. Furthermore, T_{100} is well-defined for all bursts and start (T_1) and end (T_2) times with respect to each trigger are given. We therefore opt to use this parameter as the burst duration for all 41 GRBs in our final sample. The total prompt emission of the 41 GRBs in our sample is 4960.6 s. Table 5.6 shows the spatial and temporal information for these bursts. For a full listing of photon and neutrino spectral information refer to Section 8.2.

Table 5.6: Spatial and Temporal Information for 41 GRBs Observed in 2007-2008

GRB	T_0	RA	Dec	T_1	T_2	GRB	T_0	RA	Dec	T_1	T_2
GRB070610	08:52:26	298.8	26.2	-0.8	4.4	GRB071101	05:53:46	48.2	62.5	-1.9	10.0
GRB070612A	02:38:45	121.4	37.3	-4.7	418.0	GRB071104	11:41:23	295.6	14.6	-5.0	17.0
GRB070616	04:29:33	32.2	56.9	-2.6	602.2	GRB071109	08:36:05	289.9	2.0	-5.0	35.0
GRB070704	08:05:57	354.7	66.3	-57.3	400.8	GRB071112C	06:32:57	39.2	28.4	-5.0	30.0
GRB070714B	04:59:29	57.8	28.3	-0.8	65.6	GRB071118	08:57:17	299.7	70.1	-25.0	110.0
GRB070724B	11:25:09	17.6	57.7	-2.0	120.0	GRB071122	01:23:25	276.6	47.1	-29.4	47.3
GRB070808	06:28:00	6.8	1.2	-0.7	41.4	GRB071125	01:56:42	251.2	4.5	-0.5	8.5
GRB070810B	03:19:17	9.0	8.8	0.0	0.1	GRB080121	09:29:55	137.2	41.8	-0.4	0.4
GRB070917	07:33:57	293.9	2.4	-0.1	11.4	GRB080205	07:55:51	98.3	62.8	-10.1	105.3
GRB070920A	04:00:13	101.0	72.3	15.1	75.0	GRB080211	07:23:39	44.0	60.0	-10.0	50.0
GRB071003	07:40:55	301.9	10.9	-7.6	167.4	GRB080218A	08:08:43	355.9	12.2	-12.8	18.6
GRB071008	09:55:56	151.6	44.3	-11.0	14.0	GRB080307	11:23:30	136.6	35.1	1.7	146.1
GRB071010B	08:45:47	150.5	45.7	-35.7	24.1	GRB080310	08:37:58	220.1	-0.2	-71.8	318.7
GRB071010C	10:20:22	338.1	66.2	-2.0	20.0	GRB080315	02:25:01	155.1	41.7	-5.0	65.0
GRB071011	12:40:13	8.4	61.1	-9.5	63.8	GRB080319C	12:25:56	259.0	55.4	-0.3	51.2
GRB071013	12:09:19	279.5	33.9	-5.9	23.4	GRB080319D	05:05:09	99.5	23.9	0.0	50.0
GRB071018	08:37:41	164.7	53.8	-50	417.7	GRB080320	04:37:38	177.7	57.2	-60.0	40.0
GRB071020	07:02:27	119.7	32.9	-3.0	7.4	GRB080325	04:09:17	277.9	36.5	-29.3	170.5
GRB071021	09:41:33	340.6	23.7	-31.4	252.2	GRB080328	08:03:04	80.5	47.5	-2.2	117.5
GRB071025	04:08:54	355.1	31.8	38.5	193.8	GRB080330	03:41:16	169.3	30.6	-0.5	71.9
GRB071028A	05:41:01	119.8	21.5	0.0	48.9						

Columns: T_0 – time of satellite trigger (UTC), RA – right ascension of GRB [°], Dec – declination of GRB [°], T_1 – window start relative to trigger [s], T_2 – window end relative to trigger [s]

Chapter 6

Simulation

We use off-time data to determine background rates and therefore simulation of these backgrounds is not strictly necessary in the final analyses. However, it is useful as a check of general agreement between the expectation and the measurement, as well as to give an idea of what the contamination of various backgrounds in the final data set is. Of course, we must also perform a simulation of the signal neutrinos in order to determine the sensitivity of the analyses.

Simulation proceeds in several stages. In the first, *generators* create primary particles from input flux models, assigning relevant information such as energy, direction, type, and so on. *Propagators* then transport these primaries through various media (atmosphere, rock, ice) taking into account energy losses and the production of numerous secondaries. Propagators also track the photons created via the Čerenkov mechanism. Finally, a *detector simulation* models the response of the detector. We discuss each in the following sections.

6.1 Generators

We simulate extensive air showers and propagate the resulting muons through the atmosphere with Corsika [95]. We combine single downgoing muons to create coincident muon events at the proper rate. For the AMANDA simulation, neutrinos are generated with nusim [96]. Cross sections are calculated from the MRS parton distribution functions [97]. For IceCube, a re-implementation of the neutrino generation package anis [98] is used, applying the CTEQ-5 [99] cross sections. These packages are in general quite similar. Neutrinos are generated randomly on the Earth's surface and then propagated through it, taking into account absorption by charged current interactions and energy losses due to neutral current interactions (and subsequent regeneration). The structure of the Earth is given by the Preliminary Reference Earth Model (PREM) [100]. In order to reduce computation times, it is assumed that all generated neutrinos that reach the detector interact with the nearby rock or ice to produce secondary particles (we are interested only in the muons for the analyses presented here). Each event is then assigned a weight representing the probability that the interaction occurred. It is possible to select the neutrino generation spectrum as well and the spectral slope is typically chosen to maximize statistics in the energy regime of interest. For GRB neutrinos we use signal generated with an E^{-1} spectrum, while for simulating the atmospheric neutrino background we choose E^{-2}. These choices increase event rates at high or low energies, respectively. Each event is then re-weighted to match the actual spectra of interest. For signal, the models are described in section 2.3. Atmospheric neutrinos are assumed to follow the flux given by Barr et al. [101].

6.2 Propagators

Once the neutrino interaction occurs or a muon passes through the atmosphere and penetrates the Earth, we use Muon Monte Carlo (mmc) [67] to propagate the secondaries through rock and ice and track the resulting energy losses. mmc takes both continuous and stochastic losses into account and this information is passed to the photon transport simulation.

The Čerenkov light generated by passing muons is propagated from the track through the detector volume with the software package Photonics [76]. The full structure of the ice detailed in section 3.5 is considered, varying scattering and absorption as a function of both wavelength and depth. At each point in space the photon intensity and time residual information is stored in look-up tables corresponding to different source orientations. When called, the probability distribution functions for the simulated light pattern can then be quickly given.

6.3 Detector Simulation

The detector response to simulated photons is modeled by a group of software programs operating in concert. Since AMANDA and IceCube operate on somewhat different principles, we consider each individually.

6.3.1 AMANDA

The AMANDA response to Čerenkov photons is simulated by AMASIM [102]. The detector layout is described by a geometry file. This file also includes important information for each optical module in the array, including discriminator threshold, noise rate, relative sensitivity, cable travel times, and pulse shape definitions. Most of these parameters are measured on a per OM basis during calibration tests. For example, since AMANDA uses a variety of cabling technologies (twisted wire pair, coax, optical), the pulse shapes of the PMT response can vary substantially when read at the surface. Thus, the shape for each OM can be set to most accurately reproduce measured data. The behavior of the surface amplifiers is simulated, taking into account saturation effects. In the trigger simulation, the number of overlapping pulses from hits is counted. If it exceeds the trigger condition, the event is recorded.

6.3.2 IceCube

In the IceCube detector, all event information is digitized *in situ*. Therefore, the detector response simulation starts and ends in the DOMs. The package ICESIM collects various subroutines that model each aspect of the DOM response. Geometry and calibration files are used to determine the physical locations and operating status of each DOM in the detector. As described above, each DOM queries the PHOTONICS tables to determine the photon distribution at that point in space. A simple PMT simulator then takes this light and produces an electrical waveform, assigning each photon a charge sampled from a distribution that agrees with measurements [1]. A simulation of the DOM is then performed. The discriminator threshold and ATWD launch are modeled and ATWD and fADC waveforms are filled from the PMT simulation output. Local Coincidence conditions are also checked. A simple module adds random noise hits throughout the array and a simulation then checks whether the conditions are satisfied for different physics triggers. In the case an event is triggered in simulation, the information is read out and processed identically to data.

---

[1] Angle of incidence on the PMT and wavelength dependence are folded into PHOTONICS.

Chapter 7

AMANDA-II Analysis

The AMANDA-II analysis consists of a search for high-energy muon neutrinos from 85 northern hemisphere GRBs observed during 2005-2006 by the Swift, Integral, and HETE-II satellites. The procedure by which these bursts were selected is outlined in Chapter 5. One can choose to optimize a search for contribution from individual bursts, or for the integrated signal from a *stacked* collection of bursts. In this analysis we use the latter approach and utilize a binned search method. We present the full analysis chain, beginning with data filtering. We describe the way in which we optimize the event selection and present the sensitivity and discovery potential of the analysis. Finally we discuss the results of the search. For the reader primarily interested in final event samples and results, we recommend beginning reading from section 7.5.

7.1 Filtering

We begin our analysis of this dataset with a sample of upgoing events, selected by a series of quality filters common to many analyses. Simple and fast reconstructions are applied at low filter levels, while more CPU-intensive reconstructions are applied after the dataset has been substantially reduced. Table 7.1 summarizes these filters. They are described in detail in the following sections.

7.1.1 Level 1 Filter

We first performed a selection to remove bad files from the analysis and bad OMs from events. A procedure was followed to remove those files or OMs with noise rates that deviated from the mean by more than a certain amount. Studies showed that this cleaning had similar results to those that

Filter Level	Processing / Selection
Level 1	Hit Calibration Modified Crosstalk Cleaning Bad OM cleaning Good Amplitude, TOT, LE Time selection $\theta_{\mathrm{JAMS}} > 70°$
Level 2	Multiplicity Trigger Fired ($N_{ch} > 24$) $\theta_{\mathrm{DW}} > 80°$
Level 3	Add string-triggered Level 2 events $\theta_{\mathrm{P}} > 80°$

Table 7.1: Summary of 2005-2006 AMANDA-II upgoing muon filters.

had been conducted for previous analyses. In addition, some OMs were removed completely from the analysis based on known long term problems or geometrical reasons.

We also wished to remove unstable running periods from the analysis. The bad file selection above showed that in general, the periods before February 16th and after October 31st were unstable, due to increased activity during the austral summer construction seasons. However, for GRB analyses, unlike time integrated searches, we are only concerned with the period immediately surrounding each burst. Therefore, we do not exclude these unstable periods as such, but rather apply the detector stability criteria as outlined in Chapter 5.

After the removal of unstable OMs from each remaining event, we calibrate the hits. We then perform a cleaning to remove crosstalk induced hits between electrically coupled OMs. For this analysis we made a study to improve the cleaning algorithm and minimize the remove of signal-like events. A method combining maps of electrical talkers and receivers, relations between measured charge and time over threshold, and exceptions to retain particularly energetic events was implemented. We also remove hits that are isolated in space or time, as these are likely to be due to random noise.

We reconstruct the direction of each event using the JAMS and Direct Walk algorithms described in Chapter 3. Studies comparing the reconstructed track directions with true directions of the injected neutrinos showed that JAMS had a lower fake rate for the same signal efficiency at low filter level. We therefore use JAMS as our first, loose selection of upgoing muons and require $\theta_{\mathrm{JAMS}} > 70°$.

7.1.2 Level 2 Filter

After making a loose cut on the JAMS zenith angle, the data set is reduced enough to perform more computationally intensive reconstructions. Single iteration likelihood fits are performed and the results stored. The upgoing sample is further defined by selecting only those events with a Direct Walk zenith angle above 80 degrees ($\theta_{\mathrm{DW}} > 80^\circ$). Finally, a software re-triggering is performed, checking that the 24 channel multiplicity condition is still satisfied after OM and hit cleaning.

7.1.3 Level 3 Filter

In the final level of upgoing muon filtering, we perform the most complicated reconstructions. A 16-iteration fit is conducted using the single photo-electron Pandel function described in section 3.6.4. This constitutes our most accurate unbiased reconstruction for the analysis. We also perform a 32-iteration fit with a Bayesian weighted likelihood function [1]. To increase our sensitivity to high quality events that may not have high multiplicity, we also include at this time a large sample of *string-triggered* events. These are events that may have a lower total number of hit channels, but have a number of hits per string that indicates a possible physics signature. For our full sample of events, we require that our best reconstruction indicate an upgoing (or shallow horizon) track; $\theta_{\mathrm{P}} > 80^\circ$.

7.1.4 Flare Checking

While the hit cleaning procedures we have outlined do an excellent job at removing random or cross-talk induced hits from events, they do not handle another problem prevalent in AMANDA data. Sometimes, due to surface winds, electromagnetic disturbances, and other factors, entire, completely unphysical events will coalesce in the detector. We refer to these as "flares". Flare checking procedures have been standardized to determine the likelihood that an event is unphysical in origin [103]. We removed events that appeared to be more flare-like based on these checks. Specifically, we correlated hits between strings with twisted pair cabling and coaxial cabling to check for inductance coupling as well as looking at the time-over-threshold of hits to determine if they seemed too short. Only a

---

[1] In a rare ($< 0.006\%$) subset of events, the zenith weighted reconstruction returns a track above the horizon. This should not be possible, as the distribution function for downgoing muons goes to zero in this region. This is due to a bug in the reconstruction code and these events are removed from the analysis.

very small number of events (0.02%) are classified as flary and removed from the analysis.

7.1.5 Starting Dataset

After applying the filters described above and summarized in Table 7.1, we have a sample of 5.21 million events from 2005 and 4.89 million events from 2006. The total livetimes are 199.29 days and 186.95 days, respectively. The distributions of event variables between the years at this level shows good agreement, as seen in Fig. 7.1.

	2005	2006
Livetime (days)	199.29	186.95
Raw events	2.06 B	2.00 B
L1	184 M	177 M
L2	–	–
L3	5.21 M	4.89 M
Scaled to GRB ontime (5343.8 s)	1703.9	

Table 7.2: AMANDA-II upgoing filter passing rates.

7.2 Signal Spectrum

For this analysis, we search for neutrino emission during only the prompt phase of the GRB. Using the diffuse all-sky flux calculated by Waxman and Bahcall [49, 104] (see section 2.3.1), we determine the signal contribution from each burst in our sample, assuming each GRB produces an equal number of neutrinos. We chose to use this approach rather than calculating a different neutrino fluence for each burst for several reasons. First, we are performing a stacked analysis, and so the individual contributions are not as important as the total signal expectation. Second, the optimization is only weakly dependent on the spectral distribution. Finally, it was deemed to be logistically impractical to collect the necessary burst data and perform the spectral calculations [2]. We show the response of AMANDA to the Waxman-Bahcall model after applying upgoing muon filters in Figure 7.2.

---

[2] An increase in manpower and better dissemination of observation data from satellites made per burst spectral calculation for large samples of GRBs a reality starting with the IceCube analysis presented later in this thesis.

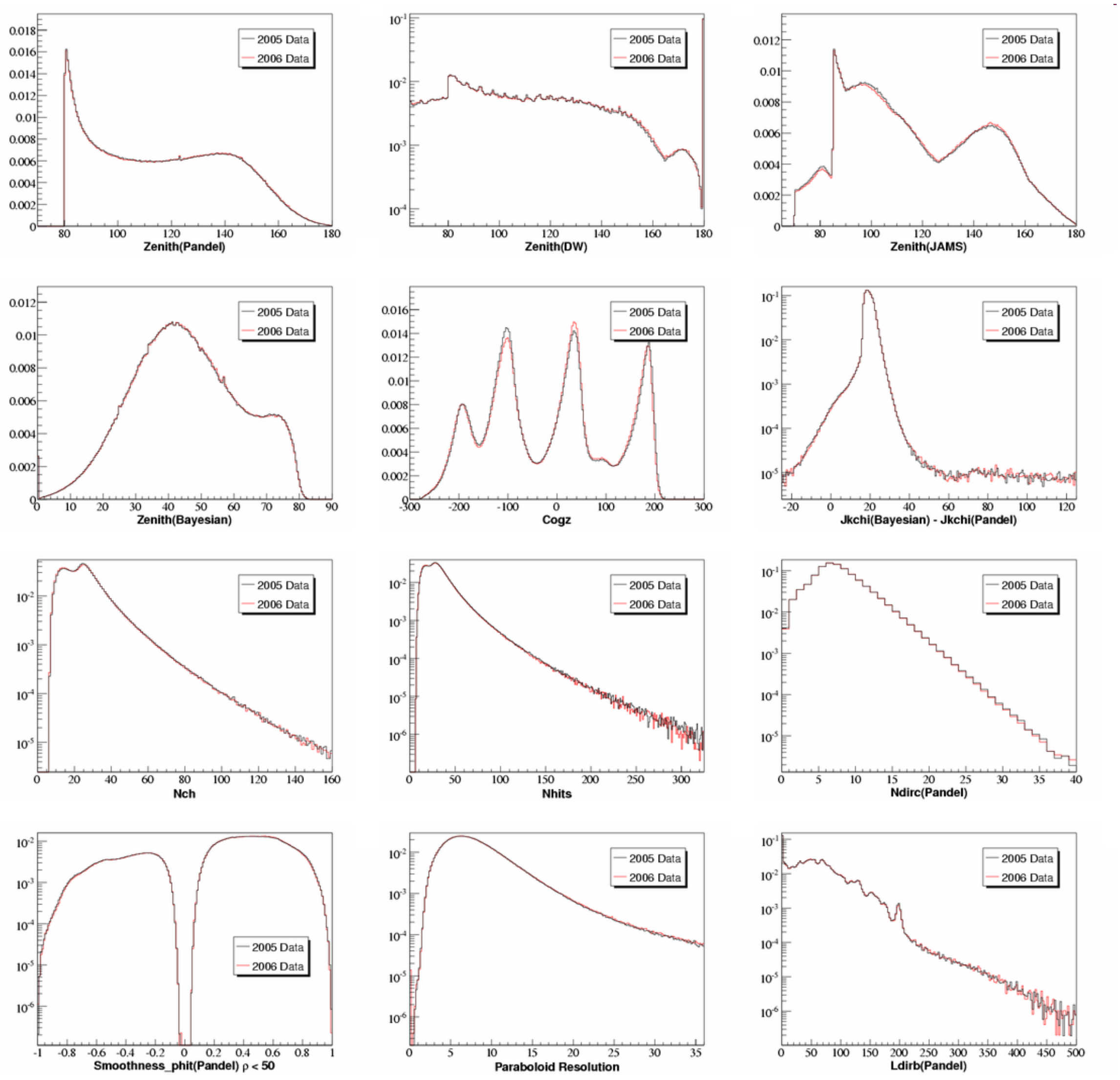

Figure 7.1: Comparison of 2005 and 2006 data after all upgoing muon filters have been applied as described in section 7.1. The difference in the center of gravity of hits between the samples is due to a different file and OM selection for each year.(Figure courtesy Jim Braun)

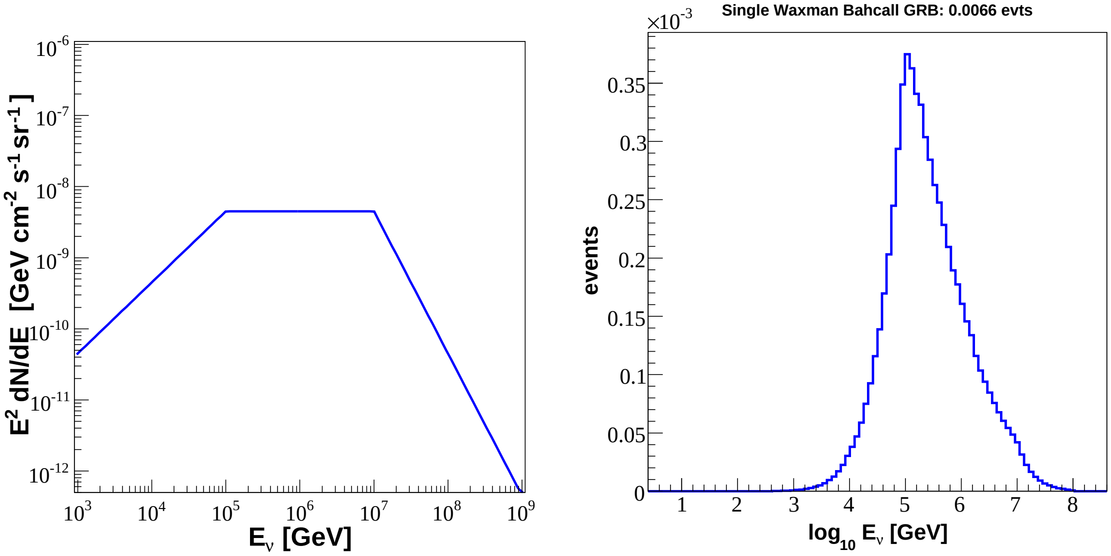

Figure 7.2: The response of AMANDA-II to the neutrino fluence predicted by the Waxman Bahcall model (shown at left) for a single average GRB. The simulation is averaged over the full sky and the result is shown at upgoing muon filter level. Convolution of the spectral shape and the detector effective area yields a strong peak in the event predication at 10^{14} eV.

7.3 Event Selection Variables

After filtering is complete, the data set is still background dominated. Mis-reconstructed cosmic-ray induced muons (downgoing but reconstructed as upgoing) dwarf the neutrino sample by a factor 10^3. Similarly, the atmospheric neutrinos are much more numerous than the predicted GRB neutrino fluence (see Fig. 7.3). The event selection thus consists of finding a set of variables that efficiently separate signal-like and background-like events and optimizing the cuts on these variables. We describe the parameters used below. We also briefly discuss several promising event variables that were investigated and the reason for their exclusion.

7.3.1 Paraboloid Sigma

We fit a parabola to the likelihood space of the iterative Pandel track reconstruction, centered at the best-fit minimum. The width of this parabola, σ, gives an estimate of the reconstruction error of the track. We perform this in 2 dimensions, obtaining σ_1 and σ_2, the error estimates along the 2

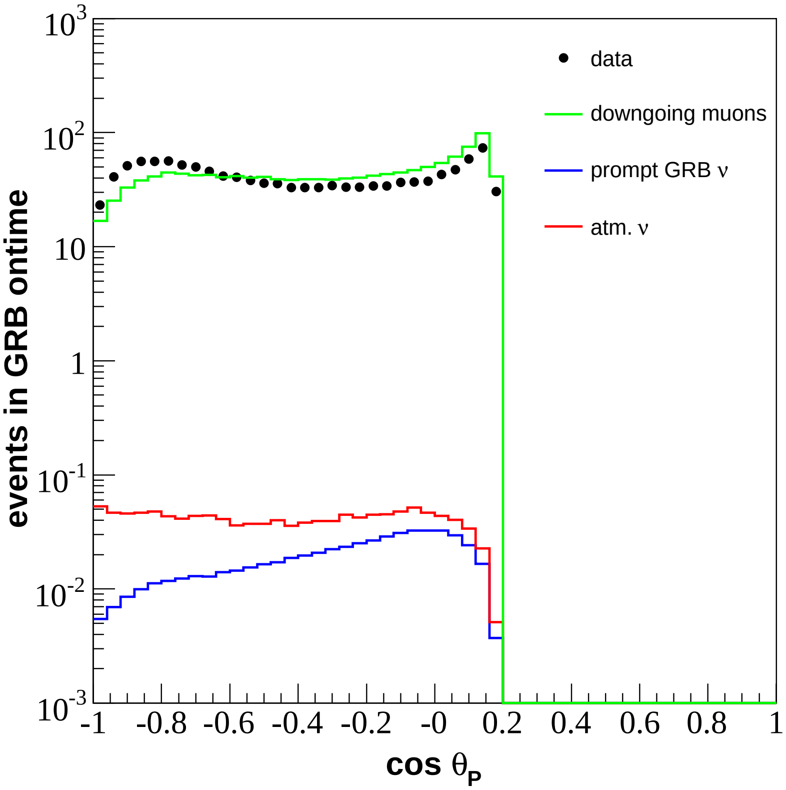

Figure 7.3: Background contamination in the 2005-2006 dataset after application of the upgoing muon filters. Data and background simulation have been rescaled to the total prompt phase GRB ontime of 5343.8 s.

axes of the error ellipse. We then combine these to a single parameter

$$\sigma = \sqrt[4]{\sigma_1^2 \sigma_2^2}. \tag{7.1}$$

Well reconstructed tracks (upgoing neutrinos) will have a small reconstruction error, while misreconstructed downgoing muons will tend to have a larger value of σ. Distributions at upgoing filter level are shown in Fig. 7.4.

7.3.2 Likelihood Ratio

Our muon reconstructions return the likelihood that the found track is correct. We can then compare the likelihood of two different reconstructions to make an estimate of which is more probable. We find that the likelihood ratio between the unbiased Pandel reconstruction and the zenith

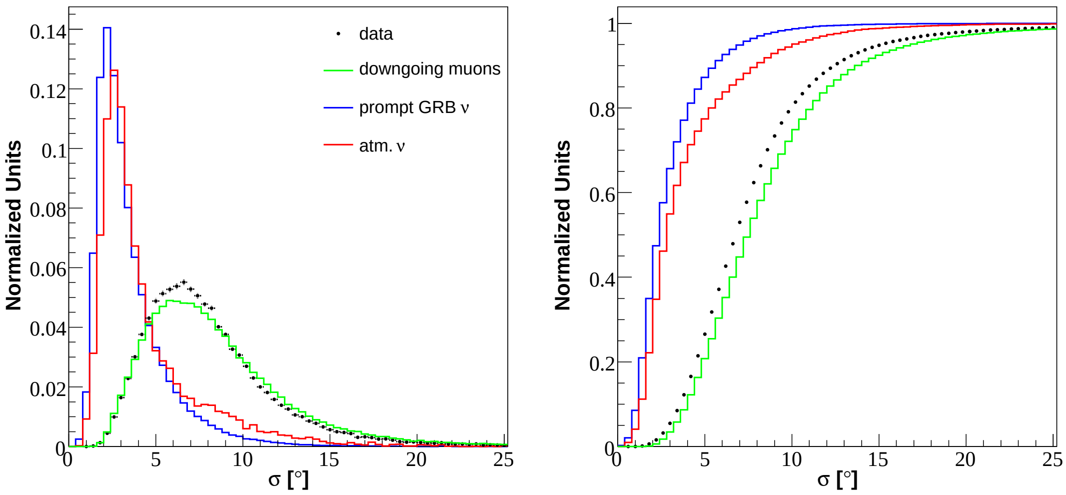

(a) differential

(b) integral

Figure 7.4: Differential and integral distributions of the track reconstruction error estimator σ at upgoing muon filter level. Vertical axes are normalized to highlight differences in shape. Note that truly upgoing events (neutrinos) have a better error estimate that mis-reconstructed muons.

weighted reconstruction $\mathcal{L}_P/\mathcal{L}_B$ forms an excellent quality parameter for rejecting mis-reconstructed downgoing muons. The strong separation power is shown in Fig. 7.5. It is important to note, however, that this parameter is strongly zenith dependent. Near the horizon, there is not much difference between an upgoing and downgoing reconstruction. Near the vertical, the separation power increases vastly.

7.3.3 Space Angle

Although mis-reconstructed downgoing events can be reduced by track quality selections as described above, there remains an irreducible background of upgoing atmospheric neutrinos. This remaining background is reduced by selecting only events that occur within an angular bin around the location of each GRB. We define this space angle ψ as the dot product between the direction of the burst and the direction of the best reconstructed track

$$\psi = \arccos\left(\sin\theta_{\mathrm{GRB}}\sin\theta_{\mathrm{P}}\cos(\phi_{\mathrm{GRB}}-\phi_{\mathrm{P}}) + \cos\theta_{\mathrm{GRB}}\cos\theta_{\mathrm{P}}\right). \tag{7.2}$$

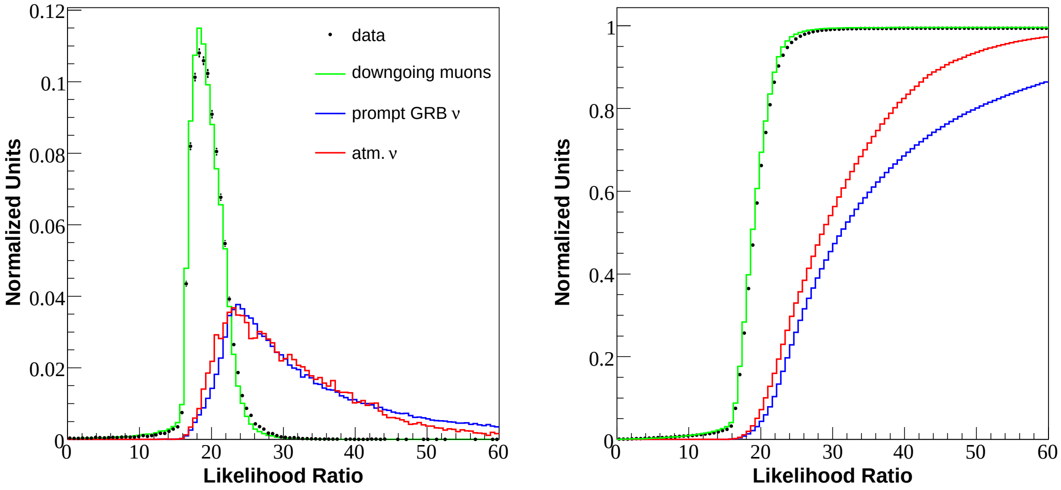

(a) differential

(b) integral

Figure 7.5: Ratio of reconstruction likelihood for unbiased vs. zenith weighted reconstructions at upgoing muon filter level. Vertical axes are normalized to highlight differences in shape. In this figure, distributions are averaged over the whole sky, projecting out the strong angular dependence.

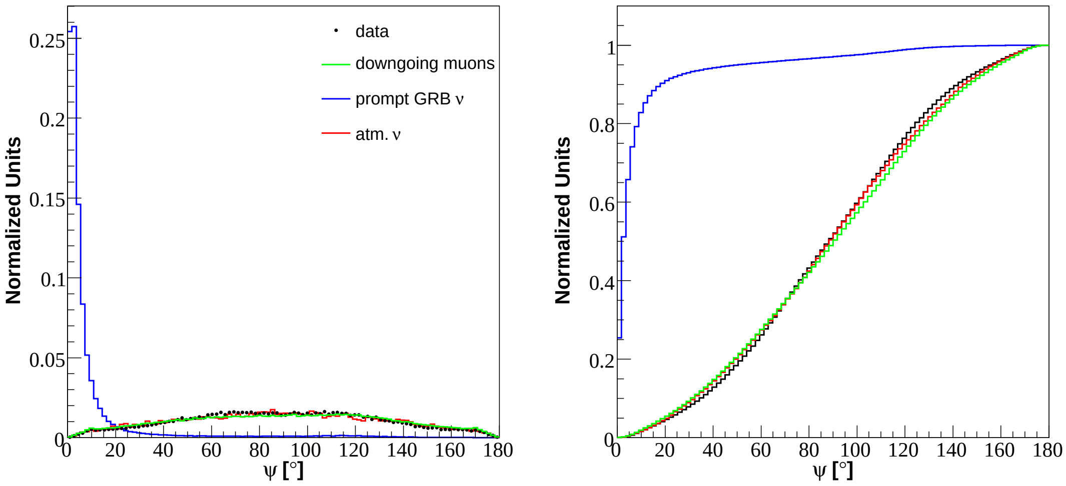

(a) differential

(b) integral

Figure 7.6: Space angle distribution at upgoing muon filter level for a sample GRB places at $\theta = 90°, \phi = 220°$. Backgrounds are isotropically distributed in relation to the burst direction, while the signal is strongly correlated.

7.3.4 Other Variables

Recall that we define direct hits as those which fall within a certain time window relative to the expectation from unscattered Čerenkov light. In principle direct hits should be an excellent event quality parameter. Many direct hits indicates a well-reconstructed track that agrees with the expected light distribution as well as indicating high energies (many hits in the detector). We therefore initially considered using direct hits in our event selection, as well as several other parameters based on direct hits such as track length and smoothness (a measure of the evenness of light deposition along the track). However, we found a peculiar feature whereby higher energy events oftentimes had a number of direct hits exactly equal to zero. In fact, the fraction of such events increases proportional to the energy (see Fig. 7.7).

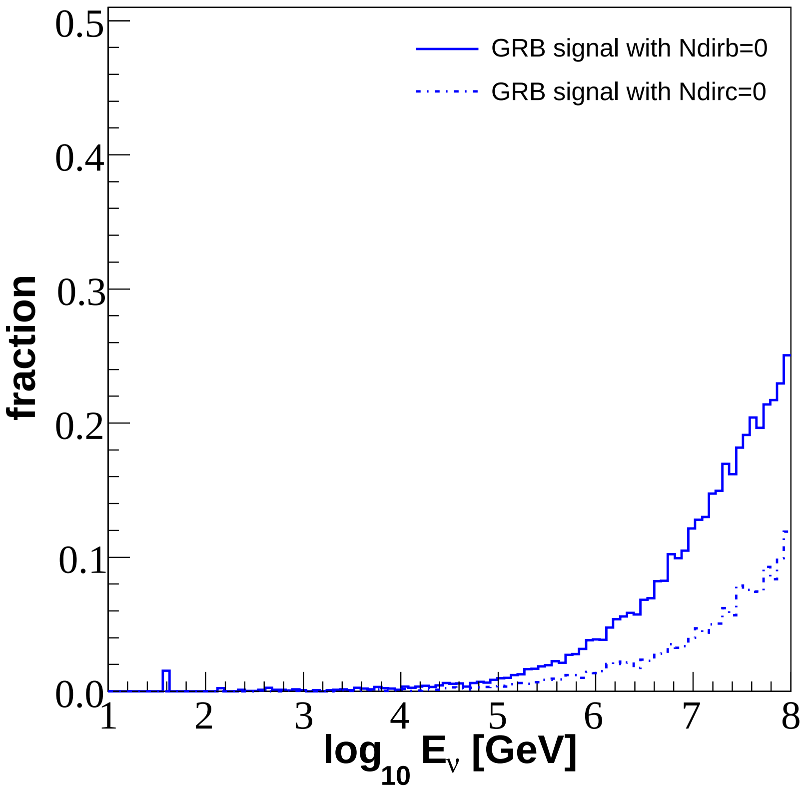

Figure 7.7: Fraction of GRB signal neutrinos with a number of direct hits exactly equal to zero. The increase proportional to energy indicates an unphysical situation. We show the distribution for two definitions of direct hits; b ($-15 < t_{res} < 25$) and c ($-15 < t_{res} < 75$), given in units of ns. Note that for a more relaxed time window, the problem is less severe, in agreement with the explanation given in the text.

It was also discovered that many of these events are extremely well-reconstructed, which does not seem to make sense. Studies of this phenomena showed that this effect was due to a feature of the reconstruction algorithm. We use the Pandel likelihood describing the probability distribution function for a *single photoelectron*. In reality, for high energy events, we have many photon hits in each optical modules. We therefore should be fitting the *first of many photoelectrons*. While the track direction itself is not affected, this causes a systematic shift to earlier vertex times [3]. Depending on the definition of the direct hit window, this causes a fraction of events with a large number of hits to register as having no direct hits. Once this problem was identified, we began to use a multi-photoelectron PDF that correctly describes the first photon of many. However, for this analysis (and the IceCube analysis we describe in Chapter 8) this MPE fit was not available and so we found alternate solutions. For the 2005-2006 analysis this consisted of removing from consideration variables based on direct hits. We found that the event variables described above were robust and sufficient to reduce the background to low levels.

7.3.5 Temporal Coincidence

The expected temporal coincidence of prompt GRB neutrinos with the observed photon emission allows for extremely powerful background suppression. Scaling the full background to the total prompt emission ontime for this analysis of 5343.8 s, we achieve a 99.98% rejection of backgrounds. By leveraging this temporal coincidence we will be able to make statistically significant discoveries with only a very few events, as we will discuss further later.

7.4 Optimization

We now address the question of how best to reject the overwhelming backgrounds while leaving ourselves able to detect the predicted signal. We must first decide what we will optimize and then how we will go about doing it. In many experiments, one uses signal over square root background as the figure of merit. However, this breaks down in the very low statistics regime in which we find ourselves. Another possibility is to choose cuts to maximize the limit setting potential in the event of a non-observation [105]. In principle this would be a sound choice. However, the ability of a stacked

---

[3] This is due to the formulation of the single photon PDF. The peak expected time is systematically later than the first of many photons, and the reconstruction tries to match each first photon to the later peak.

GRB analysis to set limits scales with the number of bursts in the sample. A previous search with AMANDA data for coincidences with a sample of over 400 bursts has been performed and an upper limit set [8]. Due to the large size differences between the data samples, we do not expect to be able to challenge this limit. Rather, our sole aim is to make a discovery. To this end, we choose to optimize our event selection to maximize such a discovery potential using the method of Hill et al. [106].

In the Model Discovery Potential (MDP) method, we determine what factor of a predicted flux is necessary in order to make an observation (discovery) at a stated significance level, and seek to minimize that factor. The concept is best illustrated by example. Let us assume we have a predicted neutrino flux $\Phi(E)$. After convolution with the detector response and application of background rejecting cuts, this flux produces a number of events in the detector n_s. With the same cuts, we have a background prediction n_b. We unblind our data and make an observation n_{obs}. In order to determine whether n_{obs} is consistent with the background only hypothesis, we must determine what the probability is of observing the same or greater number of events $P(\geq n_{obs}|n_b)$. Conversely, we can define some small probability α *a priori*, and ask what is the necessary n_{obs} to reject the background only hypothesis at that confidence level. We define the critical number of events as

$$\alpha > P(\geq n_{crit}|n_b) \tag{7.3}$$

where in our case, P is given by the Poisson distribution. Presumably an observation of n_{crit} would indicate the presence of a signal [4]. In this case, the probability (or statistical power) of observing n_{crit} is given by

$$1 - \beta = P(\geq n_{crit}|n_b + n_{lds}). \tag{7.4}$$

$1 - \beta$ tells us the percentage of hypothetical experiments that would make a discovery at the α significance level given a least detectable signal n_{lds}. The ratio of n_{lds} to the signal prediction n_s then gives the flux factor necessary for a discovery. We term this the Model Discovery Factor (MDF).

---

[4] Note that an observation inconsistent with the background only hypothesis says nothing whatsoever about the origins of the signal that is seen. It merely rejects the lack of something.

By varying the cut selection and repeating this calculation, we can minimize the MDF necessary. For the 2005-2006 AMANDA analysis, we choose to let $\alpha = 5.73 \times 10^{-7}$ and $1 - \beta = 0.9$. That is, we seek to minimize the flux needed to make a 5σ discovery in 90% of experiments.

One possible method to implement the event selection is to feed all chosen variables into a machine-learning algorithm and then optimize the discovery potential on the single output parameter. We conducted studies using a Support Vector Machine (SVM) with encouraging results. However, the gains over traditional methods were modest and the accompanying reduction in transparency was deemed too large. This method was therefore not used for this analysis. However, the technique was later adopted by collaborators in a search for GRB neutrinos in the 22-string IceCube dataset complementary to that presented in this thesis [93, 107]. The effort expended in understanding and implementing an SVM for GRB searches was thus well founded. Details of this optimization strategy may be found in Appendix C.

We choose instead to perform an iterative optimization, scanning the multidimensional parameter space of our selected event variables to find the set that globally maximizes the discovery potential of the analysis. Furthermore, even a casual inspection of Fig. 7.3 reveals a strong zenith dependence in the signal and background rates. Near the horizon, both background and signal rates are much larger than near the vertical. The reasons for this are several. In the background case, contamination from downgoing muons is greater near the horizon, where the difference in track reconstructions is not as great. For GRB neutrinos, the reason is somewhat different. At very high energies, neutrinos begin to be absorbed by the Earth (see Fig. 3.1). As more Earth is traversed the absorption increases, and thus for a hard energy spectrum like that of GRBs, we expect a peak in signal rates near the horizon. In addition to differences in rates, the distributions of our event variables have an angular dependence. Track reconstructions are generally better for more vertical events, giving a zenith dependent resolution. The likelihood ratio between the unbiased and zenith weighted reconstructions is similarly zenith dependent. Even for excellent neutrino tracks reconstructed near the horizon, the ratio is low because there is not much difference between the upgoing and downgoing track hypotheses. For all these reasons, we choose to perform a zenith dependent event selection optimization.

We therefore place fake sources at intervals of 10 degrees in zenith. Because our simulation is generated isotropically over the sky, this involves re-weighting of the Monte Carlo. In order to preserve the event distributions of the zenith angle under consideration, we choose only events that fall within a $\pm 1^\circ$ band around the chosen source location. The simulation is then scaled by the ratio of the solid angle within that zenith band to the total simulated solid angle. This procedure does a good approximation of point sources located at the positions specified without necessitating a dedicated simulation production.

We simultaneously optimize the cuts on our event variables in each zenith band, weighting the signal contribution to the full expectation from our 85 GRB sample. In each bin, a minimum MDF is found. We plot the set of optimal cuts and determine a parameterization that spans the entire zenith range based on these values. We strive to remain as close to the optimal cuts as possible, while still respecting the parameter distributions. The final cut parameterizations are depicted in Fig. 7.8 and summarized in Table 7.3. The cut on space angle is slightly tighter at higher zenith angles, reflecting the improved angular resolution away from the horizon. For the likelihood ratio, the cut must decrease near the horizon to allow for the weakening of the distinction between upgoing and downgoing reconstructions here. Away from the horizon, a strong cut is used to ensure background rejection. The Model Discovery Potential space is rather flat, so fixing the cut at high zenith values does not cause a large change in MDF. The paraboloid sigma cut decreases towards the vertical as well, once again reflecting the improved angular resolution. We choose to keep the cut tight near the horizon to help remove the relatively larger amounts of background.

Variable	Parameterized Cut
σ	$< 3.2 - 0.02 \cdot \Theta(\theta_\mathrm{P} - 105) \cdot (\theta_\mathrm{P} - 105)$
$\mathcal{L}_P/\mathcal{L}_B$	$> 36 - 0.18 \cdot \Theta(115 - \theta_\mathrm{P}) \cdot (115 - \theta_\mathrm{P})$
ψ	$< 4.6 \cdot \Theta(120 - \theta_\mathrm{P}) + 3.7 \cdot \Theta(\theta_\mathrm{P} - 120)$

Table 7.3: Parameterized event selection for the 2005-2006 AMANDA analysis. Θ is the Heaviside unit step function.

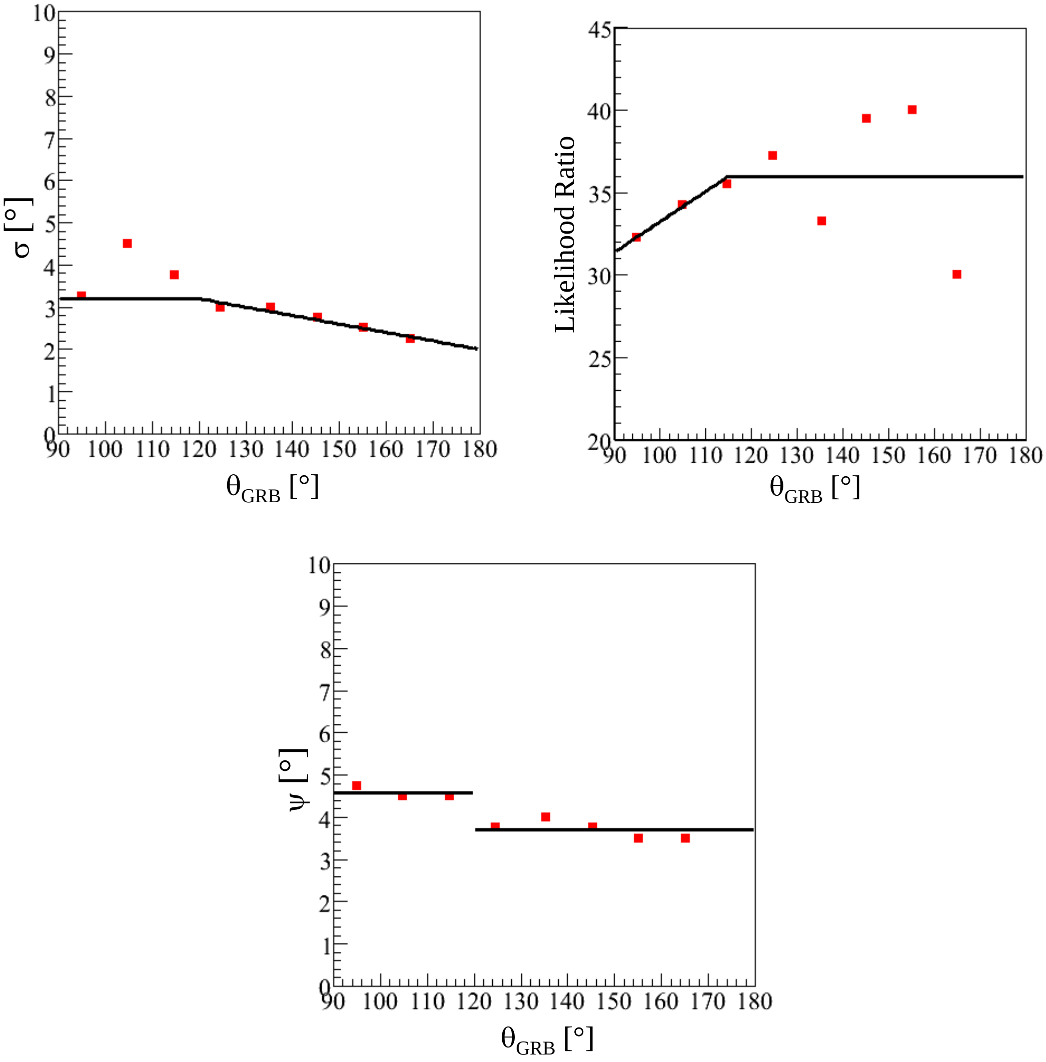

Figure 7.8: Optimized cuts and parameterization for the 2005-2006 AMANDA analysis. Red squares indicate the optimal cut in each zenith band. Solid black line shows the parameterized cuts for the full zenith range. Efforts were made to choose cuts that followed the zenith dependence of the variables while still retaining sufficient background rejection. For this reason, we tended on the side of a stricter event selection.

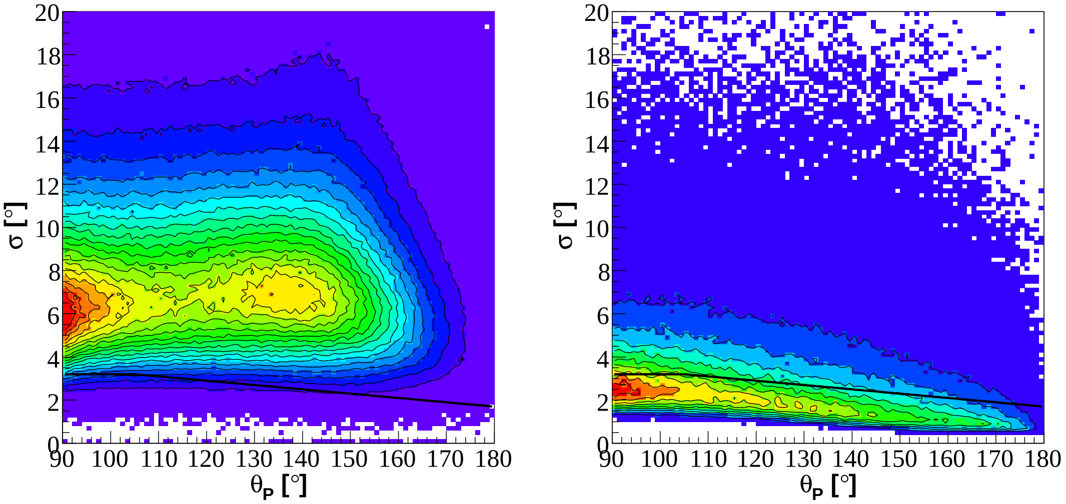

(a) data (b) GRB signal

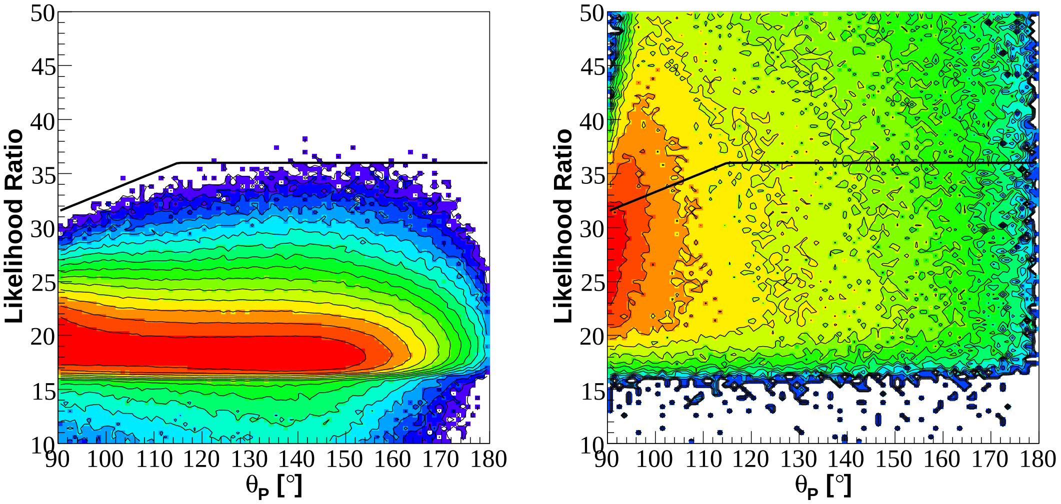

(c) data (d) GRB signal

Figure 7.9: Zenith dependence of the σ and likelihood ratio event variables. z-axes represent the probability distribution and are shown in log scale. Parameterized cuts are overlaid (solid black line). This projection clearly shows the benefit derived from the cuts selected.

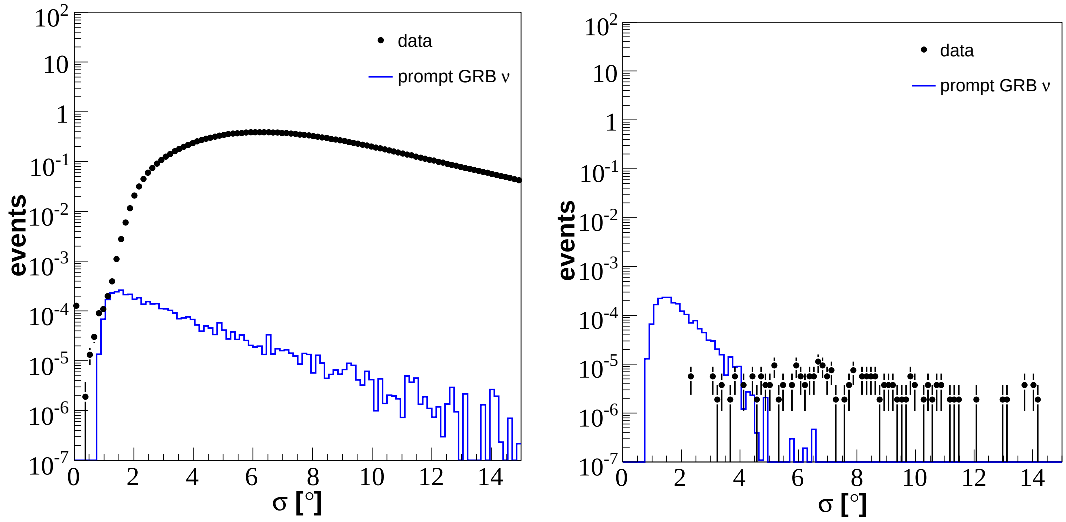

(a) filter level (b) all but σ cut

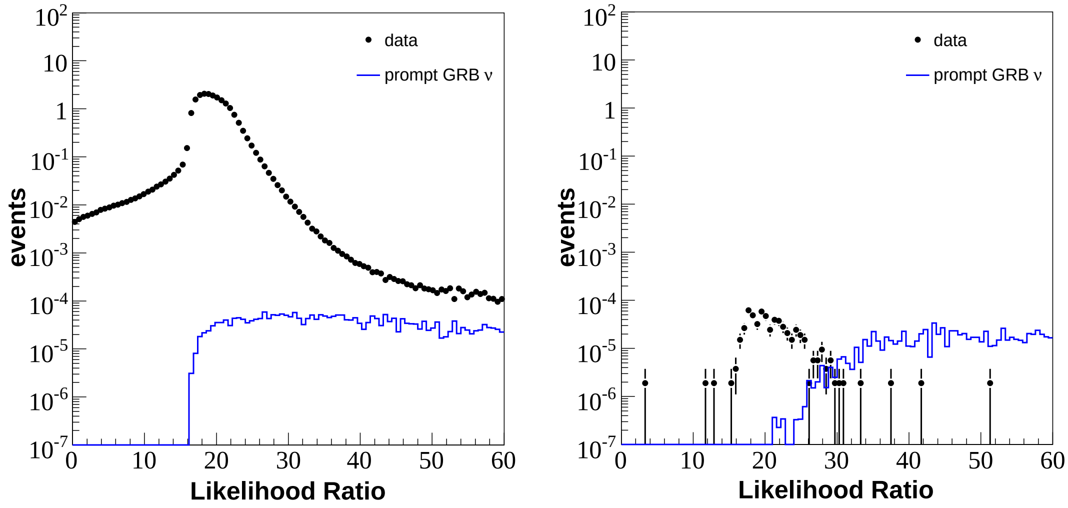

(c) filter level (d) all but likelihood ratio cut

Figure 7.10: We show here the effect of applying all final cuts except one on a given parameter. Left panels show rates of data (black dots) and GRB signal (blue lines) at filter level. Right panels show the same distributions after applying the space angle cut and either the likelihood ratio cut (top right) or σ cut (bottom right). In each case it is clear that additional separation power is available in the remaining variable, and we take advantage of this. All plots are for a fake source placed at $\theta_{\mathrm{GRB}} = 135°$.

7.5 Final Event Sample

We obtain a precise estimate of the background by applying the event selection described above to the full livetime of the 2005 and 2006 datasets and rescaling the remaining events to the summed GRB emission windows. As described in Chapter 5, we ensure that this sample contains no signal by removing 10 minutes of data centered around each burst[5]. To determine the signal retention, we re-weight our simulation to approximate point sources at the locations of each GRB using the method outlined in section 7.4. This allows us to fold in the full angular dependence of the detector response to our signal. We also take into account detector deadtime. For each GRB we consult the run logs associated with that time period and determine the deadtime fraction. For the full 2005-2006 GRB sample, the averaged deadtime is 16.6%. Simulated signal and background is downscaled accordingly. Taking this into account, we expect a stacked signal from the 85 burst sample of 0.166 events, on a background of 0.00087 events. This is summarized in Table 7.4. Our choice of optimization strategy results in an extremely low background prediction, allowing a significant detection with only a small number of events. The zenith distribution of the final sample is shown in Fig. 7.11. Distributions in our event selection parameters are shown in Figures 7.12, 7.13, and 7.14. As can be seen, with this event selection, most of the data is atmospheric neutrinos. The remaining downgoing muon contamination is estimated at 18%. Signal efficiency averaged over the whole sky is 39.7%, although there is a strong zenith dependence, as shown in Fig. 7.15.

	Filter Level	Filter Level Scaled	Final Cuts
2005-2006 Data	10.1 M	1703.9	0.00087
85 GRBs	0.418	0.418	0.166

Table 7.4: Event rates for the 2005-2006 AMANDA analysis after final event selection. We compare to earlier filter levels to show the background rejection power of the analysis. Scaling is to the total prompt phase emission time window of 5343.8 s.

---

[5] A select few bursts have duration longer than 10 minutes. For these we extend the blinded window to encompass the emission.

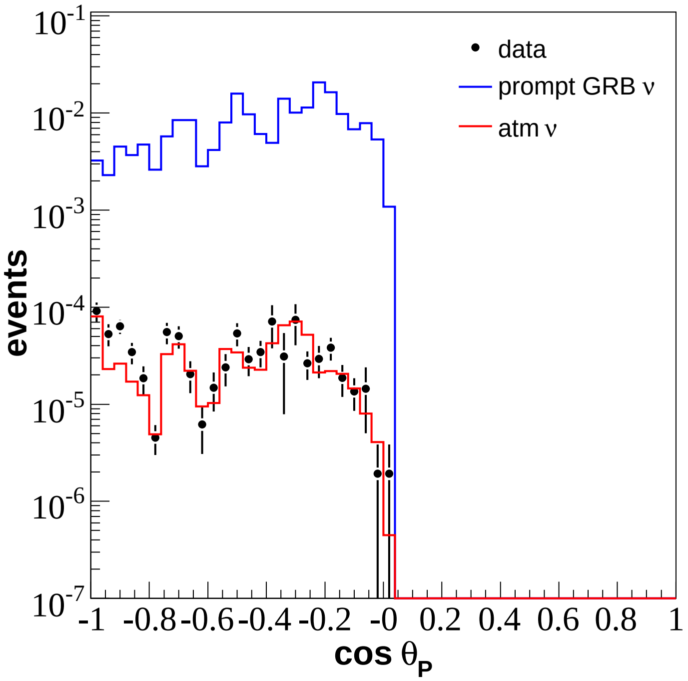

Figure 7.11: Simulation and data comparison at final cut level. No downgoing muon simulation survives all cuts. Atmospheric neutrinos simulation and data agree well and are highly supressed relative to predicted prompt GRB signal neutrinos. We can directly compare this to the upgoing muon filter level distribution of Fig. 7.3, where the backgrounds highly dominate the event rate.

7.6 Sensitivity

The sensitivity of our analysis is defined by the upper limit that can be placed in the case of a non-detection. We follow the procedure of Hill and Rawlins [105] to determine our average sensitivity given an ensemble of hypothetical experiments.

Given a dataset, theoretical prediction, and certain set of cuts, we have an expected background n_b, expected signal n_s, and observation after unblinding n_{obs}. The confidence interval is dependent on both the observation and the background expectation. We are free to chose the coverage of this interval, and in this analysis we choose 90%. In the case that the interval contains 0, we have an upper limit. For a given background and observed event number, we calculate the confidence interval using the Feldman-Cousins unified approach [108] to determine the event upper limit.

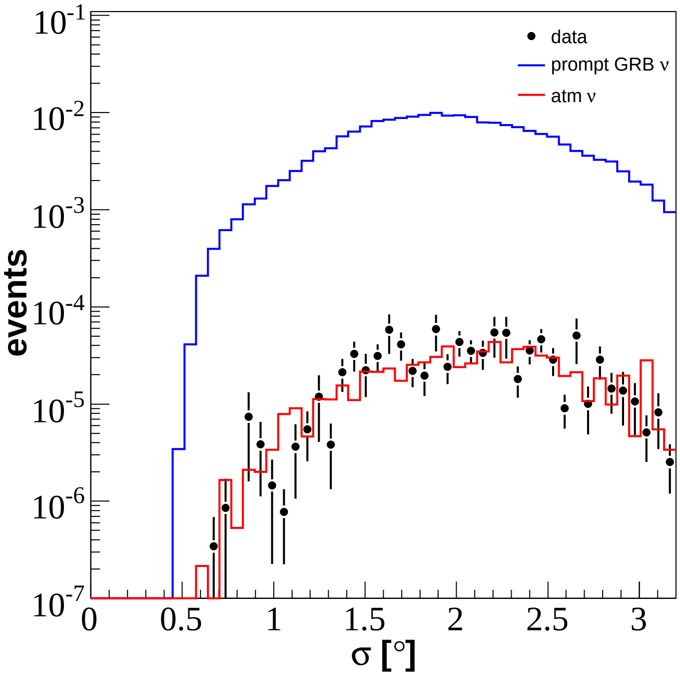

Figure 7.12: Error estimate σ of the track reconstruction at final cut level. Only simulation and data that survive the angular cuts around each of the 85 GRB locations are plotted.

$$(0.0, \mu_{eul}) = \mu_{90}(n_{obs}, n_b) \tag{7.5}$$

However, in order to calculate this, we need to know n_{obs} which is not possible in blinded data. We therefore determine the limit (sensitivity) for a collection of experiments where we allow the observed events to vary. Eq. 7.6 gives the average event upper limit for an ensemble of experiments with known background n_b and observations n_{obs} that fluctuate according to Poisson statistics.

$$\bar{\mu}_{90}(n_b) = \sum_{n_{obs}=0}^{\infty} \mu_{90}(n_{obs}, n_b) \frac{(n_b)^{n_obs}}{(n_{obs})!} e^{-n_b} \tag{7.6}$$

Our sensitivity to a model is then given by the ratio of the average upper limit for our analysis to the number of predicted signal events surviving in the final event sample

$$\frac{\bar{\mu}_{90}}{n_s}. \tag{7.7}$$

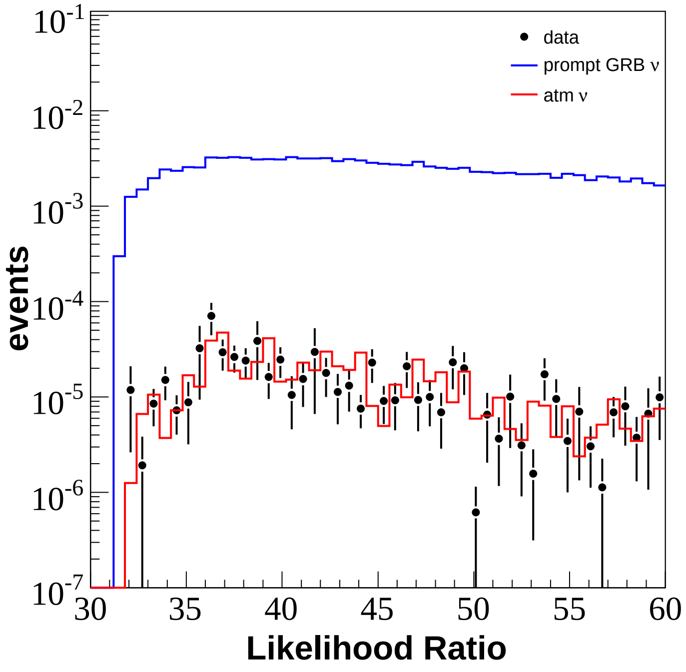

Figure 7.13: Likelihood ratio between the unbiased and zenith weighted track reconstructions at final cut level. Only simulation and data that survive the angular cuts around each of the 85 GRB locations are plotted.

This gives the multiple of the predicted fluence that we will be able to reject on average at the 90% confidence level. We therefore refer to it as the Model Rejection Factor (MRF). In the unblinded data, an upward or downward fluctuation in the background may result in a worse or better final limit.

Given our background expectation of 0.00087 events and signal prediction of 0.166 events at final cut level, we calculate our analysis to have a MRF of 14.7 with respect to the Waxman Bahcall model of neutrino emission from GRBs. This corresponds to a sensitivity of $6.6 \times 10^{-8}\,\mathrm{GeV\,s^{-1}\,cm^{-2}\,sr^{-1}}$ to the diffuse flux prediction at 100 TeV.

7.7 Discovery Potential

Our optimization strategy results in very strong background rejection that allows us to make a significant discovery with only a small number of events. With a background expectation of 0.00087 events, we can make a 5σ discovery by observing 2 events in the stacked emission window. A single

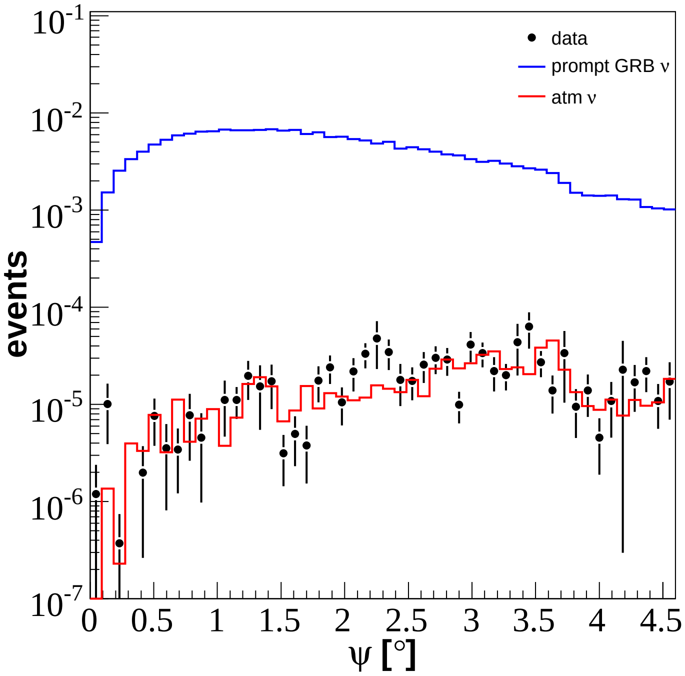

Figure 7.14: Space angle distribution at final cut level. The discrete change in the cut from 3.7° to 4.6° is clearly visible.

event would constitute a 3σ observation. It is important to recognize that by rigorously optimizing the event selection and applying tight quality criteria, a higly significant discovery can be made with very few events. This demonstrates and emphasizes the inherent advantage of searches for transient sources well-localized in both space and time.

We can evaluate what chance we have of making these observations given the final signal prediction with our flux model of 0.166 events. We compare the statistical power of the experiment to the flux factor (MDF) of the prediction necessary to produce the desired significance, shown in Fig. 7.17. Table 7.5 shows the resulting percentage of experiments that will make a discovery for different signal fluxes and significances.

7.8 Results

After unblinding the prompt emission region around each burst and applying all event selection criteria we observe 0 remaining events. This result is consistent with the low background expectation of 0.00087 events. We therefore set an upper limit on the emission of high energy neutrinos during

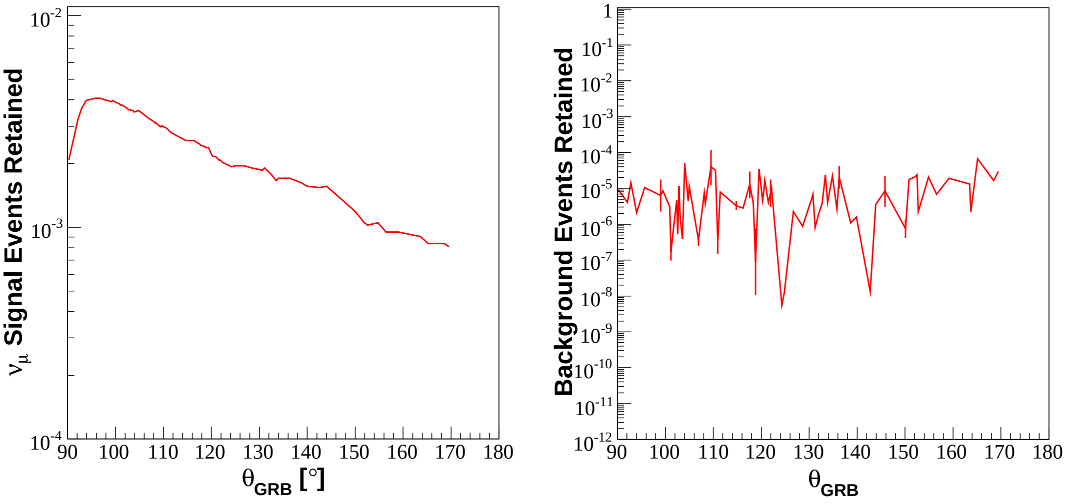

(a) signal retained per GRB

(b) background retained per GRB

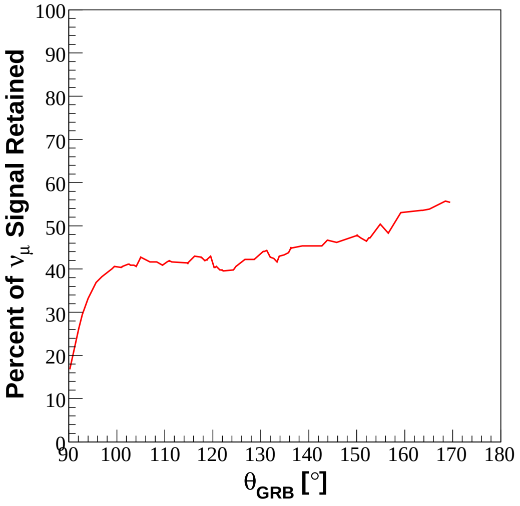

(c) percent signal retained

Figure 7.15: Signal and background retention after applying final event selection to all GRBs in the 2005-2006 sample. Note that because of the strong zenith dependence in detector acceptance, the absolute number of retained signal events decreases as zenith increases, while the percent relative to the total before cuts increases.

the prompt emission of the 85 gamma-ray bursts included in our sample. We once again utilize the Feldman-Cousins unified ordering principle [108] to determine the 90% confidence interval. This gives an event upper limit of 2.43 events. Under the assumption of emission following the Waxman-Bahcall model from an ensemble of 85 bursts this translates into an 90% C.L. upper limit on E^2 multiplied by

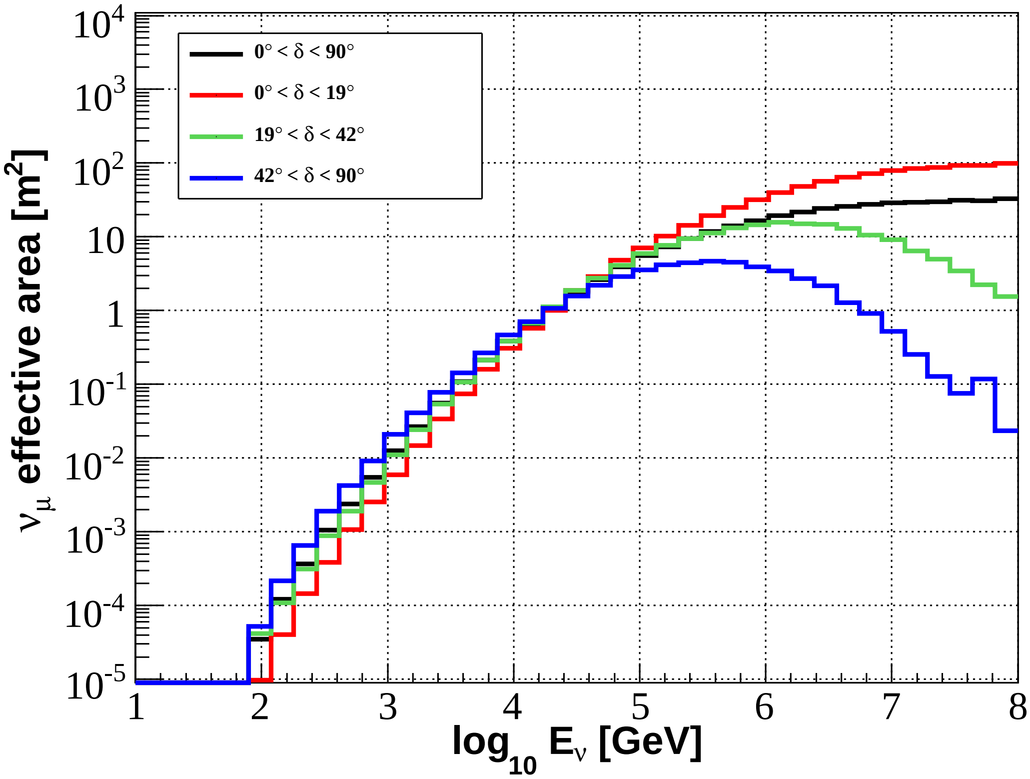

Figure 7.16: Muon neutrino effective area for the AMANDA detector as a function of energy at final cut level. Solid black line is averaged over the half sky, while the other angular ranges correspond to the most horizontal, middle, and most vertical thirds of the northern sky in $\cos\delta$. Comparison with previous work shows the effective area to be very similar, even with a very different optimization strategy.

Significance	Power	MDF
3σ	14.8%	1.0
3σ	50%	4.2
3σ	90%	13.9
5σ	1.1%	1.0
5σ	50%	10.1
5σ	90%	23.4

Table 7.5: Comparison of the discovery potential of the 2005-2006 GRB search for various significance levels and statistical powers.

the neutrino emission during the prompt phase of $6.6 \times 10^{-8}\,\mathrm{GeV\,s^{-1}\,cm^{-2}\,sr^{-1}}$ at 100 TeV. The 90% contained energy range of the analysis is 21.0 TeV to 4.9 PeV. We have converted our fluence limit

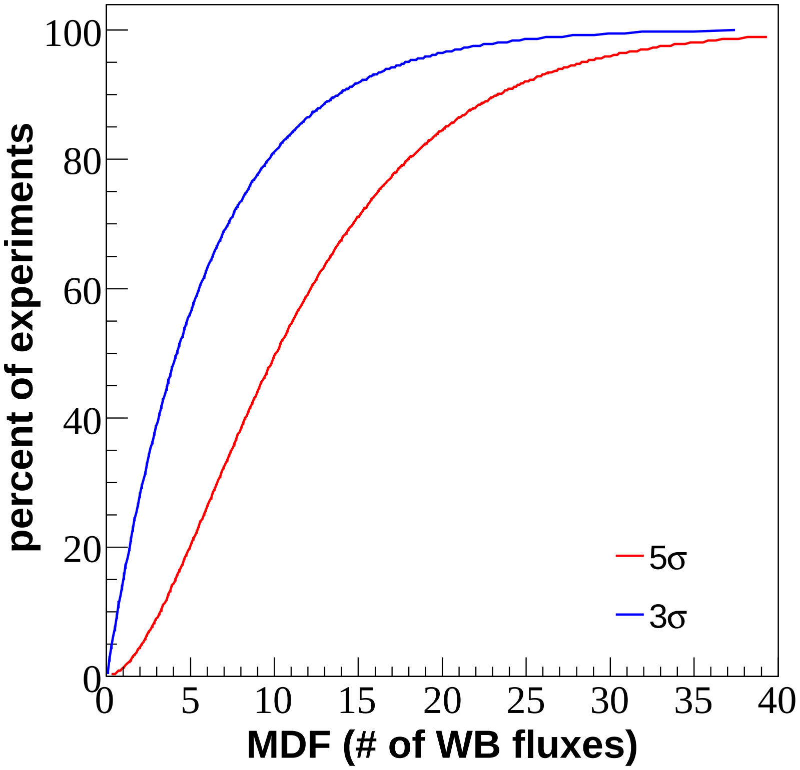

Figure 7.17: Model Discovery Potential at 3σ and 5σ confidence levels for the 2005-2006 AMANDA analysis. x-axis represents the multiple of the predicted Waxman Bahcall emission needed to make a discovery with the stated significance. y-axis shows the statistical power.

into a diffuse flux limit in order to directly compare with theory and previous results. We discuss the effect of systematic errors on our upper limit in Chapter 9.

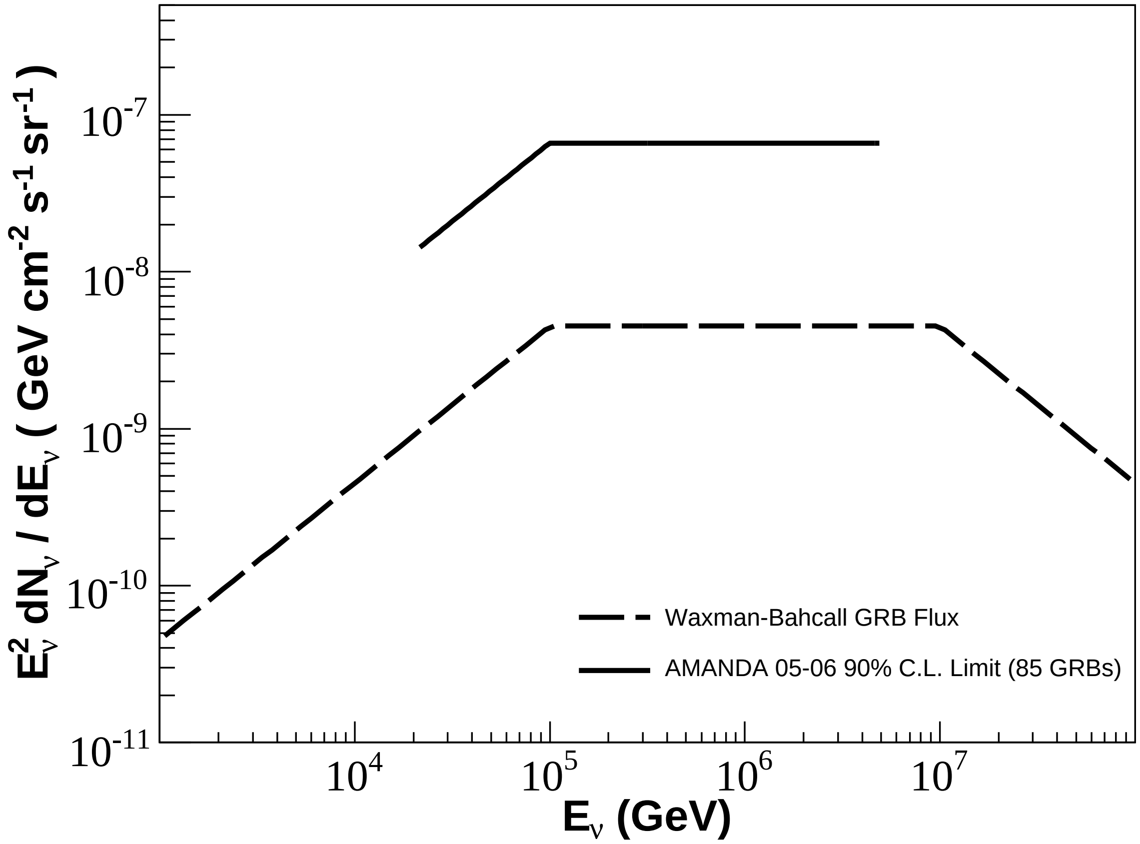

Figure 7.18: 90% Confidence Level upper limit on the emission of neutrinos during the prompt phase of Gamma-Ray Bursts. Limit is based on the non-detection of neutrinos from 85 GRBs observed in the northern sky in 2005-2006.

Chapter 8

IceCube Analysis

The data for this analysis were taken using the 22-string configuration of the IceCube detector between May 2007 and April 2008. We perform a stacked search for neutrino emission from 41 northern hemisphere GRBs observed by satellites. As in the case of the AMANDA-II analysis, the majority of these bursts were observed by Swift. The resolution of the GRB position from these satellites is better than 0.1° and hence lies well below that of the IceCube detector. It is therefore neglected in these analyses.

Rather than focusing solely on the prompt emission phase, this analysis searches for neutrinos from all phases of the GRB (see Chapter 2). Furthermore, we seek to improve our estimation of the signal by modeling the emission from each burst individually, using what electromagnetic observations we have from satellites and ground-based telescopes. For the first time in stacked GRB searches, we utilize an unbinned maximum likelihood technique to improve the sensitivity of the analysis.

A binned search on the same data set was performed utilizing a Support Vector Machine (SVM) for event selection. The intent was to compare the binned and unbinned methods to determine what percent improvement could be achieved with the more advanced technique. We present sensitivities for this search, but do not describe it in detail. For further information, see [107, 93]. An overview of the SVM optimization technique is given in Appendix C.

8.1 Filtering

In order to obtain a starting sample of quality upgoing muons on which to perform our seach, we employ a series of filters to reject downgoing muon backgrounds. These are summarized in

Table 8.1 and described below.

Filter Level	Processing / Selection
Online / Level 1	($\theta_{\mathrm{LF}} \geq 70°$ AND $N_{ch} \geq 10$) OR ($\theta_{\mathrm{LF}} \geq 60°$ AND $N_{ch} \geq 40$) OR ($\theta_{\mathrm{LF}} \geq 50°$ AND $N_{ch} \geq 50$)
Level 2	Processing of high level reconstructions
Level 3	1-iteration $\theta_{\mathrm{P}} > 80°$ 1-iteration reduced log-likelihood< 13 32-iteration $\theta_{\mathrm{P}} > 80°$

Table 8.1: Summary of 22-string IceCube upgoing muon filters.

8.1.1 Online Muon Filter / Level 1 Filter

A filter was applied in online processing during data-taking at the south pole to select a sample of candidate upgoing muon events. This filter used the fast first-guess algorithm LineFit to estimate the track direction, and used N_{ch} as an energy estimator. It was designed to select events that were clearly upgoing or alternately to allow events with less clear direction but that seemed to be of high energy. The filter settings changed throughout the year as understanding of the detector was gained, and all data was reprocessed from tape with a final configuration known as Level 1.

8.1.2 Level 2 Filter

No event selection is done during the Level 2 filtering, but rather a wide variety of standard processing is performed, yielding high level data that is useful across many analyses. These reconstructions use a hit set that has been time cleaned. The cleaning keeps only hits within 6 μs, finding that window which keeps the most hits. Single iteration unbiased reconstructions are performed, as well as the zenith-weighted fit, and a fit that splits the hit series into two parts to help reject coincident muons. These are explained in more detail in section 8.3.

8.1.3 Level 3 Filter

Performing many-iteration likelihood reconstructions is computationally intensive, and therefore some loose event selection is done on the Level 2 filtered dataset before continuing. The single iteration Pandel fit is required to give a track with $\theta_{\mathrm{P}} > 80^\circ$ and the reduced log-likelihood of the same reconstruction is required to be less than 13. After the 32-iteration Pandel reconstruction is performed, the returned angle is also required to be greater than 80°. For events that pass these filters, further event quality reconstructions (32-iteration paraboloid, umbrella) are calculated, as well as several energy estimators.

8.1.4 Starting Event Sample

After applying the upgoing muon filters described above and selecting only those data runs that correspond to stable running periods, we are left with a sample of 77 million events reconstructed as upgoing. A $\{-1\,h, +3\,h\}$ window is blinded around each burst, leaving a livetime of 268.9 days in the off-time window. We use the large dataset to precisely estimate the background contamination during the GRB emission windows. At this level, the data has a rate of 3.3 Hz and is still dominated by downgoing muons, as shown in Fig. 8.1. Given its larger size, IceCube has a much bigger contamination of coincident downgoing muons that mimic upgoing tracks than AMANDA. We will have to leverage new rejection techniques to deal with this background.

8.2 Signal Spectrum

To maximize the scope of the analysis, we search for GRB neutrinos in several emission windows. Where possible we calculate the expected neutrino fluence based on the observed photon spectrum. We describe the signal prediction for each search window below.

8.2.1 Precursor Emission

For the *precursor* phase (section 2.3.2), the fireball is expected to be optically thick and thus no photon emission is observeable. We therefore assume each GRB has a fluence given by the Razzaque et al. model [50]. The emission is expected to occur from $10 - 100\,\mathrm{s}$ preceding the prompt photons, and we take as our time window the range $\{-100\,s, 0\,s\}$ relative to the satellite trigger. The detector response to such emission from a single burst is shown in Fig. 8.2.

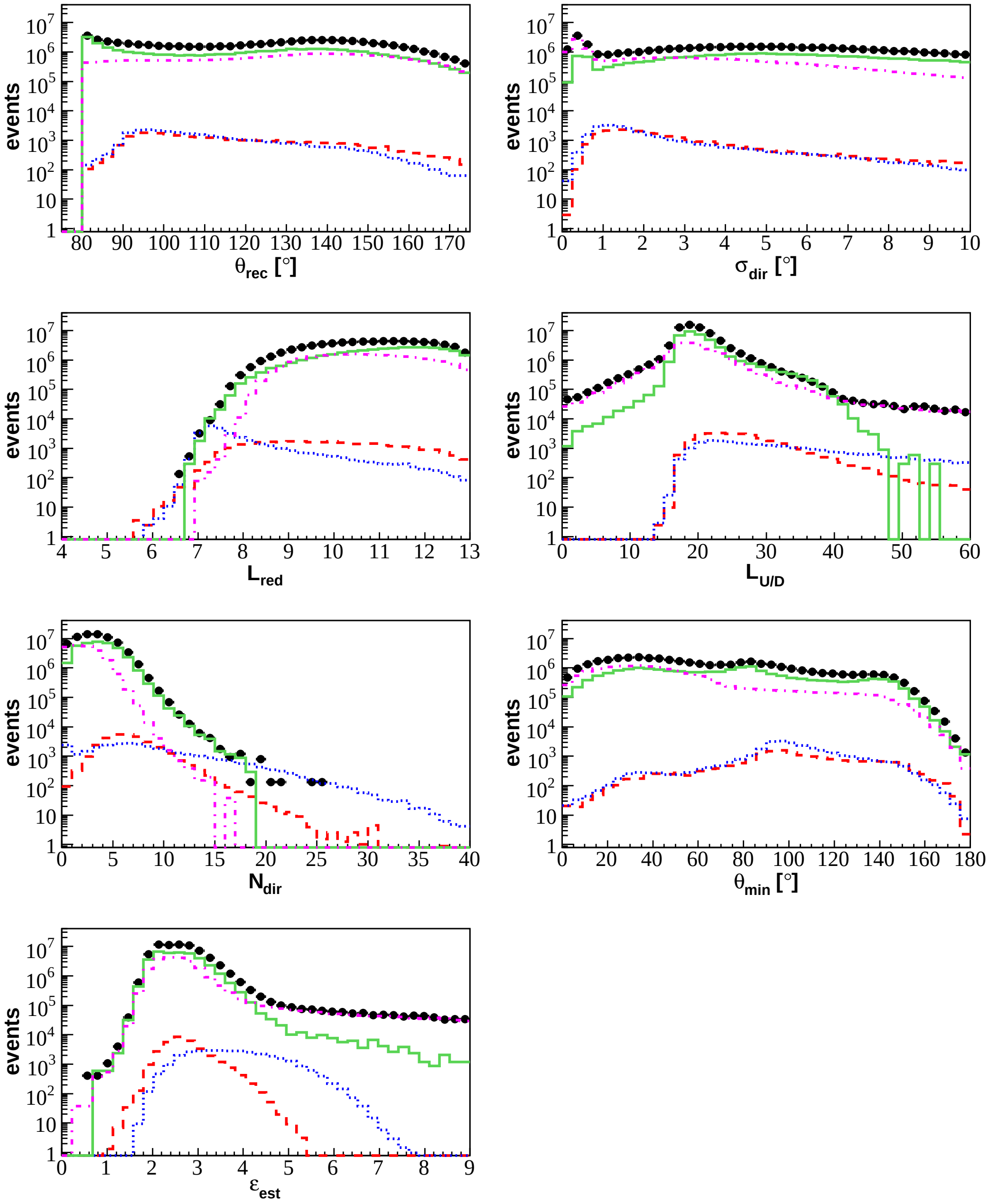

Figure 8.1: Comparison between data (solid circles) and simulation in the quality parameters used to reject mis-reconstructed atmospheric muons at upgoing muon filter level. Monte Carlo shown includes atmospheric muons (green solid), coincident muons (magenta dot-dashed), atmospheric neutrinos (red dashed), and prompt GRB neutrinos (blue dotted). As a simple shape comparison, the GRB signal is assumed to follow an average Waxman-Bahcall spectrum and is normalized to the rate of atmospheric neutrinos.

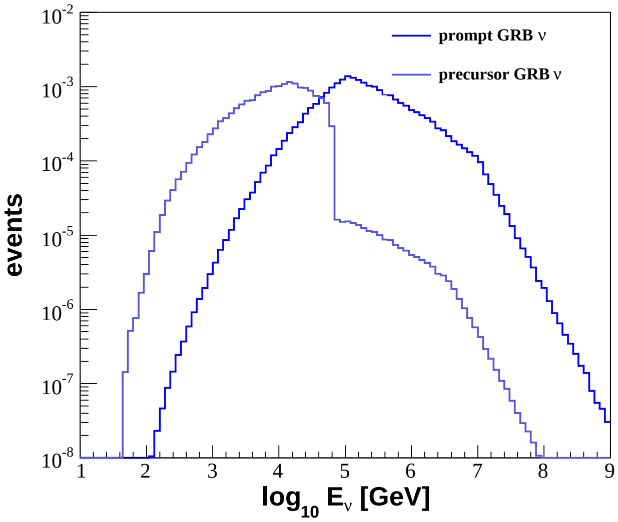

Figure 8.2: IceCube response at upgoing muon filter level to the precursor neutrino flux of Razzaque et al. [50] from one GRB. For comparison, we also shown the response to the canonical Waxman Bahcall flux from a single burst. Response is averaged over the full sky.

8.2.2 Prompt Emission

For the *prompt* phase (section 2.3.1), we use the windows calculated in section 5.4.2 for each burst (integrated emission time of 4960.6 s). GRB spectral parameters vary substantially from burst to burst, and the average values used to calculate the canonical Waxman Bahcall flux are based on data from BATSE that do not accurately represent the Swift dominated GRB sample we use. We therefore calculate the neutrino fluence on a per burst basis, using the formalism developed in section 2.3.1. The photon spectral parameters for each burst are measured by satellites and ground-based observatories and reported via GCN circulars and reports. In the case that a parameter was not measured, we use average values derived from the Swift GRB population [51], shown in Table 8.2. Some parameters needed to calculate the predicted neutrino fluence are never measured, and must be assumed. These include the time variability (t_{var}), isotropic luminosity in γ-rays (L_γ^{iso}), bulk jet Lorentz factor (Γ), fraction of jet energy in electrons (ξ_e), fraction of jet energy in the magnetic field (ξ_B), and ratio between energy in electrons and protons (f_e). For these, the best guess values based on observations and physical inferences are also shown in Table 8.2. The measured and calculated spectral parameters for each burst are presented in Table 8.3. Fig. 8.3 shows the derived neutrino spectra for the prompt phase emission for each GRB in comparison the Waxman Bahcall model. The wide variance and overall reduction in normalization highlights the importance of individual fluence modeling.

parameter	average value
f_γ	$1.3\,\mathrm{MeV}^{-1}\,\mathrm{cm}^{-2}$
z	2
ϵ_γ	$0.2\,\mathrm{MeV}$
α_γ	1
β_γ	2
L_γ^{iso}	$10^{51}\,\mathrm{erg}\,\mathrm{cm}^{-2}$
Γ	315
t_{var}	$0.01\,\mathrm{s}$
ξ_e	0.1
ξ_B	0.1
f_e	0.1

Table 8.2: Average values of GRB parameters in the Swift population.

Table 8.3: Spectral information for 41 northern sky GRBs observed in 2007-2008

GRB	z	γ-ray spectrum f_γ	ϵ^b_γ	α_γ	β_γ	ν spectrum f_ν	ϵ^b_ν	ϵ^s_ν	α_ν	β_ν	γ_ν
GRB070610	2.00	2.7e−02	0.20	1.76	2.76	1.6e−10	0.35	8.54	0.24	1.24	3.24
GRB070612A	2.00	1.5e+00	0.20	1.69	2.69	2.3e−08	0.35	8.54	0.31	1.31	3.31
GRB070616	2.00	3.3e+00	0.20	1.61	2.61	1.4e−07	0.35	8.54	0.39	1.39	3.39
GRB070704	2.00	6.0e−01	0.20	1.79	2.79	2.5e−09	0.35	8.54	0.21	1.21	3.21
GRB070714B	0.92	2.5e−01	0.20	1.36	2.36	2.7e−07	0.85	13.34	0.64	1.64	3.64
GRB070724B	2.00	4.0e−01	0.08	1.15	3.15	1.7e−04	0.85	8.54	-0.15	1.85	3.85
GRB070808	2.00	3.1e−01	0.20	1.47	2.47	8.5e−08	0.35	8.54	0.53	1.53	3.53
GRB070810B	2.00	2.8e−03	0.20	1.44	2.44	1.1e−09	0.35	8.54	0.56	1.56	3.56
GRB070917	2.00	2.0e−01	0.21	1.36	3.36	6.8e−07	0.33	8.54	-0.36	1.64	3.64
GRB070920A	2.00	7.0e−02	0.20	1.69	2.69	1.0e−09	0.35	8.54	0.31	1.31	3.31
GRB071003	2.00	1.5e+01	0.80	0.97	2.97	4.1e−04	0.09	8.54	0.03	2.03	4.03
GRB071008	2.00	6.4e−03	0.20	2.23	3.23	1.2e−13	0.35	8.54	-0.23	0.77	2.77
GRB071010B	0.95	1.8e−01	0.03	1.25	2.65	3.3e−05	5.71	13.16	0.35	1.75	3.75
GRB071010C	2.00	1.3e+00	0.20	1.00	2.00	2.2e−04	0.35	8.54	1.00	2.00	4.00
GRB071011	2.00	6.7e−01	0.20	1.41	2.41	4.1e−07	0.35	8.54	0.59	1.59	3.59
GRB071013	2.00	5.7e−02	0.20	1.60	2.60	2.8e−09	0.35	8.54	0.40	1.40	3.40
GRB071018	2.00	1.6e−01	0.20	1.63	2.63	5.4e−09	0.35	8.54	0.37	1.37	3.37
GRB071020	2.15	1.3e+00	0.32	0.65	2.65	1.5e−02	0.20	8.13	0.35	2.35	4.35
GRB071021	2.00	1.7e−01	0.20	1.70	2.70	2.3e−09	0.35	8.54	0.30	1.30	3.30
GRB071025	2.00	6.6e−01	0.20	1.79	2.79	2.8e−09	0.35	8.54	0.21	1.21	3.21
GRB071028A	2.00	2.4e−02	0.20	1.87	2.87	3.6e−11	0.35	8.54	0.13	1.13	3.13
GRB071101	2.00	2.0e−03	0.20	2.25	3.25	3.0e−14	0.35	8.54	-0.25	0.75	2.75
GRB071104	2.00	1.3e+00	0.20	1.00	2.00	2.2e−04	0.35	8.54	1.00	2.00	4.00
GRB071109	2.00	1.3e+00	0.20	1.00	2.00	2.2e−04	0.35	8.54	1.00	2.00	4.00
GRB071112C	0.82	2.2e+00	0.20	1.09	2.09	1.1e−04	0.95	14.07	0.91	1.91	3.91
GRB071118	2.00	8.1e−02	0.20	1.63	2.63	2.7e−09	0.35	8.54	0.37	1.37	3.37
GRB071122	1.14	6.3e−02	0.20	1.77	2.77	2.6e−10	0.69	11.97	0.23	1.23	3.23

Continued on next page...

Table 8.3: (continued)

GRB	z	γ-ray spectrum f_γ	ϵ_γ^b	α_γ	β_γ	ν spectrum f_ν	ϵ_ν^b	ϵ_ν^s	α_ν	β_ν	γ_ν
GRB071125	2.00	7.9e+00	0.30	0.62	3.10	2.3e−01	0.24	8.54	-0.10	2.38	4.38
GRB080121	2.00	2.4e−04	0.20	2.60	3.60	5.9e−17	0.35	8.54	-0.60	0.40	2.40
GRB080205	2.00	8.9e−02	0.20	2.08	3.08	1.0e−11	0.35	8.54	-0.08	0.92	2.92
GRB080211	2.00	8.7e+00	0.35	0.61	2.62	1.4e−01	0.20	8.54	0.38	2.39	4.39
GRB080218A	2.00	1.2e−02	0.20	2.34	3.34	6.0e−14	0.35	8.54	-0.34	0.66	2.66
GRB080307	2.00	9.1e−02	0.20	1.78	2.78	4.3e−10	0.35	8.54	0.22	1.22	3.22
GRB080310	2.43	4.6e−02	0.20	2.32	3.32	3.5e−13	0.27	7.47	-0.32	0.68	2.68
GRB080315	2.00	1.5e−03	0.20	2.51	3.51	1.1e−15	0.35	8.54	-0.51	0.49	2.49
GRB080319C	1.95	2.3e+00	0.11	1.01	1.87	7.2e−04	0.68	8.68	1.13	1.99	3.99
GRB080319D	2.00	2.2e−02	0.20	1.92	2.92	1.8e−11	0.35	8.54	0.08	1.08	3.08
GRB080320	2.00	3.6e−02	0.20	1.70	2.70	4.7e−10	0.35	8.54	0.30	1.30	3.30
GRB080325	2.00	6.9e−01	0.20	1.68	2.68	1.2e−08	0.35	8.54	0.32	1.32	3.32
GRB080328	2.00	2.0e+00	0.28	1.13	3.13	6.5e−05	0.25	8.54	-0.13	1.87	3.87
GRB080330	1.51	3.5e−03	0.20	2.53	3.53	1.5e−15	0.50	10.20	-0.53	0.47	2.47

Columns: f_γ [MeV^{-1} cm^{-2}], ϵ_γ [MeV], f_ν [GeV^{-1} cm^{-2}], ϵ_ν^b [PeV], ϵ_ν^s [PeV]. The parameters f_γ and f_ν are the fluxes at ϵ_γ and ϵ_ν^b of the gamma-ray and neutrino spectrum, respectively.

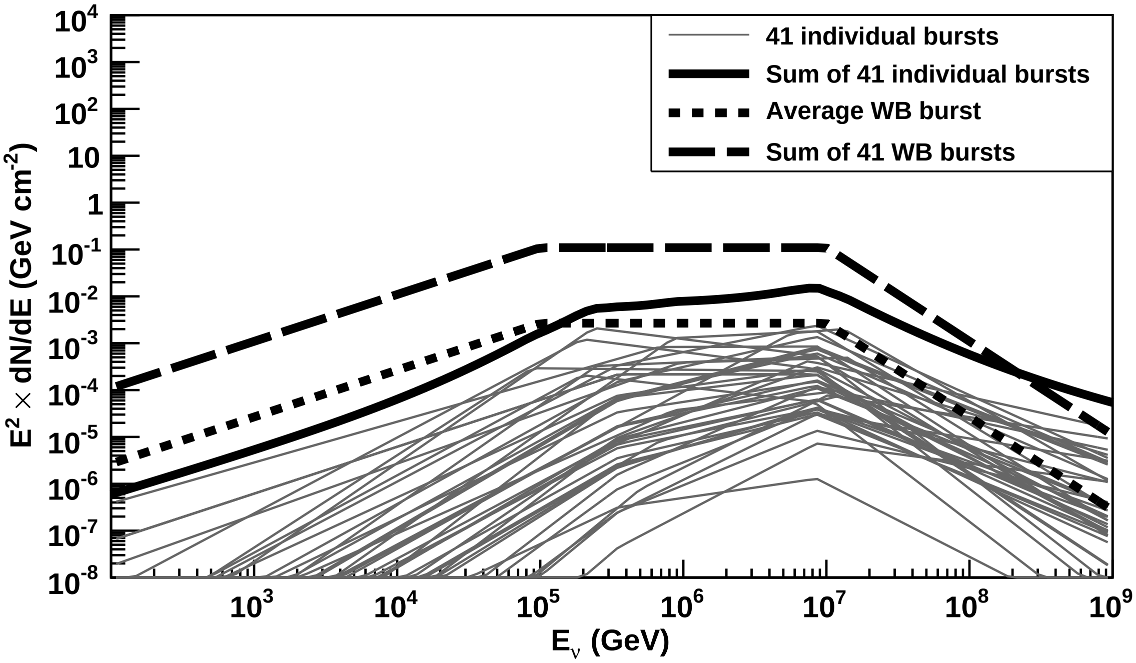

Figure 8.3: Neutrino energy spectra for 41 northern sky GRBs observed by satellites in 2007-2008. Comparison is made to the Waxman Bahcall spectrum calculated from average parameters of the BATSE satellite. Overall reduction in normalization is due to the significantly weaker burst population observed by Swift.

8.2.3 Extended Window Search

One limitation of GRB searches is that in order to maximize the sensitivity, we typically allow the search to be very model dependent. In the *extended* search window, we seek to mitigate this bias. Rather than incorporate the measured and assumed quantities, along with the many accompanying uncertainties, into a signal prediction we instead assume a simple, hard, E^{-2} energy spectrum for all bursts. We search in a time window $-1\,h, +3\,h$ around each GRB trigger. This window is motivated by a desire to include potential precursor and afterglow emission in the search, while still retaining significant background rejection from a short time window. For a few of the bursts in our sample, data in the full search window is incomplete. For these bursts, we search in shortened time windows defined in Table 8.4.

	$T_1 - T_0$ [s]	$T_2 - T_0$ [s]
GRB070610	−1593	+10800
GRB070714B	−3600	+3930
GRB071021	−3600	+5391
GRB071109	−3022	+10800
GRB080205	−3600	+6289
GRB080211	−3600	+8399
GRB080320	−389	+8440

Table 8.4: Modified extended time windows for GRBs with gaps in the data.

8.3 Event Selection

A positive detection in our search consists of an excess of events over background in coincidence in space and time with known GRBs. We can increase the significance of a detection by reducing the background of mis-reconstructed atmospheric muons in our data sample. If we do this perfectly, however, we are still left with a sample of atmospheric neutrinos. These events can only be statistically distinguished from our signal, leveraging the differences in energy spectrum and spatial distribution. We therefore gain no benefit from reducing our data sample beyond a set of high-quality neutrino candidates. For the final GRB search, we will employ a maximum likelihood technique (described in section 8.4). At the moment, we strive to find an event selection that removes the majority of downgoing muons while retaining a large fraction of neutrino candidates. We investigate a set of event variables that have good background rejection potential.

8.3.1 Reduced Log-Likelihood

Each of our advanced reconstructions returns a likelihood that the found track represents reality. When we divide this likelihood by the number of degrees of freedom of the fit, we are left with a parameter, $\mathcal{L}_{red}$ that is largely unbiased and gives a good measure of the quality of the reconstruction for each event. We take the $\log_{10}$ for mathematical convenience and use the resulting reduced log-likelihood associated with our highest iteration Pandel fit.

8.3.2 Bayesian Likelihood Ratio

The Bayesian likelihood ratio is defined by the ratio between log-likelihoods of the unbiased and zenith weighted reconstructions. We present it variously as $\mathcal{L}_B$ or $L_{U/D}$. As in the AMANDA analysis, it provides a strong discrimination between truly upgoing events and mis-reconstructed downgoing muons.

8.3.3 Paraboloid Sigma

Similar to the AMANDA analysis, we fit a parabola to the likelihood space of the iterative Pandel track reconstruction, centered at the best-fit minimum. The definition of the error ellipse is slightly different, given by

$$\sigma = \sqrt{\frac{\sigma_1^2 + \sigma_2^2}{2}}. \tag{8.1}$$

8.3.4 Umbrella Likelihood Ratio

The Umbrella likelihood reconstruction searches for a subset of events that reconstruct in the wrong hemisphere. In this respect, it is somewhat like the Bayesian likelihood. However, the implementation is quite different. The best unbiased Pandel track reconstruction is used as a seed. The parameter space is then restricted to the opposing hemisphere (evocative of an umbrella, hence the name) and a new likelihood is minimized using the inversion of the Pandel track as the seed. The likelihood ratio between the two tracks, $\mathcal{L}_P/\mathcal{L}_{Um}$ gives a good estimator of whether the track was reconstructed in the proper hemisphere. This parameter is good at discriminating against small, ‘blob’-like events that can equally well reconstruct in a variety of directions. In addition, it helps to find and retain a particular class of events that for unknown reasons reconstruct about 120° away from their true direction.

8.3.5 Split Reconstruction Minimum Zenith

In the split reconstruction we divide the hit set into two parts, split at the median time. Each of these hit sets is then treated as a separate event and new reconstructions performed. If the original event was truly upgoing, it is likely that both split reconstructions will point in the same, upgoing direction. On the other hand, if the event was caused by a coincident muon, one or both of the split reconstructions are likely to be downgoing. We use the minimum zenith angle θ_{min} of the two fits as a figure of merit for rejecting background.

8.3.6 Direct Hits

Direct hits represent light that reaches the PMTs of the detector in agreement with the prediction of a Čerenkov cone. We define the time window for direct hits by $-15\,\mathrm{ns} < t_{res} < 75\,\mathrm{ns}$. Although we use the same reconstruction algorithms as in the AMANDA analysis, and thus still suffer from the so-called direct hits problem (see section 7.3.4), we may make use of it if careful. For example, a high energy neutrino that has zero direct hits due to shifted vertex times may still be very well reconstructed. In this case, we could employ an OR condition with the reduced log-likelihood $\mathcal{L}_{red}$ to retain the event, while rejecting those background events that are both poorly reconstructed and have few hits in the detector.

8.3.7 Cut Selection and Neutrino Level Sample

In order to choose which cuts will be most effective in rejecting the background, we plot the efficiency of each, shown in Fig. 8.4. We see that the most efficient cuts are the reduced log-likelihood of the Pandel fit and the Bayesian likelihood ratio. We investigated several combinations of cuts and eventually settled on the same selection as used in a time integrated point source search conducted on 22-string IceCube data [109]. This event selection yielded the best sensitivity as well as retaining a large fraction of low energy signal. This property makes these cuts appropriate for the precursor phase GRB search as well, which peaks at 10 TeV. The chosen cuts are summarized in Table 8.5 and the resulting distributions of our selection variables are shown in Fig. 8.5. Note the use of a box cut in the reduced log-likelihood vs. direct hits parameters space that allows us to retain high energy events that suffer from the shifted vertex time bug.

Applying these cuts results in a sample of more than 90% atmospheric neutrinos. The event rate has been reduced to 2.1×10^{-4} Hz. We show the cumulative point spread function of the surviving events in Fig. 8.6 and the muon neutrino effective area in Fig. 8.7. Signal efficiency is depicted in Fig. 8.8 and summarized in Table 8.6.

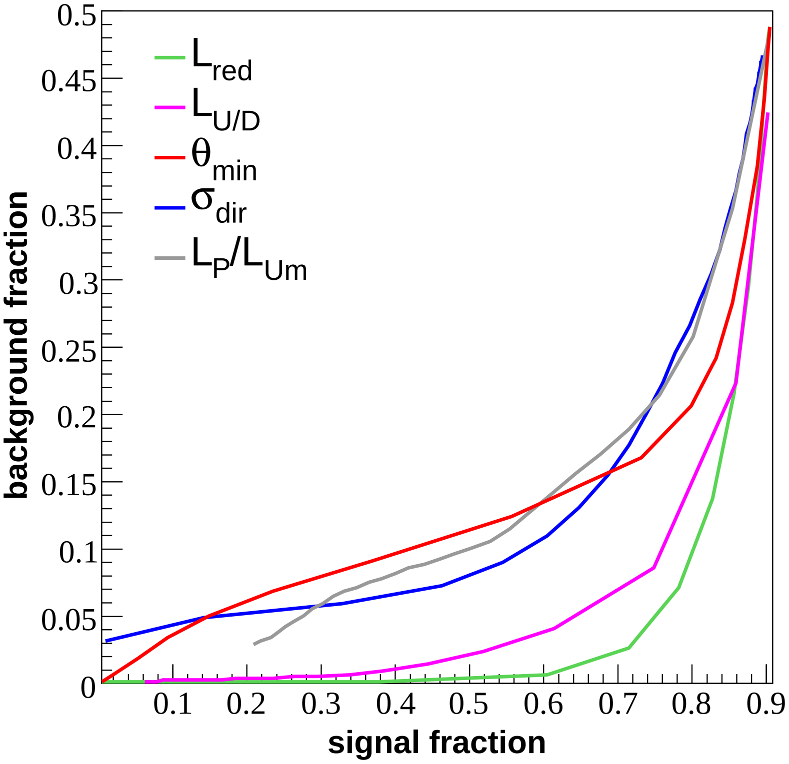

Figure 8.4: Cut efficiency for several event selection parameters. Reduced log-likelihood of the best guess track reconstruction is by far the most efficient rejector of background.

Variable	Cut Value
θ_{P}	$> 85°$
σ	$< 3°$
θ_{min}	$> 70°$
$\mathcal{L}_P/\mathcal{L}_B$	> 30
$\mathcal{L}_P/\mathcal{L}_{Um}$	> 15
$\mathcal{L}_{red}$	< 9.5
$\mathcal{L}_{red}$	< 8.5 for $N_{dir} < 8$
$\mathcal{L}_{red}$	< 7.8 for $N_{dir} < 7$
N_{dir}	> 8 for $\mathcal{L}_{red} > 8$
N_{dir}	> 7 for $\mathcal{L}_{red} > 7.8$

Table 8.5: Event selection criteria for the 2007-2008 IceCube GRB search.

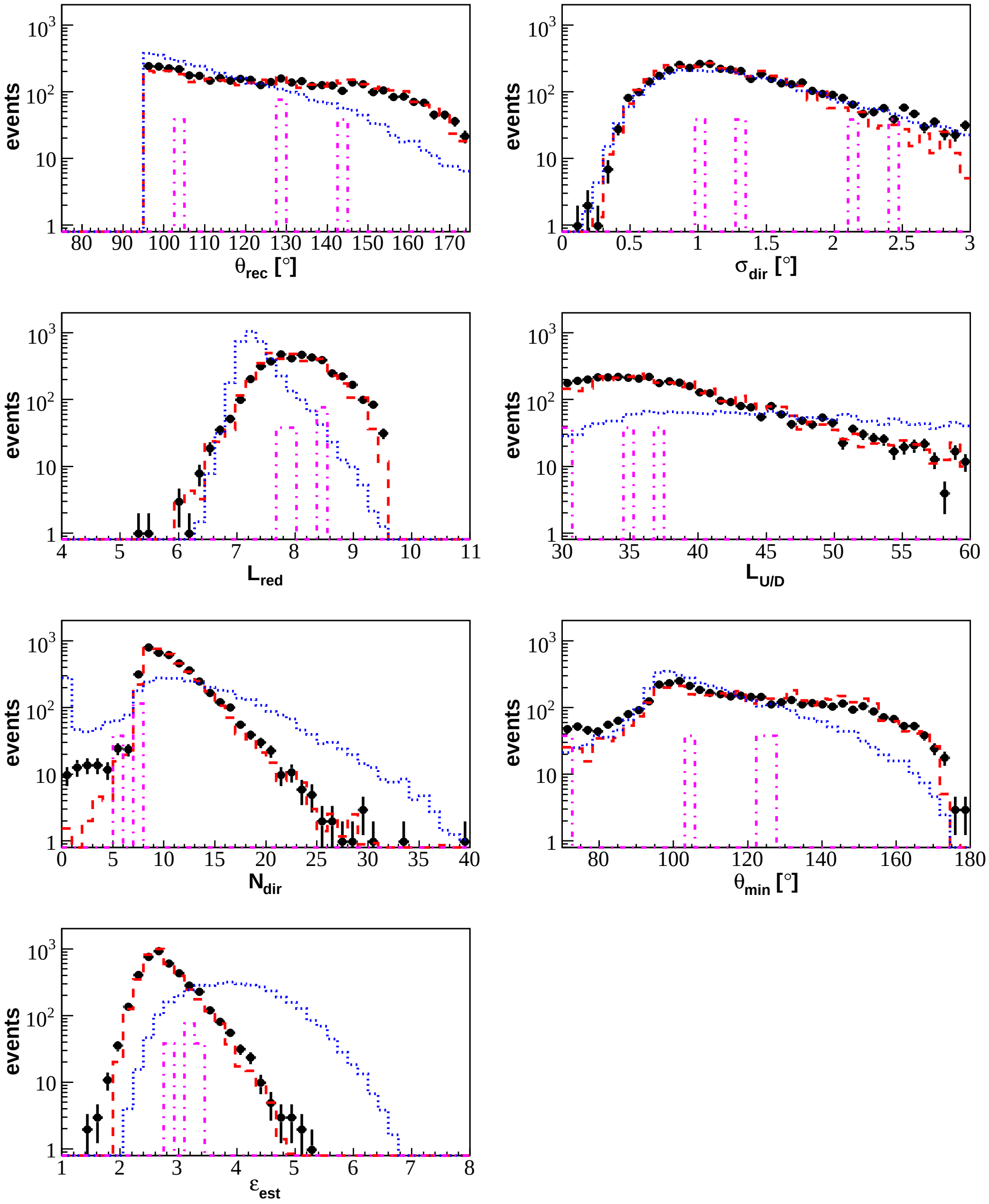

Figure 8.5: Comparison between data (solid circles) and simulation in the quality parameters used to reject mis-reconstructed atmospheric muons at neutrino level. Monte Carlo shown includes atmospheric muons (solid lines), coincident muons (dot-dashed lines), atmospheric neutrinos (dashed lines), and prompt GRB neutrinos (dotted lines). As a simple shape comparison, the GRB signal is assumed to follow an average Waxman-Bahcall spectrum and is normalized to the rate of atmospheric neutrinos.

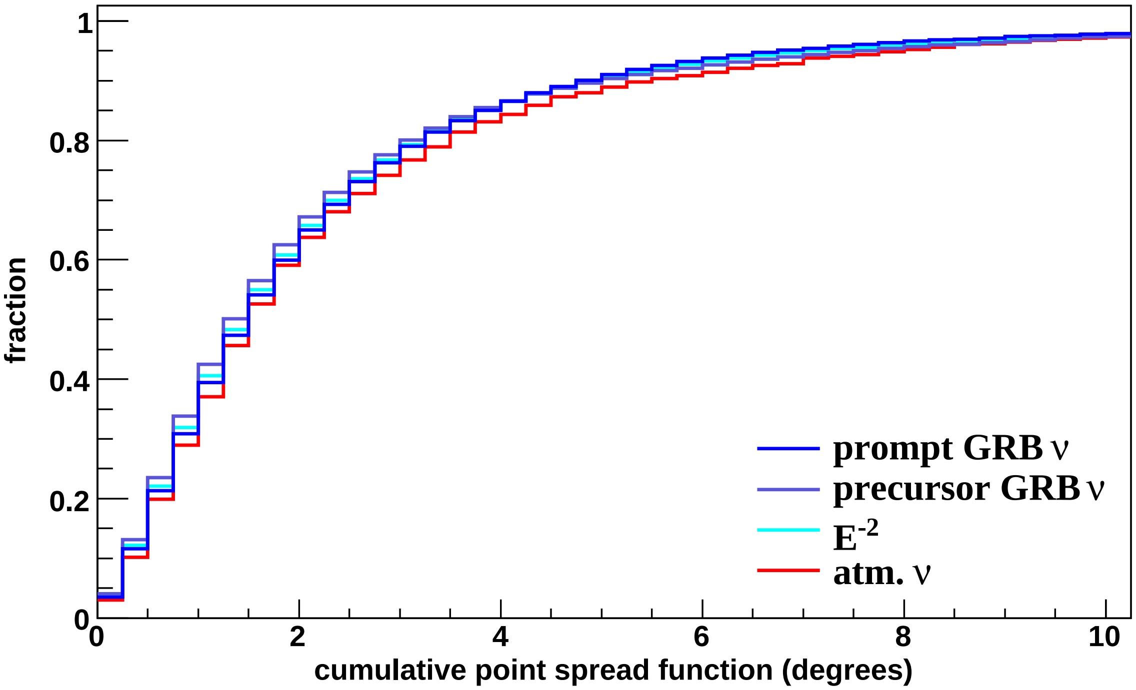

Figure 8.6: Cumulative point spread function for 2007-2008 analysis at final cut level.

	Filter Level		Final Cuts	
	evts	eff.	evts	eff.
2007-2008 Data	77 M	100%	4988	6.5×10^{-4}%
prompt spectrum	0.062	100%	0.033	53%
precursor spectrum	1.8	100%	0.53	29%
E^{-2}	–	100%	–	37%

Table 8.6: Event rates for the 2007-2008 IceCube analysis after final cuts. Efficiency is given relative to upgoing muon filter level. Rates for the prompt and precursor emission are calculated for 41 GRBs using the spectra described in section 8.2. Normalization of the E^{-2} fluence is arbitrary. The unbinned likelihood search will be applied to the surviving events to distinguish GRB signal neutrinos from background atmospheric neutrinos.

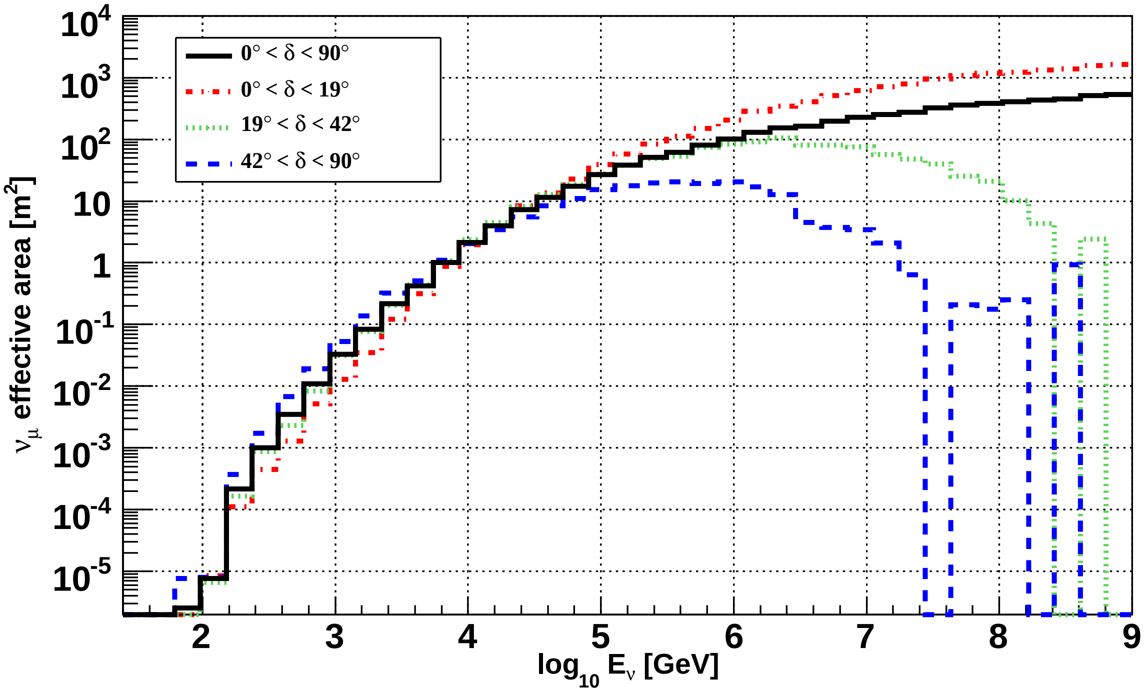

Figure 8.7: Muon neutrino effective area for the 22-string IceCube detector as a function of energy at final cut level. Solid black line is averaged over the half sky, while the other angular ranges correspond to the most horizontal, middle, and most vertical thirds of the northern sky in $\cos\delta$.

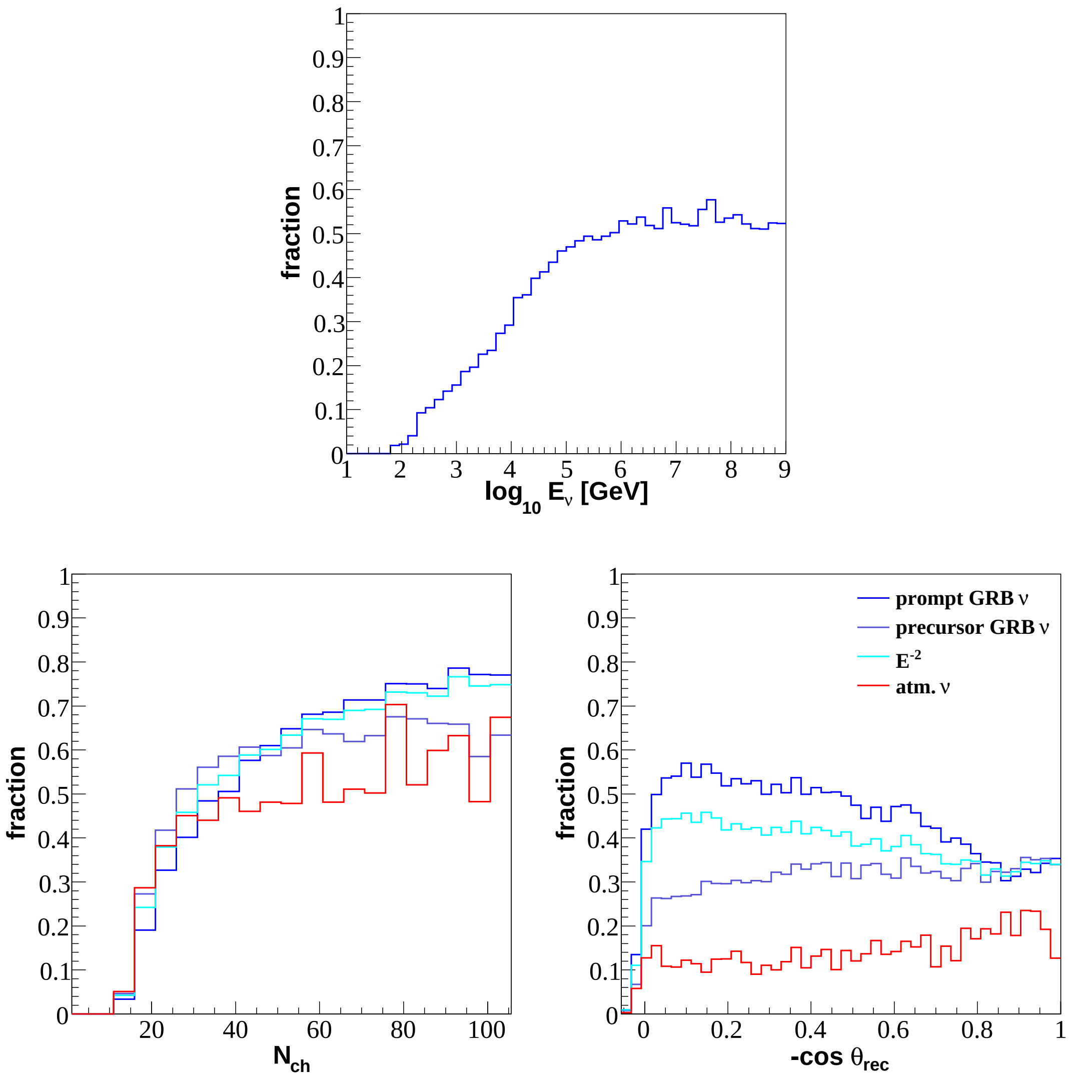

Figure 8.8: Signal efficiency at neutrino level relative to upgoing muon filter level for 2007-2008 IceCube analysis. Top panel shows efficiency as a function of neutrino energy. However, many high energy events skim the detector, so a better measure of efficiency is perhaps vs. number of hit channels. We can see this distribution in the bottom left panel for several energy spectra. The efficiency looks very good already at $N_{ch} = 100$. Bottom right panel shows efficiency as a function of zenith angle. Harder spectra are suppressed towards the vertical, but the overall efficiency is higher. With the chosen event selection we have an excellent chance of observing events that deposit a lot of energy in the detector.

8.4 Unbinned Analysis Method

For the first time in stacked GRB searches, we implement an unbinned maximum-likelihood approach. The method is similar to that described by Braun et al. [110] and has been employed previously in a search for emission from the single extremely bright burst GRB080319B. [13] We describe the method in detail.

After the event selection described above we are left with a high-purity sample of neutrino candidates. These belong either to the background distribution of atmospheric neutrinos, or the signal distribution from our GRB sample. In order to distinguish them, we make use of the spatial and temporal clustering expected from GRB neutrinos. We also note that our signal exhibits a harder energy spectrum than the background neutrinos [1]. This information is incorporated into probability distribution functions (PDFs) for both signal, $\mathcal{S}(\vec{x}_i, t_i, \epsilon_i)$, and background, $\mathcal{B}(\vec{x}_i, t_i, \epsilon_i)$.

We define the probability of occurrence via the *extended maximum likelihood function* [111]. In the standard maximum likelihood definition, the PDF $P(\mathbf{x}_i|\mathbf{a})$ is normalized to one. We instead employ a definition where the normalization is allowed to scale with the total number of observed events N. This is useful in cases where we do not know *a priori* what the event rate will be. Given a mean background contribution n_b and signal contribution n_s, we then have

$$\int Q(\mathbf{x}_i|\mathbf{a})\, dx \equiv n_t \int P(\mathbf{x}_i|\mathbf{a})\, dx = n_t \tag{8.2}$$

$$n_t = n_s + n_b \tag{8.3}$$

We can relate the probability of observing N given the expectation n_t via Poisson statistics. Convoluting this with the PDF and summing over all observed events gives the likelihood function

---

[1] Atmospheric neutrinos follow an $E^{-3.7}$ power law, while in the region of highest sensitivity (TeV-PeV) signal neutrinos from all phases of the emission follow power laws between E^{-1} and E^{-3}.

$$\begin{aligned}
\mathcal{L} &= e^{-n_t}\frac{n_t^N}{N!} \times \prod_{i=1}^{N} P(\mathbf{x}_i|\mathbf{a}) \\
\ln(\mathcal{L}) &= -n_t + N\ln n_t - \ln N! + \sum_{i=1}^{N} \ln\left(P(\mathbf{x}_i|\mathbf{a})\right) \\
&= -n_t - \ln N! + \sum_{i=1}^{N} \ln\left(n_t P(\mathbf{x}_i|\mathbf{a})\right) \\
&= -n_t + \sum_{i=1}^{N} \ln\left(Q(\mathbf{x}_i|\mathbf{a})\right) \qquad (8.4)
\end{aligned}$$

where we note that $N!$ is just an offset that is independent of the relative contributions of signal and background and can thus be removed. Recall that $Q(\mathbf{x}_i|\mathbf{a})$ is the likelihood of observing the set of parameters $\mathbf{x}_i$ given some hypothesis $\mathbf{a}$ for a single event i. We rewrite this in terms of the reconstructed direction, time, and energy estimate of each event i in our final event sample, $(\vec{x}_i, t_i, \epsilon_i)$, the known mean background measured from off-time data, n_b, and a hypothetical signal contribution, n_s:

$$\ln(\mathcal{L}) = -n_s - n_b + \sum_{i=1}^{N} \ln\left(n_s\, \mathcal{S}^{tot}(\vec{x}_i, t_i, \epsilon_i) + n_b\, \mathcal{B}(\vec{x}_i, t_i, \epsilon_i)\right) \qquad (8.5)$$

In the case of no signal contribution, the likelihood is instead given by

$$\ln(\mathcal{L}_0) = -n_b + \sum_{i=1}^{N} \ln\left(n_b\, \mathcal{B}(\vec{x}_i, t_i, \epsilon_i)\right) \qquad (8.6)$$

By taking the ratio between the likelihood that a data set contains signal, $\mathcal{L}$, and the likelihood that it is composed entirely of background, $\mathcal{L}_0$, we form a test statistic $\ln(\mathcal{R})$.

$$\ln(\mathcal{R}) = \ln\left(\frac{\mathcal{L}}{\mathcal{L}_0}\right) = -n_s + \sum_{i=1}^{N} \ln\left(\frac{n_s\, \mathcal{S}^{tot}(\vec{x}_i, t_i, \epsilon_i)}{n_b\, \mathcal{B}(\vec{x}_i, t_i, \epsilon_i)} + 1\right) \qquad (8.7)$$

We then maximize $\ln(\mathcal{R})$ by varying the mean signal contribution n_s. The maximum likelihood $\ln(\mathcal{R}(\hat{n}_s))$ then tells us the most probable number of signal events $\hat{n}_s$ in our data set.

In Eq. 8.7, $\mathcal{S}^{tot}(\vec{x}_i, t_i, \epsilon_i)$ represents a weighted sum of the signal PDFs for each of the 41 bursts in our sample. Similar strategies have been successfully employed in the past [112]. We expand it as

$$\mathcal{S}^{tot}(\vec{x}_i, t_i, \epsilon_i) = \frac{\sum_j w_j \mathcal{S}_j(\vec{x}_i, t_i, \epsilon_i)}{\sum_j w_j}. \tag{8.8}$$

Here $\mathcal{S}_j(\vec{x}_i, t_i, \epsilon_i)$ is the signal PDF for the jth GRB and w_j is a weight that corresponds to how much we think a particular burst will contribute to the total signal. For the precursor and prompt phase searches, w_j is proportional to the calculated neutrino fluence for each burst, as well as the zenith dependent detector response. For the extended window search we set $w_j = 1$ for all bursts to maintain generality.

All that remains is to define our PDFs, $\mathcal{S}_j(\vec{x}_i, t_i, \epsilon_i)$ and $\mathcal{B}(\vec{x}_i, t_i, \epsilon_i)$. Each is composed of spatial, temporal and energy dependent terms.

$$\mathcal{S}_j(\vec{x}_i, t_i, \epsilon_i) = \mathcal{S}_j^{\mathrm{S}}(\vec{x}_i) \times \mathcal{S}_j^{\mathrm{T}}(t_i) \times \mathcal{S}_j^{\mathrm{E}}(\epsilon_i) \tag{8.9}$$

$$\mathcal{B}(\vec{x}_i, t_i, \epsilon_i) = \mathcal{B}^{\mathrm{S}}(\vec{x}_i) \times \mathcal{B}^{\mathrm{T}}(t_i) \times \mathcal{B}^{\mathrm{E}}(\epsilon_i) \tag{8.10}$$

We investigate the form of each of these partial probability distributions.

$\mathcal{S}_j^{\mathrm{S}}(\vec{x}_i)$ represents the probability that an observed event i with reconstructed direction $\vec{x}_i$ was produced at a true source location $\vec{x}_j$ associated with the GRB j. In order to quantify this, we make use of the event by event reconstruction error σ to describe the distribution as a Gaussian

$$\mathcal{S}_j^{\mathrm{S}}(\vec{x}_i) = \frac{1}{2\pi\sigma^2} \exp\left(-\frac{|\vec{x}_i - \vec{x}_j|^2}{2\sigma^2}\right) \tag{8.11}$$

Recall, however, that we utilize a 2-dimensional error estimate of the track reconstruction. To incorporate this into the general spatial PDF given by Eq. 8.11, we rotate each event into the coordinate system centered on the error ellipse and oriented along its axes. The location of the GRB j relative to the event i is then given simply by distance along these axes (x_1, x_2) and we rewrite $\mathcal{S}_j^{\mathrm{S}}(\vec{x}_i)$ as

$$\mathcal{S}_j^{\mathrm{S}}(\vec{x}_i) = \frac{1}{2\pi\sigma_1^2\sigma_2^2}\ \exp\left(-\frac{x_1^2}{2\sigma_1^2} - \frac{x_2^2}{2\sigma_2^2}\right) \tag{8.12}$$

A sample distribution is shown in Fig. 8.9.

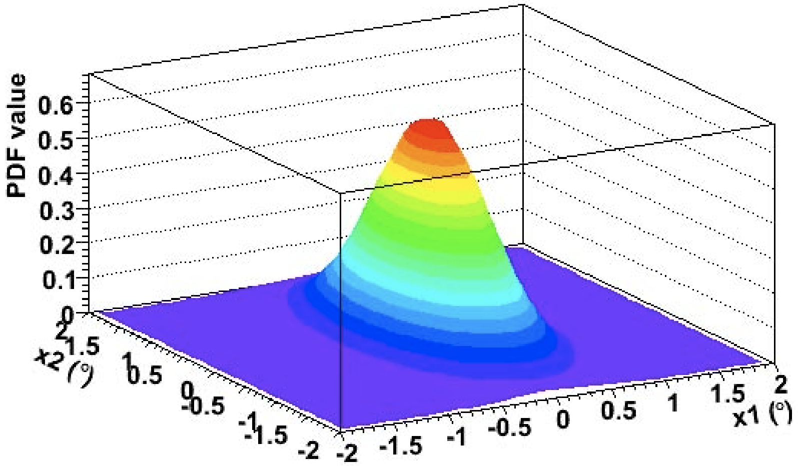

Figure 8.9: Spatial probability density function rotated to the coordinate system of the 2-dimensional track reconstruction error ellipse.

The spatial PDF of the background, $\mathcal{B}^{\mathrm{S}}(\vec{x}_i)$, must incorporate the known asymmetry of the IceCube detector. We create a probability map in the detector coordinate system from all remaining events in our off-time data sample, shown in Fig. 8.10. We perform a Gaussian smearing between bins to remove discontinuities in the probability space.

The temporal signal PDF represented by $\mathcal{S}_j^{\mathrm{T}}(t_i)$ is assumed to be flat over the on-time window of each burst. For the prompt phase search this is given by the range $\{T_1, T_2\}$ defined for each GRB in Table 5.6. For the precursor search the range is given by $\{-100\,s, 0\,s\}$ relative to the satellite trigger for all bursts, and in the extended window, we search the range $\{-1\,h, +3\,h\}$. The likelihood falls off smoothly in a Gaussian on either side to avoid discontinuities and allow for small shifts in the neutrino emission. The width of this Gaussian is set to be equal to the search window with a minimum of 2 s and a maximum of 25 s. Variable widths were chosen to allow some padding around bursts while ensuring that the tails do not dominate the PDF. We show an example of such a temporal PDF in Fig. 8.11. For the background, $\mathcal{B}^{\mathrm{T}}(t_i)$ is assumed to be flat, corresponding to a constant

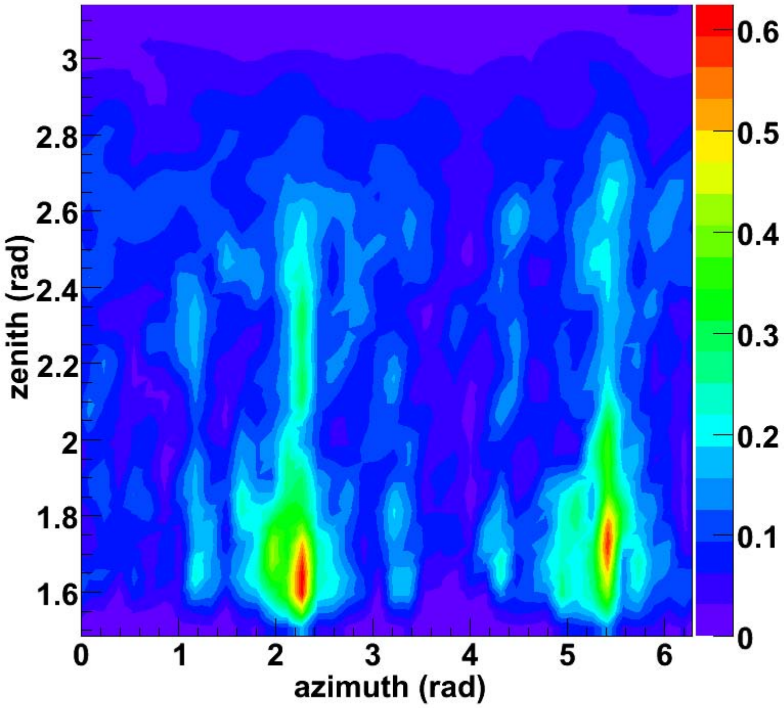

Figure 8.10: Probability map of off-time data for the 22-string IceCube detector. Events are at neutrino level and are shown in the detector coordinate system. The 22-string configuration is highly asymmetric, resulting in higher data rates in the direction of the long axis.

average rate over the year. We discuss the systematic error associated with seasonal variations in the the background rate in Chapter 9.

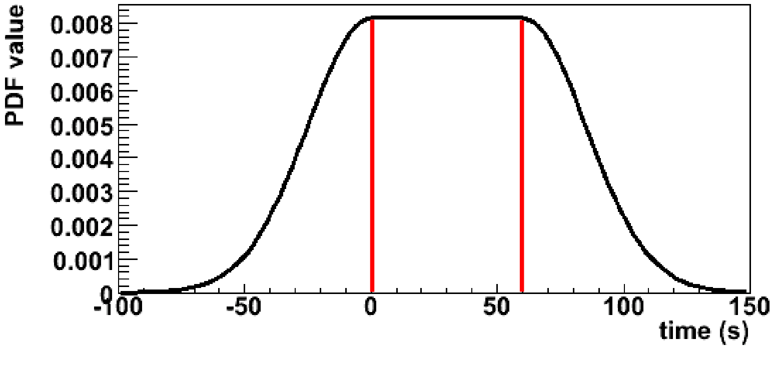

Figure 8.11: Temporal probability density function for a sample GRB of duration 60 s. x-axis is in units of time with respect to the burst trigger. Note that in this example we have not enforced the restriction on the maximum width of the Gaussian tails of 25 s.

$\mathcal{S}_j^{\mathrm{E}}(\epsilon_i)$ and $\mathcal{B}^{\mathrm{E}}(\epsilon_i)$ incorporate the information we know about the energy of the event, where ϵ_i represents an estimator of that energy. We determine the probability that the event comes from an energy distribution given by the signal spectrum under consideration, $P(\epsilon_i|\phi_{sig})$. As energy estimator, we take the reconstruction given by the MUE algorithm of section 3.6.7.2. This estimator shows clear separation between signal spectra and background. The PDFs for several input spectra are shown in Fig. 8.12. Studies were conducted as part of this work that showed minimal differences in final sensitivity between using the calculated prompt spectra from each GRB and simply assuming an E^{-2} spectrum for all GRBs. We therefore employ the more generic method [2]. This has the added benefit of increasing our chances of discovery if the true spectra turn out to be softer than the prediction. We use the precursor GRB neutrino spectrum for that search. While in principle we could use the distribution of data for the background PDF, in practice the low statistics at final cut level lead us to estimate the distribution with a simulation weighted to the Barr et al. [101] atmospheric neutrino flux. We note from Fig. 8.5 the excellent agreement between data and simulation in this parameter. Because the detector response to a given energy is highly dependent on zenith angle, we use a different PDF for each GRB location in our 41 burst sample.

---

[2] Note, however, that we utilize the calculated spectra for each burst to determine the expected event rate and thus the weighting for that burst in the likelihood function.

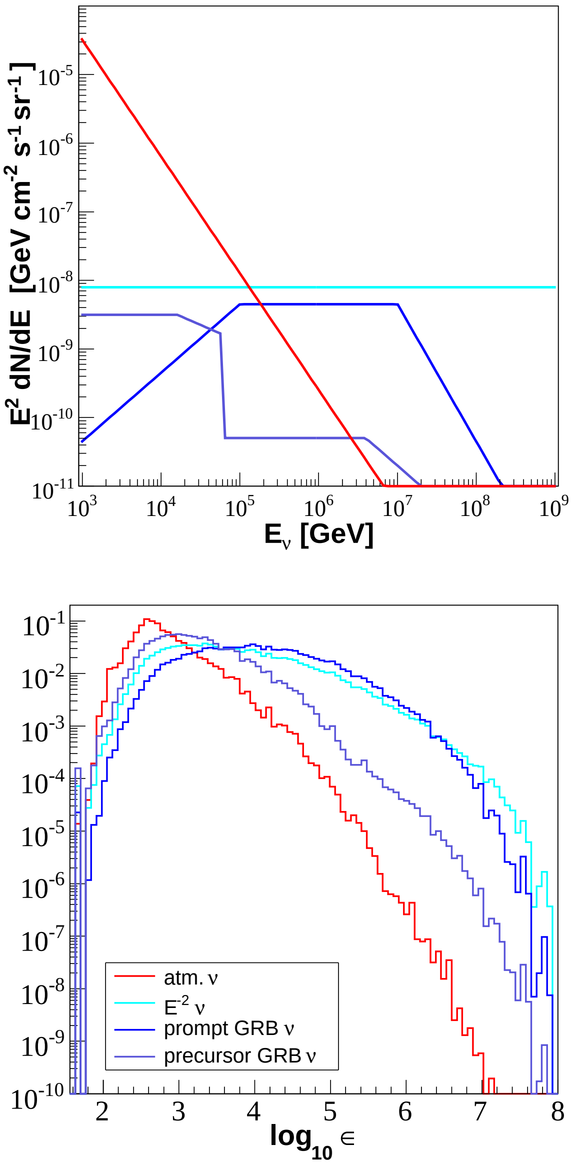

Figure 8.12: Probability distributions for several neutrino energy spectra. True signal neutrino spectra are shown for reference. Note the clear separation between signal and the background atmospheric neutrinos. Prompt signal shown is for the canonical Waxman Bahcall spectrum. Detector response is averaged over the full sky. ϵ is uncalibrated and thus does not correspond to a specific energy.

8.5 Sensitivity and Discovery Potential

The best estimate of the signal contribution in our data set $\hat{n}_s$ gives us a maximum value of the test statistic $\ln(\mathcal{R}(\hat{n}_s))$ for that data set. In order to assess the significance of our observation, we must determine the probability of obtaining a value of $\ln(\mathcal{R}(\hat{n}_s))$ equal to or greater than we see. This is accomplished by determining the value of $\ln(\mathcal{R}(\hat{n}_s))$ for a large sample of background only data sets. We implement this by performing 10^8 randomizations of our final off-time data sample, taking into account the up-time of the detector [3]. For each randomized skymap, we compute the value of $\ln(\mathcal{R}(\hat{n}_s))$. This forms a distribution, shown in Fig. 8.13. When we perform our observation on the actual data, we compare $\ln(\mathcal{R}(\hat{n}_s))$ to this distribution and determine what fraction of background only datasets have the same or greater value. This represents the p-value of the analysis.

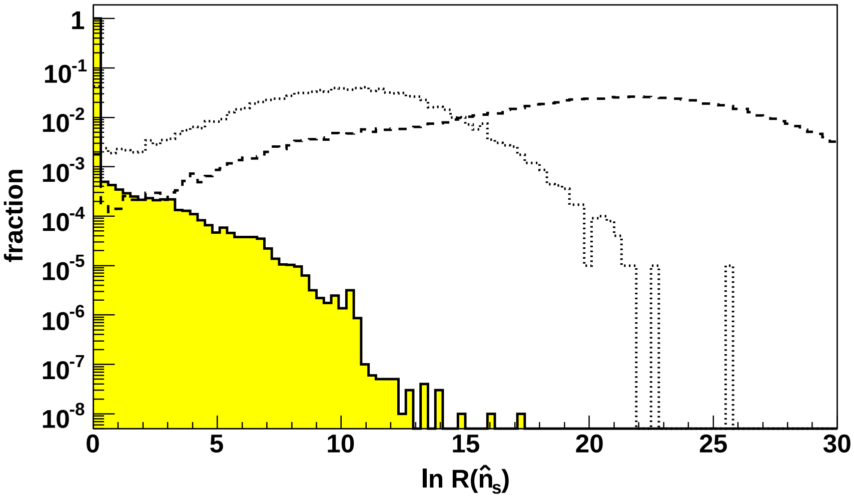

Figure 8.13: Distribution of the test statistic $\ln(\mathcal{R}(\hat{n}_s))$ for the prompt phase search. 10^8 randomized background only datasets are shown in yellow (solid line). Distributions for one and two injected signal events are shown with dotted and dashed lines, respectively.

We calculate the probability of observing a certain significance (discovery potential), in the following way. We choose a significance level, and determine the value of $\ln(\mathcal{R}(\hat{n}_s))$ above which

---

[3] The events are randomized in time. After coordinate transformation, this is identical to randomization in Right Ascension.

the appropriate fraction of data sets exist. For example, if we choose 5σ significance, we must find the value of $\ln(\mathcal{R}(\hat{n}_s))$ where only $10^8 \cdot 5.73 \times 10^{-7} = 57$ data sets have a higher value. We then choose a statistical power P and determine the mean number of signal events needed such that a fraction P of data sets containing the injected signal pass this $\ln(\mathcal{R}(\hat{n}_s))$ threshold. In principle, this means we must generate the full $\ln(\mathcal{R}(\hat{n}_s))$ distribution for each infinitesimal increase in n_s. Such a procedure is computational prohibitive, however, so instead we inject only discrete signal events ($N = 0, 1, 2, ...$), distributed among the GRBs according to their relative weights w_j. We then form a set of $\ln(\mathcal{R}(\hat{n}_s))$ distributions, one for each integer amount of injected signal. The statistical power of a mean signal fluence n_s is then given by weighting the power of each discrete distribution by the Poisson probabilities $P(N|n_s)$ and summing them. We can then rapidly search the space of n_s to find the mean signal strength that gives us the desired power P. Recall that the Model Discovery Factor (MDF) is the multiple of the predicted flux that must exist for us to make the observation. Given the above, it is then found by dividing the necessary number of mean signal events by the number of events expected given our model prediction. We show the distribution of MDF versus statistical power for various discovery significances in Fig. 8.14, comparing to a binned search that was conducted on the same data. At the 5σ with 50% power, the unbinned method we have implemented shows a factor 1.8 improvement over the binned search.

The 90% C.L. sensitivity of the analysis is given by the mean signal strength for which 90% of data sets containing that amount of signal have an equal or higher value of $\ln(\mathcal{R}(\hat{n}_s))$ than the mean of a large number of background only data sets. For the distribution of Fig. 8.13, the mean is at 0, and hence we quote this case. In the event of a non-detection, the actual event upper limit will depend on the value of $\ln(\mathcal{R}(\hat{n}_s))$ measured in the unblinded skymap. We summarize the sensitivity and discovery potential for our three searches in Table 8.7.

8.5.1 Trials Factors

Since we conduct both the unbinned search outlined above and a complementary binned search [93] on the same data set, there is an issue of trials factors. For a diffuse or point source search with two analyses, where ~ 10 signal events would be needed for a discovery, one would typically choose the more sensitive analysis *a priori* and use the second analysis as a check. This is what

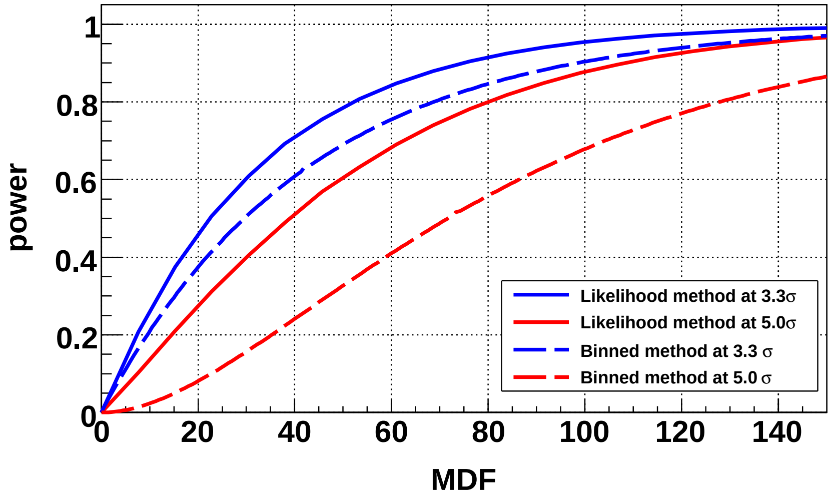

Figure 8.14: Discovery potential for the 2007-2008 IceCube prompt phase GRB Search. We compare the unbinned likelihood search (solid) with a binned search on the same data (dashed). Shown is the fraction of data sets with at least the desired significance (power) as a function of the the factor of the predicted flux required to make the observation (MDF). Similar distributions exist for the precursor and extended searches, though no binned analysis was performed for these time windows.

	Sensitivity (90% C.L.)	Discovery Potential (50% Power)		
	factor	C.L.	factor	evts
prompt	73	3.3σ	23	0.74
		5σ	39	1.3
precursor	9.7	3.3σ	3.4	0.9
		5σ	8.0	2.1
extended	–	5σ	–	3.6

Table 8.7: Sensitivity and discovery potential for the prompt, precursor, and extended window unbinned likelihood GRB searches. Columns: factor – multiple of the predicted fluence, evts – mean signal events necessary to make the detection. The normalization of the E^{-2} flux used in the extended search is arbitrary and we therefore quote event rates.

was done in the case of 22-string IceCube point source searches, for example. However, in the GRB search, where only 2 events are needed for a 5σ discovery, it is entirely possible that one of these critical events could reside in the less sensitive data set [4]. In light of this fact, we need to be able to

---

[4] This is a result of using the a point source optimized event selection for the unbinned search, and a GRB specific SVM optimized selection for the binned analysis. If we were using the same data set for both analyses, we would just pick the more sensitive one.

quote a significance for an observation in either of the 2 analyses. We outline the procedure below.

In each analysis there is a p-value distribution for the case of the null hypothesis. For the binned analysis, the p-values are discrete, corresponding to $0, 1, 2, ...n$ events on time, on source in a randomized skymap. In the unbinned analysis, the distribution is a continuum, corresponding to the distribution of the likelihood test statistic for zero injected signal and randomized background. In order to calculate the significance of the combined analysis, we want to know how often one analysis is more sensitive than the other. We do many (20 million) randomizations of the background only skymaps for each analysis in a synchronized way. (Each event is randomized in time according to its event number, run number, and a seed number that is common to both analyses). We then take the smallest of the two p-values that result and form a new p-value distribution. When we perform the actual analysis we will once again take the maximum resultant p-value and compare it to this combined distribution to obtain the final significance. We need only apply this procedure in the event of a positive detection. Otherwise, we will set an upper limit based on the more sensitive of the analyses.

8.6 Results

Unblinding consists of applying the likelihood analysis to the unscrambled dataset, determining the value of the test statistic, and calculating the resultant p-value. The procedure is identical for each of our searches; we just change the PDFs in the likelihood function to match the signal prediction. For all emission scenarios considered (prompt, precursor, extended), the value of the $\ln(\mathcal{R}(\hat{n}_s))$ and of $\hat{n}_s$ are zero and thus consistent with the background only hypothesis. We therefore calculate the 90% C.L. upper limit on the neutrino fluence from the 41 GRBs in our sample in the prompt phase of $3.7 \times 10^{-3}\,\mathrm{erg\,cm^{-2}}$ (72 TeV – 6.5 PeV) and in the precursor phase of $2.3 \times 10^{-3}\,\mathrm{erg\,cm^{-2}}$ (2.2 TeV – 55 TeV). The energy ranges given correspond to the 90% containment region for predicted signal events. In neither case is the limit strong enough to constrain the model. For the extended search, we place a limit of $2.7 \times 10^{-3}\,\mathrm{erg\,cm^{-2}}$ (3 TeV – 2.8 PeV) on an E^{-2} flux. These results are summarized in the context of the predictions in Table 8.8 and limits for the prompt and precursor searches are shown in Fig. 8.15. We discuss the impact of systematic errors on our upper limits in Chapter 9.

	n_{exp}	n_{limit}	factor
prompt	0.033	2.4	72
precursor	0.26	2.5	9.7
extended	–	2.7	–

Table 8.8: Upper limits for three searches performed on 22-String IceCube data taken in 2007-2008. Columns: n_{exp} – number of expected events from 41 GRBs at final cut level, n_{limit} – 90% C.L. event upper limit, factor – multiple by which the upper limit exceeds the model prediction.

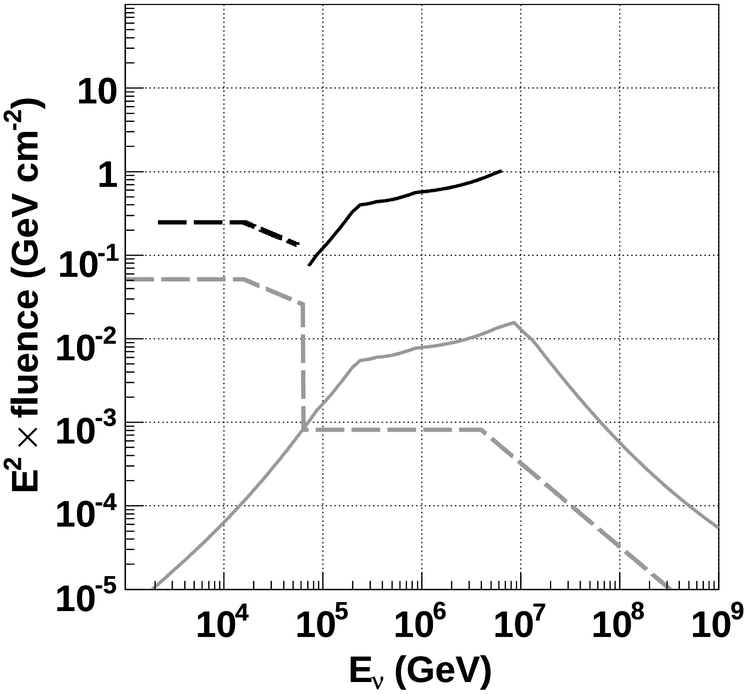

Figure 8.15: 90% C.L. upper limits (black) on the neutrino fluence from 41 northern hemisphere GRBS observed in 2007-2008. Shown are the precursor (dashed) and prompt (solid) phase results with model predictions (grey) for comparison.

Chapter 9

Systematic Error Analysis

We use off-time all sky data from the entire livetime to estimate the background in the search window surrounding each gamma-ray burst. This gives us a precision determination of our background that is largely free from systematic errors that would arise from the use of simulation. However, this method makes the assumption that the data rate is constant in time. In addition, we make use of Monte Carlo simulation for signal prediction and limit setting. We thus consider the various sources of systematic error introduced and the effect on our calculated limits. These errors are typically nonlinear and dependent on the spectrum under consideration. We therefore vary each parameter in the simulation and re-perform the analysis in order to determine the final effect. The results of these studies are summarized in Table 9.1 and Table 9.2 for the AMANDA and IceCube analyses, respectively. We describe the sources of systematic error in detail below.

Error	prompt (WB)
neutrino cross section	±3%
muon propagation	±2%
reconstruction bias	+5%
ice simulation	±5%
timing resolution	±2%
DOM efficiency	+6%
background rate	$< 1\%$
sum	$^{+10}_{-7}\%$

Table 9.1: Effect of systematic errors on upper limits in the 2005-2006 AMANDA-II GRB Search. Each burst is assumed to follow a Waxman-Bahcall energy spectrum.

Error	prompt	precursor	extended
neutrino cross section	±3%	±3%	±3%
muon propagation	±3%	±3%	±3%
reconstruction bias	+5%	+5%	+5%
ice simulation	±10%	±10%	±10%
timing resolution	±2%	±2%	±2%
DOM efficiency	±5%	±10%	±7%
background rate	$< 1\%$	$< 1\%$	$< 1\%$
sum	$^{+13}_{-12}\%$	$^{+16}_{-15}\%$	$^{+14}_{-13}\%$

Table 9.2: Effect of systematic errors on upper limits in the 2007-2008 IceCube GRB Search. For the prompt search, each GRB has an individually modeled fluence. For the precursor search all bursts follow the Razzaque et al. model [50] which is well approximated by an E^{-2} spectrum below 10 TeV. For the extended search, we use an E^{-2} spectrum.

9.1 Sources of Systematic Error

9.1.1 Neutrino Cross-Section

Uncertainty on the neutrino cross section will create a change in the normalization of the expected signal fluence. We estimate this uncertainty from the errors in the Parton Distribution Functions used in the neutrino generation simulation. For AMANDA, a 3% error in the charged current deep-inelastic neutrino-nucleon cross-section is estimated. For IceCube, the CTEQ5 structure functions are implemented and an error of 2% is estimated from the errors given on the CTEQ6 PDFS in the energy range 100 TeV to 1 PeV [113]. The differences in cross-section between CTEQ5 and CTEQ6 are only present above $10^{8.5}$ GeV and are thus beyond the range of our analyses.

9.1.2 Muon Propagation / Earth Model

The cross-sections for muon energy loss mechanisms at the energies of interest to GRB analyses are known to within a few percent [114]. We adopt the estimate of [115] in a 1% effect on the neutrino event rate, independent of muon energy. The event rate is also affected by the density of the bedrock input into the propagation simulation. Applyng a 10% variation in the rock density [115] yields a 2% variation in event rate in the AMANDA detector for a hard spectrum at angles near the horizon where most events lie. An independent study for the deep sea ANTARES detector shows a comparable 3%

variation in event rates [116].

9.1.3 Reconstruction Bias

In both the AMANDA and IceCube analyses we utilize as an error estimate on the track direction a fit of a paraboloid to the likelihood space. These error estimates are systematically lower by about 8% for simulation compared to data, indicating that we may be reconstructing simulated events better than real events. To account for this we increase the point spread function and repeat our analyses. This results in a ~5% worsening of our limits for all searches.

9.1.4 Ice Properties

The largest source of uncertainty is our understanding and modeling of the detector medium. While extremely clear, the ice of the south pole contains many layers of dust (see Section 3.5). These layers result in depth dependent variations in the scattering and absorption coefficients of the ice that must be modeled correctly if we are to reproduce the structures seen in data. Even if the properties of the ice are perfectly understood, if we do not propagate the photons from the track to the PMTs correctly (using PHOTONICS), errors will be introduced. Because changes in the ice and propagation affect light detection on the most basic level, resulting in perhaps completely different event reconstructions, we must generate new Monte Carlo to study the effect. For the AMANDA analysis, we adopt the 5% error result of [115].

For the IceCube analysis, we consider the worst imaginable case; that the ice is twice as clear or dirty as we believe it to be. We thus stretch the nominal AHA ice model by a factor of two around the average values (see Fig. 9.1). This results in a 40% reduction in the efficiency for GRB neutrinos. However, as seen in Fig. 9.2(a), the effect on the structure is negligible. Only an overall reduction in rate is observed. We thus adopt a new approach. The efficiency of each DOM is scaled as a function of depth to match the differences between observed data and simulation. In order to be conservative, we double this scaling, shown in Fig. 9.2(b). We then perform the likelihood analyses on the rescaled simulation to determine the effect on our upper limits. We note that the DOM efficiency is not the actual cause of the systematic differences, but is merely used to simulate the effect of our lack of understanding of the ice and photon propagation.

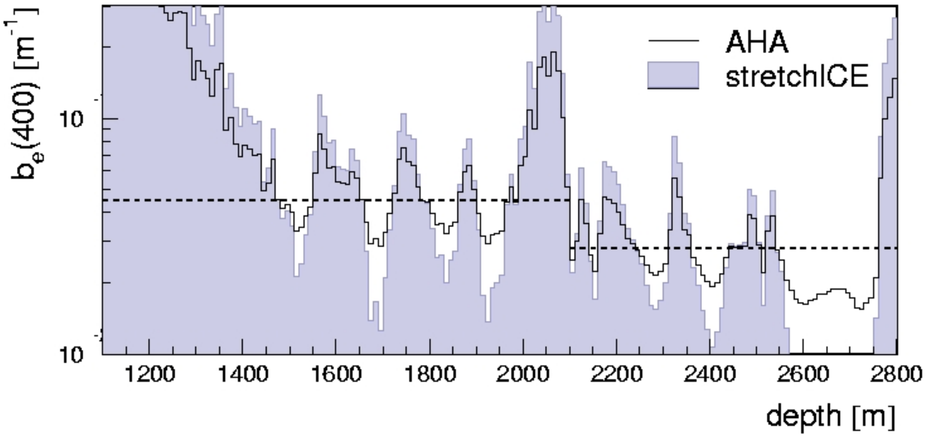

Figure 9.1: Scattering coefficient at 400 nm for the stretched ice model compared to the default AHA model. Deviations from average were stretched by 100% around the mean. (courtesy Kurt Woschnagg)

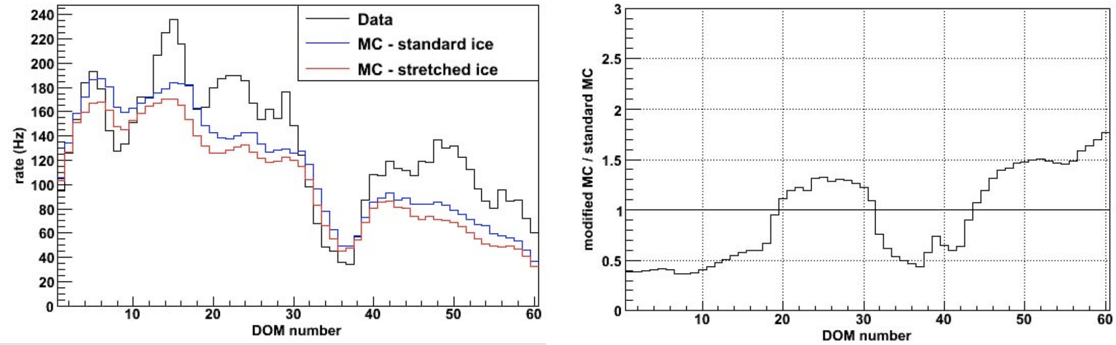

(a)

(b)

Figure 9.2: Panel (a) depicts the lack of effect on structure due to stretching the AHA ice model by 100%. Only an overall reduction in rate is visible. Panel (b) shows the depth dependent scaling of DOM efficiency relative to the AHA ice model used to account for uncertainties in the ice and photon propagation. Increasing DOM number on a string corresponds to increasing depth below the antarctic surface. (courtesy Alexander Kappes)

9.1.5 Timing Resolution

The timing of the Optical Modules in AMANDA is known to better than 5 ns, measured with YAG laser pulses. IceCube's DOMs are internally calibrated to a precision of better than 2 ns. This results in an overall impact on the final event rates of less than 2%, adopted from [115].

9.1.6 (D)OM Efficiency

The efficiency of the Optical Modules (or DOMs for IceCube) depends on the PMT quantum efficiency, glass and gel transmission, and the re-frozen hole ice surrounding the strings. Studies with atmospheric neutrinos in the AMANDA detector have constrained the uncertainty in OM efficiency to $+10\%/-7\%$ around a nominal value of 85% [117]. Measurements of IceCube DOMs in a controlled setting at Chiba University set DOM uncertainty at 8%. We apply a conservative variation of 10%. Because the effect of changing the (D)OM efficiency is both nonlinear and spectrally dependent we generate simulation with the extreme values and determine the resulting changes in final event rates.

9.1.7 Seasonal Background Variations

The background in our analyses is estimated from a measurement of the off-time all sky data in the full livetime. While this provides a precise determination of the rate, it tends to smear out any variation that could occur on a per burst basis. In fact, the downgoing muon rate is highly seasonally dependent, varying based on the temperature of the atmosphere. A cold, thin atmosphere decreases interaction rates while a warm, thick atmosphere increases the rate of background muons. This is shown for the full 22-string IceCube livetime in Fig. 9.3. After final event selection, mostly atmospheric neutrinos remain and the variation is of only a few percent. To be conservative we allow the rate to vary by up to 10% [1]. Due to the extremely high background rejection in our analyses, this results in a $< 1\%$ change in the upper limits.

---

[1] Another reason we allow for a large variation is to take into account detector asymmetries in the AMANDA analysis. For the IceCube analysis, asymmetries are incorporated into the background PDF in the likelihood function.

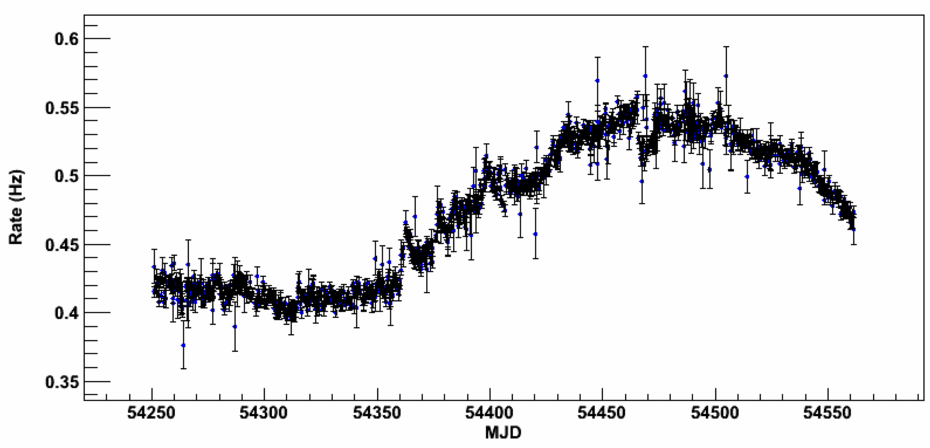

Figure 9.3: Seasonal variation in data rate for the full 22-string IceCube livetime at upgoing muon filter level

Chapter 10

Conclusions

10.1 Summary

We have performed searches for muon neutrinos from gamma-ray bursts using both the AMANDA-II and IceCube neutrino telescopes. The 2005-2006 AMANDA analysis searched for prompt phase emission from 85 northern sky GRBs. This analysis utilized a binned method, optimized for discovery potential. No events were observed in the on-time window at final cut level, allowing us to set an upper limit on muon neutrino emission from these 85 bursts. The 90% C.L. upper limit on the diffuse flux is a factor 14.7 times higher than the model prediction of Waxman-Bahcall. 90% of simulated signal events are containing in the energy region 21.0 TeV to 4.9 PeV. The normalization of E^2 times this flux limit is $6.6 \times 10^{-8}\,\mathrm{GeV\,s^{-1}\,cm^{-2}\,sr^{-1}}$ at 100 TeV.

The 22-string IceCube analysis searched for prompt and precursor phase emission from 41 northern sky GRBs observed in 2007-2008. In addition, a generic search for high energy emission from GRBs was performed over a wide time window. For the first time in stacked GRB searches, an unbinned maximum likelihood technique was used. In all cases examined the on-time data were consistent with the background only hypothesis. We therefore set limits on the muon neutrino fluence for each search. For the prompt phase, the 90% C.L. upper limit is a factor 72 times higher than the predicted neutrino fluence summed over all bursts in the sample. The 90% energy containment region is 72 TeV to 6.5 PeV. The integral fluence limit over this range is $3.7 \times 10^{-3}\,\mathrm{erg\,cm^{-2}}$. For the precursor phase, the 90% C.L. upper limit is a factor 9.7 times higher than the predicted neutrino fluence of Razzaque et al.. The 90% energy containment region is 2.2 TeV to 55 TeV. The integral fluence limit over this range is $2.3 \times 10^{-3}\,\mathrm{erg\,cm^{-2}}$. The 90% energy containment region for the extended search is 3 TeV to 2.8 PeV, yielding a 90% C.L. upper limit on the integrated fluence of $2.7 \times 10^{-3}\,\mathrm{erg\,cm^{-2}}$. In none of our searches is the limit strong enough to constrain the models.

10.2 Discussion

10.2.1 Previous Results

We compare our results with previous work, focusing on the muon neutrino channel. AMANDA has performed searches for emission of neutrinos during the prompt and precursor phases for a large sample of GRBs observed between 1997 and 2003 [8, 118]. These searches utilized binned methods and in all cases, no events survived in the final on-time sample. In the search for prompt phase emission, an average Waxman-Bahcall flux was assumed for each of 419 GRBs. For the precursor search, a subset of 60 GRBs from 2001-2003 were analyzed. The event predictions and upper limits of these experiments are summarized in Table 10.1. We see that in the case of the prompt phase search, a downward fluctuation in the background allowed that analysis to set an upper limit significantly better than the sensitivity.

	N_{Bursts}	n_b	n_s	n_{obs}	event upper limit	factor
1997-2003 prompt	419	1.74	0.78	0	1.1	1.3
2005-2006 prompt	85	0.00087	0.166	0	2.4	14.7
2007-2008 prompt	41	–	0.033	–	2.4	72
2001-2003 precursor	60	0.20	0.16	0	2.3	14
2007-2008 precursor	41	–	0.26	–	2.5	9.7

Table 10.1: Results of previous and current searches for muon neutrinos from GRBs with both AMANDA-II and IceCube. Columns: n_b – mean background expected, n_s – mean signal expected, factor – multiple of the predicted fluence excluded at 90% C.L. [8, 118].

We also note that the achievable limit for a stacked GRB search is directly proportional to the number of bursts analyzed. For this reason, it was known *a priori* that the 2005-2006 AMANDA analysis on 85 GRBs would not be competitive in terms of limit setting. This was partial motivation for the decision to focus on the detectability of a signal in that analysis.

For a pair of binned analyses it is straightforward to combine results. One simply combines the expected background in order to calculate a new event upper limit and then divides to the combined mean signal expectation to determine the corresponding flux factor. If we apply this method to the 97-03 and 05-06 analyses, we find that the limit improves from a factor 1.3 above the prediction to 1.2. This reinforces the point that given the same detector, we require large additional data sets to significantly improve our limits. We should note as well that the GRBs in the 05-06 analysis tend to be fainter than the bursts used in the 97-03 analysis, and thus combining results assuming that they come from the same population (and hence model) is not entirely correct. However, because the potential gains are so small, we do not undertake a detailed examination of this effect here.

A more interesting question would be whether we can combine the AMANDA limits with those set by our 22-string IceCube analysis, as the effective area for the latter is so much larger. In Fig. 10.1, we compare the prompt and precursor IceCube results with those of the published AMANDA work, converting the diffuse flux limits to per burst fluences and scaling to the 41 burst dataset of 2007-2008. We see that in the case of the prompt search, with a factor 10 fewer bursts in our sample, we are only a factor ~ 3 worse in limit setting ability. For the precursor search, we do substantially better, giving the strongest limits to date on such emission from GRBs.

While it is attractive to combine these results, it is not practical to do so. The reason is that one search is binned while the other is not. We presented above the straightforward method for the combination of limits for a pair of binned searches, namely the calculation of a combined event upper limit based on the summed background expectation and observed events in each analysis. However, for an unbinned search, there is no such "background expectation". Rather, we have a large (~ 5000) sample of neutrino candidates for which we evaluate the likelihood that each belongs to the signal or background distribution. The event upper limit comes not from a background number prediction, but rather from the distribution of the test statistic of the unblinded data (see section 8.5). Thus, in order to produce a combined result, one would have to reanalyze the AMANDA data with an unbinned search and determine the p-value of the combined unblinded data. Such an analysis is beyond the scope of this work.

As a final question, we ask whether the downward fluctuation of the earlier analysis impacts the significance of a future discovery. That is, as we observed 0 events on a predicted background

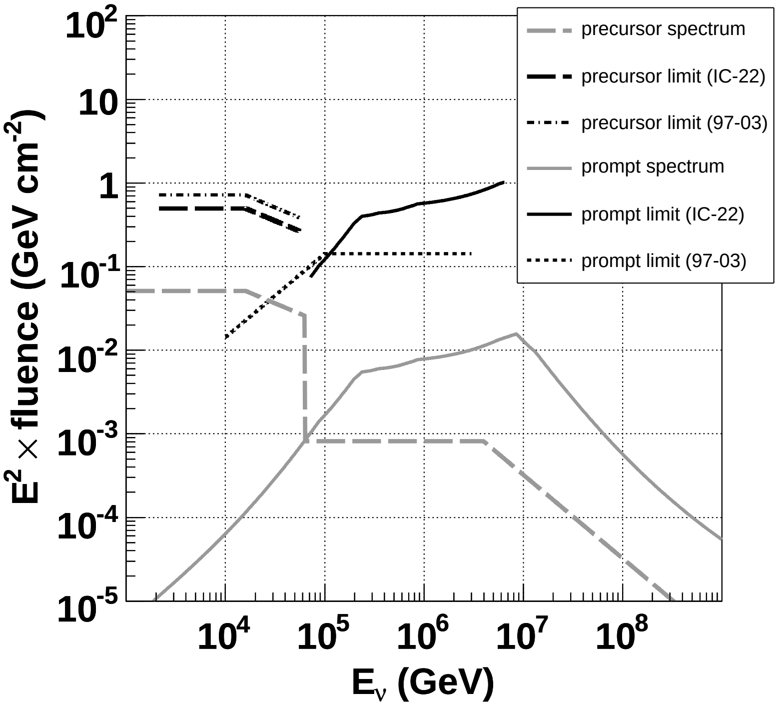

Figure 10.1: Comparison of 22-string IceCube results with previous AMANDA limits. Dark solid and dashed lines indicate the 22-string limits with light lines showing the prediction from 41 bursts. Dark dotted and dot-dashed lines show the fluence limits derived from the AMANDA diffuse GRB flux limits of [8, 118].

of ~2, are we “due an event”? To answer this we consider two approaches. First, we compare the analysis techniques to determine whether it is reasonable to penalize future work in this way. We then look at the problem from a different direction, disregarding such arguments and instead performing a conservative calculation of the combined significance of a set of GRB analyses, including some with null result.

There are several reasons we might argue that previous work should not penalize future discoveries. Previous analyses were optimized to maximize the limit setting potential (section 7.6), while current and future searches maximize the potential for making a significant discovery. Because of this, higher background rates were tolerated when choosing event selections, leading to the possibility for a downward fluctuation as was observed. The improved angular resolution of IceCube relative to AMANDA as well as updated event selection strategies have resulted in near-zero backgrounds in the latest searches. Furthermore, GRBs are individual events. It is well known that the most likely scenario for a positive detection in neutrinos is a bright, nearby burst. It is therefore not surprising that we observe a large sample of bursts with no neutrinos before making a discovery. In fact, we expect this. Even in the case where the summed contribution from many bursts is in excess of one event, this simply means that we have more chances for that single, rare, upward fluctuation. What we should focus on is increasing the signal expectation with the fewest number of bursts in the sample, rather than analyzing large samples of bursts. In this way, each GRB need fluctuate less to contribute a detectable signal event.

Let us now disregard the above considerations and proceed from a purely statistical standpoint. To determine a combined significance for an ensemble of experiments, we would like to be able to combine the likelihood that each observation was *not* due to the background only hypothesis. If one makes an observation in excess of the expected background, this is straightforward. In our case, the probability of observing n_{obs} on an expected background of n_b is given by the Poisson probability $P(n_{obs}|n_b)$. However, a downward fluctuation represents an unexpected case. For example, the 97-03 prompt GRB search has $P(0, 1.74) = 0.176$. However, this certainly does not mean that the null hypothesis is rejected at 82.4% C.L.. Rather, it just tells us that the chance of this particular downward fluctuation from the prediction is 17.6% [1]. It is difficult to incorporate such a probability into a combined significance. We therefore consider a slightly modified question. We define the p-value for each analysis as the probability that *the same or a more extreme observation would be made in repeated experiments.* Thus, an observation of 0 will always correspond to a p-value of 1 (all experiments will observe at least 0 events), while observations of more events will have p-values depending on the background expectation. In this case for a given observation n_{obs} and background expectation n_b, we have

$$p(n_{obs}, n_b) = 1 - \sum_{i=0}^{n_{obs}-1} P(i|n_b) \tag{10.1}$$

where $P(i|n_b)$ is once again the Poisson probability. We can then combine the final p-values for

---

[1] We note here that if the background hypothesis were determined via simulation, we might argue that it was overestimated. However, the background is known from off-time experimental data, and thus the fluctuation does not correspond to a rejection of the null hypothesis.

our ensemble of n independent analyses into one test statistic via Fisher's combined probability test [119, 120].

$$\chi^2_{2n} = -2 \sum_{i=1}^{n} \ln(p_i) \tag{10.2}$$

The p-value of χ^2 is then interpolated from a chi-square table having $2n$ degrees of freedom. The chi-square integral can be solved analytically, giving the combined significance as

$$p_{tot} = k \sum_{i=0}^{n-1} \frac{(-\ln(k))^i}{i!} \tag{10.3}$$

where $k = p_1 \cdot p_2 \cdot \ldots \cdot p_n$ is the product of the p-values for all analyses. In the case of combining only two analyses, this becomes $p_{tot} = k - k\ln(k)$. Let us now consider our example of combining a highly significant (5σ, $p = 5.73 \times 10^{-7}$) discovery of a future analysis with our previous result of observing 0 on an expectation of 1.74 ($p = 1$) [2]. In this case we have $k = 5.73 \times 10^{-7}$ and $p_{tot} = 8.8 \times 10^{-6}$, still an order of magnitude more significant than 4σ. A less significant discovery (3σ, $p = 2.7 \times 10^{-3}$) would be reduced to $p = 0.019$ in the same situation. In this case it makes sense that we wouldn't consider this discovery significant, as it was marginal in the first case. This example serves to emphasize why we choose a high threshold for discovery (5σ). It shields us against previous null results and trial factors we may miss.

10.2.2 Sensitivity to gamma rays from GRBs

It has been proposed that IceCube could be used as an observatory for TeV gamma-ray sources in the southern sky [121, 122, 123], and AMANDA has set a limit on the photon emission from the giant soft-gamma repeater SGR 1806-20 [124]. We investigate whether it is possible to observe such a TeV scale gamma flux from GRBs, likely associated with π^0 decay (see section 2.3).

Gamma rays interact in the atmosphere to produce muons which then propagate through the Earth to the detector. The muons and hence gammas must have a certain minimum energy in order to penetrate the ∼1.5 km ice overburden. However, we must also consider the suppression of

---

[2] Note that the large downward fluctuation is incorporated here. If we had observed 1 on 1.74 for example, we would instead have $p = 0.82$.

cosmological high energy photons due to pair-pair interactions on the cosmic microwave background (CMB) and extragalactic background light (EBL). Finally, we take into account the large background rates of cosmic ray-induced downgoing muons.

The absorption model of Stecker et al [125] (Fig. 10.2) shows that even for relatively nearby sources the suppression of TeV scale gamma-rays due to EBL and CMB pair production processes is large. To determine the feasibility of further studies, we perform a test case ignoring this suppression. The nearest GRB so far recorded was at a redshift of $z = 0.008$, and we claim that the EBL absorption from this distance could be negligible. We take the TeV photon emission from the test GRB to follow an E^{-2} power law, in agreement with predictions of the accelerated protons, and apply a standard flux normalization of $10^{-11}\,\mathrm{TeV}^{-1}\,\mathrm{cm}^{-2}\,\mathrm{s}^{-1}\,\mathrm{sr}^{-1}$ at 1 TeV. We apply a cut-off to the the energy spectrum at 100 TeV, allowing for possible absorption at high energies and incorporating a lack of knowledge of the exact burst physics.

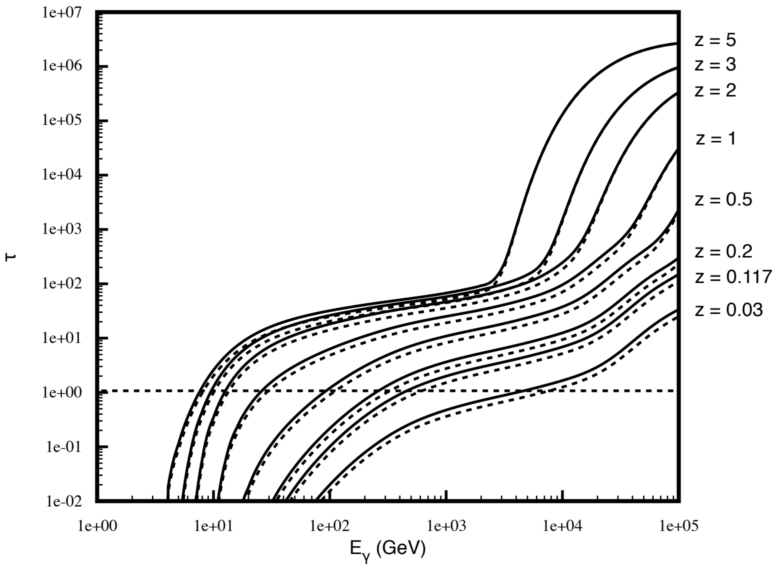

Figure 10.2: Opacity of the universe to high energy photons. Absorption on the combined CMB and EBL background light is shown for several redshifts. The average GRB is located at $z = 1 - 2$. (from [125])

Assuming such a flux incident at Earth, we adopt the analytical solution of the cascade equations of Ó Murchadha [126], which updates earlier estimates [127] of the gamma-induced muon flux.

This work includes pion and kaon production in the atmosphere and subsequent decay, as well as muon pair production both directly and via electrons. Resulting muons and muon bundles are propagated through the Earth assuming the standard energy loss equations in order to determine the remaining flux at the depth of IceCube.

$$\left\langle \frac{dE}{dx} \right\rangle = -a - bE \tag{10.4}$$

Here, $a = 2.59 \times 10^{-6}\,\mathrm{TeV}\,(\mathrm{g/cm^2})^{-1}$ and $b = 3.63 \times 10^{-6}\,\mathrm{TeV}\,(\mathrm{g/cm^2})^{-1}$ [67]. The effective area of IceCube is calculated from Monte Carlo event rates at zenith angles of 0, 30, and 45 degrees with respect to the downgoing vertical.

For a test GRB located at the zenith, following the flux described above, and with 10 s of photon emission, we calculate 2.3 background muons and 0.00031 signal gamma-induced muons. In order to instead have a 5σ discovery, the flux normalization would have to increase to $2.5 \times 10^{-7}\,\mathrm{TeV^{-1}\,cm^{-2}\,s^{-1}\,sr^{-1}}$ at 1 TeV. This result is roughly the same if the GRB is instead located at 30° from vertical.

Based on these results for the most optimistic case of an extremely close, short burst, we conclude that the prospects for detecting TeV-scale gamma-rays from GRBs are slim to non-existent. A burst would have to be both very nearby and exceedingly bright to offer any hope of detection. In this case an observation would certainly not be unique to IceCube, and in fact the predicted neutrino flux would be quite large.

10.3 Outlook

With the launch of the Fermi Gamma Space Telescope [28] in July of 2008, the rate of GRB observations has nearly tripled. In addition, Fermi is sensitive to higher energies than Swift, allowing measurement of photon spectral break indices and creating a complementary satellite network with both full sky coverage and excellent pointing resolution (when Swift is able to slew to make afterglow measurements). These additional opportunities for neutrino detection will be exploited in the future to rapidly improve the sensitivity of analyses.

Furthermore, our detector is itself growing every year. IceCube has been operating in a 40-

string configuration since April 2008 and first analyses using this data are nearing maturity. With this geometry IceCube is already as large as the full detector along the major axis, giving us the increased angular resolution that comes from longer lever arms. 19 additional strings were deployed during the 2008-2009 austral summer, and the 59-string detector began data taking in May of 2009. In the 2009-2010 deployment season, the remainder of the low-energy Deep Core system will be installed, extending our sensitivity in the sub TeV regime, notably for precursor GRB emission. Work is ongoing to optimize the layout of the final 9 strings of the detector to extend sensitivities at the highest energies. We discuss our efforts on this front and the implications for GRB searches in Appendix B.

Initial studies of the sensitivity of the full detector to high energy neutrinos from GRBs [128] are encouraging, with preliminary results showing that IceCube will be able to detect the leading models with a high level of significance within the first year of operation. These calculations are described in detail in Appendix B. Fig. 10.3 illustrates the substantial increase in neutrino effective area as the detector grows in physical size.

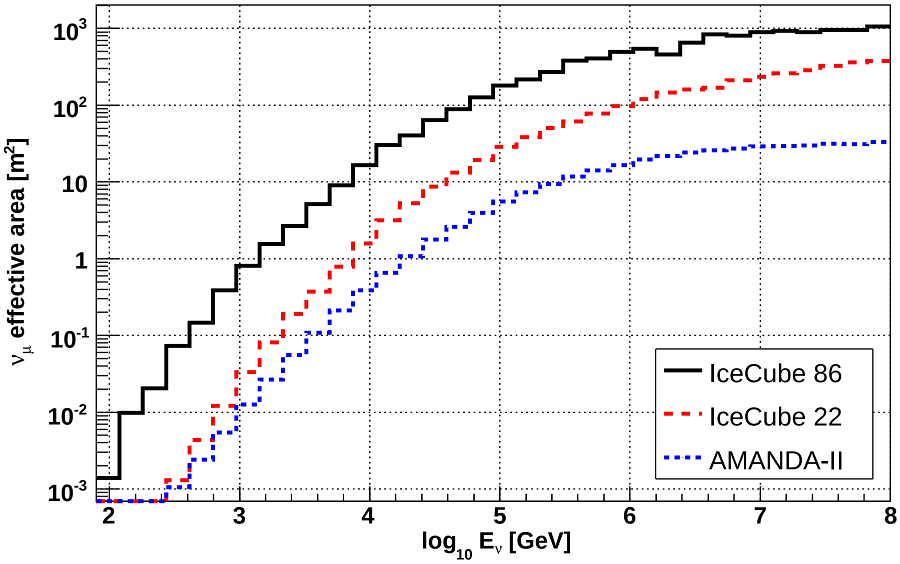

Figure 10.3: Muon neutrino effective area angle-averaged over the northern hemisphere for AMANDA-II, the 22-string configuration of IceCube, and the full 86-string IceCube detector. The Deep Core extension extends the effective area at low energies for the full detector.

While the analyses presented in this thesis have not constrained models of neutrino emission from GRBs, they have demonstrated important new search techniques. It has been shown that by implementing careful and stringent event selections, a highly significant discovery of a transient source can be made with only a few observed events. Furthermore, by incorporating the energy information of each event in an unbinned likelihood analysis, nearly a factor of two improvement in discovery potential can be achieved relative to the prototypical analysis that searches for events within a specified spatial and temporal bin around a source location and time. We have also demonstrated that substantial sensitivity is gained by modeling the neutrino emission from individual GRBs based on observed photon spectral characteristics. By building on the knowledge gained through these analyses and leveraging increasing data samples and collection area, IceCube will soon see the first neutrinos from gamma-ray bursts or else will set strong constraints on the emission of such neutrinos. In either case, we will gain valuable insight into the physical processes that occur within these fascinating astrophysical objects.

Bibliography

[1] T. Stanev, P. Biermann, and T. Gaisser, "Cosmic rays IV. the spectrum and chemical composition above 10^4 GeV," *A&A* **274** (1993) 902, `astro-ph/9303006`.

[2] J. Hoerandel, "On the knee in the energy spectrum of cosmic rays," *Astropart. Phys.* **19** (2003) 193, `astro-ph/0210453`.

[3] J. Cronin, S. Swordy, and T. Gaisser, "Cosmic rays at the energy frontier," *Sci. Am.* **276** (1997) 32.

[4] M. Longair, *High Energy Astrophysics Vol. 2*. Cambridge, 1981.

[5] R. Blandford and J. Ostriker, "Particle acceleration by astrophysical shocks," *ApJ* **221** (1978) L29.

[6] A. Bell, "The acceleration of cosmic rays in shock fronts. I," *Mon. Not. R. astr. Soc.* **182** (1978) 147.

[7] A. Hillas, "The origin of ultra-high-energy cosmic rays," *Ann. Rev. Astron. Astrophys.* **22** (1984) 425.

[8] **IceCube** Collaboration, A. Achterberg *et al.*, "The search for muon neutrinos from northern hemisphere gamma-ray bursts with AMANDA," *ApJ* **674** (2008) 357, `arXiv:0705.1186`.

[9] R. Bay, *Search for High Energy Emission from Gamma-Ray Bursts with the Antarctic Muon and Neutrino Detector Array (AMANDA)*. PhD thesis, University of California, Berkeley, 2000.

[10] R. Hardtke, *The Search for High Energy Neutrinos from Gamma-Ray Bursts with the AMANDA Detector*. PhD thesis, University of Wisconsin-Madison, 2002.

[11] **IceCube** Collaboration, A. Achterberg *et al.*, "Search for neutrino-induced cascades from gamma-ray bursts with AMANDA," *ApJ* **664** (2007) 397, `arXiv:astro-ph/0702265`.

[12] M. Stamatikos, *Probing for Correlated Neutrino Emission from Gamma-Ray Bursts with Antarctic Cherenkov Telescopes: a Theoretical Modeling and Analytical Search Paradigm in the Context of the Fireball Phenomenolgy*. PhD thesis, State University of New York, Buffalo, 2006.

[13] **IceCube** Collaboration, R. Abbasi *et al.*, "Search for high-energy muon neutrinos from the 'naked-eye' GRB 080319B with the IceCube neutrino telescope," *accepted for publication in ApJ* (2009) , `arXiv:0902.0131`.

[14] NASA, "The Vela satellite program," 1965. `http://heasarc.gsfc.nasa.gov/docs/vela5b/vela5b.html`.

[15] R. Klebesadel, I. Strong, and R. Olson, "Observations of gamma-ray bursts of cosmic origin," *ApJ* **182** (1973) L85.

[16] W. Wheaton *et al.*, "The direction and spectral variability of a cosmic gamma-ray burst," *ApJ* **185** (1973) L57.

[17] T. Cline, U. Desai, R. Klebesadel, and I. Strong, "Energy spectra of cosmic gamma-ray bursts," *ApJ* **185** (1973) L1.

[18] NASA, "Burst and Transient Source Experiment - BATSE," 1991. `http://www.batse.msfc.nasa.gov/batse/`.

[19] C. Kouveliotou *et al.*, "Identification of two classes of gamma-ray bursts," *Astrophys. J. Lett.* **413** (1993) no. 2, L101–L104.

[20] C. Meegan *et al.*, "Spatial distribution of γ-ray bursts observed by BATSE," *Nature* **355** (1992) 143–145.

[21] W. Paciesas *et al.*, "The fourth BATSE gamma-ray burst catalog (revised)," *Astrophy. J. Suppl.* **122** (1999) 465–495, `astro-ph/9903205`.

[22] ASI, "BeppoSAX," 1996. `http://www.asdc.asi.it/bepposax/`.

[23] M. Metzger *et al.*, "Spectral constraints on the redshift of the optical counterpart to the γ-ray burst of 8 May 1997," *Nature* **387** (1997) 878–880.

[24] N. Gehrels *et al.*, "The Swift gamma-ray burst mission," *ApJ* **611** (2004) 1005.

[25] NASA, "Swift satellite," 2004. `http://swift.gsfc.nasa.gov/docs/swift/swiftsc.html`.

[26] N. Gehrels *et al.*, "A short γ-ray burst apparently associated with an elliptical galaxy at redshift z = 0.225," *Nature* **437** (2005) 851, `astro-ph/0505630`.

[27] J. Greiner *et al.*, "GRB 080913 at redshift 6.7," *ApJ* **693** (2009) 1610, `arXiv:0810.2314`.

[28] NASA, "Fermi Gamma Space Telescope," 2008. `http://www.nasa.gov/mission_pages/GLAST/main/index.html`.

[29] **Fermi** Collaboration, A. Abdo *et al.*, "Fermi observations of high-energy gamma-ray emission from GRB 080916C," *Science* **323** (2009) 1688.

[30] S. Woosley, "Gamma-ray bursts from stellar mass accretion disks around black holes," *ApJ* **405** (1993) 273.

[31] S. Woosley and A. Heger, "The progenitor stars of gamma-ray bursts," *ApJ* **637** (2006) 914, `astro-ph/0508175`.

[32] T. Galama *et al.*, "Discovery of the peculiar supernova 1998bw in the error box of GRB980425," *Nature* **395** (1998) 670, `astro-ph/9806175`.

[33] D. Eichler, M. Livio, T. Piran, and D. N. Schramm, "Nucleosynthesis, neutrino bursts and γ-rays from coalescing neutron stars," *Nature* **340** (1989) 126.

[34] C. Fryer, S. Woosley, and D. Hartmann, "Formation rates of black hole accretion disk gamma-ray bursts," *ApJ* **526** (1999) 152, `astro-ph/9904122`.

[35] P. Meszaros and M. J. Rees, "Relativistic fireballs and their impact on external matter - models for cosmological gamma-ray bursts," *ApJ* **405** (1993) 278.

[36] P. Meszaros, "Gamma-ray bursts," *Rept. Prog. Phys.* **69** (2006) 2259–2322, `astro-ph/0605208`.

[37] D. Band *et al.*, "BATSE observations of gamma-ray burst spectra: I. spectral diversity," *ApJ* **413** (1993) 281.

[38] E. Molinari *et al.*, "REM observations of GRB 060418 and GRB 060607A: the onset of the afterglow and the initial fireball Lorentz factor determination," *A&A* **469** (2007) L13.

[39] J. Rhoads, "The dynamics and light curves of beamed gamma ray burst afterglows," *ApJ* **525** (1999) 737, `astro-ph/9903399`.

[40] R. Sari, T. Piran, and J. Halpern, "Jets in GRBs," *ApJ* **519** (1999) L17, `astro-ph/9903339`.

[41] F. Harrison *et al.*, "Optical and radio observations of the afterglow from GRB990510: Evidence for a jet," *ApJ* **523** (1999) L121, `astro-ph/9905306`.

[42] D. Frail *et al.*, "Beaming in gamma-ray bursts: Evidence for a standard energy reservoir," *ApJ* **562** (2001) L55, `astro-ph/0102282`.

[43] J. Bloom, D. Frail, and S. Kulkarni, "Gamma-ray burst energetics and the gamma-ray burst Hubble diagram: Promise and limitations," *ApJ* **594** (2003) 674, `astro-ph/0302210`.

[44] B. Zhang, "Gamma-ray bursts in the Swift era," *Chin. J. Astron. Astrophys.* **7** (2007) 1–50, `astro-ph/0701520`.

[45] E. Waxman and J. N. Bahcall, "High-energy neutrinos from cosmological gamma-ray burst fireballs," *Phys. Rev. Lett.* **78** (1997) 2292, `astro-ph/9701231`.

[46] D. Guetta *et al.*, "Neutrinos from individual gamma-ray bursts in the BATSE catalog," *Astropart. Phys.* **20** (2004) 429, `astro-ph/0302524`.

[47] F. Halzen and D. Hooper, "High-energy neutrino astronomy: The cosmic ray connection," *Rep. Prog. Phys.* **65** (2002) 1025, `astro-ph/0204527`.

[48] E. Waxman, S. Kulkarni, and D. Frail, "Implications of the radio afterglow from the gamma-ray burst of May 8, 1997," *ApJ* **497** (1998) 288, `astro-ph/9709199`.

[49] E. Waxman and J. Bahcall, "High energy neutrinos from astrophysical neutrinos: An upper bound," *Phys. Rev.* **D59** (1999) 023002, `hep-ph/9807282`.

[50] S. Razzaque, P. Meszaros, and E. Waxman, "Neutrino tomography of gamma ray bursts and massive stellar collapses," *Phys. Rev.* **D68** (2003) 083001, `astro-ph/0303505`.

[51] J. K. Becker, "High-energy neutrinos in the context of multimessenger astrophysics," *Phys. Rep.* **458** (2008) 173–246, `arXiv:0710.1557`.

[52] E. Waxman and J. N. Bahcall, "Neutrino afterglow from gamma-ray bursts: $\sim 10^{18}$ eV," *ApJ* **541** (2000) 707, `astro-ph/9909286`.

[53] R. Davis Jr., "Solar neutrinos. II. experimental," *Phys. Rev. Lett.* **12** (1964) no. 11, 303–305.

[54] J. Bahcall and R. Davis Jr., "Solar neutrinos: a scientific puzzle," *Science* **191** (1976) 264–267.

[55] Q. Ahmad *et al.*, "Measurement of the rate of $\nu_e + d \rightarrow p + p + e^-$ interactions produced by 8B solar neutrinos at the Sudbury Neutrino Observatory," *Phys. Rev. Lett.* **87** (2001) 071301, `nucl-ex/0106015`.

[56] H. Athar, C. Kim, and J. Lee, "The intrinsic and oscillated astrophysical neutrino flavor ratios," *Mod. Phys. Lett.* **A21** (2006) 1049–1066, `hep-ph/0505017`.

[57] T. Kashti and E. Waxman, "Flavoring astrophysical neutrinos: Flavor ratios depend on energy," *Phys. Rev. Lett.* **95** (2005) 181101, `astro-ph/0507599`.

[58] R. Gandhi *et al.*, "Neutrino interactions at ultrahigh energies," *Phys. Rev.* **D58** (1998) 093009, `hep-ph/9807264`.

[59] J. Learned and K. Mannheim, "High-energy neutrino astrophysics," *Annu. Rev. Nucl. Part. Sci.* **50** (2000) 679–749.

[60] P. Lipari and T. Stanev, "Propagation of multi-TeV muons," *Phys. Rev.* **D44** (1991) 113543.

[61] P. Price and K. Woschnagg, "Role of group and phase velocity in high-energy neutrino observatories," *Astropart. Phys.* **15** (2001) 97, `hep-ex/0008001`.

[62] P. Čerenkov, "Visible emission of clean liquids by action of radiation," *C. R. Ac. Sci. U.S.S.R.* **8** (1934) 451.

[63] P. Čerenkov, "Visible radiation produced by electrons moving in a medium with velocities exceeding that of light," *Phys. Rev.* **52** (1937) 378–379.

[64] I. Frank and I. Tamm, "Coherent radiation of fast electrons in a medium," *C. R. Ac. Sci. U.S.S.R.* **14** (1937) 107.

[65] M. Longair, *High Energy Astrophysics Vol. 1.* Cambridge, 1981.

[66] J. Jackson, *Classical Electrodynamics.* Wiley, 1998.

[67] D. Chirkin and W. Rhode, "Muon Monte Carlo: A high-precision tool for muon propagation through matter," *preprint* (2004) , `hep-ph/0407075`.

[68] G. Fiorentini, V. Naumov, and F. Villante, "Atmospheric neutrino flux supported by recent muon experiments," *Phys. Lett.* **B510** (2001) 173, `hep-ph/0106014`.

[69] **AMANDA** Collaboration, P. Desiati *et al.*, "Response of AMANDA-II to cosmic ray muons," in *Proc. 28th International Cosmic Ray Conference (ICRC'03)*, p. 1373. Tsukuba, Japan, 2003.

[70] **AMANDA** Collaboration, M. Ackermann *et al.*, "Optical properties of deep glacial ice at the South Pole," *J. Geophys. Res.* **111** (2006) D13203.

[71] **AMANDA** Collaboration, J. Ahrens *et al.*, "Muon track reconstruction and data selection techniques in AMANDA," *Nucl. Inst. Meth.* **A524** (2004) 169, `astro-ph/0407044`.

[72] **ANTARES** Collaboration, J. Aguilar *et al.*, "Transmission of light in deep sea water at the site of the Antares neutrino telescope," *Astropart. Phys.* **23** (2005) 131, `astro-ph/0412126`.

[73] S. Grullon, D. Boersma, and G. Hill, "Photonics-based log-likelihood reconstruction in IceCube," Tech. Rep., IceCube, 200807001-v3, 2008.

[74] M. Ackermann, *Searches for Signals from Cosmic Point-like Sources of High Energy Neutrinos in 5 Years of AMANDA-II Data.* PhD thesis, Humboldt-Universität zu Berlin, Germany, 2006.

[75] A. Karle, "Monte Carlo simulation of photon transport and detection in deep ice: Muons and cascades," in *Proc. Simulation and Analysis Methods for Large Neutrino Telescopes*, p. 174. DESY, Zuethen, Germany, 1999.

[76] J. Lundberg *et al.*, "Light tracking for glaciers and oceans: Scattering and absorption in heterogeneous media with Photonics," *Nucl. Inst. Meth.* **A581** (2007) 619, `astro-ph/0702108`.

[77] **IceCube** Collaboration, J. Zornoza, D. Chirkin, *et al.*, "Muon energy reconstruction and atmospheric neutrino spectrum unfolding with the IceCube detector," in *Proc. 30th International Cosmic Ray Conference (ICRC'07)*. Merida, Mexico, Aug. 2007. `arXiv:0711.0353`.

[78] NASA, "Gamma-Ray Burst Coordinates Network - GCN," 2009. `http://gcn.gsfc.nasa.gov`.

[79] NASA, "High Energy Transient Explorer - HETE-II," 2000. `http://space.mit.edu/HETE/`.

[80] ESA, "International Gamma-Ray Astrophysics Laboratory - INTEGRAL." `http://www.sciops.esa.int/index.php?project=INTEGRAL&page=index`.

[81] IPN, "3$^{\text{rd}}$ interplanetary network - IPN3," 1990. `http://www.ssl.berkeley.edu/ipn3/`.

[82] ISAS, "Suzaku," 2005. `http://www.isas.jaxa.jp/e/enterp/missions/suzaku/index.shtml`.

[83] M. Tavani *et al.*, "The AGILE space mission," *Nucl. Inst. Meth.* **A588** (2008) 52–62.

[84] ASI, "AGILE," 2007. `http://agile.rm.iasf.cnr.it/`.

[85] **AMANDA** Collaboration, E. Andres *et al.*, "The AMANDA neutrino telescope: Principle of operation and first results," *Astropart. Phys.* **13** (2000) 1–20, `astro-ph/9906203`.

[86] **AMANDA** Collaboration, P. Askebjer *et al.*, "Optical properties of the south pole ice at depths between 0.8 and 1 km," *Science* **267** (1995) 1147, `astro-ph/9412028`.

[87] **IceCube** Collaboration, R. Abbasi *et al.*, "The IceCube data acquisition system: Signal capture, digitization, and timestamping," *Nucl. Inst. Meth.* **A601** (2009) 294–316, `arXiv:0810.4930`.

[88] R. Stokstad, D. Lowder, J. Ludvig, D. Nygren, and G. Przybylski Tech. Rep., LBNL, 43200, 1998.

[89] R. Quimby, "GRBlog homepage," 2009. `http://grad40.as.utexas.edu/`.

[90] AMANDA Collaboration, "AMANDA monitoring homepage," 2006. `http://butler.physik.uni-mainz.de/amanda-monitoring/html/mainmenu.html`.

[91] NASA, "HEASARC software homepage," 2009. `http://heasarc.gsfc.nasa.gov/docs/software.html`.

[92] N. Butler *et al.*, "A complete catalog of Swift GRB spectra and durations: Demise of a physical origin for pre-Swift high-energy correlations," *ApJ* **671** (2007) 656–677, `arXiv:0706.1275`.

[93] A. Roth, *A Search for Muon Neutrinos from Gamma-Ray Bursts with the IceCube 22-String Detector*. PhD thesis, University of Maryland, 2009.

[94] **IceCube** Collaboration, K. Hoffman, K. Meagher, P. Roth, I. Taboada, *et al.*, "Search for neutrinos from GRBs with IceCube," in *Proc. 31st International Cosmic Ray Conference (ICRC'09).* Łódź, Poland, 2009.

[95] D. Heck *et al.*, "CORSIKA: A monte carlo code to simulate extensive air showers," Tech. Rep., FZKA, 6019, 1998.

[96] G. Hill, "Detecting neutrinos from AGN: New fluxes and cross sections," *Astropart. Phys.* **6** (1997) 215, `astro-ph/9607140`.

[97] A. Martin, R. Roberts, and W. Stirling, "Pinning down the glue in the proton," *Phys. Lett.* **B354** (1995) 155, `hep-ph/9502336`.

[98] A. Gazizov and M. O. Kowalski, "ANIS: High energy neutrino generator for neutrino telescopes," *Comp. Phys. Comm.* **172** (2005) 203, `astro-ph/0406439`.

[99] H. Lai, J. Huston, S. Kuhlmann, J. Morfin, F. Olness, J. Owens, J. Pumplin, and W. Tung, "Global QCD analysis of parton structure of the nucleon: CTEQ-5 parton distributions," *Eur. Phys. J.* **C12** (2000) 375, `hep-ph/9903282`.

[100] Dziewonski and Anderson, "Preliminary reference Earth model," *Phys. Earth. Planet. Int.* **25** (1981) 297–356.

[101] G. D. Barr *et al.*, "Three-dimensional calculation of atmospheric neutrinos," *Phys. Rev.* **D70** (2004) 023006, `astro-ph/0403630`.

[102] S. Hundertmark, *Simulation und Analyse von Myonereignissen im AMANDA-B4-Neutrinoteleskop.* PhD thesis, Humboldt-Universität zu Berlin, Germany, 1999.

[103] A. Pohl, *A Statistical Tool for Finding Non-Particle Events from AMANDA Neutrino Telescope.* Licentiate thesis, Uppsala and Kalmar Universities, Sweden, 2004.

[104] J. Bahcall and E. Waxman, "High energy astrophysical neutrinos: The upper bound is robust," *Phys. Rev.* **D64** (2001) 023002, `hep-ph/9902383`.

[105] G. Hill and K. Rawlins, "Unbiased cut selection for optimal upper limits in neutrino detectors: the model rejection potential technique," *Astropart. Phys.* **19** (2003) 393, `astro-ph/0209350`.

[106] G. C. Hill, J. Hodges, B. Hughey, A. Karle, and M. Stamatikos, "Examining the balance between optimising an analysis for best limit setting and best discovery potential," in *Proc. PHYSTAT O5: Statistical Problems in Particle Physics.* Oxford, United Kingdom, Sep, 2005.

[107] **IceCube** Collaboration, R. Abbasi *et al.*, "Search for muon neutrinos from Gamma-Ray Bursts with the IceCube neutrino telescope," *In Prep.* (2009) .

[108] G. Feldman and R. Cousins, "A unified approach to the classical statistical analysis of small signals," *Phys. Rev.* **D57** (1998) 3873, `physics/9711021`.

[109] **IceCube** Collaboration, R. Abbasi *et al.*, "First neutrino point-source results from the 22-string icecube detector," *Submitted to ApJ. Lett.* (2009) , `arXiv:0905.2253`.

[110] J. Braun, J. Dumm, F. de Palma, C. Finley, A. Karle, and T. Montaruli, "Methods for point source analysis in high energy neutrino telescopes," *Astropart. Phys.* **29** (2008) 299, `arXiv:0801.1604`.

[111] R. J. Barlow, *Statistics.* Wiley, 1989.

[112] **HiRes** Collaboration, R. Abbasi *et al.*, "Search for cross-correlations of ultrahigh-energy cosmic rays with BL Lacertae objects," *ApJ* **636** (2006) 680, `arXiv:astro-ph/0507120`.

[113] J. Pumplin, D. Stump, J. Huston, H. Lai, P. Nadolsky, and W. Tung, "New generation of parton distributions with uncertainties from global QCD analysis," *J. High Energy Phys.* **0207** (2002) 12, `hep-ph/0201195`.

[114] E. Bugaev, I. Sokalski, and S. Klimushin, "Simulation accuracy of long range muon propagation in medium: analysis of error sources," `hep-ph/0010323`.

[115] **IceCube** Collaboration, A. Achterberg *et al.*, "Five years of searches for point sources of astrophysical neutrinos with the AMANDA-II neutrino telescope," *Phys. Rev.* **D75** (2007) 102001, `astro-ph/0611063`.

[116] T.Montaruli and I. Sokalski, "Influence of neutrino interaction and muon propagation media on neutrino-induced muon rates in deep underwater detectors," Tech. Rep., ANTARES-Phys, 2003-001, 2003.

[117] J. Kelley, *Searching for Quantum Gravity with High-Energy Atmospheric Neutrinos and AMANDA-II.* PhD thesis, University of Wisconsin-Madison, 2009.

[118] K. Kuehn, *The Search for Muon Neutrinos from Northern Hemisphere Gamma-Ray Bursts with AMANDA-II.* PhD thesis, University of California, Irvine, 2007.

[119] R. Fisher, *Statistical Methods for Research Workers.* Oliver and Boyd, 1925.

[120] R. Fisher, "Combining independent tests of significance," *Amer. Stat.* **2** (1948) no. 5, 30.

[121] F. Halzen, T. Stanev, and G. Yodh, "Gamma ray astronomy with muons," *Phys. Rev.* **D55** (1997) 4475, `astro-ph/9608201`.

[122] J. Alvarez-Muniz and F. Halzen, "Muon detection of TeV gamma rays from gamma ray bursts," *ApJ* **521** (1999) 928, `astro-ph/9902039`.

[123] F. Halzen and D. Hooper, "Gamma ray astronomy with IceCube," *JCAP* **0308** (2003) 006, `astro-ph/0305234`.

[124] **IceCube** Collaboration, A. Achterberg *et al.*, "Limits on the high-energy gamma and neutrino fluxes from the SGR 1806-20 giant flare of December 27th, 2004 with the AMANDA-II detector," *Phys. Rev. Lett.* **97** (2006) 221101, `astro-ph/0607233`.

[125] F. Stecker, M. Malkan, and S. Scully, "Intergalactic photon spectra from the far IR to the UV lyman limit for $0 < z < 6$ and the optical depth of the universe to high energy gamma-rays," *ApJ* **648** (2006) 774, `astro-ph/0510449`.

[126] F. Halzen, A. Kappes, and A. Ó Murchadha, "Gamma-ray astronomy with muons: Sensitivity of IceCube to PeVatrons in the southern sky," *In Prep.* (2009) .

[127] F. Halzen, K. Hikasa, and T. Stanev, "Particle physics with cosmic accelerators," *Phys. Rev.* **D34** (1986) 2061.

[128] **IceCube** Collaboration, A. Kappes, P. Roth, and E. Strahler, "Searches for neutrinos from GRBs with the IceCube 22-string detector and sensitivity estimates for the full detector," in *Proc. 31st International Cosmic Ray Conference (ICRC'09).* Łódź, Poland, July, 2009.

[129] D. Chirkin, "A new method for identifying neutrino events in IceCube data," in *Proc. 31st International Cosmic Ray Conference (ICRC'09).* Łódź, Poland, July, 2009.

[130] V. Vapnik, *The Nature of Statistical Learning Theory.* Springer-Verlag, 1995.

[131] C. Cortes and V. Vapnik, "Support-vector networks," *Machine Learning* **20** (1995) no. 3, 273.

[132] C. Burges, "A tutorial on support vector machines for pattern recognition," *Data Min. Knowl. Discov.* **2** (1998) 121–167.

[133] R. Fletcher, *Practical Methods of Optimization.* Wiley, 1987.

[134] M. Aizerman, E. Braverman, and L. Rozonoer, "Theoretical foundations of the potential function method in pattern recognition learning," *Automation and Remote Control* **25** (1964) 821.

[135] T. Joachims, "Making large-scale SVM learning practical," Tech. Rep., MIT Press, 1998.

[136] T. Joachims, "SVM^{light} homepage," 1999. `http://svmlight.joachims.org/`.

[137] C. Hsu, C. Chang, and C. Lin, "A practical guide to support vector classification," Tech. Rep., Department of Computer Science, National Taiwan University, 2003.

Appendix A

List of Abbreviations

ADC	Analog to Digital Converter
AGILE	Astro-rivelatore Gamma a Immagini Leggero
AHA	the Norwegian pop music band
AMANDA	Antarctic Muon and Neutrino Detector Array
ATWD	Analog Transient Waveform Digitizer
BAT	Burst Alert Telescope
BATSE	Burst and Transient Source Experiment
CGRO	Compton Gamma Ray Observatory
CMB	Cosmic Microwave Background
CP	Charge-Parity
CTEQ	Coordinated Theoretical-Experimental Project on QCD
DAQ	Data Acquisition System
DOM	Digital Optical Module
EBL	Extragalactic Background Light
EGRET	Energetic Gamma Ray Experiment Telescope
fADC	Fast Analog to Digital Converter
FPGA	Field-Programmable Gate Array
FREGATE	French Gamma-ray Telescope
GBM	Gamma-ray Burst Monitor

GCN	Gamma-ray Burst Coordinate Network
GRID	Gamma-ray Imaging Detector
GRB	Gamma-ray Burst
GZK	Greisen-Zatsepin-Kuzmin
HE	High Energy
HEASARC	NASA's High Energy Astrophysics Science Archive Research Center
HETE-II	High Energy Transient Explorer
HXD	Hard X-ray Detector
IBIS	Imager on Board INTEGRAL
INTEGRAL	International Gamma-Ray Astrophysics Laboratory
IPN3	Third Interplanetary Network
ISM	Interstellar Medium
JAMS	Just Another Muon Search
JEM-X	Joint European X-ray Monitor
LAT	Large Area Telescope
LE	Leading Edge
LC	Local Coincidence
PDF	Probability Distribution Function
PMT	Photomultiplier Tube
MDF	Model Discovery Factor
MDP	Model Discovery Potential
MMC	Muon Monte Carlo
MNS	Maki-Nakagawa-Sakata
MPE	Multiple Photo-Electron
MRF	Model Rejection Factor
MRS	Martin-Roberts-Stirling
OM	Optical Module

PREM	Preliminary Reference Earth Model
RA	Right Ascension
RAPCal	Reciprocal Active Pulsing Calibration
RQPM	Recombination Quark Parton Model
SBM	Subset Browsing Method
Sne	Supernovae
SPE	Single Photo-Electron
SPI	Spectrometer on INTEGRAL
SVM	Support Vector Machine
SWAMP	Swedish Amplifier
SXC	Soft X-ray Camera
TDC	Time to Digital Converter
TE	Trailing Edge
TOT	Time Over Threshold
TWR	Transient Waveform Recording
UHECR	Ultra-High Energy Cosmic Ray
UTC	Coordinated Universal Time
UVOT	UV and Optical Telescope
WB	Waxman-Bahcall
WXM	Wide Field X-ray Monitor
XRF	X-ray Flasher
XRT	X-ray Telescope
YAG	Yttrium Aluminium Garnet crystal (Nd:$Y_3Al_5O_{12}$)

Appendix B

Sensitivity Studies for the Full Detector

The full IceCube detector is scheduled to be completed during the 2010-2011 austral summer. With the inclusion of Deep Core, this will result in 86 instrumented strings in the ice. There exists an opportunity to optimize the configuration of the final nine strings for physics analyses. Given that Deep Core extends the detector towards lower energies, we instead look towards a geometry that enhances the response to the highest energy events. With highly peaked emission in the 100 TeV - 10 PeV energy range, GRBs make a natural candidate for the investigation of potential improvements. We present a study of the sensitivity of the full IceCube detector to muon neutrinos from GRBs considering a geometry selected to increase the effective area for high energy events.

B.1 Geometries

We consider two geometries for the 86 strings of the full detector in our study. The six strings of Deep Core are located in identical positions for both. In the *default* configuration, the 80 In-Ice strings are spaced in a hexagonal grid, as illustrated in Fig. B.1(a). In the *extended* geometry, the final nine strings are instead arranged in a circle of radius 423 m, as shown in Fig. B.1(b). Such spacing is dictated by logistics, as it enables the drill camp to be located at the center of the ring and the hot water drill hose to reach all proposed hole locations within a single season.

B.2 GRB Sample

Satellite observation rates yield about 200 GRBs/yr detected by Fermi and 100/yr by Swift. Because many photon spectral parameters are correlated, we sample entire bursts from a large number observed by both detectors between 2007 and 2009 according to these rates. These bursts are then distributed randomly and isotropically in detector coordinates to achieve a representative GRB

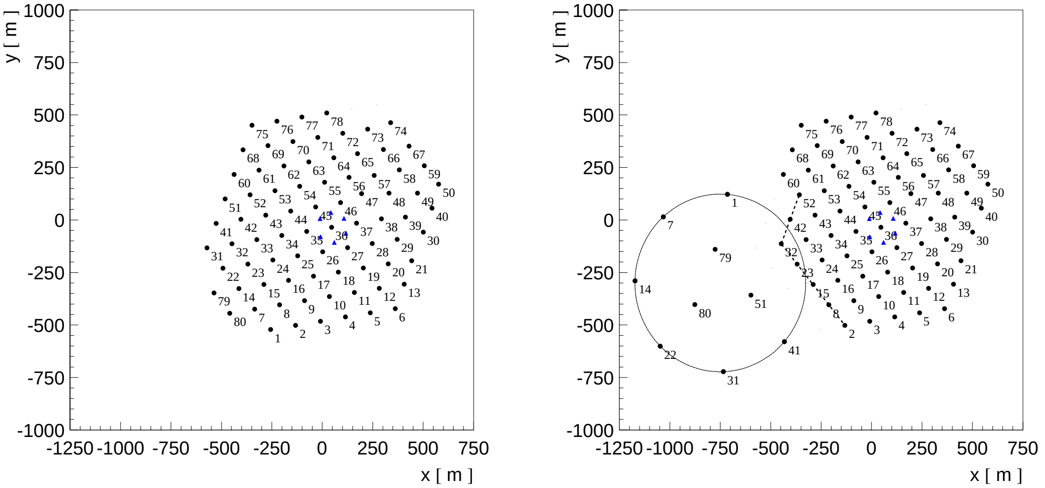

(a) default

(b) extended

Figure B.1: Default and extended configurations of the 86-string IceCube detector.

sample. Applying this procedure to 365 days of detector livetime results in 142 GRBs in the northern hemisphere with a total prompt emission window of 6839 s. For bursts in which all spectral parameters were not measured we use the same average parameters as in Table 8.2 with one exception. The Fermi satellite observes higher energy bursts akin to BATSE, and thus for Fermi bursts we set $L_{\gamma}^{iso} = 10^{52}$ erg/s. For each burst we then calculate the neutrino fluence via the method described in section 2.3.1. The result of these calculations is shown in Fig. B.2. We will calculate the response of IceCube to these GRBs assuming both the individual parameters and also assuming each has an average Waxman-Bahcall spectrum. We also perform a sensitivity study for precursor neutrinos assuming each burst has a Razzaque et al. spectrum of duration 100 s.

B.3 Event Selection

Neutrinos and atmospheric muons are simulated over the full sky with both detector geometries. These events are then reconstructed using a standard 32-iteration multi-photoelectron fit [1]. We separate neutrinos from the muon background using a machine-learning algorithm known as an SBM [129]. Relatively low simulation statistics limit the background rejection potential, however.

---

[1] We note that the reconstruction algorithms used are optimized for the DOM spacing of the default detector configuration. To properly gage the improvement of the extended geometry the reconstructions would have to be re-tuned to take into account the greater distance between DOMS. Nevertheless, a good 'first guess' may be made without changes.

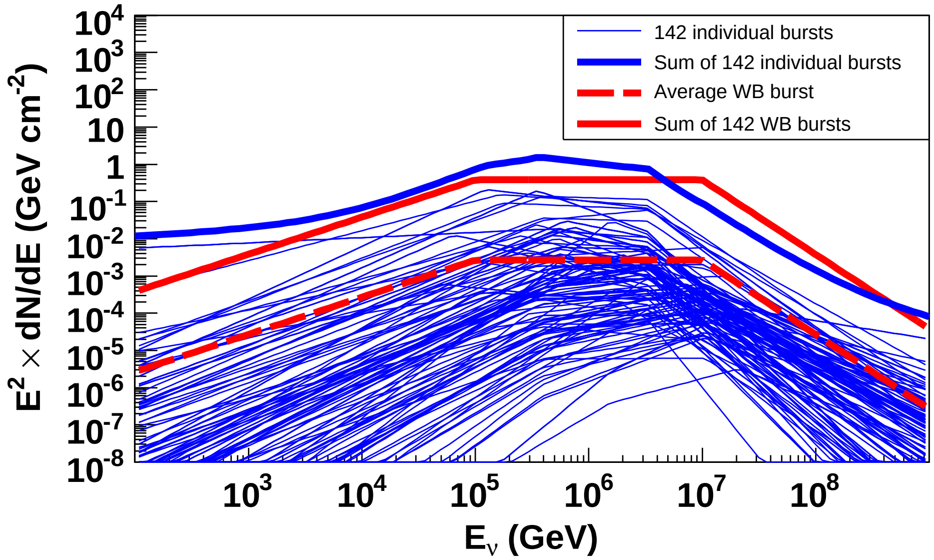

Figure B.2: Neutrino spectra for 142 northern sky GRBs. This corresponds to 1 yr. of IceCube livetime assuming Fermi and Swift observation rates. We compare to the result from the average Waxman-Bahcall spectra calculated from BATSE parameters.

Table B.1 illustrates simulated events remaining after this initial selection.

	neutrinos	downgoing muons	coincident muons
default	7292	7	4
extended	7361	6	7

Table B.1: Unweighted simulated events remaining after application of SBM event selection. Low statistics limit the characterization of the background (each background event has a weight of several hundred in the analysis).

We now tighten the cut on the SBM parameter to eliminate all downgoing muons above 85° in detector coordinates. We show the initial SBM parameter distribution and the angular distribution after the final quality cut for the default geometry in Fig. B.3 and for the extended geometry in Fig. B.4. We show the effective area of the default configuration as well as the increase with the extended configuration in Fig. B.5

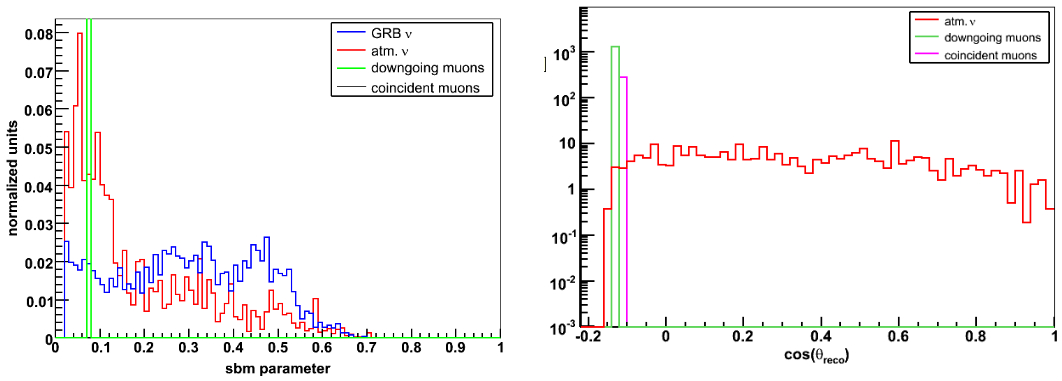

Figure B.3: Default geometry event selection. Left panel shows the distribution in the SBM parameter above 85° for simulated signal and background before final cut. Right panel shows the zenith angle distribution at final cut level.

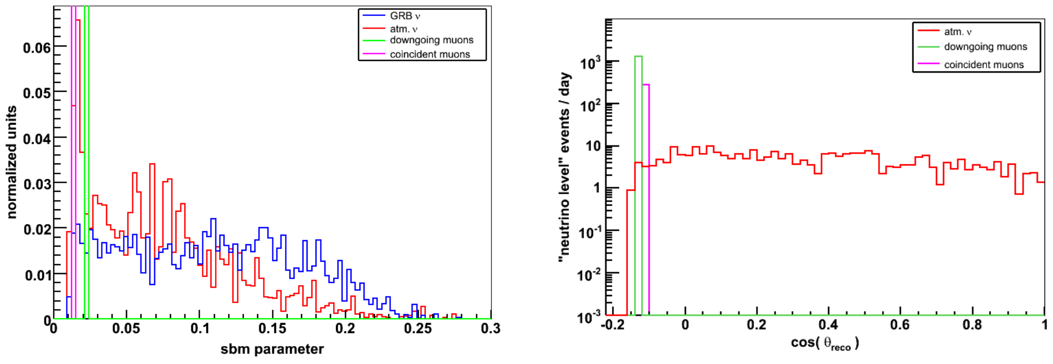

Figure B.4: Extended geometry event selection. Left panel shows the distribution in the SBM parameter above 85° for simulated signal and background before final cut. Right panel shows the zenith angle distribution at final cut level.

B.4 Method

We employ a strategy similar to the 2005-2006 AMANDA binned analysis to get a fast estimation of the sensitivity. The simulated neutrinos are re-weighted to approximate point sources located at the locations of each of the 142 GRBs in the fake data sample. This is accomplished by taking all simulated GRB signal events in a zenith band within 2.5° of the GRB position, weighting by the appropriate solid angle ratio, and transforming the azimuth coordinates in the detector frame to fall on the GRB location. This method preserves all information about the reconstruction resolution for individual events. Background simulation is scaled to the summed emission window

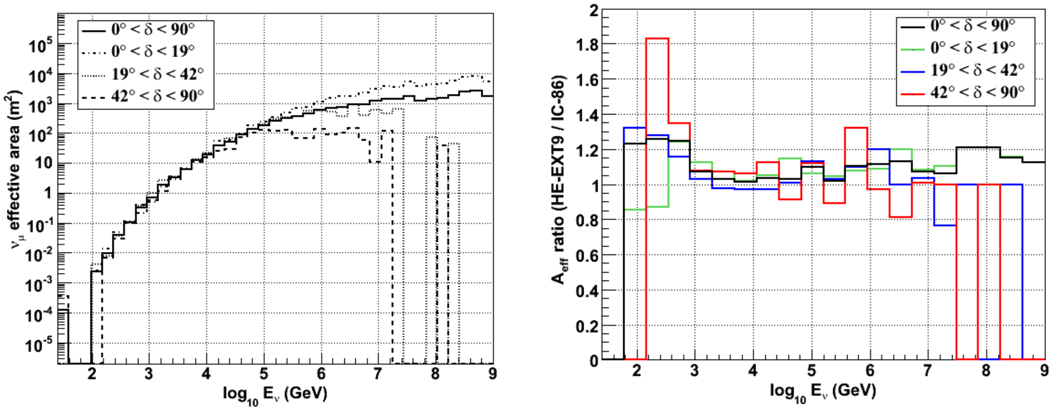

Figure B.5: Muon neutrino effective areas for the 86-string IceCube detector after final event selection. Left panel shows the default configuration in several zenith bands. Right panel shows the ratio in effective area between the extended and default geometries. An increase of ∼20% is seen near the horizontal for the highest energies. A small statistical sample at low energies means that ratios below 1 TeV should be disregarded.

of the 142 bursts. We then make an angular cut of 2° around the position of each burst to remove remaining background. This value is estimated based on the predicted angular resolution of the full IceCube detector of $< 1°$. This cut retains 70–90% of the signal depending on declination and energy spectrum. Recall that we consider three cases. First, that each burst follows an average Waxman-Bahcall spectrum. Second, that each burst has a spectrum calculated according to individual photon parameters. Finally, precursor emission assuming the Razzaque et al. flux. For the case of individual flux modeling, we have not applied the angular cut to simulation. However, based on Fig. B.2, we argue that the average spectral shapes are similar and apply the same overall passing rate as for the Waxman-Bahcall flux. The final event counts and passing rates for both geometries are shown in Table B.2. We compare the discovery potential (see section 7.4) of the two configurations in Fig. B.6. We have not shown the final sensitivity for the individual flux modeling, but because the background is the same, it will simply scale linearly from the average model. We see that for the average prompt and precursor fluxes, the difference between the geometries using the method outlined here is negligible. This could be considered surprising, as the effective area for the extended geometries increases at high energies. However, the event rate for GRBs is highly peaked at 100 TeV, and falls off rapidly as energy increases. Therefore, in a simple counting experiment such as we have proposed, little benefit is to be gained from a high energy extension. One must consider methods that incorporate the energy of each event such as the unbinned analysis presented in this thesis to truly take advantage of the additional effective area at the highest energies. What we should focus on in Fig. B.6, rather, is that we will be able to detect an average prompt emission in greater than 90% of potential experiments within a single year of full IceCube operations. In the event that we make no such detection, we will be able to set meaningful limits on the emission scenarios.

	signal events	passing rate	background events
Default			
prompt (Waxman-Bahcall)	6.17	78%	0.006
prompt (individual)	14.72	78%	0.006
precursor	5.2	69%	0.015
Extended			
prompt (Waxman-Bahcall)	6.22	75%	0.0047
prompt (individual)	15.2	75%	0.0047
precursor	5.16	65%	0.009

Table B.2: Final event rates for signal and background for the default and extended 86-string IceCube geometries. Three emission models are considered. Columns: signal events – mean GRB neutrinos after all cuts, passing rate – angle and energy averaged signal passing rates after angular cut relative to SBM cut level, background events – background events expected after scaling to total emission ontime window.

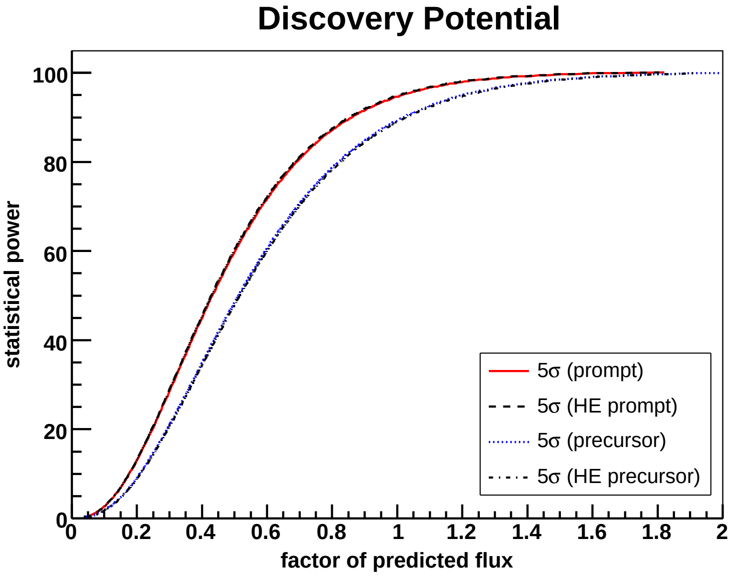

Figure B.6: Discovery Potential for 1 yr. of 86-string IceCube operations. 142 gamma-ray bursts are included in the fake data set. In this figure, prompt refers to an average Waxman-Bahcall spectrum for all bursts. x-axis represents the multiple of the predicted emission needed to make a discovery with the stated significance. y-axis shows the statistical power. Based on this study, we will be able to discover the Waxman-Bahcall flux at greater than 90% power within a single year.

Appendix C

Event Selection with Support Vector Machines

Support Vector Machines (SVMs) [130, 131] are a set of related supervised learning methods used for classification and regression. For the purposes of physics analysis, we will restrict ourselves to the classification case. SVMs have the useful property of simultaneously minimizing the classification error and maximizing the margin between classes; that is, they maximally separate signal and background while having low mis-classification. We present here an overview of the theory of SVMs, describing the method by which they operate and the algorithms solved by software implementations. We then show the application to a GRB analysis, with examples from the 2005-2006 AMANDA-II dataset. For a more thorough description of the underlying principles and extensive details, see the SVM tutorial by Burges [132].

Support vector machines map input vectors to a higher dimensional space where a maximal separating hyperplane can be constructed. (In 2-dimensional space, a hyperplane is a line, in 3-dimensional space it is a plane, and we generalize to higher dimensions.) Two parallel hyperplanes are then constructed on each side of the hyperplane that separates the data. The best separating hyperplane is that which maximizes the distance between the two parallel hyperplanes. Fig. C.1 illustrates this concept schematically.

Before exploring the operation of SVMs in more detail, we summarize the basic concepts of what tools we use and what we wish to accomplish. In the sections that follow, we illustrate examples for the case of *2*-dimensional data to simplify the discussion.

- We represent each data point as an n-dimensional vector. In the case of a physics analysis, this vector contains all the variables of interest for each event.

- Each data point belongs to one of 2 classes, signal or background.

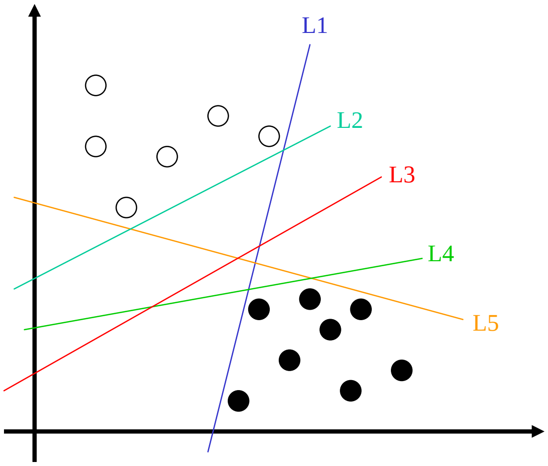

Figure C.1: There are many possible hyperplanes that separate these classes of 2-dimensional data. However, only one such hyperplane (not illustrated) maximally separates them.

- We want to separate the data classes using an "$n-1$"-dimensional hyperplane. We want the separation to be maximal.
- We want to minimize the mis-classification of background events as signal (and vice versa).

C.1 Fully Separable, Linear Case

From a pedagogical standpoint, it is most useful to start with the simplest case (linearly separable, fully separable) and then advance to the more general case of a real analysis (non-linear separation, not fully separable). To that end, let's look at the formalization of the problem. We organize our data to take the form

$$\{(\mathbf{x}_1, y_1), (\mathbf{x}_2, y_2), \ldots, (\mathbf{x}_n, y_n)\} \tag{C.1}$$

where the y_i is either 1 (signal) or -1 (background). Each $\mathbf{x}_i$ is a n-dimensional vector corresponding to the event variables of interest. We call this data set the *training data*, as it consists of events which are known to be either background or signal [1]. The separating hyperplane then looks like

---

[1] This is precisely why an SVM is well suited for GRB analysis. In order to properly train the machine, distinct signal and non-signal classes must exist. For signal we may input simulated neutrino events, weighted to the spectrum of interest. Non-signal is in general more difficult, as it requires extremely well-simulated background. However, in the case of GRBs, the signal is strongly time-dependent, so an off-time measurement of the data yields a known"signal free" training set.

$$\mathbf{w} \cdot \mathbf{x} + b = 0. \tag{C.2}$$

The vector $\mathbf{w}$ points perpendicular to the separating hyperplane. Adding the offset parameter b allows more generalization, permitting solutions that do not pass through the origin. We are interested in maximizing the separation between signal and background, so we create another pair of parallel hyperplanes such that all data i in our training set obey

$$y_i(\mathbf{w} \cdot \mathbf{x}_i + b) - 1 \geq 0 \tag{C.3}$$

The problem is then reduced to minimizing $\mathbf{w}$ subject to the above constraints, as demonstrated by the geometry in Fig C.2.

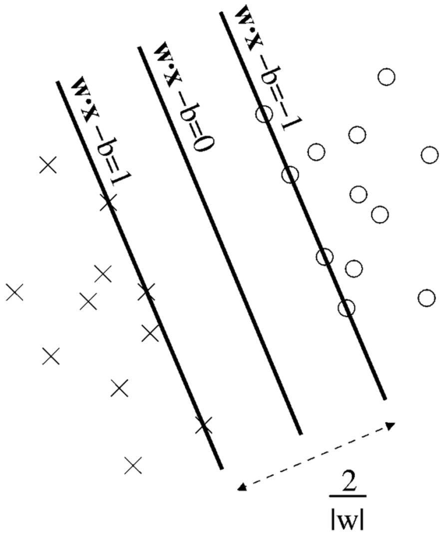

Figure C.2: Diagram of a maximally separating hyperplane in the linear, fully separable case. The solution is that hyperplane which minimizes $\mathbf{w}$. The hyperplanes whose solutions are 1 and -1 are known as the *margins*.

Let us now switch to a Lagrangian formulation of the problem. We do this for two reasons.

- The constraints above will be replaced by constraints on the Lagrange multipliers, which are easier to work with.
- After reformulation, the data will only appear as dot products between vectors. This will turn out to be useful later.

We assign a Lagrange multiplier α_i to each inequality given by Eq. C.3, and write the Lagrangian:

$$\mathcal{L} \equiv \frac{1}{2}\|\mathbf{w}\|^2 - \sum_i \alpha_i y_i (\mathbf{w} \cdot \mathbf{x}_i + b) + \sum_i \alpha_i \tag{C.4}$$

We can solve this problem by minimizing $\mathcal{L}$ with respect to $\mathbf{w}$ and b, and requiring that all the derivatives with respect to α_i vanish. Also, by our formulation, each of the $\alpha_i \geq 0$. This can be reformulated once more into a Wolfe dual problem (see the book by Fletcher [133] for the method). In this formulation, we *maximize* $\mathcal{L}_D$ such that the gradients with respect to $\mathbf{w}$ and b vanish, as well as our conditions on the Lagrange multipliers. These constraints give the conditions:

$$\mathbf{w} = \sum_i \alpha_i y_i \mathbf{x}_i \tag{C.5}$$

$$\sum_i \alpha_i y_i = 0 \tag{C.6}$$

Since this problem is dual to the original Lagrangian formulation, we may substitute these conditions to arrive at

$$\mathcal{L}_D = \sum_i \alpha_i - \frac{1}{2}\sum_{i,j} \alpha_i \alpha_j y_i y_j \mathbf{x}_i \cdot \mathbf{x}_j. \tag{C.7}$$

Any data point in the training sample that has $\alpha_i > 0$ is called a *support vector* and lies on the margin. If all other training points (with $\alpha_i = 0$) were removed, the SVM would find the same solution.

C.2 Non-Separable, Linear Case (Soft Margin)

For actual data, it is not usually the case that signal and background are completely separable. Therefore we would like to allow for “mislabeled examples” in our minimization. In this case, there is no hyperplane that cleanly separates the two classes (see Fig C.3. Instead, we introduce slack variables ξ_i which measure how badly misclassified the data is. The constraint of Eq. C.3 then becomes

$$y_i(\mathbf{w} \cdot \mathbf{x}_i + b) \geq 1 - \xi_i \tag{C.8}$$

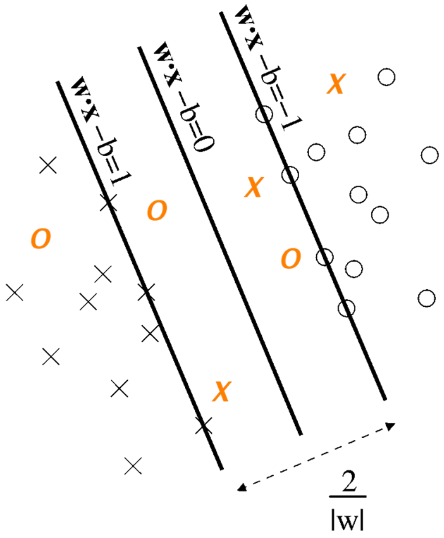

Figure C.3: The case of a linear, non-separable dataset in SVM classification. The data of Fig. C.2 have been augmented with additional points (in orange) that cannot be cleanly separated. We must now draw the separation hyperplane that minimizes the mis-classification.

The problem to be solved is now slightly more complicated, as we seek to simultaneously maximize the separation between signal and background while minimizing the mis-classification. We introduce a function that penalizes non-zero ξ_i and get our new objective function

$$\min\left(\frac{1}{2}\|\mathbf{w}\|^2 + C\sum_i \xi_i\right) \tag{C.9}$$

where C is the penalty factor for data points that lie on the wrong side of the separating hyperplane. We now substitute this into our dual Lagrangian C.7, where our earlier and well considered choices mean that the ξ_i do not appear in the problem. In fact, the only difference is that we now have the constraint that the α_i have an upper bound of C.

$$0 \leq \alpha_i \leq C \tag{C.10}$$

If we want to be more sophisticated, we can assign different penalty parameters C^+, C^- to the signal and background training data. This lets us, for example, penalize a misclassified signal data point more strongly than a misclassified background point. We will denote the ratio between these cost factors as j.

C.3 Non-Linear Case

Let us now consider the situation where the training data is not linearly separable at all. That is, there does not exist a separating hyperplane in $n-1$ space. In order to deal with this we must construct some function to map our data to a higher dimensional space

$$x \rightarrow \varphi(x) \tag{C.11}$$

where the data becomes linearly separable. While the principle is simple, the difficulty lies in determining the mapping function φ. But note that in Eq. C.7 we formulated our algorithm to only depend on the dot products of pairs of support vectors, so in the mapped space, this would look like

$$\varphi(x) \cdot \varphi(x') \tag{C.12}$$

While this does not seem to be particularly helpful, it in fact allows us to apply what is known as the *kernel trick*. This is an application of Mercer's theorem that states that any continuous, symmetric, positive semi-definite kernel function $K(x, x')$ can be expressed as a dot product in a high-dimensional space [134]. That is to say, there exists:

$$K(x, x') \equiv \varphi(x) \cdot \varphi(x'). \tag{C.13}$$

Thus, if we can find some suitable $K(x, x')$, we need not know φ and may instead replace the dot product in Eq. C.7 with the kernel function. Fortunately, there exist several suitable kernel functions in the literature that are in common use in SVM work.

$$
\begin{aligned}
\text{Polynomial (homogeneous)} &: k(\mathbf{x},\mathbf{x}') = (\mathbf{x}\cdot\mathbf{x}')^d \\
\text{Polynomial (inhomogeneous)} &: k(\mathbf{x},\mathbf{x}') = (\mathbf{x}\cdot\mathbf{x}'+1)^d \\
\text{Radial Basis Function} &: k(\mathbf{x},\mathbf{x}') = e^{-\gamma\|\mathbf{x}-\mathbf{x}'\|^2}, \text{ for } \gamma > 0 \\
\text{Gaussian Radial basis function} &: k(\mathbf{x},\mathbf{x}') = e^{-\frac{\|\mathbf{x}-\mathbf{x}'\|^2}{2\sigma^2}} \\
\text{Sigmoid} &: k(\mathbf{x},\mathbf{x}') = \tanh(\kappa\mathbf{x}\cdot\mathbf{x}'+c) \\
&\quad \text{for some (not every) } \kappa > 0 \text{ and } c < 0
\end{aligned}
$$

Now we replace the dot product in our Lagrangian by the chosen kernel function, allowing us to map our data to some higher dimensional space (possibly infinite), where it becomes linearly separable. Solving the linear problem now gives us some $\mathbf{w}$ that lives in this high dimensional space. This can once again be rewritten in terms of the kernel function to provide solutions in the real variable space (see Burges [132]). Fig. C.4 shows a sample application of this principle.

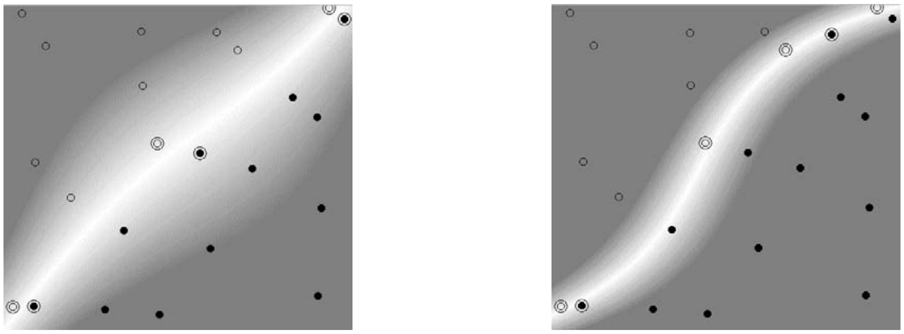

Figure C.4: SVM classification using a 3 degree polynomial kernel function. Left panel depicts the linearly separable case, which the kernel function emulates well. Right panel depicts the non-linear case. In this case the data is mapped to a higher dimension with the kernel function and linearly separated. In the real data space the (now very clean) separation takes the form of some curve. (from [132])

C.4 Example Application to a GRB Analysis

SVMs are very well suited to application in a GRB analysis due to the known signal free off-time data set. As an example, we consider the case of separation of signal neutrinos from background for the representative burst GRB050319. Following the procedure described in Chapter 5, we blind a 10 minute window around the trigger time and use the remaining data in a 2 hour window around the trigger as a signal-free background set. We will use this 2 hour data to train the SVM. To obtain a signal training sample, we simulate a point source of neutrinos at the location of the GRB and weight the events according to the Waxman-Bahcall prescription [45].

We first must choose an SVM software implementation. Several packages exist, including a class in ROOT. However, for the purposes of this study, we choose the package SVM^{light} [135, 136]. This software is easy to set up, straightforward to run, and has some useful features. It allows for many thousands of training examples and support vectors, it is fast, and it allows for the training data to be weighted. This last feature is vital, as it allows many thousands of simulated signal neutrinos to be weighted as the signal from a single GRB.

We next choose a set of features on which to train the SVM. these should be event variables that clearly distinguish signal from background. In order to keep the analysis as unbiased as possible, we exclude energy variables from consideration.

- **Smoothness (sphit):** A measure of how the hits are distributed relative to a cylinder constructed around the reconstructed track direction. An excellent track will have a smoothness close to 0 as the hits are evenly spaced. Smoothness near 1 or -1 corresponds to a majority of events clumped at one or the other end of the track.

- **Direct Length (ldirb):** A measure of the length of the track, calculated relative to direct hits. High energy (GRB) events are likely to have a longer track length than cascades or low energy atmospheric muons.

- **Number of Direct Hits (ndirc):** The number of hits which are in time agreement with the reconstructed track (within -25 to +75 ns). A well-reconstructed, high-energy track will have many direct hits.

- **Space Angle (psi):** The difference in direction between the reconstructed track and the direction of the GRB. GRB neutrinos will have a small space angle, while the background will be distributed essentially isotropically.

- **Ratio between upgoing and downgoing reconstructions (jkchi):** The ratio between the unbiased reconstruction likelihood and that of a reconstruction weighted with the zenith distribution of downgoing muons. Upgoing neutrinos will have a higher value of this parameter than mis-reconstructed muons.

We now create *5*-dimensional feature vectors for each event in our datasets and assign a value of $\langle +1 \rangle$ to simulated signal neutrinos and $\langle -1 \rangle$ to the off-time background. Each event is also assigned a weight. Signal is weighted according to the GRB spectrum and then to a total normalization, while background is weighted to the duration of the GRB and the same normalization. In this way, the SVM classifies based on the shapes of the distributions rather than on magnitude.

We adopt the procedure outlined by Hsu et al. [137] to optimize our study. Since the SVM algorithm works by taking dot products of the feature vectors, it is important that all data is at about the same scale. If we let track length remain in the range $\{0, 400\}$ while smoothness ranges from $\{-1, 1\}$, for example, the SVM will not optimize effectively. We therefore rescale the data such that most structure for each variable is in the $\{-1, 1\}$ range. It is acceptable for outliers to exist. The distributions of the feature vectors after rescaling are shown in Fig. C.5.

Since there may be a non-linear relationship between our class labels and the feature vectors, we should choose a kernel function that maps non-linearly to high dimensional space. We choose the Radial Basis Function (RBF) kernel for several reasons. First, it performs the necessary mapping while performing as well as a linear kernel. Second, it has only a few parameters to optimize (γ, C), which greatly speeds the analysis. Third, the function is well bounded, and cannot go off to infinity like polynomial kernels. Thus for our purposes, the RBF kernel is most well-suited. Recall that the RBF kernel function is given by

$$k(\mathbf{x}, \mathbf{x}') = e^{-\gamma \|\mathbf{x} - \mathbf{x}'\|^2}, \text{ for } \gamma > 0 \tag{C.14}$$

Having chosen a kernel, we must optimize 2 parameters; γ, the RBF kernel parameter, and C, the penalty factor applied to support vectors off the margins. This is best accomplished via a grid search. We want to choose parameters such that we can correctly identify unknown (testing) data, rather than solely the known training data. The best way to do this is via cross-validation. The training set is thus split into v parts and is trained on a $v - 1$ subset of the data. The remaining (untrained) single data set is then tested and the accuracy computed. This procedure is then iterated v times, with the total accuracy being the average. Such cross-validation can prevent the over-fitting problem (see Fig. C.6). A set of parameters could cleanly separate a training set but then perform

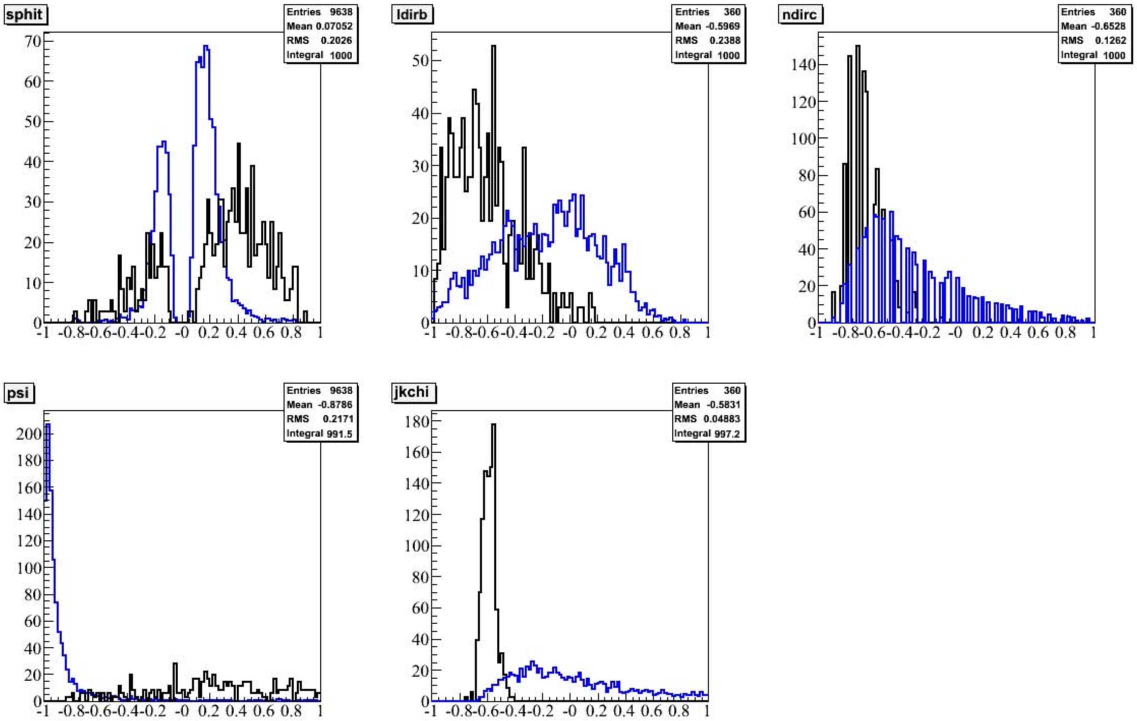

Figure C.5: Distribution of signal (blue) and background (black) for 5 feature vectors. Normalization of rates encourages classification based solely on the shape of the distributions. All variables have been rescaled to fall in the range (-1,1).

poorly on a test set. By cross-validating, we check to make sure that this does not occur in our final unknown (blinded) sample.

We now perform the grid search described above, varying γ and C and performing a 5-fold cross-validation at each point in the parameter space. In addition, we must perform this optimization over a range of $j \equiv C^+/C^-$, the ratio in penalty factors for mis-classifying signal versus background. For each j we choose the (γ, C) that minimizes the Model Rejection Factor (see Chapter 7). Fig. C.7 shows this minimization for several j.

As the SVM classifies each feature vector, it assigns an SVM output value representative of how like each class the event is. Fig. C.8 illustrates how changes in the kernel function drastically change the shape of the background and signal SVM output distributions.

We perform the grid search over a wide range of (γ, C, j) to determine the best possible SVM for classifying the data. This gives us a set of parameters that globally minimizes the MRF for our particular data. The SVM thus constructed is extremely efficient, yielding signal retention of $\sim$96%

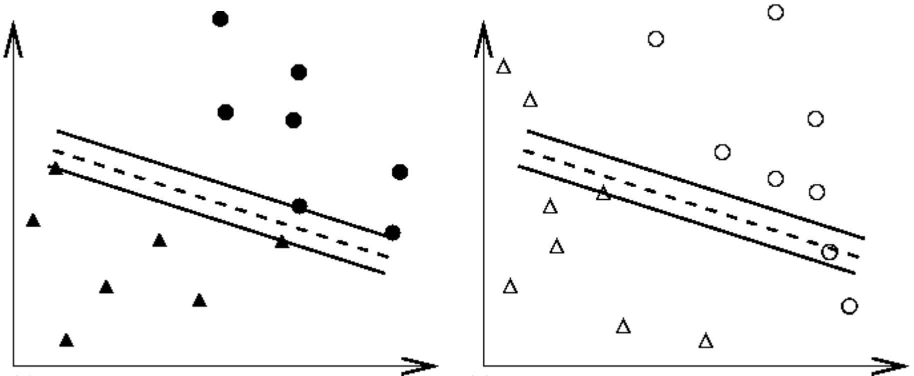

(a) Training data and an overfitting classifier (b) Applying an overfitting classifier on testing data

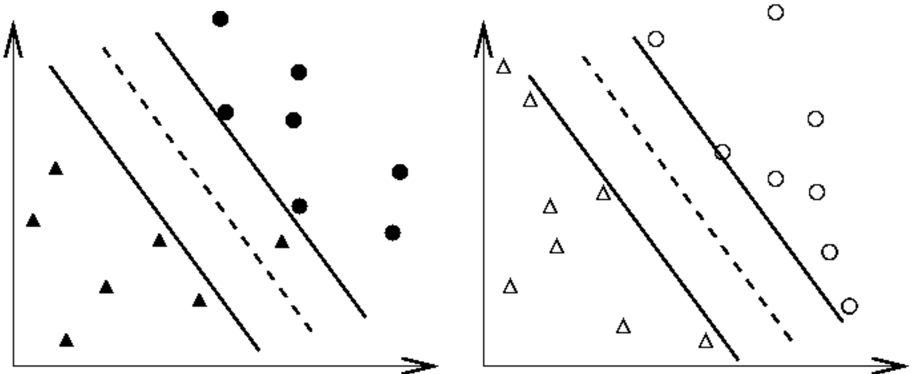

(c) Training data and a better classifier (d) Applying a better classifier on testing data

Figure C.6: The over-fitting problem in SVM classification. If the SVM is trained on only a single set of training data (a), the solution hyperplane may be too strict. In this case, when the SVM is applied to the testing data (b) mis-classification will occur. On the other hand, cross-validation leads to the training of a better classifier (c), which then separates the testing data more accurately (d). (from [137])

while retaining only 0.03% of background (see Fig. C.9). However, the cross-validation and grid search is computationally intensive, and the SVM method is somewhat of a“black box” approach. A simpler optimization making linear cuts on each of the same parameters loses only 4% of signal and retains only 1% more background. For this reason, the SVM technique was not adopted for event selection in our analyses. However, it has since been used in other work, notably a search of 22-string IceCube data for GRBs complementary to that presented in this thesis [93, 107]. It is an extremely powerful technique and resistance to machine learning algorithms for efficient background rejection is waning, so we expect to see an increased presence of SVMs in future analyses.

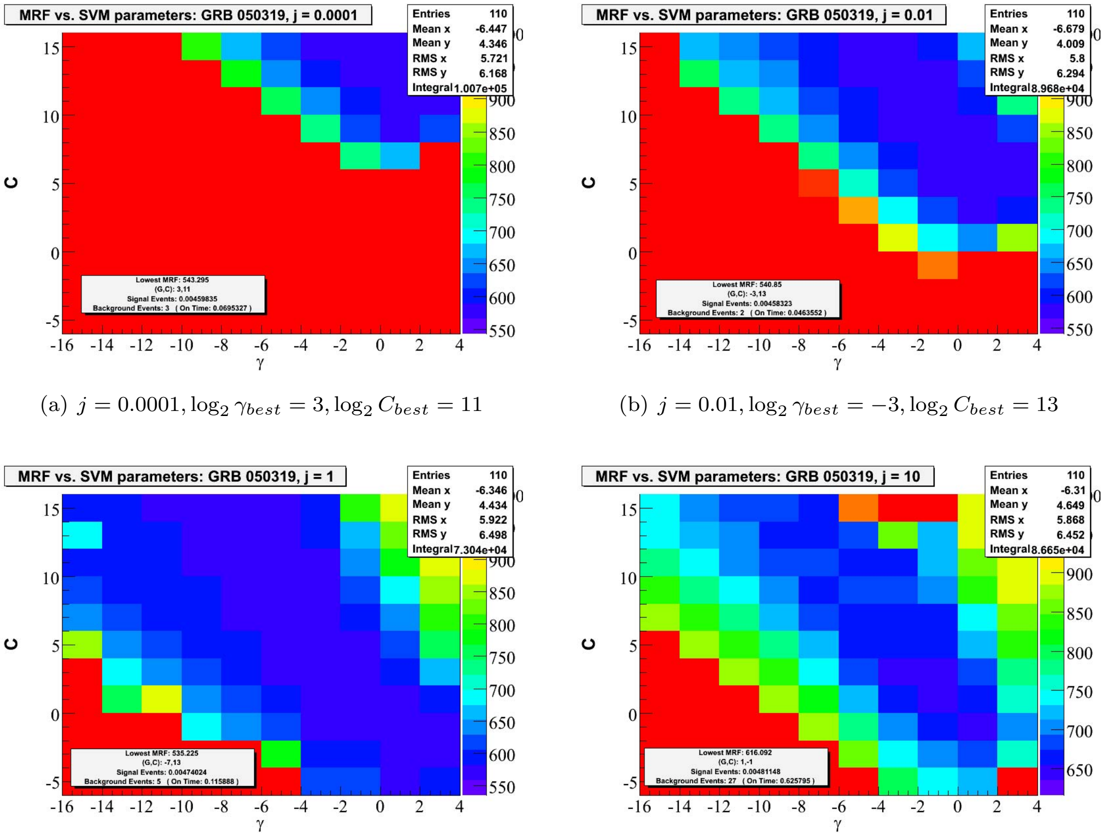

(a) $j = 0.0001, \log_2 \gamma_{best} = 3, \log_2 C_{best} = 11$

(b) $j = 0.01, \log_2 \gamma_{best} = -3, \log_2 C_{best} = 13$

(c) $j = 1, \log_2 \gamma_{best} = -7, \log_2 C_{best} = 13$

(d) $j = 10, \log_2 \gamma_{best} = 1, \log_2 C_{best} = -1$

Figure C.7: Grid search for best RBF kernel function parameters (γ, C) for several cost penalty ratios j. In these figures, the values on the axes represent $\log_2$ of the parameter in question. Thus the range of the search depicted here is both coarse and wide. In each case, we choose the point in the parameter space where a 5-fold cross-validated SVM using that particular radial basis function minimizes the MRF (maximizes sensitivity).

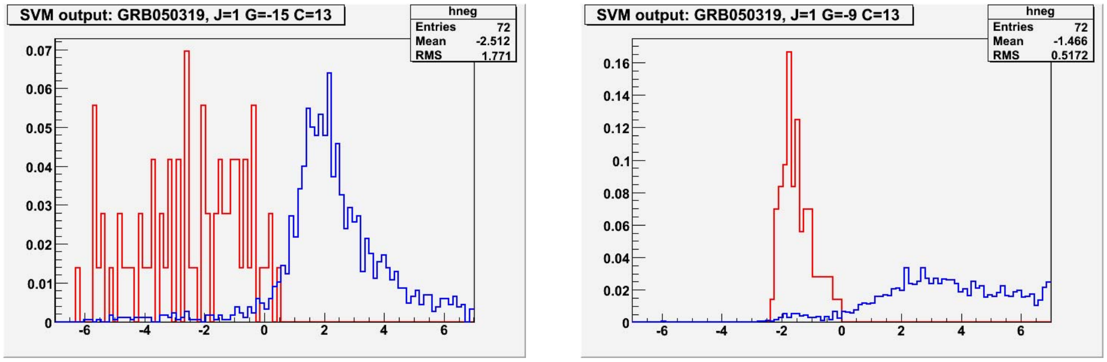

(a) $j = 1, \log_2 \gamma = -15, \log_2 C = 13$ (b) $j = 1, \log_2 \gamma = -9, \log_2 C = 13$

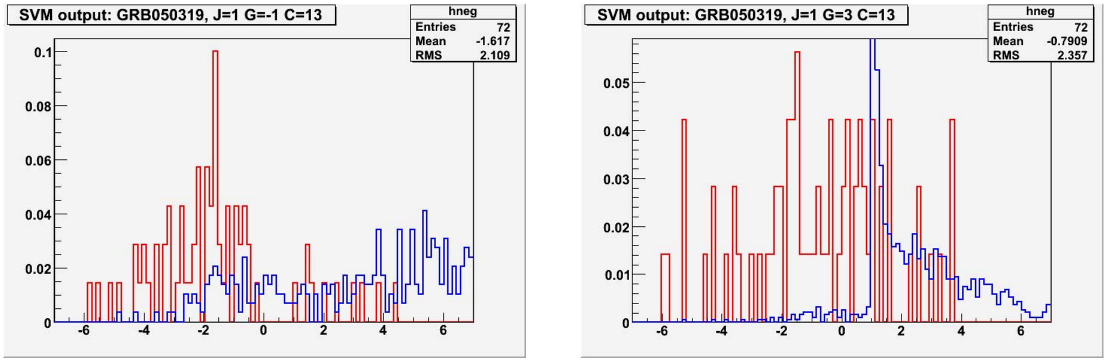

(c) $j = 1, \log_2 \gamma = -1, \log_2 C = 13$ (d) $j = 1, \log_2 \gamma = 3, \log_2 C = 13$

Figure C.8: Effect of variation of kernel parameter γ on SVM output. Here we keep j and C fixed. In these figures, the values on the axes represent $\log_2$ of the parameter in question. Blue denotes signal training data, red denotes background training data. Note that for some choices of the kernel function parameters, signal and background are well-separated, while for others they are not. This demonstrates the importance in scanning the full range of the kernel function space to ensure an effective SVM classification.

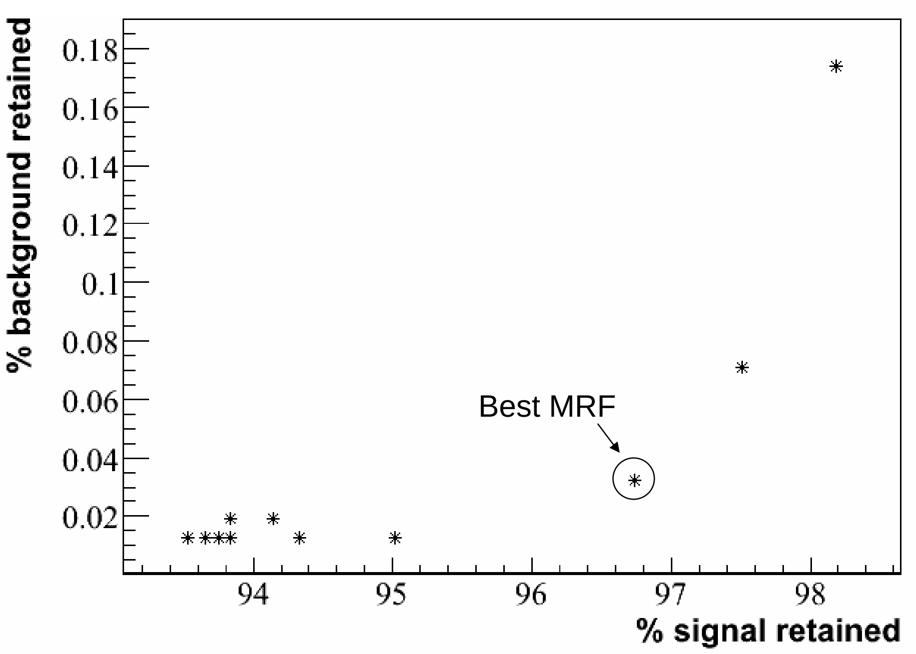

Figure C.9: Global optimization of SVM kernel function parameters. Each data point represents the best set of (γ, C) for a given j. The set of all parameters that gives the best sensitivity (lowest MRF) is chosen as the final SVM for classifying the unknown (blinded) dataset.

Appendix D

Light Curves of 2005-2006 Northern Sky GRBs

050319

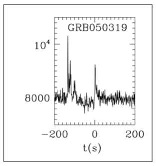

050401

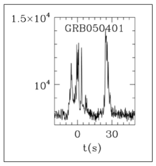

050408

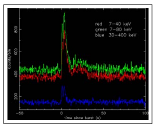

050410

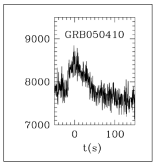

050416A

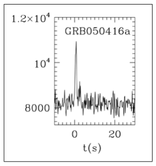

050416B

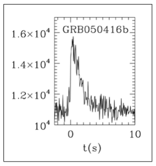

050421

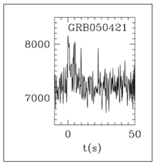

050422

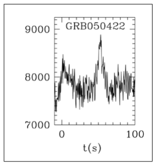

050502A

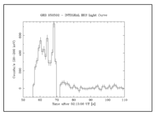

050502B

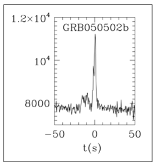

050504

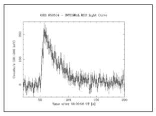

050505

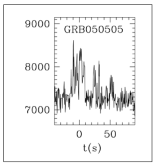

050509A

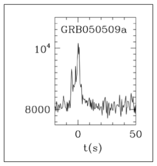

050509B

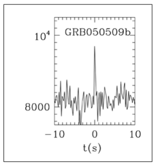

050520

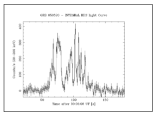

050522

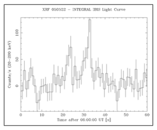

050525A

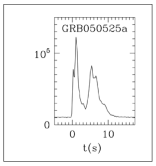

050528

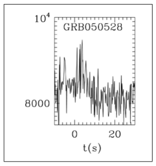

050607

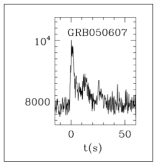

050712

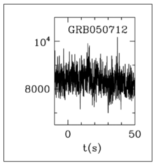

050713B

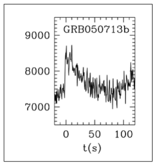

050714

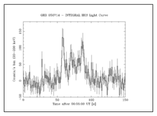

050802

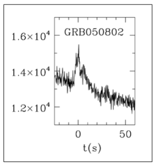

050803

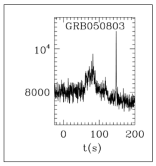

050813

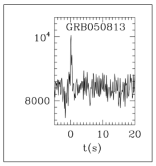

050814

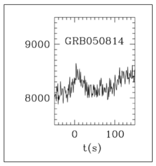

050815

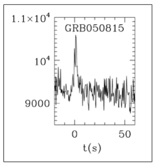

050819

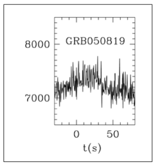

050820A

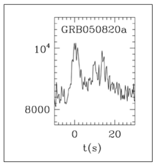

050824

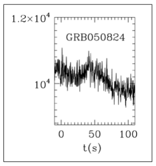

050827

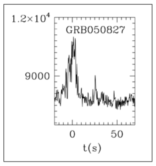

050904

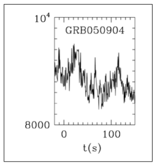

050925

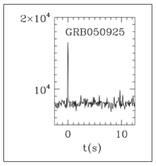

051006

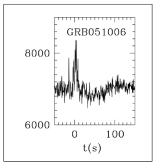

051008

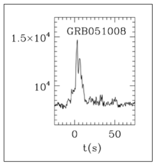

051016B

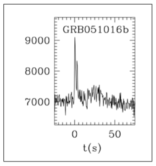

051021A

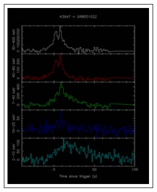

051022

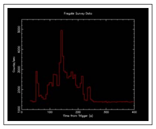

051105A

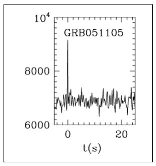

051109A

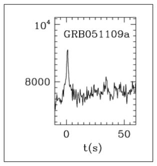

051109B

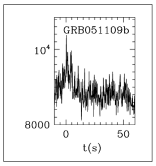

051111

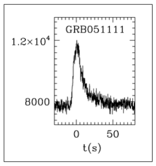

051114

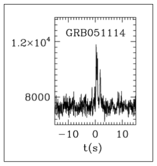

051117A

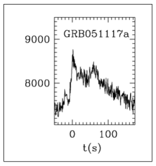

060105

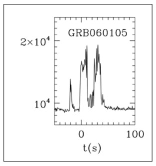

060108

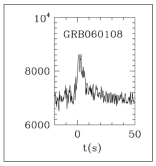

060109

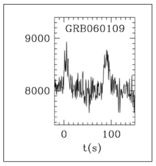

060110

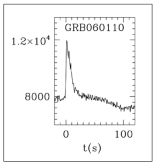

060111A

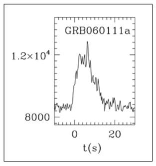

060202

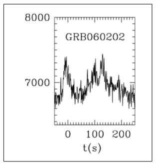

060204B

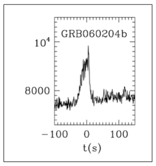

060211A

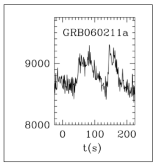

060211B

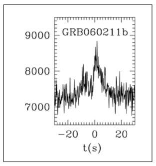

060218

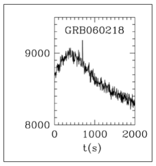

060219

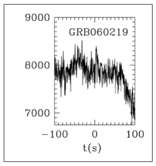

060312

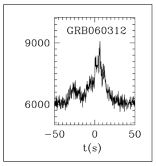

060319

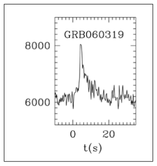

060323

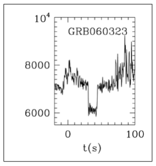

060403

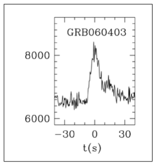

060413

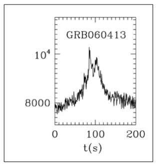

060421

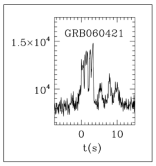

060424

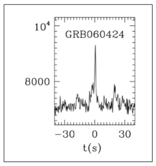

060427

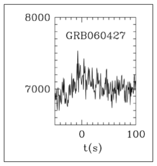

060428B

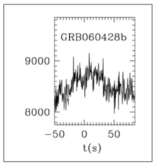

060501

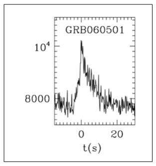

060502A

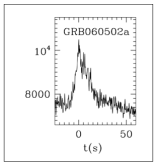

060502B

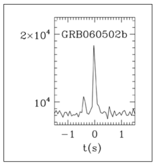

060507

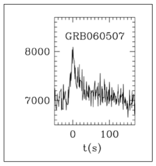

060510B

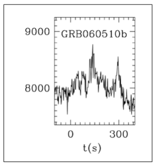

060512

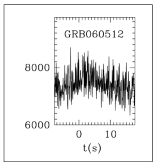

060515

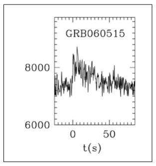

060522

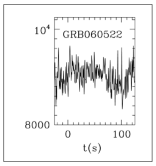

060526

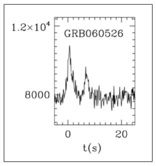

060602A

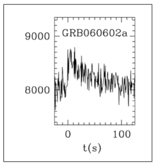

060607B

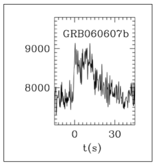

060712

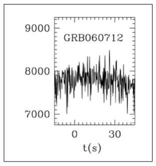

060717

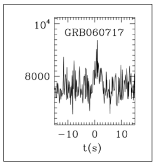

060801

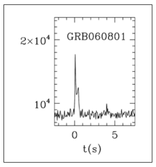

060805

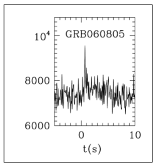

060807

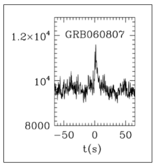

060814

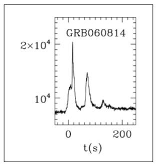

060825

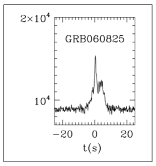

060904A

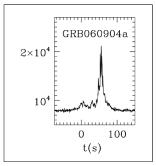

060906

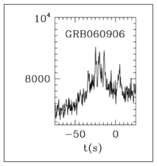

060912

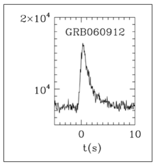

060923A

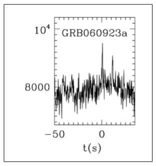

060923C

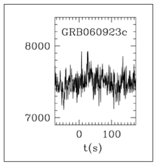

060926

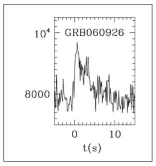

060929

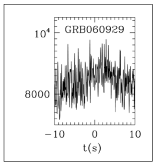

061002

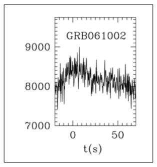

061019

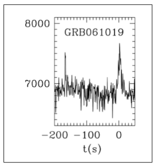

061028

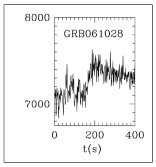

061110B

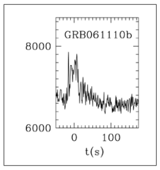

Appendix E

Stability Plots for 2005-2006 Northern Sky GRBs

E.1 Filter Level Rates in Background Windows

050319

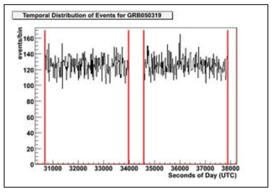

050401

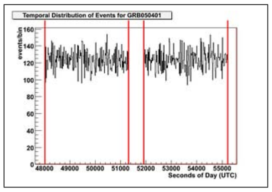

050408

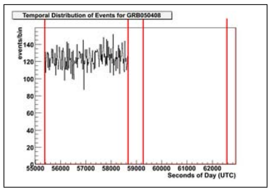

050410

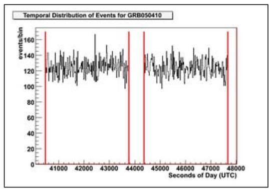

050416A

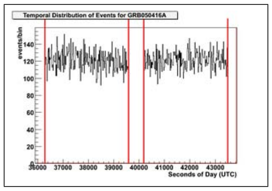

050416B

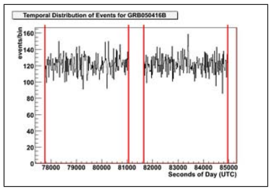

050421

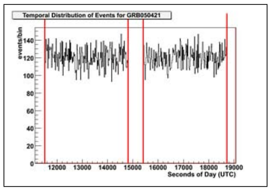

050422

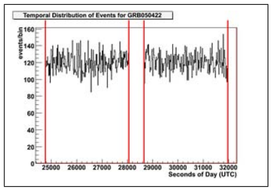

050502A

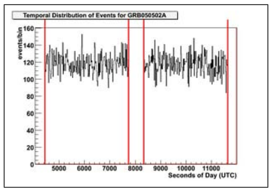

050502B

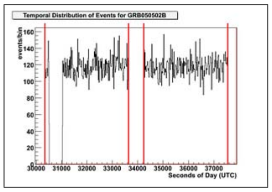

050504

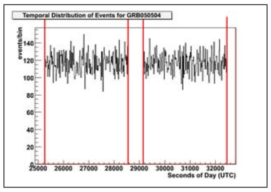

050505

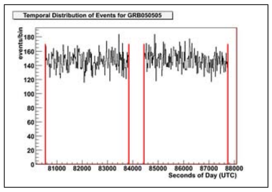

050509A

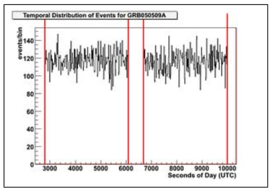

050509B

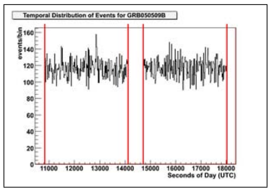

050520

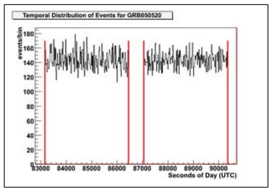

050522

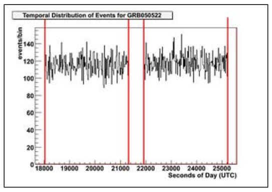

050525A

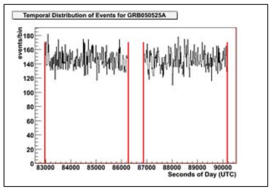

050528

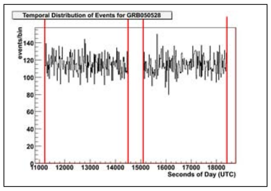

050607

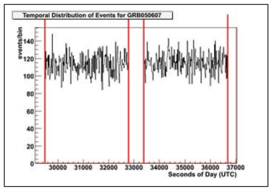

050712

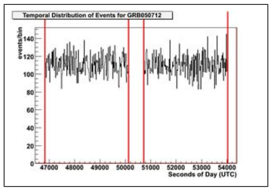

050713B

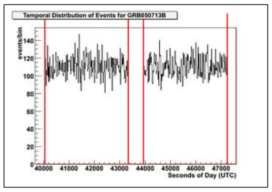

050714A

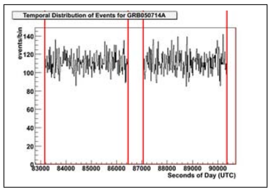

050802

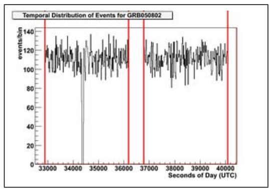

050803

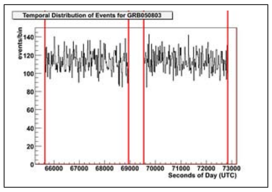

050805B

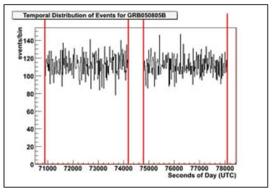

050813

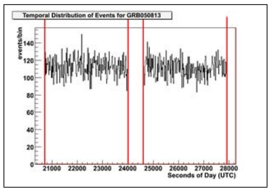

050814

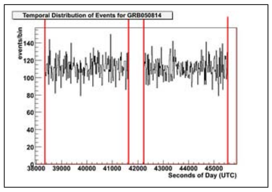

050815

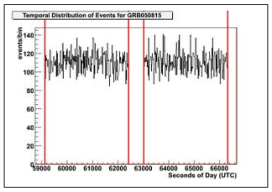

050819

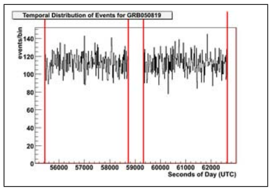

050820A

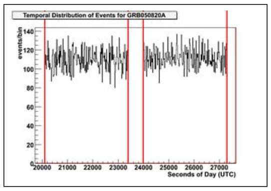

050824

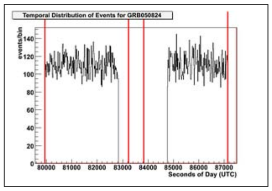

050827

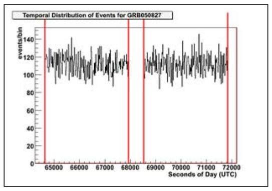

050904

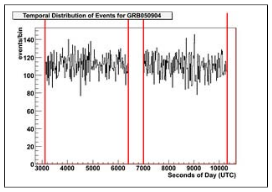

050925

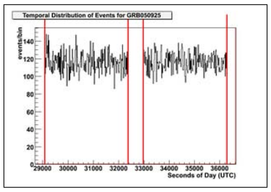

051006

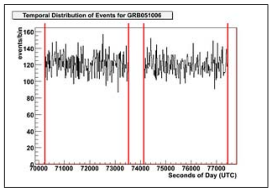

051008

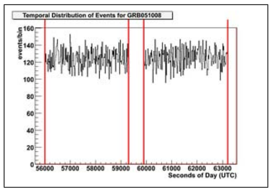

051016B

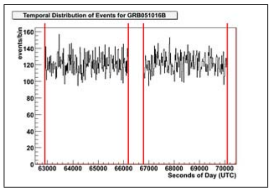

051021A

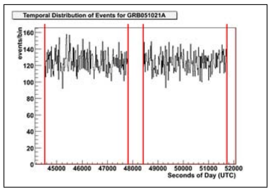

051022

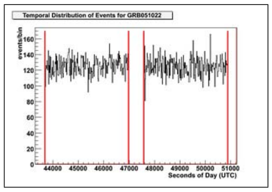

051105A

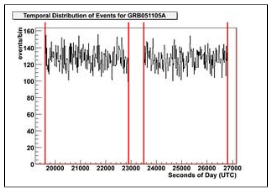

051109A

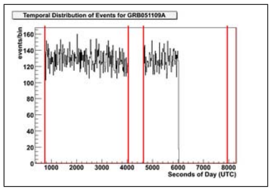

051109B

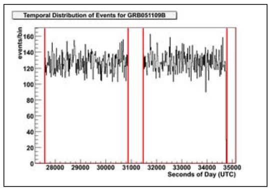

051111

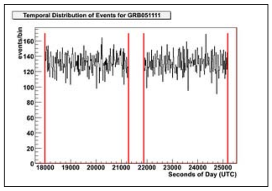

051114

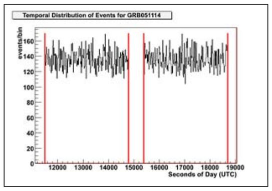

051117A

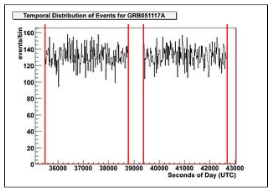

060105

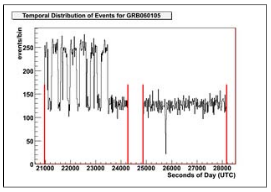

060108

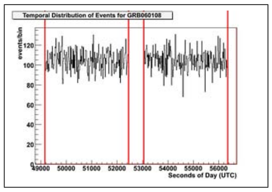

060109

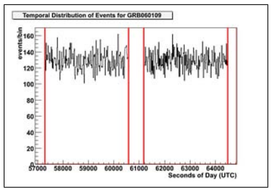

060110

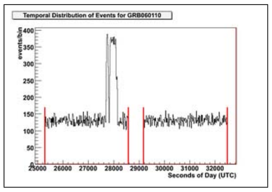

060111A

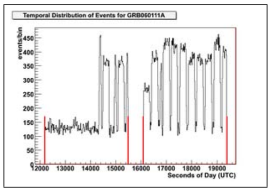

060202

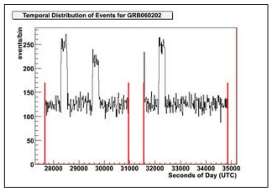

060204B

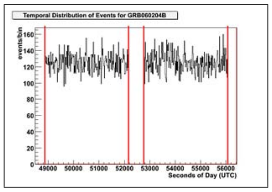

060211A

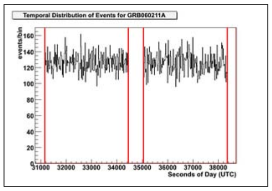

060211B

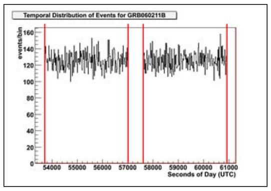

060218

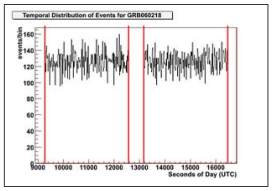

060219

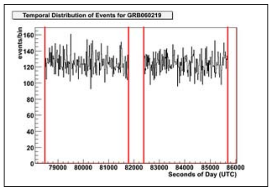

060312

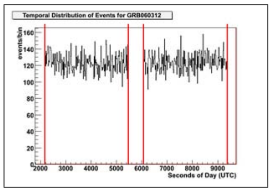

060319

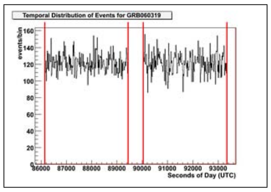

060323

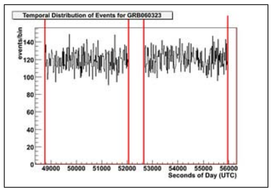

060403

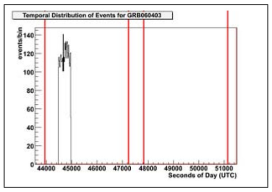

060413

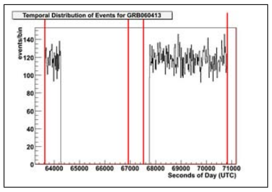

060421

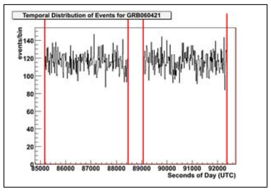

060424

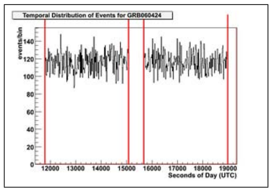

060427

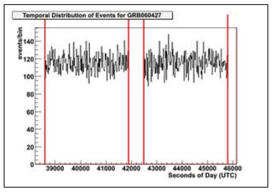

060428B

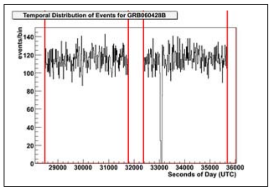

060501

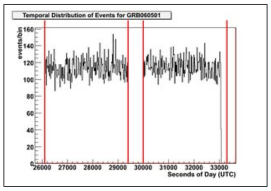

060502A

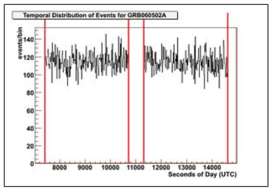

060502B

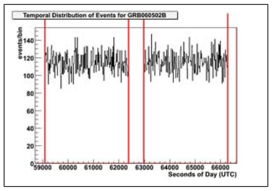

060507

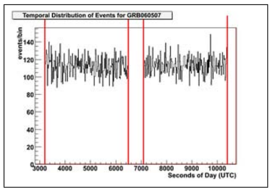

060510B

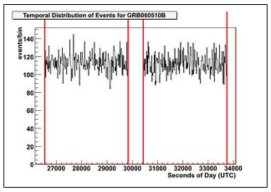

060512

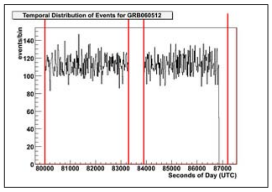

060515

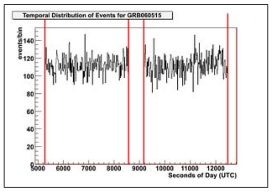

060522

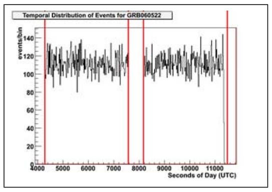

060526

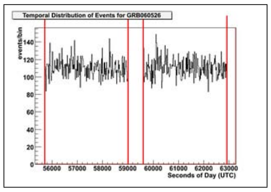

060602A

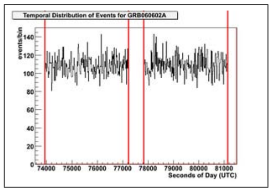

060607B

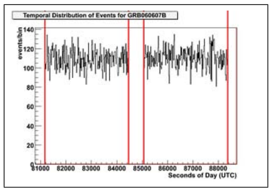

060712

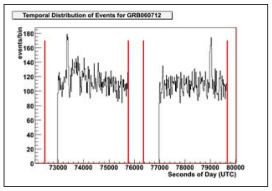

060717

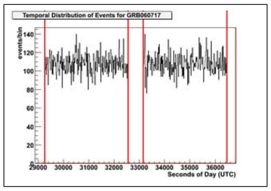

060801

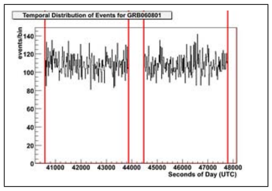

060805

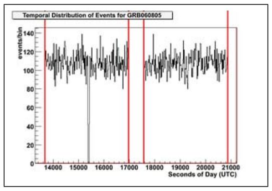

060807

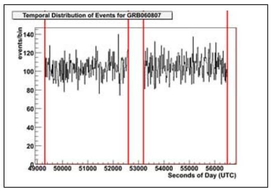

060814

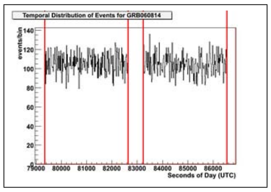

060825

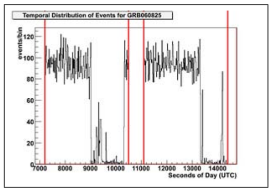

060904A

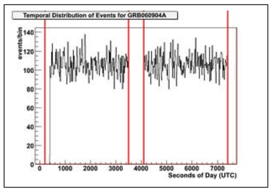

060906

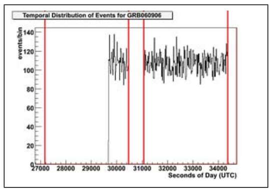

060912A

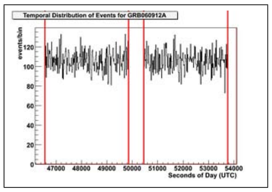

060923A

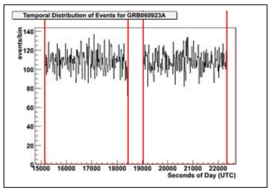

060923C

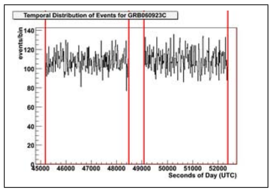

060926

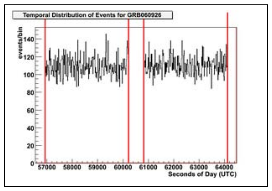

060929

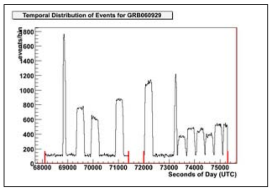

061002

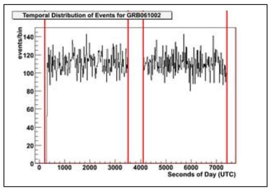

061019

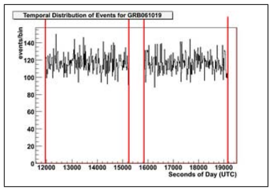

061028

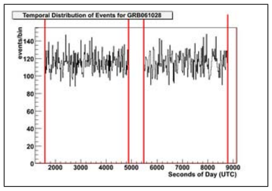

061110B

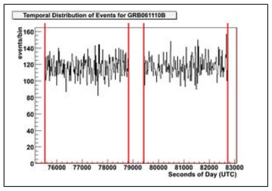

E.2 Distribution in Filter Level Rate per 10s

050319

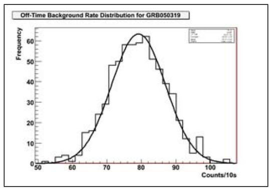

050401

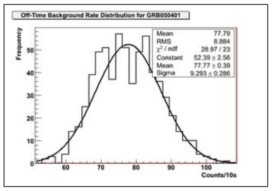

050408

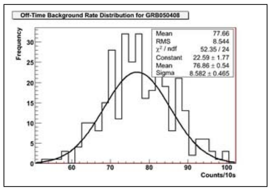

050410

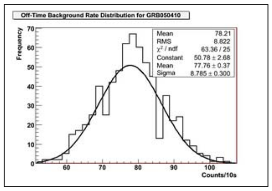

050416A

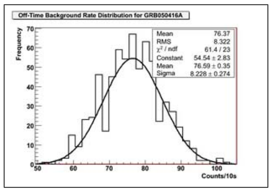

050416B

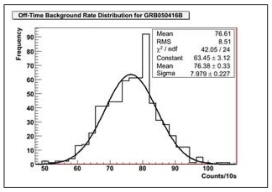

050421

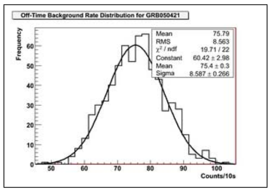

050422

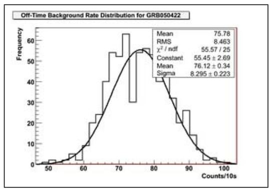

050502A

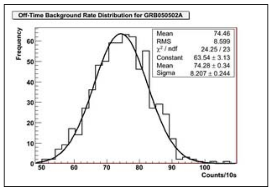

050502B

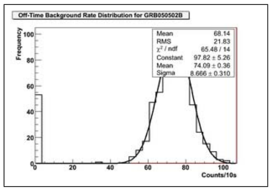

050504

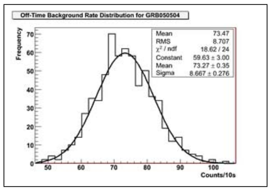

050505

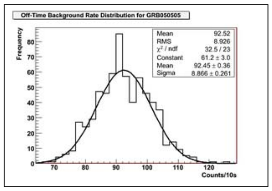

050509A

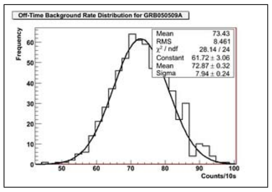

050509B

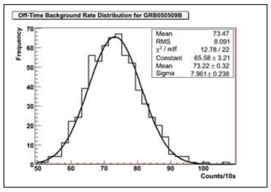

050520

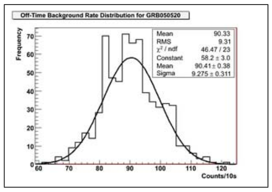

050522

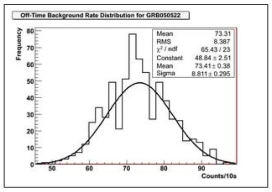

050525A

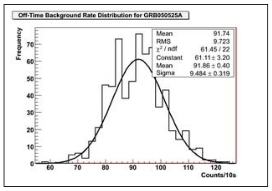

050528

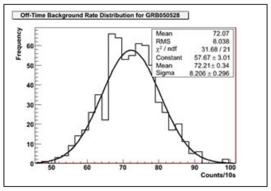

050607

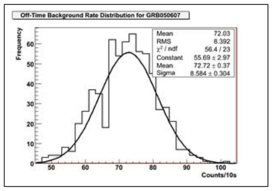

050712

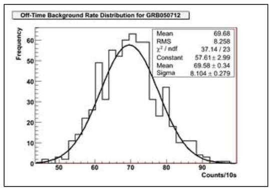

050713B

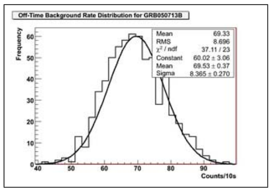

050714A

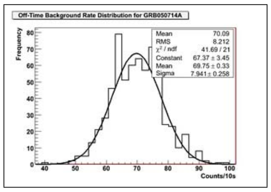

050802

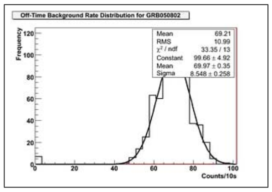

050803

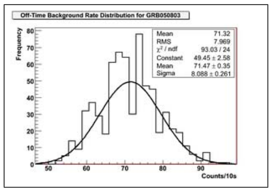

050805B

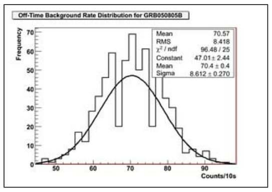

050813

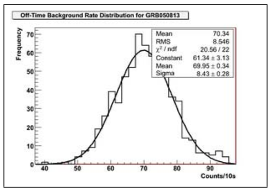

050814

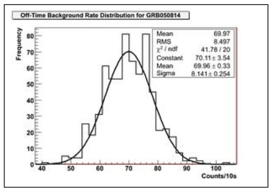

050815

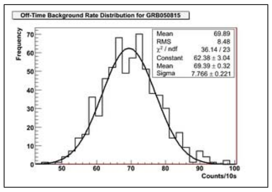

050819

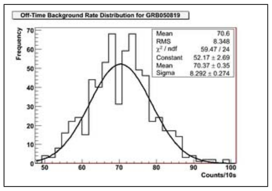

050820A

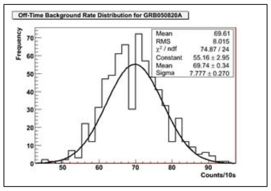

050824

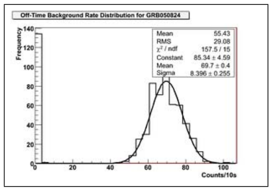

050827

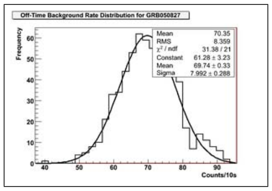

050904

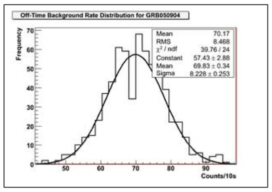

050925

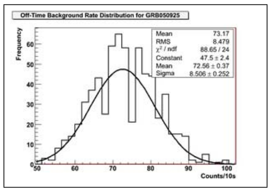

051006

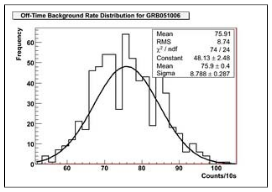

051008

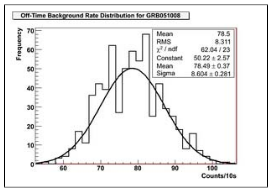

051016B

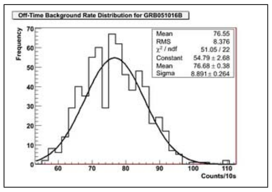

051021A

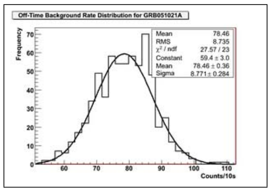

051022

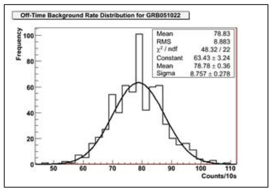

051105A

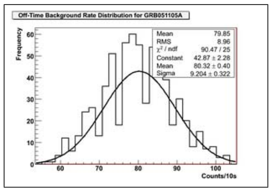

051109A

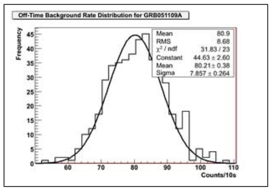

051109B

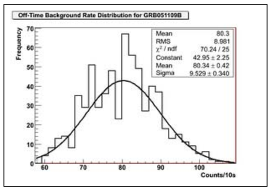

051111

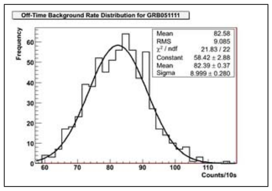

051114

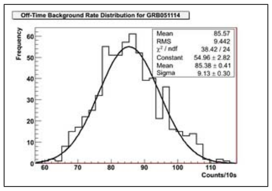

051117A

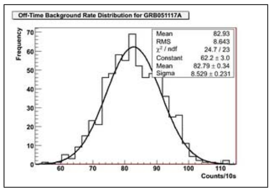

060105

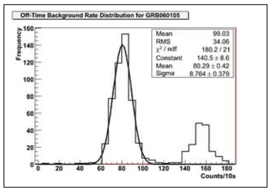

060108

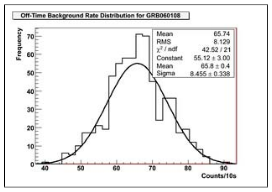

060109

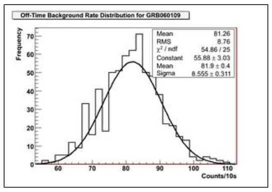

060110

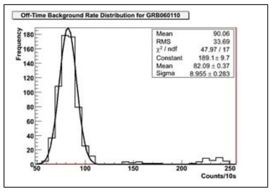

060111A

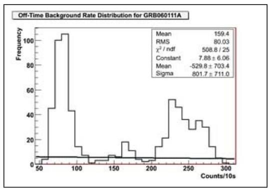

060202

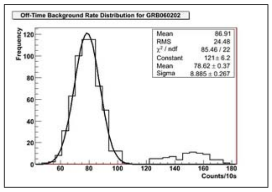

060204B

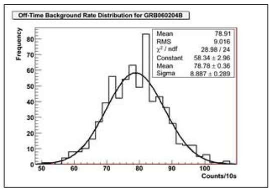

060211A

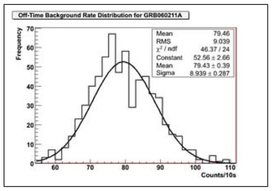

060211B

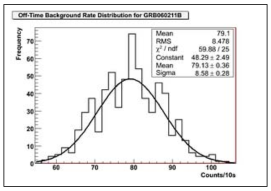

060218

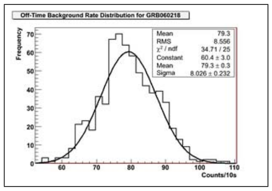

060219

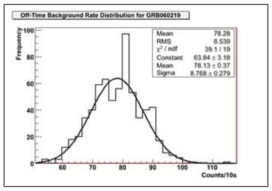

060312

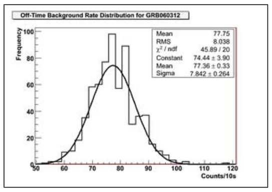

060319

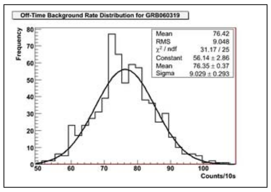

060323

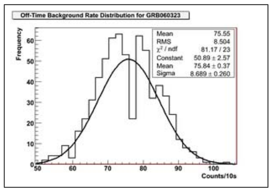

060403

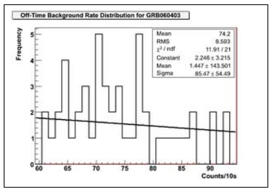

060413

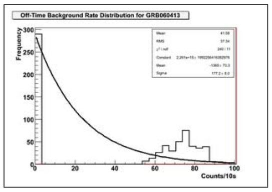

060421

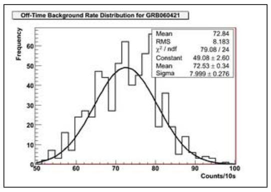

060424

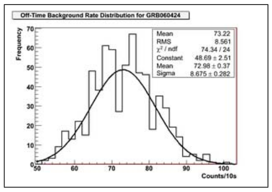

060427

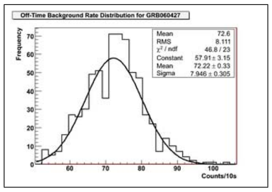

060428B

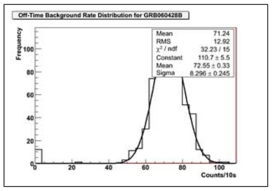

060501

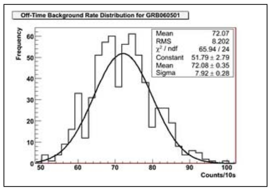

060502A

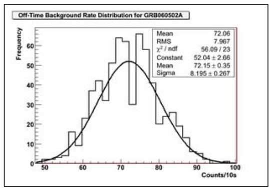

060502B

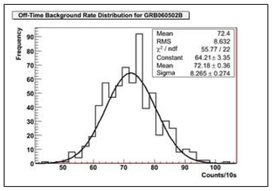

060507

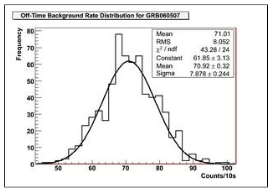

060510B

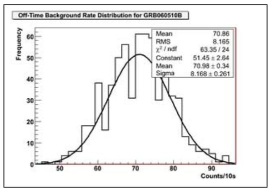

060512

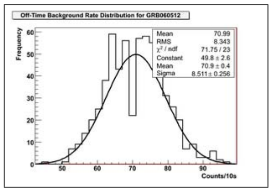

060515

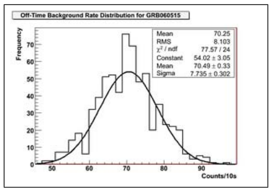

060522

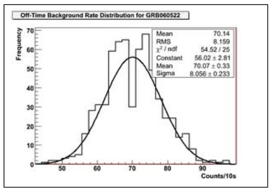

060526

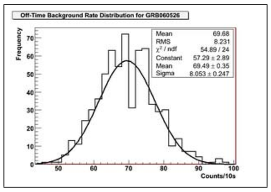

060602A

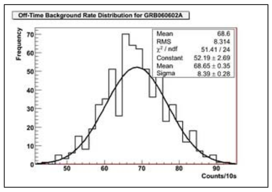

060607B

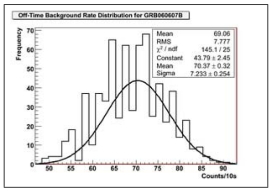

060712

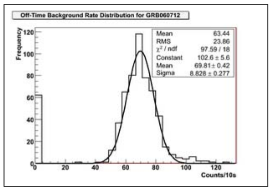

060717

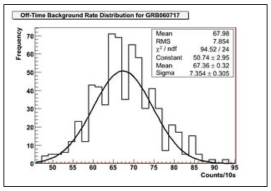

060801

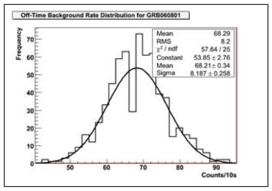

060805

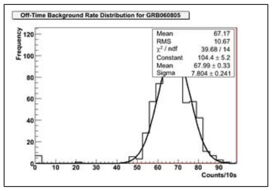

060807

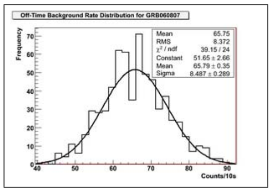

060814

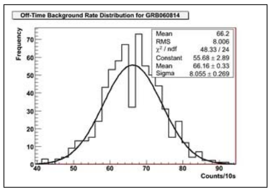

060825

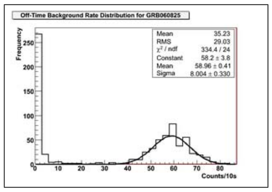

060904A

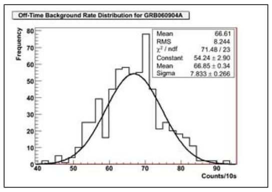

060906

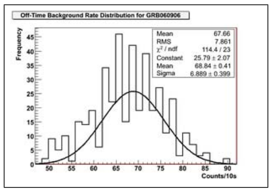

060912A

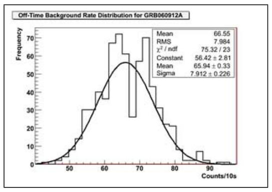

060923A

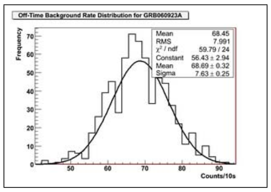

060923C

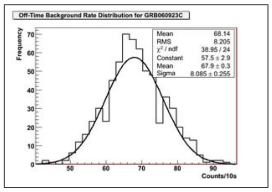

060926

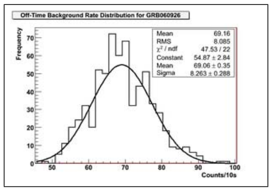

060929

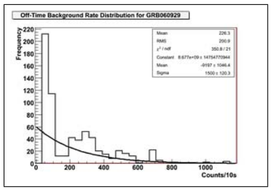

061002

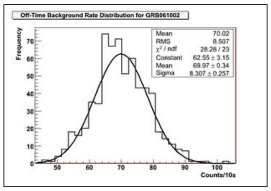

061019

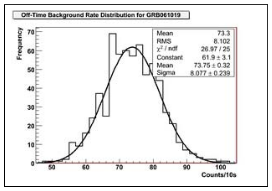

061028

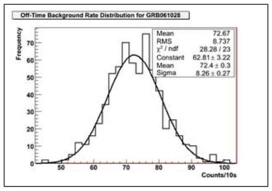

061110B

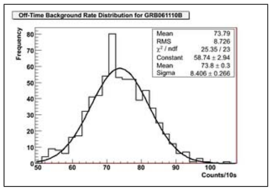

E.3 Time Differences Between Subsequent Events

050319

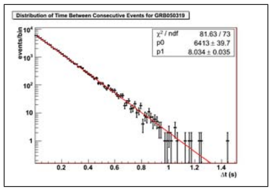

050401

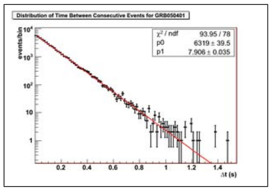

050408

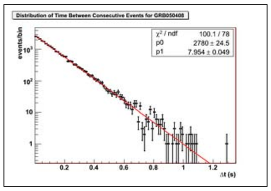

050410

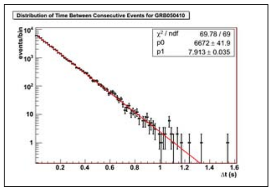

050416A

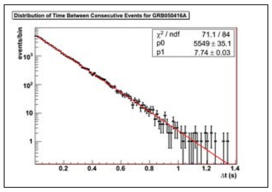

050416B

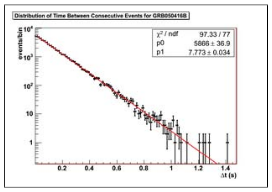

050421

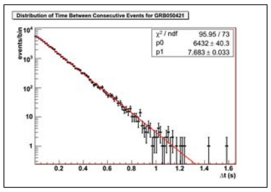

050422

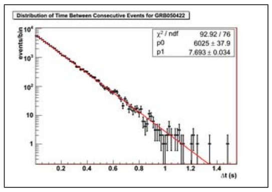

050502A

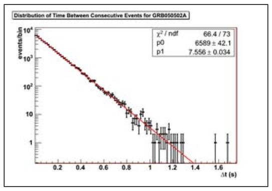

050502B

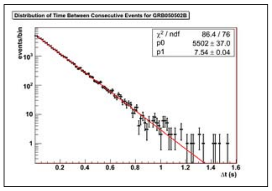

050504

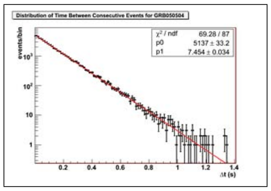

050505

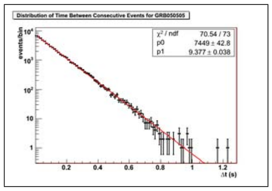

050509A

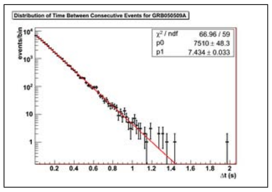

050509B

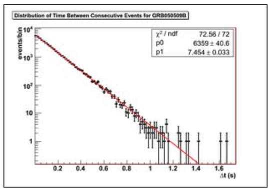

050520

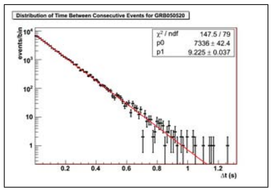

050522

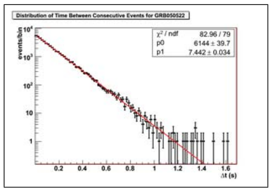

050525A

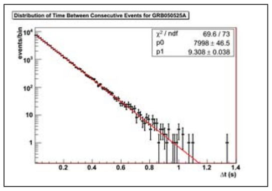

050528

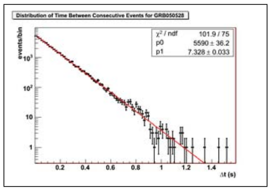

050607

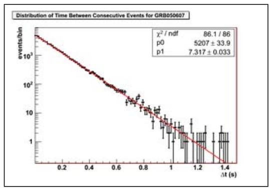

050712

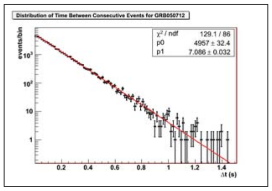

050713B

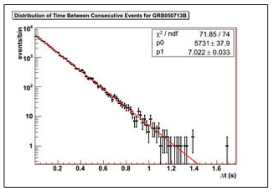

050714A

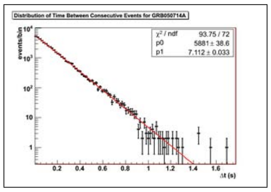

050802

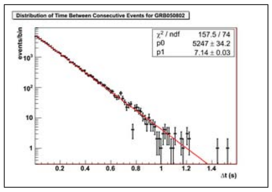

050803

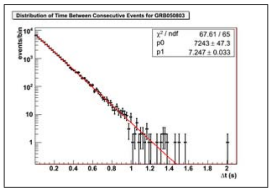

050805B

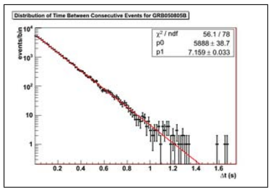

050813

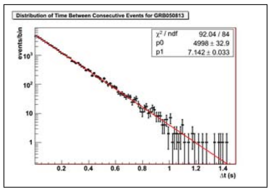

050814

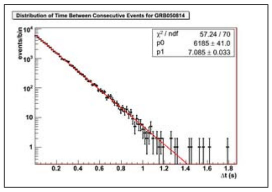

050815

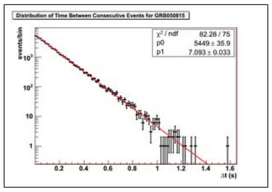

050819

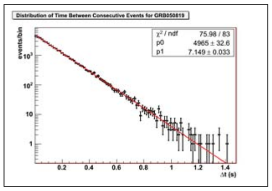

050820A

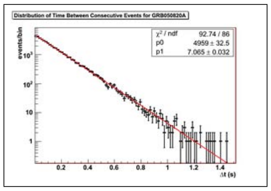

050824

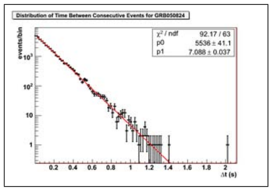

050827

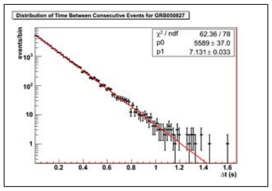

050904

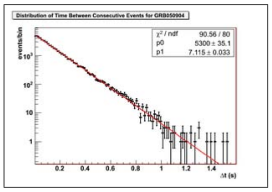

050925

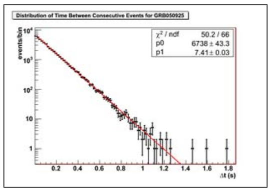

051006

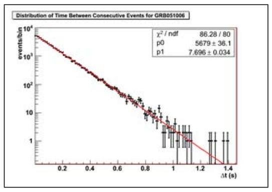

051008

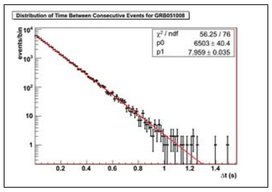

051016B

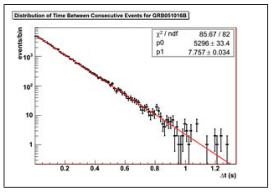

051021A

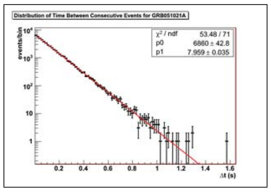

051022

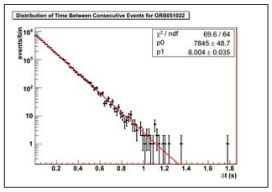

051105A

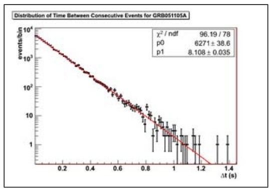

051109A

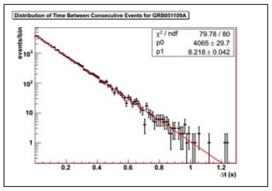

051109B

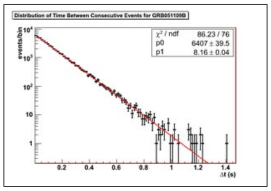

051111

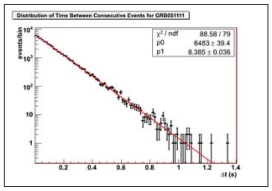

051114

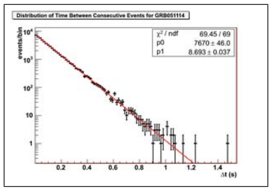

051117A

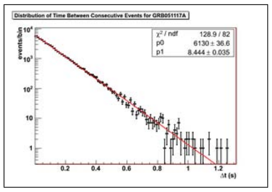

060105

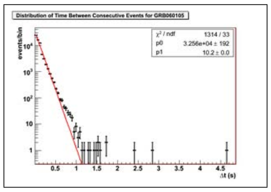

060108

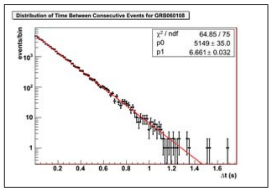

060109

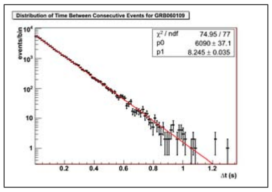

060110

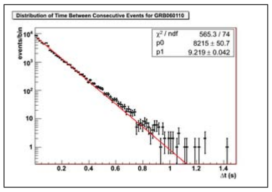

060111A

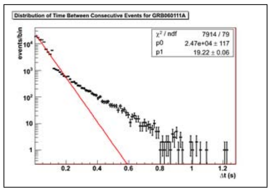

060202

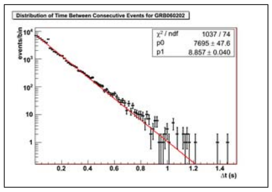

060204B

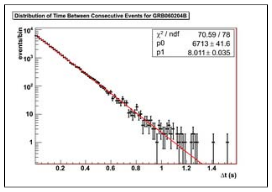

060211A

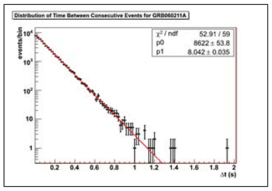

060211B

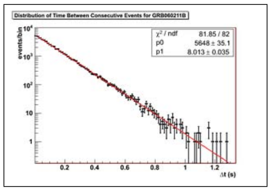

060218

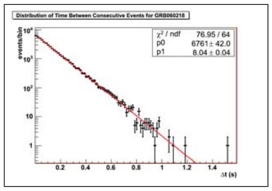

060219

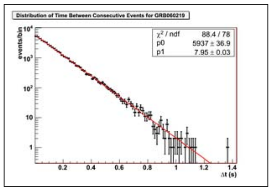

060312

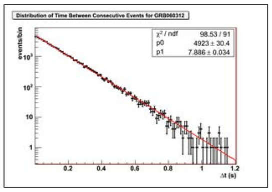

060319

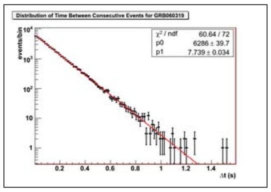

060323

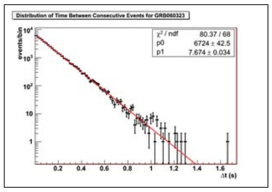

060403

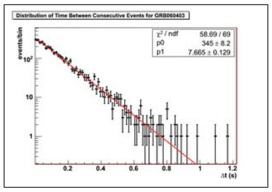

060413

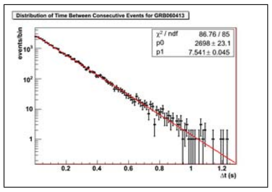

060421

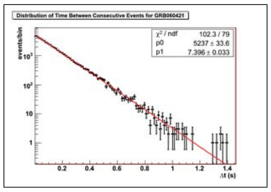

060424

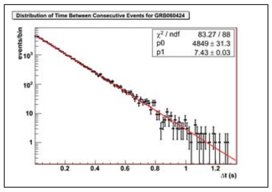

060427

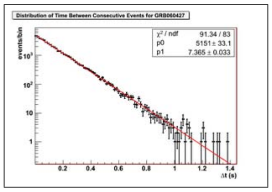

060428B

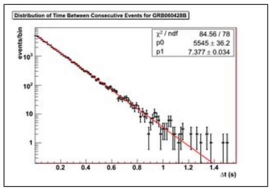

060501

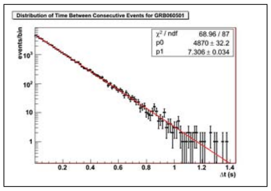

060502A

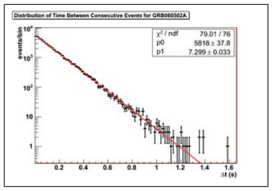

060502B

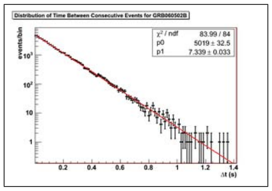

060507

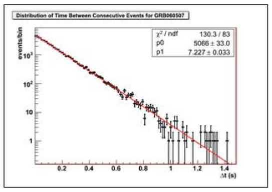

060510B

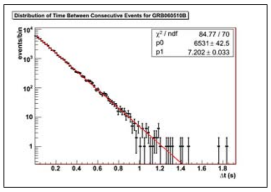

060512

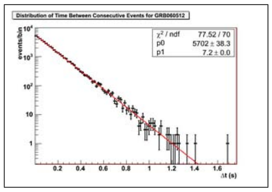

060515

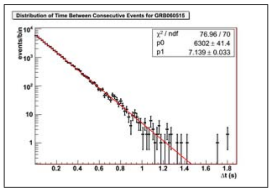

060522

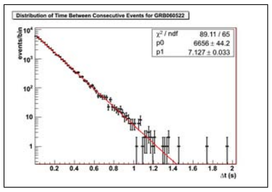

060526

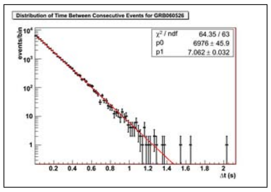

060602A

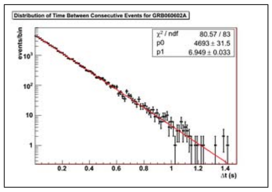

060607B

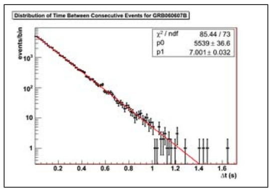

060712

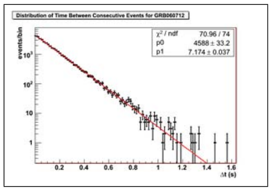

060717

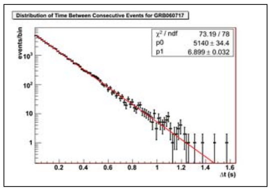

060801

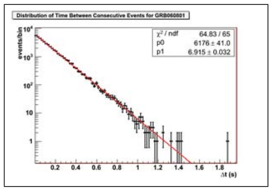

060805

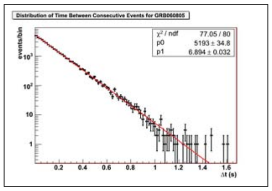

060807

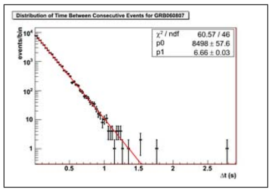

060814

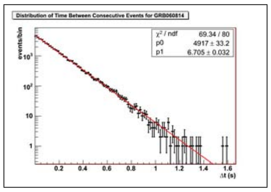

060825

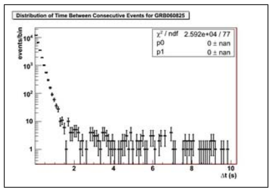

060904A

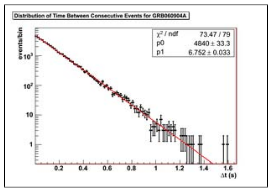

060906

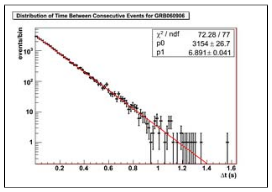

060912A

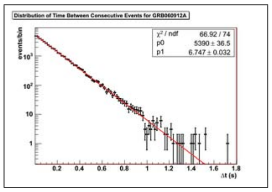

060923A

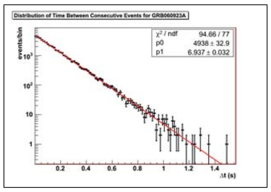

060923C

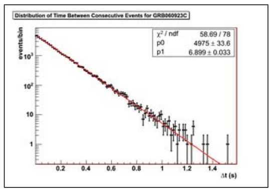

060926

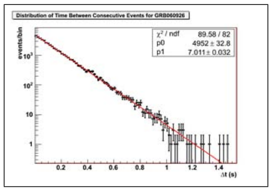

060929

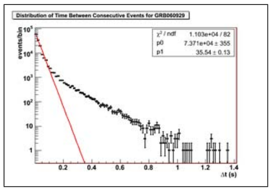

061002

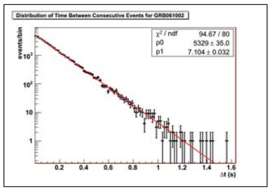

061019

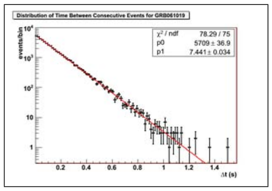

061028

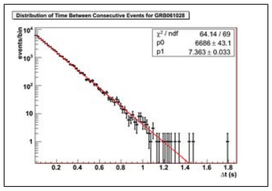

061110B